## About Journal

The University of Sistan and Baluchestan entered into strategic partnership with Iranian Association of Electrical and Electronic Engineers (IAEEE) to publish the **International Journal of Industrial Electronics Control and Optimization (IECO)**. The IECO is a refereed international journal which presents to the international scientific community important results of work in these fields, whether in the form of modeling simulation, analysis, fundamental research, development, application, design or real-time implementation. The scope of IECO is broad, encompassing all aspects of Industrial Electronics, Control and Optimization.

**Note**: International Journal of Industrial Electronics, Control and Optimization (IECO) has qualified to **ACADEMIC RESEARCH JOURNAL ( ELMI-PAJOHESHI)** status certified by the ministry of Science, Research and Technology of Iran ( No. 231566/3/18 dated 1396/10/09), and is published by the University of Sistan and Baluchestan through a formal partnership ( No. 952/2/1500 dated 1395/11/04) with Iranian Association of Electrical and electronic Engineers ( IAEEE) in order to develop scientific and research cooperation.

### Aims and Scope

International Journal of Industrial Electronics, Control and Optimization (IECO) is a Peer reviewed journal of advanced and state-of-the-art in the science and engineering of Industrial Electronics, Control and Optimization. Its Scope encompasses the applications of Industrial Electronics, power systems, control, optimization and computational intelligence for the enhancement of industrial and manufacturing system and processes. The scope of the journal include the following:

### I. Industrial Electronics

- *Low and high power converters*
- *Renewable energy*
- *Drive control techniques*
- *Techniques for advanced power semiconductor devices*
- *Power quality and utility applications*
- *Communications*
- *Flexible AC Transmission Systems (FACTS)*
- *Control in power electronics*
- *Electromagnetic and thermal performance of electronic power converters*
- *Motion control, robotics, sensors and actuators*
- *Fault detection and diagnosis*
- *Power systems*
- *Factory automation, communication, and computer networks*

### II. Control

- *Adaptive control*
- *Control of process systems*
- *Control theory*
- *Data processing*
- *Design of control systems*
- *Hybrid systems*
- *Identification and observation*
- *Intelligent systems*
- *Model-predictive control*
- *Optimal control*
- *Robust control*
- *Fractional order systems*

### III. Optimization

- *Ant Colony*
- *Chaos Theory*
- *Evolutionary Computing*
- *Fuzzy Computing*
- *Hybrid Methods*
- *Immunological Computing*
- *Neuro Computing*

- *Particle Swarm*
- *Probabilistic Computing*
- *Rough Sets*
- *Wavelet*

International Journal of Industrial Electronics, Control and Optimization © 2021 IECO
Vol. 4, No. 3, pp. 267-276, July (2021)

# Robust Sliding Mode-based UPQC for Transient Conditions in Weak/ Islanded Networks

Omid Moradi[1], Saeed Abazari[2†],Nima Mahdian Dehkordi[3]

[1,2] Department of Engineering, Shahrekord University, Shahrekord, Iran
3 Department of Electrical Engineering, Shahid Rajaee Teacher Training University, Tehran, Iran

**ABSTRACT**

*This paper proposes a nonlinear model by an optimal stabilizing controller for weak/islanded grids using a unified power quality conditioner (UPQC). The UPQC can be employed to stabilize a grid-tie inverter (GTI) or a synchronous generator (SG) with minimum control effort. The idea that GTI behavior is like synchronous generator is implemented in this study. The research aims at using advanced controller to reduce oscillations and achieve stability in a micro-grid. Here, the robust sliding mode controller-based UPFC is employed to design an optimal grid stabilizer. The paper considers variations in UPQC terminal voltage during the transient period of the system, unlike other articles that assume it to be constant. The performance of the proposed algorithm is evaluated by two benchmark networks. The paper presents a comparative study of transient stability in a micro-grid system under different loads. Simulation results reflect the robustness of the proposed sliding mode controller for oscillation reduction in comparison with the Lyapunov-based nonlinear optimal controller and PI controller. In addition, results show the effectiveness of the proposed nonlinear controller in controlling both GTI and SG in the micro-grid system.*

**Article Info**

***Keywords:***
Micro-grid, Power system stability , Sliding Mode Controller (SMC), Virtual synchronous generator (VSG).

***Article History:***
**Received** 2020-10-02
**Accepted** 2020-12-20

## I. INTRODUCTION

Recently, several researchers have paid significant attention to the problem of integrating renewable energy sources into power systems by similar characteristics of synchronous machines (SMs)[1]. The interaction between the power network and the corresponding micro-grid has been one of the most important issues in the electrical industry for the past few years. These networks face faults thataffect stability and protections [2].

The main difference between power networks and micro-grids is their energy-saving capabilities. Power networks have big power machines, and they have high potential for energy saving when a fault occurs, so they use this energy to achieve stability after clearing the error[3].However, in micro-grids, the energy-saving capability is very low so, these networks usually with fewer variations have most oscillations against. In micro-grids, renewable generators are usually applied, which connect to the network through a grid-tie inverter (GIT). By applying a proper controller method on DC links, the capacity of energy stability can be increased in a limited level. These phenomena have not been addressed in recent researches adequately.

For renewable generators (RG), the idea that GTI behavior is similar to a synchronous generator is implemented in many studies [4-9].Most studies in this field do not consider the capacitor stability and total stability of the system. In [4], the concepts of virtual synchronous machines (VSM) are presented. In this case, power electronic devices can produce virtual inertia that equals the rotor inertia of the synchronous generator. However, in this research, it is assumed that the inverter has unlimited energy. Moreover, the DC-link dynamic is not considered. In [5] and [7], the renewable source is connected to the main grid, and the inverter power is controlled. In this study, the inverter is modeled similar to an SG by considering a fictitious rotor angle, and the GTI phase angle mimics an SG rotor angle. In [10], an effective damping method to improve the VSM responses is proposed.

†**Corresponding Author**: abazari-s@eng.sku.ac.ir
Tel: +98-9133144539, University of Shahrekord, Faculty of Electrical and Computer Engineering, University of Shahrekord, Iran

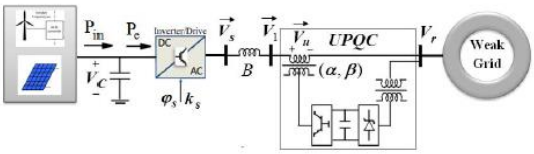


**Fig. 1**. RG connected to weak grid

But the DC-link voltage stability is not considered. In [11], a short-timeenergy reservoir is added to the network inverter and imaginary virtual inertia is obtained. This method eventually leads to the high cost of the combination compared to the DC-link capacitor. In [12], it is assumed that the capacitor dynamic is negligible, and small-signal analysis is used for the performance study of the islanding mode. This method extremely depends on DC-link with large capacity, and it is not practical in some cases. Also in applying rotating mass in virtual SG (VSG), the method needs the derivation of speed signal. In [13], a VSM control algorithm is proposed that simulates the traditional synchronous machine features. However, the synchronous machine inertia and the damping characteristics need to be changed, which makes the cost and simplicity of the operation economically important.

In all the above methods, SG-like behavior is assumed for flawless power systems. This assumption may not be correct in weak networks during fault occurrence. In stability discussion, the linear system theorem has been used for many years [14-15]. In most of these works, the nonlinear power grid model has been linearized around an operating point. However, these approaches assume that network variables are located in a small range of the reference operating point. In general, linear models of nonlinear systems are reliable only in specific regions, i.e., the operating point in which the system is linear. The model of a power network is nonlinear, especially during short circuits and transient behavior. Therefore, the linear system theorem is not applicable, and nonlinear controller designing is desirable for these systems.

The goal of optimal control in a power system is not only to maintain the system stability but also to reduce the speed of the oscillations with minimal effort to keep the desire performance. This case leads to the reduction of electrical stress on devices. Distributed flexible ac transmission systems (DIFACTS) elements are utilized to enhance control performance in distribution and micro-grid systems. This fact extends the control area to some broader stability. One of the most complete elements in micro-grid networks is UPQC. In distribution systems and micro-grids, UPQC can be equipped to increase network stability[16-17]. In addition to stability, these methods can improve power quality [18] and increases nonlinear loads [19]. In this paper, a robust sliding mode controller-based UPFC that uses intelligent algorithms is employed which can lead to a high degree of transient stability improvement. The typical characteristics of the SMC are that it is discontinuous and forces the system variables to slide along a pre-defined sliding surface to maintain stability. The controller is robust and can handle modeling inaccuracies.

This paper focuses on micro-grid and power network nonlinear features. Also, variations in terminal voltages are considered during the transient period, unlike previous works in which only a kind of single machine system connected to an infinite bus is used. Furthrmore, this idea that GTI behaviour is alike synchronous generator is implemented and the capacitor stability and total stability of the system is consider. A sliding mode controller (SMC) is presented to generator oscillation reduction. Further in order to better compare results, the Lyapunov controller and PI controller are designed.

This paper first describes the appropriate model of the renewable generator dynamics along with UPQC and the idea that the GTI behaves similar to the synchronous generator in Section II. The model is suitable for networks with renewable energy sources connected through GTI and the networks with SG. Next, Section III presents the system oscillation equation.Subsequently, Section IV discusses the design of a sliding mode controller to improve stability and reduce fluctuations after a fault. In general, the optimized proposed nonlinear controller is impressionable to operational changing conditions. It leads to the desired operation of the system even with topology or fault location changes. In Section V, in two benchmark networks, simulation results are proven for both low and high powers to consideration and optimization of the proposed optimal controller in comparison with a Lyapunov controller and a PI controller. Eventually, the paper is closed with some conclusions in Section VI.

## II. DYNAMIC MODEL OF THE RENEWABLE GENERATOR WITH UPQC

This section presents the dynamic model of a renewable generator connected to the GTI along with UPQC shown in Fig. 1. The presented model applies for both RG and SG, so the proposed sliding mode controller (introduced later) can be used for both.

### *A. Renewable generator*

where $V_c$ is the dc link voltage of the renewable source, $P_{in}$ is the power injected into the dc link by renewable energy sources, and $P_e$ is the power delivered to the inverter. The electrical power $P_e$ can be expressed as.

$$CV_C\dot{V}_C = P_{in} - P_e \quad (1)$$

Where $C$ is the capacitance, $V_c$ is the dc link voltage of the renewable source, $P_{in}$ is the power injected into the dc link by renewable energy sources, and $P_e$ is the power delivered to the inverter. The electrical power $P_e$ can be expressed as

$$P_e = V_S V_1 B \sin(\phi_s - \theta_1) \quad (2)$$

where $V_s$ is inverter output terminal voltage, $\varphi_s = \widehat{\varphi_s} + \varphi_{s0}$ is the inverter voltage phase angle, $\widehat{\varphi_s}$ and $\varphi_{s0}$ are the phase steady- state and error values, respectively, and $V_1$ and $\theta_1$ are the voltage and phase angle of the grid bus connected through B admittance, respectively. To regulation the RG output power, the phase angle of the GTI ($\varphi_s$) can be changed and thus acts like the rotor angle in a synchronous generator [20]. An auxiliary variable $\upsilon$ is used to control $\varphi_s$ in a renewable generator and can be determined such that

$$\dot{\widehat{\varphi}}_s = \upsilon \quad (3)$$

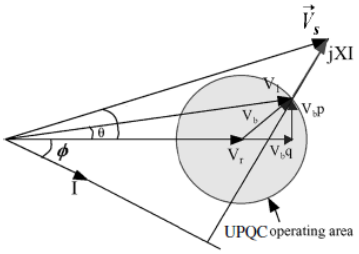


**Fig. 2**. Vector diagram of a UPQC connected to a network

The variable $\upsilon$ is similar to the rotor speed in a synchronous generator. In synchronous generators, speed is related to the kinetic stored energy in the rotor, and since the stored energy of the dc link capacitor can be changed by the GTI output power (via the output voltage phase error), it can be written as follows in order to create a significant relationship between $\upsilon$ and the energy stored in the dc link:

$$\dot{\upsilon} = V_C \dot{V}_C = (1/C) \times (P_{in} - P_e) \quad (4)$$

Here, saved energy is calculated based on the capacitor voltage $V_C$ according to Eq. (1). Therefore, the inverter phase angle error $\widehat{\varphi_s}$ is determined as a new state variable besides the variable v which mentions the capacitor saved energy changing.

$$\upsilon = (V_C^{\,2} - V_{C0}^{\,2}) / 2 \quad (5)$$

Eq. (5) indicates the amount of change in the stored energy of the dc link with *Vco* as the steady-state value of $V_C$. In a renewable generator, capacitor *C* plays the role of inertia of the machine, which means that its higher size reduces oscillation and contributes to dynamic stability.

In the proposed *GTI* model, by controlling the phase angle and gain, the renewable generator is modeled like synchronous generator dynamic where dc-link capacitor acts as energy storage like the rotor of the synchronous generator. Unlike the current VSG models [4-8] where imaginary inertia is considered, energy reserved in the dc-link capacitor plays the role of kinetic energy storage and appears as a dynamic state.

In the proposed method, GTI can be controlled with a simulation mechanism like an automatic voltage regulator (AVR) and a power system stabilizer (PSS) and their equivalent nonlinear features. Here, the equivalent classical-model SG, $M = C/\tau$ is inertia, $\delta = \varphi_S$ is rotor angle and $\omega = \upsilon$ is rotor speed error (capacitor voltage indicator) [2]. Therefore, the dc-link capacitor dynamic in Eq. (4) is taken into account like the rotor dynamic in the classic model of the generator. For the proposed model, there is no storage device or enormous capacitor capacity, and energy is provided by a usual dc-link capacitor.

### *B.UPQC Modelling*

A simplified scheme of a UPFC connected to the grid is shown in Fig. 1. UPQC includes a series transformer with $X_{SR}$ reactance, a shunt transformer with $X_{SH}$ reactance, two three-phase voltage source converters, and one dc-capacitor link. $C_{dc}$ and $v_{dc}$ are capacitance and dc-link voltage, respectively. According to the single-line diagram shown in Fig. 1, the UPQC vector diagram connected to the network is shown in Fig. 2 [22].

According to Fig. 2, *Vbp* and *Vbq* are the components of the series voltage of UPFC and can be written as

$$V_{bq} = V_r \beta(t) \quad and \quad V_{bp} = V_r \gamma(t) \quad (6)$$

where $\beta(t)$ and $\gamma(t)$ are converter gains for generating voltage $\vec{V}_u$ in UPQC series transformer. Neglecting network losses, according to Eq. (2), the electrical power can be expressed as

$$P_e = V_S V_1 B \sin(\delta - \theta_1) = V_S V_1 B (\sin\delta\cos\theta_1 - \cos\delta\sin\theta_1) \quad (7)$$

According to Fig. 2, it can be shown that $\cos\theta = (V_r + V_{bq})/V_1$ and $\sin\theta = V_{bp}/V_1$. As a result, according to Eq. (4), it can be used to obtain

$$\dot{\omega} = \left(\frac{1}{C}\right)\left(P_{in} - V_S V_r B \sin(\delta) + V_S B \cos(\delta) V_{bp} - V_S B \sin(\delta) V_{bq}\right) \quad (8)$$

In this paper, variations in terminal voltage $V_r$ are considered during the transient period of the system, unlike [23] that assumes $V_r$ to be constant. Therefore, the shunt terminal voltage can be decomposed into two fixed components $\bar{V}_r$ (steady-state value) and the variable part $D$ (disturbance) such that $V_r = \bar{V}_r + D$. Thus, Eq. (8) can be rewritten as

$$\begin{aligned}\dot{\omega} &= \left(\frac{1}{C}\right)(P_{in} - V_S V_r B \sin(\delta)) \\ &+ \left(\frac{1}{C}\right)(V_S B \cos(\delta) V_{bp} - V_S B \sin(\delta) V_{bq}) \\ &- \left(\frac{1}{C}\right)(V_S B \sin(\delta)) D\end{aligned} \quad (9)$$

## III. SYSTEM OSCILLATION EQUATIONS

The dynamic behavior of the system, as shown in Fig. 1, can be described by the swing equation as

$$\begin{cases}\dot{\delta} = \omega \\ \dot{\omega} = \hat{f} + \Delta f + \left(\frac{1}{M} P_{1u} - \frac{1}{M} P_{2u}\right)\end{cases} \quad (10)$$

Where $\omega$ is the relative rotor speed and $\delta$ is the relative rotor angle similar toasynchronous generator, defined as $\delta = \delta - \delta_0$ and $\omega = \omega - \omega_0$, respectively. Also, function $\hat{f}$, disturbance part $\Delta f$, and the powers $P_{1u}$ and $P_{2u}$ delivered to the system by UPQC are given by

$$\hat{f} = \left(\frac{1}{M}\right)\left(P_{in} - V_S V_r B \sin(\delta)\right)$$

$$\Delta f = \left(-\frac{1}{M}\right)\left(V_S B \sin(\delta)\right) D$$

$$P_{1u} = V_S B V_{bp} \cos(\delta)$$

$$P_{2u} = V_S B V_{bq} \sin(\delta)$$

Note that since the reactance of the transmission line is much greater than its resistance, the value of the resistance is assumed to be zero in all calculations. This can simplify the equations without having a significant effect on the transient response. In the above system, under a steady state, the relative speed $\omega$ is zero and the angle $\delta$ remains unchanged. In the event of an error, the structure of the system changes and accelerates or decelerates the rotor speed of the generators, leading to power oscillations. In this case, power oscillations must be controlled very quickly for transient stability to occur. Sliding mode controllers can quickly and continuously adjust the reactive power to amplify the system damping by rapidly changing the UPQC impedance or equivalent by adjusting the line voltage at the UPQC location.

## IV. Design of Local Sliding Mode Controller

SMC is a robust control approach appropriate for the control of time-variant systems in the presence of external disturbances. SMC uses a high-speed switched feedback control to sustain the control variable on the sliding surface. The gain in the feedback path switches between two values according to a rule that depends on the value of the variable at each instant. The aim is to drive the plant's state trajectory onto a pre-specified surface in the state space and to maintain it on this surface for subsequent time. A Lyapunov approach is used to characterize the switched control design that will maintain the plant state on the surface after interception [24].

The design procedure involves two steps: the selection of a sliding surface and the computation of a control law to force the system's trajectory towards and keeping it on the sliding surface. Consider the second-order system

$$\ddot{x} = f(x) + g(x)u \tag{11}$$

Where $u$ is the control input, x is the state vector, and the dynamics f (possibly nonlinear or time-varying) is not exactly known but estimated as $\hat{f}$ .We have state equations by

$$\begin{cases} \dot{x}_1 = x_2 \\ \dot{x}_2 = f(x) + g(x)u \end{cases} \tag{12}$$

The estimation error of $f$ is assumed to be bounded by some known function $F = F(x, \dot{x})$ ;

$$\left|f - \hat{f}\right| \le F \tag{13}$$

Let $e = x_d - x$ be the tracking error in the variablex. Furthermore, let us define a surface S in the state-space R(2) by

$$S = \dot{e} + \lambda e \tag{14}$$

and $\lambda$ is a strictly positive constant. Differentiation of the sliding variable gives

$$\dot{S} = \ddot{x}_d - \ddot{x} + \lambda(\dot{x}_d - \dot{x}) \tag{15}$$

This implies that

$$\dot{S} = \ddot{x}_d - \hat{f} - \Delta f - g(x)u + \lambda\dot{e} \tag{16}$$

The simplified, l St-order problem of keeping the scalar S at zero can now be achieved by choosing the control law u of Eq.(1) such that outside of S. This control law was formulated by the use of the Lyapunov stability theorem.

$$\frac{1}{2}\frac{d}{dt}s^2 \le -\eta|s| \;\Rightarrow\; \dot{s}\,\mathrm{sgn}(s) \le -\eta \tag{17}$$

where $\eta$ is a strictly positive constant. We then have

$$(\ddot{x}_d - \hat{f} - \Delta f - g(x)u + \lambda\dot{e})\,\mathrm{sgn}(s) \le -\eta \tag{18}$$

The best of a control law that would achieve $\dot{s} = 0$ is thus

$$g(x)u = \ddot{x}_d - \hat{f} + \lambda\dot{e} \tag{19}$$

In order to satisfy sliding condition (17) despite uncertainty on the dynamics f, we add to Eq. (19) a term discontinuous across the surface s=0, so

$$g(x)u = \ddot{x}_d - \hat{f} + \lambda\dot{e} + k\,\mathrm{sgn}(s) \tag{20}$$

By choosing k to be large enough, we can now guarantee that Eq. (17) is verified. Indeed, we have from Eq. (18) and (20)

$$k + \Delta f\,\mathrm{sgn}(s) \ge \eta \tag{21}$$

So that, letting

$$k = F + \eta \tag{22}$$

Here $F$ is a known bound for error estimation. If g(x) is known, the control law from Eq. (20) is as follows

$$u = \frac{1}{g(x)}\left(\ddot{x}_d - \hat{f} + \lambda\dot{e} + (F+\eta)\mathrm{sgn}(s)\right), g(x) \ne 0 \tag{23}$$

If $g_{\min} < |g(x)| < g_{\max}$ we have

$$u = \frac{\left(\ddot{x}_d - \hat{f} + \lambda\dot{e} + (F+\eta)\mathrm{sgn}(s)\right)}{g_{\min}}\mathrm{sgn}(g) \tag{24}$$

A higher value of k essentially compensates for a larger uncertainty, and results in better tracking.

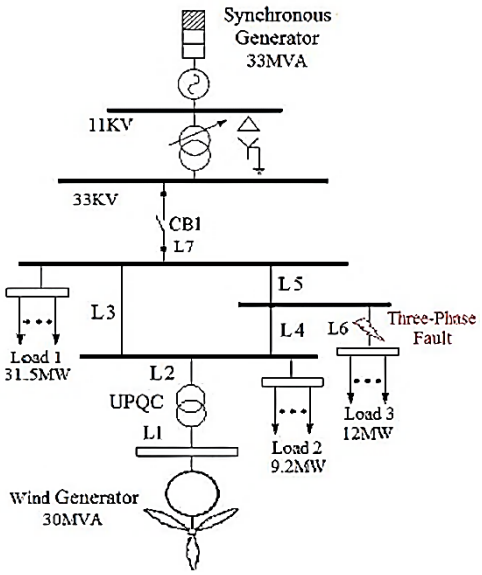


**Fig. 3**. Wind farm connected to the weak network [25].

However, this benefit comes at the expense of an undesirable higher control activity (chattering) around the sliding surface. A typical solution in this paper is to replace the discontinuous *signum* function, in *sgn(s)* in Eq. (20), by the smoother function sat(x/ φ ), where φ >0. With such modification all control signals would be continuous with no high-frequency (chattering) activities.

In this paper, the PSO algorithm is applied to approximate the unknown coefficients required in the controller.

## V. Simulation Results

In this section, the realization of stability through simulation to illustrate the effectiveness of the sliding mode controller in reducing the power oscillations on weak and islanded grids using UPQC is presented by implementing two scenarios. The two scenarios are implemented in a similar way to [25].

### *A. Case Study1*

In this section, controller performance is considered in oscillation damping for a wind farm connected to a small power grid [26] through a GTI according to Fig. 3. As previously mentioned, all available excitation control methods for the simultaneous generator can be used for a renewable generator equipped with a proposed mechanism such as GTI excitation. The PSO algorithm is applied to approximate the unknown coefficients required in the controller. Further, to enhance the performance of the UPFC, PSO-based SMC, Lyapunov controller, and PI controller [27] are designed to improve the damping of oscillations and transient stability of the system. Transient responses of the three controllers are compared in RG dc-link voltage, SG speed, series voltage, and injected power of UPQC. The network is simulated using Table I data in Matlab software.

**TABLE I**

Microgrid Parameters for High Power Scenario [25].

| | | |
|---|---|---|
| Generator Characteristic | Base Power | 33MVA |
| | Base Voltage | 11KV |
| | $x_d$ | 0.264pu |
| | $H = \omega_s M / 2$ | 1.3S |
| Load | Load 1 | 31.5 MW(PF=0.98) |
| | Load 2 | 9.2MW(PF=0.98) |
| | Load 3 | 12MW(PF=1) |
| Line | Resistance(R) | $0.02546\,\Omega/km$ |
| | Inductance(L) | $0.9337\,mH/km$ |
| | Capacitance(C) | $0.0127\,\mu F/km$ |
| | Total Length of grid=5km | |
| Renewable Sources | Power | 21.6MW |

**TABLE II**

Microgrid Parameters for Low Power [25].

| | | |
|---|---|---|
| Scenario Load | Load 1 | 15.75Mw(pf=0.98) |
| | Load 2 | 4.6MW(PF=0.98) |
| | Load 3 | 6MW(PF=1) |
| Renewable Sources | Power | 18MW |

Speed governor and PSS are applied to the SG in all simulations. To prove the robustness of the controllers, the analysis is tested under different loads according to Tables I and II. As is seen in Fig. 3, a three-phase fault occurs in one of the lines. To run the simulation, at first, there is no fault in simulation for 0.2s, and a fault is then imposed for 50ms. The controller does not inter during the fault to prevent the exorbitance series voltage injection. In fact, the controller will inter after fault clearing. The process has robustness and satisfactory performance in a wide range. Figs. 4 and 5 show the ability of the proposed controller (SMC) to improve the system oscillations in high power scenarios.

Fig. 4a shows the RG dc-link voltage and Fig. 4b shows the SG speed according to which system oscillations are considerable after fault occurrence and the system tends to instability. Then, using the UPQC with the proposed controllers, the oscillations are greatly reduced. As shown in Figs. 4c and 5, the UPQC series voltage and power into the transmission line using the optimal proposed controller (SMC) are in acceptable ranges where the maximum UPQC power is around 1.1 MW that is about 4% of the transmission line power. In the proposed method, the robustness of the optimal controller is provable with the execution of the second scenario under a low load level according to Table II. According to Fig. 6, it is observed from the transient response of the microgrid system that the oscillations are minimized because of the proposed controllers and are subsequently died out with minimum settling time and overshoots. Also, the simulation shows the satisfactory damping performance of the proposed SMC controller verifying the robustness of the optimal controller working at different loads.

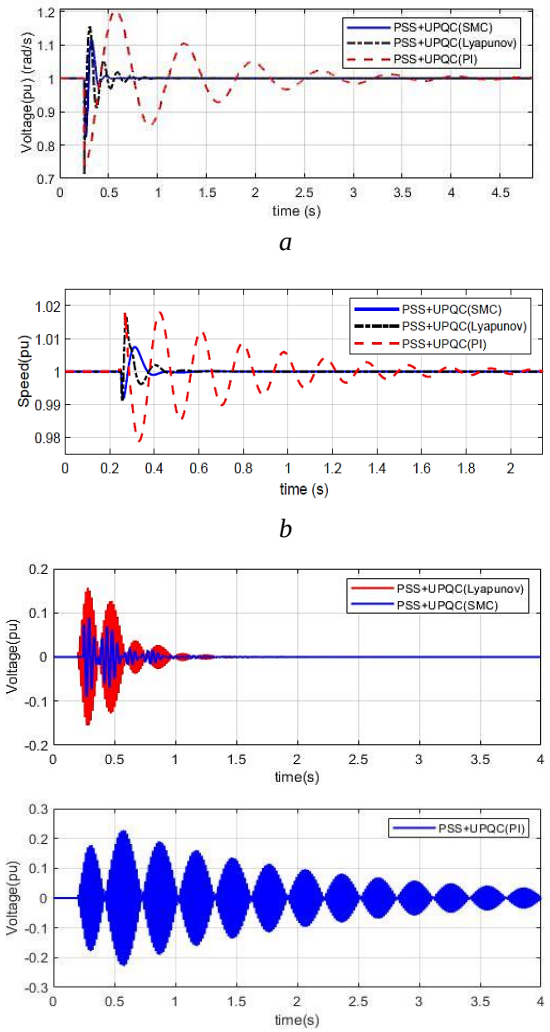


**Fig. 4**. Case study 1- high load levels: comparison of the proposed optimal nonlinear controller by SMC, Lyapunov controller and PI controller

a:RG dc-link voltage, b: SG speed, c: UPQC series voltage

*B. Case Study2*

In the second simulation scenario, the damping of power system oscillations is investigated by comparing the performance of the proposed optimal controller with the Lyapunov controller and PI controller. Here, the effectiveness of the proposed controllers in the islanded microgrid is studied in which oscillations in SG are controlled by UPQC. As shown in Fig. 7, the microgrid contains SG, renewables source, and loads. Table III shows the specifications of the test system.

Here, the proposed nonlinear optimal controller and two other controllers are applied to the UPQC series transformer to improve the transient characteristics. In all simulations, the speed governor and PSS are active. According to Table III, the loads are constant impedance with a power factor of 1 and 0.9.

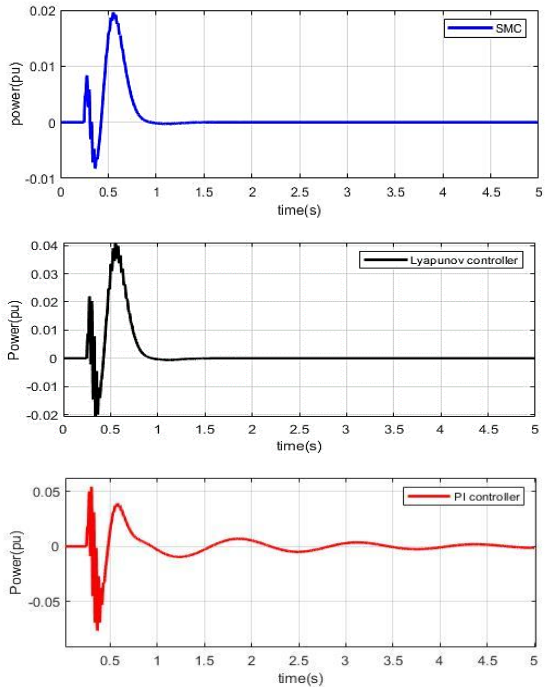


**Fig. 5**. Case study 1- high load levels: Injected power of UPQC comparison of the proposed optimal nonlinear controller by SMC, Lyapunov controller and PI controller.

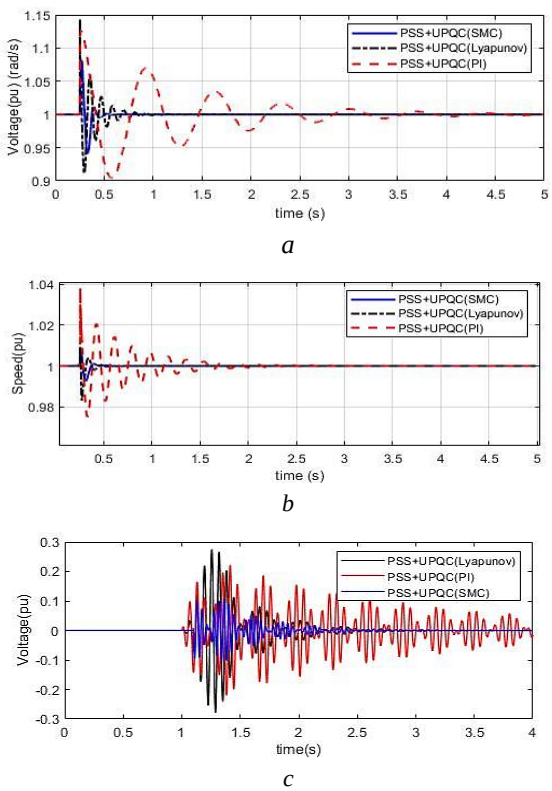


**Fig. 6**.Case study 1- low load levels: comparison of the proposed optimal nonlinear controller by SMC, Lyapunov controller and PI controller

a:RG dc-link voltage, b: SG speed, c: UPQC series voltage

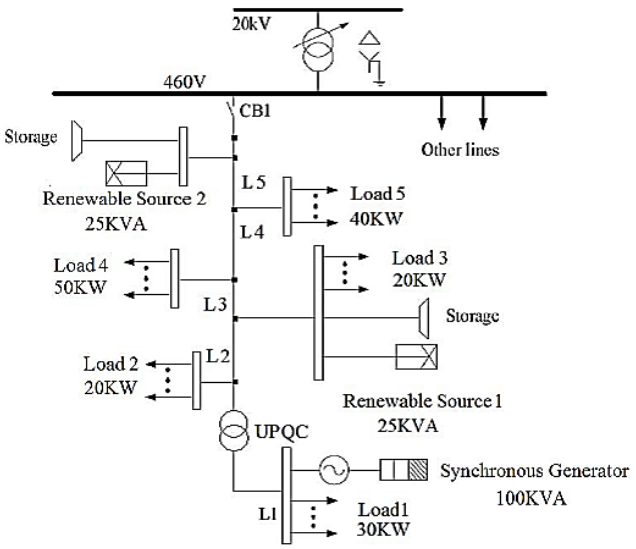


**Fig.7** . Benchmark low-voltage microgrid [25].

**TABLE III**

Grid Parameters with High Load Levels [25].

| | | |
|---|---|---|
| Generator Characteristic | Base Power | 100 KVA |
| | Base Voltage | 460 V |
| | $x_d$ | 0.17 pu |
| | $H = \omega_s M / 2$ | 0.1268 S |
| load | Load 1 | 30KW(PF=1) |
| | Load 2 | 20 KW(PF=1) |
| | Load 3 | 20 MW(PF=0.9) |
| | Load 4 | 50 KW(PF=1) |
| | Load 5 | 40 KW(PF=0.9) |
| Line | Resistance(R) | $0.02546\,\Omega / km$ |
| | Inductance(L) | $0.9337\,mH / km$ |
| | Capacitance(C) | $0.0127\,\mu F / km$ |
| | Total Length of grid=5km | |
| Renewable Sources | Power | 30 KW |

Renewable energy sources have been used to transfer fixed power to the grid. These sources are connected to the network via impedance. Here, to help reduce sudden energy fluctuations, renewable energy sources are equipped with storages, unlike the previous scenario. A three-phase fault occurs in the UPQC bus.

To perform the simulation, the system is first simulated for 1 second without any faults; then, a three-phase fault is applied for 100ms. The controller acts after fault removal (t=1.1s). Figs. 8 and 9 show the damping effect of the UPQC controller by the proposed algorithm with the SMC method compared to the Lyapunov and PI controller in the presence of PSS and governor.

The SG speed in Fig. 8a is shown, according to which the proposed nonlinear optimal controller can reduce post-fault oscillations with less amplitude and time compared to the figure 8band 8c Lyapunov and PI controller. The UPQC series voltages in Fig. 8 and the power injected UPQC to the line are shown in Fig. 9. According to Figs. 8b and 9, the injected series voltage is less than 0.1PU, and the maximum power injected by UPQC is about 0.28 of the line power and about 1.5 kW. It is clearly evident that the proposed controller has a better transient response and the voltage and power injected by the UPQC series transformer are lower than those of the Lyapunov and PI controller.

Next, the error time is increased to 0.2s and the performance of the SMC with the Lyapunov and PI controller are compared. It is notable that the speed of response and the settling time are improved using SMC in comparison with the Lyapunov and PI controller.

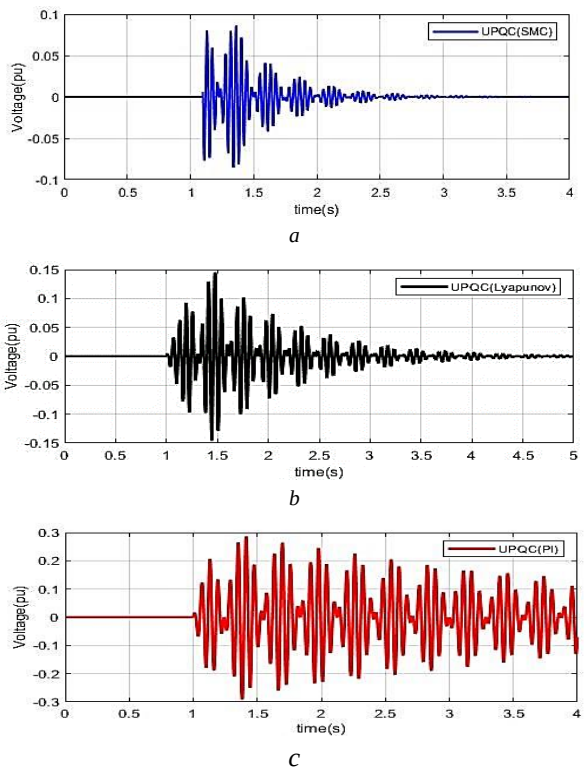


**Fig. 8**. Case study 2 -Comparison of the proposed optimal a:nonlinear controller (SMC), b:Lyapunov controller c: PI controller; fault duration 0.1 s.
a:SG speed, b: UPQC series voltage

Due to changing conditions after the network error, as shown in Figs. 10 and 11, the performance of the PI controller is different from the performance of the SMC and Lyapunov controller. This is due to the fact that the linear models of the nonlinear systems are reliable only in specific regions, i.e., the operating point, in which the system is linear [28]. It is clear that the PI controller, even with more effort to control, cannot reduce the oscillations to the size of the proposed controller.

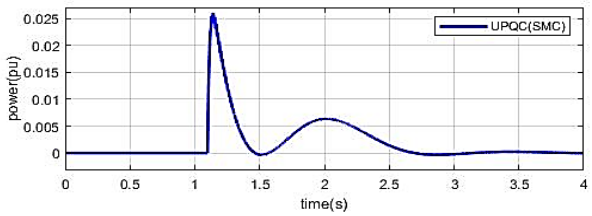


a

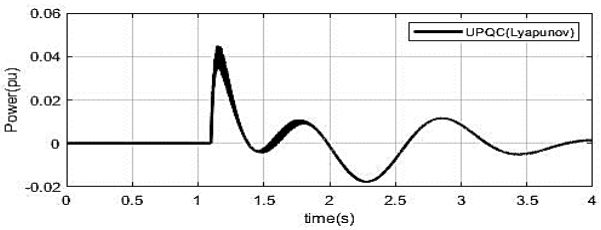


**b**

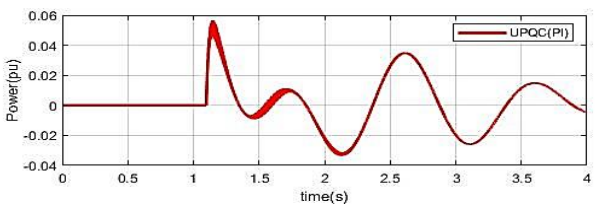


**c**

**Fig. 9**. Case study 2- Comparison of the proposed optimal a:nonlinear controller (SMC), b:Lyapunov controller c: PI controller - Injected power of UPQC; fault duration 0.1s.

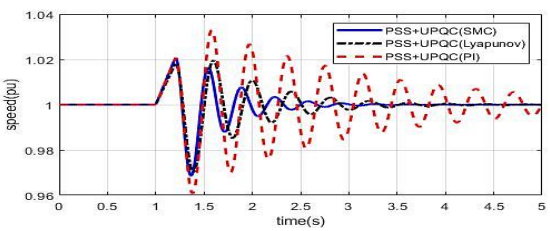


*a*

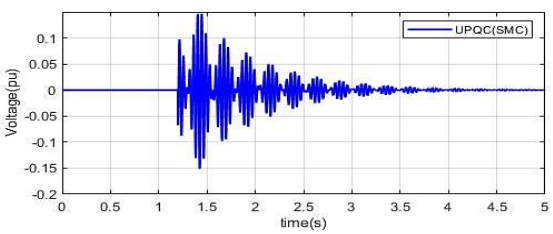


*b*

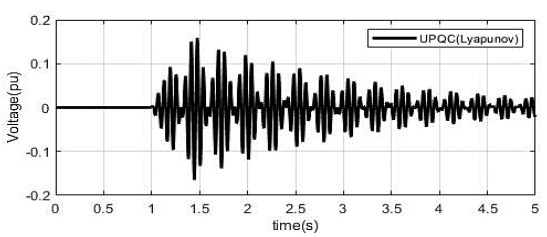


*c*

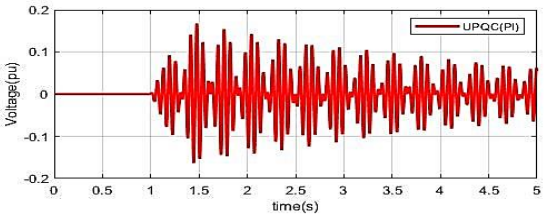


*d*

**Fig. 10**. a:Case study 2 -Comparison of the proposed optimal nonlinear controller (SMC), Lyapunov controller and PI controller; fault duration 0.2 s.
b: UPQC series voltage(SMC)c: UPQC series voltage(Lyapanov) d: UPQC series voltage(PI)

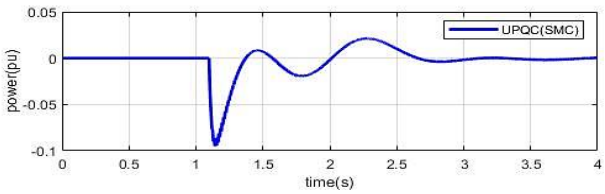


a

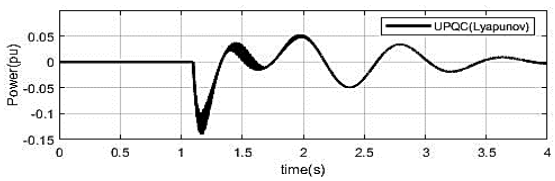


b

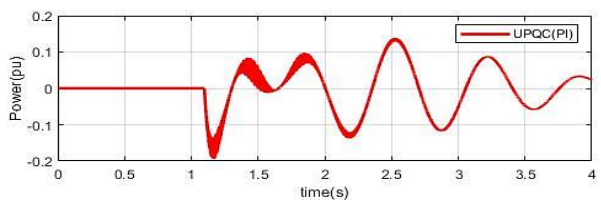


**c**

**Fig. 11**. Case study 2- a:Comparison of the proposed optimal nonlinear (SMC)b: Lyapunov controller c: PI controller- Injected power of UPQC; fault duration 0.2 s.

## VI. Conclusion

In this paper, a nonlinear optimal controller is used to reduce oscillations in a renewable energy source and in the synchronous generator connected to the weak grid and microgrid. Using the new modeling approach, a network equipped with UPQC is modeled as a nonlinear dynamic system. In addition to its power quality tasks, UPQC acts as a motive controller by series voltage injection. In this study, a dynamic model of the network with a third rank model of SG and UPQC as a stabilizer element is used. After standard form determination, a sliding mode controller (SMC) is presented to generator oscillation reduction. To optimize the controller

parameters, a PSO algorithm is presented according to the new acceleration coefficient. The method is practicable without complicated calculations and makes a good balance between the general and local search of the main algorithm. The results show that the proposed algorithm achieves an exact solution for all problems. In this paper, the realization of stability through simulation to illustrate the effectiveness of the sliding mode controller in reducing the power oscillations on weak and islanded grids using UPQC by implementing two scenarios is proven. Further, to better compare the results, the Lyapunov controller and PI controller are designed. According to the simulation results, the proposed algorithm has a considerable impact on oscillation reduction. Also, it is sustained against variations of load and error time. Robustness against parameters' variations and disturbance rejection properties are two important capabilities of the proposed SMC. Besides, these two properties are the main weaknesses of the linear controllers and cannot be ignored in practical applications because high order dynamics, measurement errors, modeling errors, and the nonlinear nature of power systems are inevitable.

## References


[1] M. Ashabani, J. Jung, ''Synchronous Voltage Controllers: Voltage-Based Emulation of Synchronous Machines for the Integration of Renewable Energy Sources '', *IEEE Access*., 10, (8), pp 49497–49508,2020.

[2] S. Kazemlou, S. Mehraeen ,''Novel Decentralized Control of Power Systems With Penetration of Renewable Energy Sources in Small-Scale Power Systems'', *IEEE Trans. Power Electron*., 29,(4), pp. 1–11,2014.

[3] S. Wei, Y. Zhou, G. Xu, et al.:''Motor-generator pair: a novel solution to provide inertia and damping for power system with high penetration of renewable energy'', *IEEE Trans. Power Syst.*, 32,(2), pp. 1422–1429,2017.

[4] H.-P. Beck, R. Hesse,''Virtual synchronous machine'', *In Proc. 9th Int.Conf. EPQU*, pp. 1–6, 2007.

[5] Q.-C. Zhong, G. Weiss, ''Synchronverters: Inverters that mimic synchronous generators'', *IEEE Trans. Ind. Electron*., 58,(4),pp. 1259–1267, 2011.

[6] J. Driesen, K. Visscher, ''Virtual synchronous generators'', *In Proc.IEEE Power Energy Soc. Gen. Meeting Convers. Del. Elect. Energy 21stCentury*, pp. 1–3, 2008.

[7] S. D'Arco, J.A. Suul, ''Virtual synchronous machines—Classificationof implementations and analysis of equivalence to droop controllers for microgrids'', *In Proc. IEEE Grenoble Power Tech*, pp. 1–7, 2013.

[8] Q.-C. Zhong, ''Virtual synchronous machines: A unified interface for smart grid integration'', *IEEE Power Elec. M*, 3,(4), pp. 18-27, 2014.

[9] M. P. N. Van Wesenbeeck, S. W. H. De Haan, P. Varela, et al.:''Grid tied converter with virtual kinetic storage'', *IEEE Bucharest Power Tech*, pp. 1–7, 2009.

[10] M. Ebrahimi, S.A. Khajehoddin, ''An improved damping method for virtual synchronous machines '', *IEEE Trans. On sustainable Energy*, 10, (3), pp. 1491–1500, 2019.

[11] Y. Ma, W. Cao. L., F. Wang, ''Virtual Synchronous Generator Control of Full Converter Wind Turbines with Short Term Energy Storage'',*IEEE Trans. on Industrial Electronics*,64, (11),pp. 8821–8831, 2017.

[12] O. Mo, S. D'Arco, ''Evaluation of Virtual Synchronous Machines with Dynamic or Quasi-Stationary Machine Models'', *IEEE Trans. on Industrial Electronics*, 64, (7), pp. 5952–5962, 2017.

[13] D. Chen, Y. Xu, ''Integration of DC Microgrids as Virtual Synchronous Machines into the AC Grid'',*IEEE Trans. on Industrial Electronics*, 64, (9), pp. 7455–7466, 2017.

[14] H. Wang, '' A unified model for the analysis of FACTS devices indamping power system oscillations. III. Unified power flow controller'',*IEEE Trans. Power Del.*,15, (3), pp. 978–983, 2000.

[15] C.-T. Chang, Y.-Y. Hsu, '' Design of UPFC controllers and supplementarydamping controller for power transmission control and stabilityenhancement of a longitudinal power system'', *IEE Proc.-Generat.,Transmiss., Distrib*., 149,(4), pp. 463–471, 2002.

[16] A. Mohanty, S. Patra, P. K. Ray, ''Robust fuzzy-sliding mode based UPFCcontroller for transient stability analysis inautonomous wind-diesel-PV hybrid system'', *IET Gener. Transm. Distrib*., 10, (5), pp. 1248–1257, 2016.

[17] C. Leonardo, S. Sérgio, O. Azauri, et al.: ''Power Flow and Stability Analyses of a Multifunctional Distributed Generation System Integrating a Photovoltaic System With Unified Power Quality Conditioner'', *IEEE Transactions on Power*, 34, (7), pp 6241-6256, 2019.

[18] L. Shubh, G. Sanjib, ''Modelling and allocation of open-UPQC-integrated PV generation system to improve the energy efficiency and power quality of radial distribution networks '', *IET Renewable Power Generation*, 12, (5), pp 605-613, 2018.

[19] C. Saurav, D. Anubrata, A. Sandeep, et al.: ''Adaptive shunt filtering control of UPQC for increased nonlinear loads'', *IET Power Electronics*, 12, (2), pp 330-336, 2019.

[20] P.W. Sauer and M. A. Pai, "Power system dynamics and stability," *Stipess*, Jan. 2007.

[21] M. Abido, ''Parameter optimization of multi machine power system stabilizers using genetic local search'', *Int JElectr Power Energy Syst*, pp.785–794, 2001.

[22] Y. Ma, W. Cao. L., F. Wang, ''Improving of Transient Stability of Power Systems Using UPFC'',*IEEE Trans. on Power Delivery*, 20, (2),pp. 1677–1682, 2005.

[23] H. Nazaripouya and S. Mehraeen, "Control of UPFC using Hamilton–Jacobi–Bellman formulation based neural network," in Proc. *IEEE PES General Meeting*, San Diego, CA, USA, pp. 1–8, 2012.

[24] A. Mohanty, S. Patra, A. Mohamed, et al: ''Robust fuzzy-sliding mode based UPFC controller for transient stability analysis in autonomous wind-diesel-PV hybrid system' *IET Gener., Transm. &Distrib*., pp.1–10, 2016.

[25] H. Nazaripouya, S. Mehraeen, ''Modeling and Nonlinear Optimal Control of Weak/Islanded Grids Using FACTS Device in a Game Theoretic Approach'', *IEEE Trans. Power Electron*. 29,(4), pp 1–11, 2015.

[26] Z. Saad-Saoud, M.L. Lisboa, J.B. Ekanayake, et al.,: ''Application of STATCOMs to wind farms'', *IEE Proc.-Generat., Transmiss., Distrib*., 145,(5), pp. 511–516, 1998.

[27] M. A. Kamarposhti, " Optimal Control of Islanded Micro grid Using Particle Swarm Optimization Algorithm", *IECO*, 1(1), pp.53-60, 2018.

[28] A, Ajami. A.M., Shotorbani, M.P., Aagababa,: 'Application of the direct Lyapunov method for robust finite-time power flow control with a unified power flow controller', *IET GT&D*, 6, (9), pp. 822–830, 2012.

**Omid Moradi** received his B.Sc. degree in electrical engineering from Islamic Azad University, Khomienishahr, Iran, in 2005, the M.Sc. degreein electrical engineering from Sajad University of Technology, Mashad, Iran, in 2007,. He joined the the Department of Electrical Engineering, Jahad Daneshgahi higher Education Institute, Isfahan, Iran, in 2009, where he is currently an Instructor. He admitted to Shahrekord University in 2014 as a Ph. D student .His research interests include power systems, control systems, nonlinear control, controlledof FACTS elements in power and microgrid systems.

**Saeed Abazari** received his B.Sc. degree in electrical engineering from Isfahan University of Technology, Isfahan, Iran, in 1989, the M.Sc. degree from Ferdowsi University, Mashhad, Iran, in 1992 and the Ph.D. degree from Sharif University of Technology, Tehran, Iran, in 2002. Currently, He is a Professor of the Electrical Engineering Department at the Shahrekord University, Shahrekord, Iran. His research interests are electric power distribution system, smart grid, power system operation and control and FACTS controllers.

**Nima Mahdian Dehkordi** received the M.Sc. and Ph.D. degrees from Sharif University of Technology, Tehran, Iran, in 2012 and 2016, respectively, both in electrical engineering. He joined the the Department Shahid Rajaee Teacher Training University Tehran, Iran, in2017, where he is currently an Assistant Professor. His research interests include control systems, applications of control theory in power electronics, microgrid control, distributed and cooperative control, internet of things, nonlinear control, and network control.

International Journal of Industrial Electronics, Control and Optimization © 2021 IECO
Vol. 4, No. 3, pp. 277-284, July (2021)

# Discrimination among Winding Mechanical Defects in Transformer Using Noise Detection and Data Mining Boosting Method

Zahra Moravej[1,†], Seyed Mahmoud Mortazavi[2], Mojtaba Mohseni[3]

[1,2]Faculty of electrical and computer engineering, Semnan university, Semnan, Iran
[3]Faculty of electrical engineering, Amirkabir university, Tehran, Iran

**ABSTRACT**

*This paper proposes, an efficient method to detect and discriminate mechanical defects of transformer winding based on extracting the winding frequency responses using outlier data detection and ensemble algorithms, which together constitutes an efficient hybrid method. First, the frequency response of the high voltage winding of a real transformer model (1.6 MVA) was extracted in different condition and arranged as primary data. Then, due to the high standard deviation of the characteristics and the weight of the outlier samples above the threshold of 1.1, the Local Outlier Factor (LOF) method was used to clean the samples. Finally, data mining algorithms have been used to detect and distinguish mechanical defects. Based on the results, the decision tree bagging ensemble method reported the best accuracy compared to other techniques and improved the accuracy of the decision tree with total accuracy of 92.68% by LOF. These results also showed that all methods improved accuracy by LOF. It can, therefore, be claimed that the proposed method is capable of discriminating transformer winding mechanical defects accurately.*

**Article Info**

***Keywords:***
Decision tree, Ensemble algorithms, Frequency response, Local Outlier Factor.

***Article History:***
**Received** 2020-12-07
**Accepted** 2021-03-22

## I. INTRODUCTION

Transformers play a major role in electric power generation, transmission, distribution and utilization, from both technical and economic perspectives. Transformer performance at different levels has a vital and effective role in maintaining the stability and improving the reliability of the power system. Therefore, it is paramount to use of efficient protection systems to clear faults as fast and safe as possible. One way to predict failure or defects is to use data mining methods. Data mining can be defined as the process of discovering meaningful relationships and patterns by examining large volumes of data [1]. This concept has recently been the subject of many scientific papers, conferences and dissertations. Data mining is a combination of machine learning techniques, pattern recognition and statistical methods.

According to [2, 3], the most common techniques in fault prediction are regression methods and neural network. The paper [4] evaluates data mining techniques in predictive maintenance (PdM) to predict the insulation fault using the analysis of data on the gas dissolved in oil of power transformers. In this evaluation, the accuracy and efficiency of the RBF artificial neural network is compared with Gaussian kernel methods in the support vector machines (SVMs) model, the C4.5 decision tree and the nearest neighbor K.

Ref. [5], proposes a new approach with wavelet transform

[†]**Corresponding Author**:zmoravej@semnan.ac.ir,
Tel: +982331532678, Electrical & Computer Engineering Faculty, Semnan University, Semnan, Iran

method and modeling with LS-SVM method to predict the amounts of dissolved gases in oil-immersed transformers. The particle optimization algorithm was used to optimally select the parameters in the wavelet transform. The results were compared with several neural network models, regression and support vector machines, and the error of the proposed model was evaluated less with a large difference. The importance of feature selection and removal of excess space is examined to detect the pattern in the Ref. [6], They used the RF random forest technique to select effective features. In Ref. [7], ANN neural network method was applied to the data to distinguish among mechanical defects of windings and other electrical faults. This paper is dependent on the training data and if the location of the windings was changed, the model error would be reduced.

In [8], a fault prediction model is proposed by first determining the parameters and signals in MATLAB software and changing them to a suitable value to detect mechanical defects in the data preparation step, the internal and external fault types of the device and the input current of the transformer are simulated. These signals are then converted into the properties of the training model by wavelet transform and, during the training, the decision tree classifier and artificial neural network are used to do modeling.

Various intelligent methods have also been used in the articles for detecting and classifying types of faults, including decision tree (DT) methods [9], artificial neural network (ANN) [10], SVMs [11], Fuzzy algorithm [12].also methods used to extract feature vector have included intelligent transformations such as wavelet transform [13], S transform [14-15], Time-time conversion [16], mathematical indicator [17], numerical indices [18] which have good learning capability and generalizability.

This paper used ensemble machine learning techniques to identify and distinguish transformer fault with two types of axial deformation (AD) and radial deformation (RD) faults. Algorithms in a comparative mode include the C4.5 decision tree base methods, the support vector machines ,the bagging ensemble methods, the random forest, and the new boosting gradient method which has received less attention in recently published articles about transformer fault prediction , were also tested in this research.

## II. STUDY OF TRANSFORMER WINDING MECHANICAL DEFECTS

Many transformer insulation faults are a direct result of reduced insulation strength due to mechanical faults in transformers winding. Two types of common mechanical faults are AD and RD which are investigated in this paper.

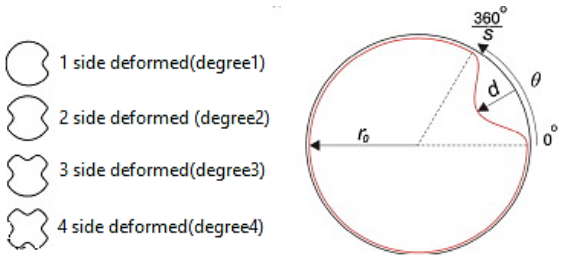


**Fig. 1**. Different degrees of radial deformation

As shown in Figure 1, the recessed shape of the winding has a sinusoidal curve with a certain depth and width. This condition increases the capacitance between the coils and decreases the capacitance between the high-voltage winding and the ground. r(θ) can be modeled as Equ.(1).

$$r(\theta) = \begin{cases} r_0 + \frac{d}{2}(\cos(s\theta - 1) & for\ 0 < \theta < \frac{2\pi}{s} \\ r_0 & otherwise \end{cases} \quad (1)$$

where, d represents the depth of the deformation and, s represents the width of the deformation. Furthermore, $\theta$ is the angle of deformation extent level and $r_0$ is the radius of the winding in the healthy state. Figure 2 shows an example of this fault on the transformer winding.


**Fig. 2**. Radial deformation on the transformer winding

In the detailed model, the parallel capacitor represents the electric field between the disks with each other or with the ground. In the defective state, the parallel capacitor $C_i$ is calculated by Equ.(2) [19].

$$C_i = \sum_{\theta=0}^{2\pi} \left[ \frac{2\pi\varepsilon_0\varepsilon_r}{Ln\left(\frac{r_0}{r(\theta)}\right)} \right] . \Delta\theta \quad (2)$$

The results of the experimental and numerical research confirm the relationship between the change of the detailed model parameters and the mechanical deformation of the winding. To model the axial displacement defect of the winding, it is assumed that the high-voltage winding is displaced by an impact in the direction of its axis. Figure 3 shows an example of this type of fault.

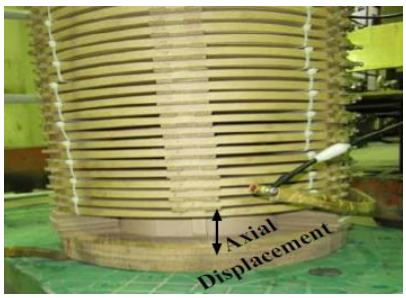


**Fig. 3**. Axial displacement fault on the transformer winding

According to the studies, it is clear that the axial displacement changes the components of the inductance matrix (M) that describes the mutual inductances between the components of the winding.

## III. RESEARCH METHOD

The method presented in this paper is composed of three parts. After obtaining the technical specifications of a real transformer from the manufacturer and simulating this transformer with CST software , the frequency response of the transformer winding was firstly calculated in different modes of mechanical defects. Then, according to the high standard deviation of the characteristics and the weight of the outlier samples exceeding the threshold of 1.1, the LOF method was used to remove the samples and finally, the machine learning methods were used to classify and to detect the type of Fault. Figure 4 shows the classification method.

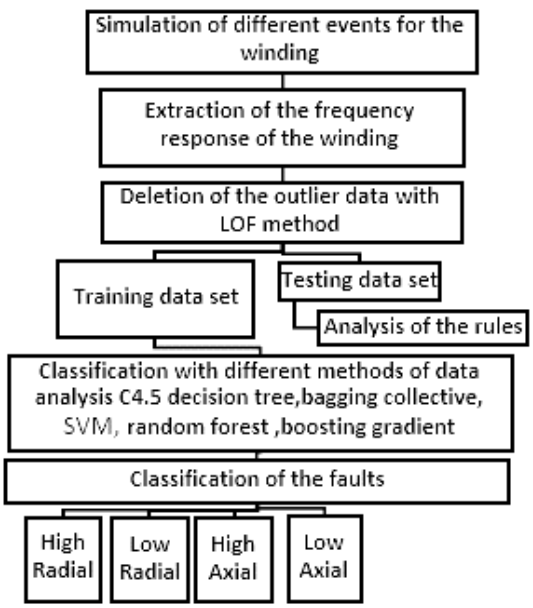


**Fig. 4**. Classification method diagram of transformer mechanical faults

### A. *Frequency response of the transformer winding*

The winding of each transformer has a unique frequency response, known as the fingerprint of that winding. the slightest mechanical and electrical change in the winding causes a change in the frequency response of them. In the dataset of this investigation, the resulting data from frequency response of the winding and their correlation index were used in various events.

### B. *LOF method to samples purging*

Outlier data is an observation that is farther away from other data and is different from the expected value [20]. In this method, three steps are performed to calculate data discrepancy. In the first step, a point is calculated for each K point to the nearest neighbor. Then, the maximum value of the distance between two points $(dis(p,o))$ and K to its nearest neighbors $(k-distance(o))$ is considered to calculate the accessible distance of one point relative to other points (reach-dist) Equ.(3).

$$reach-distA(p,o)=\max\{k-dist.(o),dis(p,o)\} \quad (3)$$

In the next step, the local density of each point is equal to the inverse of the mean K of the nearest neighbors Equ.(4). Finally, the rank of the outlier data is calculated which is equal to the average local density rate of each data sample relative to its neighbors, Equ. (5).

$$LRd_k(\mathrm{p})=1/\frac{\sum reach-dist_k(\mathrm{p},\mathrm{o})}{K} \quad (4)$$

$$(LoF_k\ (p))=\frac{\sum\frac{LRd_k(\mathrm{o})}{LRd_k(\mathrm{p})}}{K} \quad (5)$$

### C. *Classification of faults*

In the fault type classification step, several basic decision tree classifications were used, including support vector machines and collective methods of bagging, random forest and boosting gradient.

The main idea of bagging algorithms is to use several learning methods and to combine their predicted result as a group of classifiers to increase the overall accuracy of learning. Each member of this group of learners is called a base classifier. The use of collective algorithms reduces error. One of the collective methods is the bagging method. Random tree forest produces many decisions. To classify a new type, it places the input vector at the end of each random forest tree. Each tree provides a classifier, and it is said that this tree gives that class a "vote." The forest chooses the category with the most votes (among all the trees in the forest). The boosting gradient method uses "weak" decision trees like a random forest. The big difference between these two methods is that in the boosting gradient method, the trees are trained one after the other. Each subset tree is primarily trained with data that was erroneously predicted by the previous tree. This makes the model less focused on issues that are easy to predict.

## IV. TRANSFORMER UNDER STUDY AND SIMULATION

The specifications of a transformer of 20/0.4 kV and 1.6

MVA with Dyn11 connection were obtained from the manufacturer to perform the study and simulations. The characteristics of the geometric dimensions of the transformer are given in Table I. The high-voltage winding of this transformer consists of 20 disks, of which the first four and last disks of 20 loops and 16 intermediate disks have 21 loops. The LV winding also consists of two 13-loop layers.

**Table I**.
Dimension Specification of the Transformer Winding

| Description | (mm) | Description | (mm) |
|---|---|---|---|
| Internal radius LV | 93 | Cross section LV | 11.8*3.35 |
| External radius LV | 106 | Cross section HV | 8.5*2.12 |
| The channel between two layers LV | 4 | Thickness of insulating paper | 0.5 |
| The channel between two layers LV, HV | 12.5 | Coil height LV | 536 |
| Internal radius HV | 118.5 | Height HV | 494 |
| Internal radius HV | 176.5 | Core radius | 90 |

The high frequency module of the powerful CST software was used to describe the real behavior of the transformer and to extract the frequency response as accurately as possible. For this purpose, the complete specifications of a sample transformer Table I, were entered in the model. The three-dimensional model of the transformer is shown in Figure (5) and the three-dimensional models of several different events for the high voltage coil are displayed in Figure (6). The meshing was done with high accuracy and in an optimized way with three-dimensional elements. considering a compromise between time and simulation accuracy, the number of elements reached 10,600 so that the minimum element size was defined as 3 mm and the maximum as 13 mm. The simulation was performed by defining the appropriate ingredients and boundary conditions as well as the frequency band of 1 to 900 MHz.

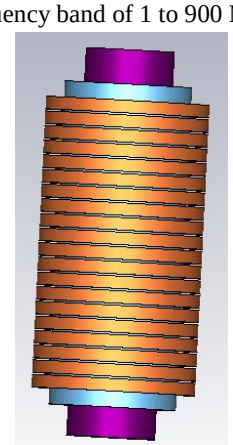

**Fig. 5**. Three-dimensional model of the phase A of the transformer in the healthy condition

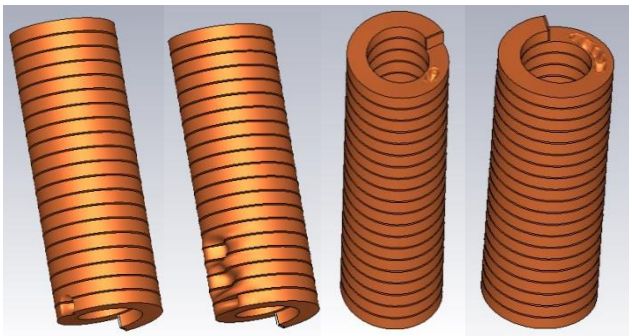

**Fig. 6.** HV winding in the condition of low and high radial fault, and low and high axis fault

## V. EVALUATION OF THE SIMULATION RESULTS

### *A. Results of radial and axial deformation*

Figure 7 shows the healthy frequency voltage response and a sample of low and high axial deformation, and Figure 8 displays the voltage frequency response in the healthy mode and a sample of low and high radial deformation. A total of 348 received signal samples is defined with four independent frequency characteristics, healthy state correlation index, high fault state correlation index, and low fault correlation index. The standard deviation reports a high-frequency characteristic that indicates outlier data. To calculate the correlation indices, the CST results are exported to MS-Excel Format. Then, in the data Analysis tab of MS-Excel software, the correlation option is selected and a new window opens, in this window by selecting the input/output range of data the correlation coefficients will be calculated.

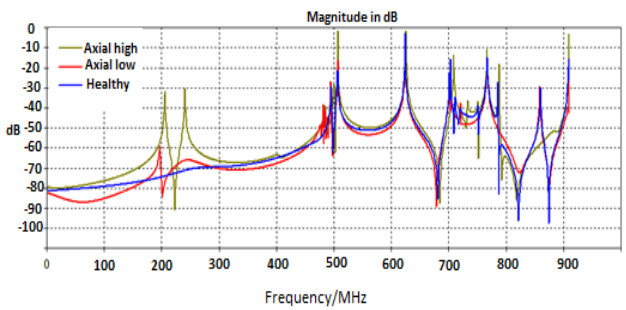


**Fig. 7.** Frequency response magnitude of axial deformation

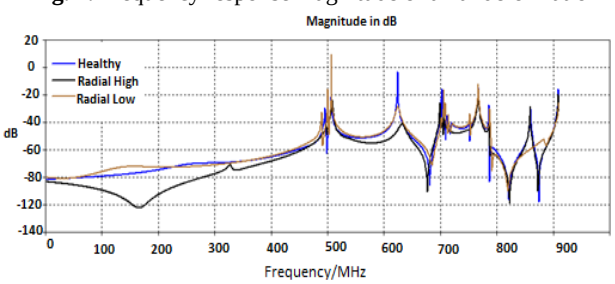


**Fig. 8.** Frequency response magnitude of radial deformation

No missing data can be seen in the columns. According to Table II, the average correlation index in the healthy mode of

the device with a value of 95.57 is between the two values of the correlation index in the high mode (94.71) and that in the low mode (93.8). The mean and a minimum correlation indices in the low fault mode (axial and radial) than in the high fault mode (axial and radial).

**TABLE II.**
The Statistical Information Of The Dataset

| Index name | Type | Miss data | Statistical information | | | |
|---|---|---|---|---|---|---|
| | | | Min | Max | Ave. | Dev. |
| Frequency (kHz) | Real | 0 | 1930.1 | 906707.8 | 152503 | 223362.5 |
| Corr. with healthy | Real | 0 | 4.336 | 100 | 95.57 | 11.8 |
| Corr. with high defect | Real | 0 | 4.715 | 100 | 94.71 | 13.11 |
| Corr.with low defect | Real | 0 | 4.336 | 100 | 93.8 | 14.656 |

Given that some data are discarded based on the variances and graphs specified in the input data topic, deleting this data can help improve the model. Therefore, the technique of removing the detection and deleting the LOF outlier data was applied to the data at this step. The method with values of k = 10 (the value of the nearest neighbor) reported the results of Table III in which the rank of the outlier data shows the outlying data that should be removed.

**TABLE III**.
Outlier Data Detection Algorithm Setting

| Outlier variable: real number | Setting | Method |
|---|---|---|
| Outlier data rank :1.349-1.043<br>Mean :1.07<br>Standard deviation :0.042 | K Small :10<br>K Large:20<br>Distance: Euclidean<br>Combined measurement | LOF |

This algorithm introduces an outlier data rate of approximately higher than 1 and 1.1 [21]. The data weighing less than 1.1 were considered normal and the rest were deleted. After applying this algorithm, out of 348 samples, 18 outlier data samples were deleted and 330 samples remained.

*B. Results of events classification unit*

The confusion matrix Table IV, shows how the classification algorithm works according to the input dataset by different types of classification problem categories. The concepts of True Positive, False Positive, True Negative and False Negative are as follows.

**TABLE IV.**
Confusion Matrix

| | | Predicted Value | |
|---|---|---|---|
| | | Negative(-) | Positive(+) |
| Actual values | Negative(-) | TN | FP |
| | Positive(+) | FN | TP |

TP: The actual value is positive (error) and the classifier has correctly identified as positive.
FP: The actual value is negative (no error) and the classifier has incorrectly identified as positive.
TN: The actual value is negative (no error) and the classifier has correctly identified as negative.
FN: The actual value is positive (error) and the classifier has incorrectly identified as negative.

We have two evaluation criterions are the precision criterion ,Equs.(6),(7).

$$Recall = \frac{Ntp}{Ntp + Nfn} \tag{6}$$

$$Accuracy = \frac{Ntp}{Ntp + Nfp} \tag{7}$$

According to the results of Table V, the ensemble methods that use several decision tree classifiers have more accurate results than the tree base model and, the tree accuracy is developed in both of the gradient method and the bagging method. In general, tree methods reported higher accuracy in detecting the type of transformer fault. In the fault type classification step, several basic decision tree classifications, support vector machines, and ensemble methods of bagging, random forest and boosting gradient. To train the models, the data were divided into two categories of training (75%) and test data (25%) by validation method in the software environment. In the training phase, the classifiers are applied to the training data and the prediction function predicts the test data for each model, category and type of fault. To evaluate the models, the prediction results are compared with the actual values and the accuracy of the model is evaluated based on the parameters of total accuracy and accuracy of each type of fault. The parameter for each classifier are set.

For the decision tree of the information gain index, the maximum depth were considered 10, the minimum leaf size were considered 3 and minimum number of separation records were considered 4. In the support vector machine with linear kernel and boosting gradient with 20 trees, the learning rate was considered 0.08 and the random forest were considered with 20 tree models. In Table V, the results of the methods were simulated once without removing outlier data and once with the LOF method of removing the outlier data, and it was compared and analyzed based on the evaluation parameters.The accuracy of all models has been increased when the outlier samples were discaded. In tree methods, the model was improved by, on average of 9% by removing outlier samples. The results of the fault type classifications show that the bagging C4.5+ LOF with 92.68% total accuracy is the best and the least faulty model in detecting each fault sample. In the class of being healthy with no fault, 100% accuracy with the bagging method, and on average, in each type of class, high accuracy was reported to detect the

type of fault with the proposed Bagging + LOF technique. The support vector machine method performed poorly in fault type classification. Even with the removal of the outlier data, an an average accuracy of 43.55% was achieved in this method. The matrix presented in Table VI, specifies the number of correctly predicted samples and the fault ,only 1 error was noticed in the low axial class, 2 errors in the high axial, and 3 errors in the low radial.

**TABLE V.**
Accuracy of the Classifiers

| Model | Accuracy (ACC) | Recall healthy | Recall axial high | Recall axial low | Recall radial high | Recall radial low |
|---|---|---|---|---|---|---|
| C4.5 | 86.21% | 100% | 66.67% | 85.71% | 94.12% | 77.78% |
| C4.5+LOF | 89.15% | 100% | 82% | 83% | 78% | 89% |
| SVM | 40.07% | 58% | 0% | 15% | 18% | 27% |
| SVM+LOF | 43.55% | 58% | 50% | 25% | 33% | 36% |
| Bagging C4.5 | 83.91% | 100% | 66.67% | 92.86% | 76.47% | 77.78% |
| Bagging C4.5+LOF | 92.68% | 100% | 87.50% | 83.33% | 100% | 84.62% |
| Random forest | 86.21% | 100% | 66.67% | 85.71% | 94.12% | 77.78% |
| Random forest+LOF | 89.22% | 100% | 93.75% | 83.33% | 70.20% | 76.92% |
| GTB | 88.50% | 100% | 82% | 75% | 87% | 79% |
| GTB+LOF | 89.45% | 100% | 82.30% | 83% | 78% | 89% |

**TABLE VI.**
The Matrix Of the Decision Tree Bagging Confusion

| | healthy | axial low | axial high | radial low | radial high |
|---|---|---|---|---|---|
| healthy | 31 | 0 | 0 | 0 | 0 |
| axial low | 0 | 11 | 0 | 3 | 0 |
| axial high | 0 | 0 | 14 | 0 | 0 |
| radial low | 0 | 1 | 0 | 10 | 0 |
| radial high | 0 | 0 | 2 | 0 | 10 |

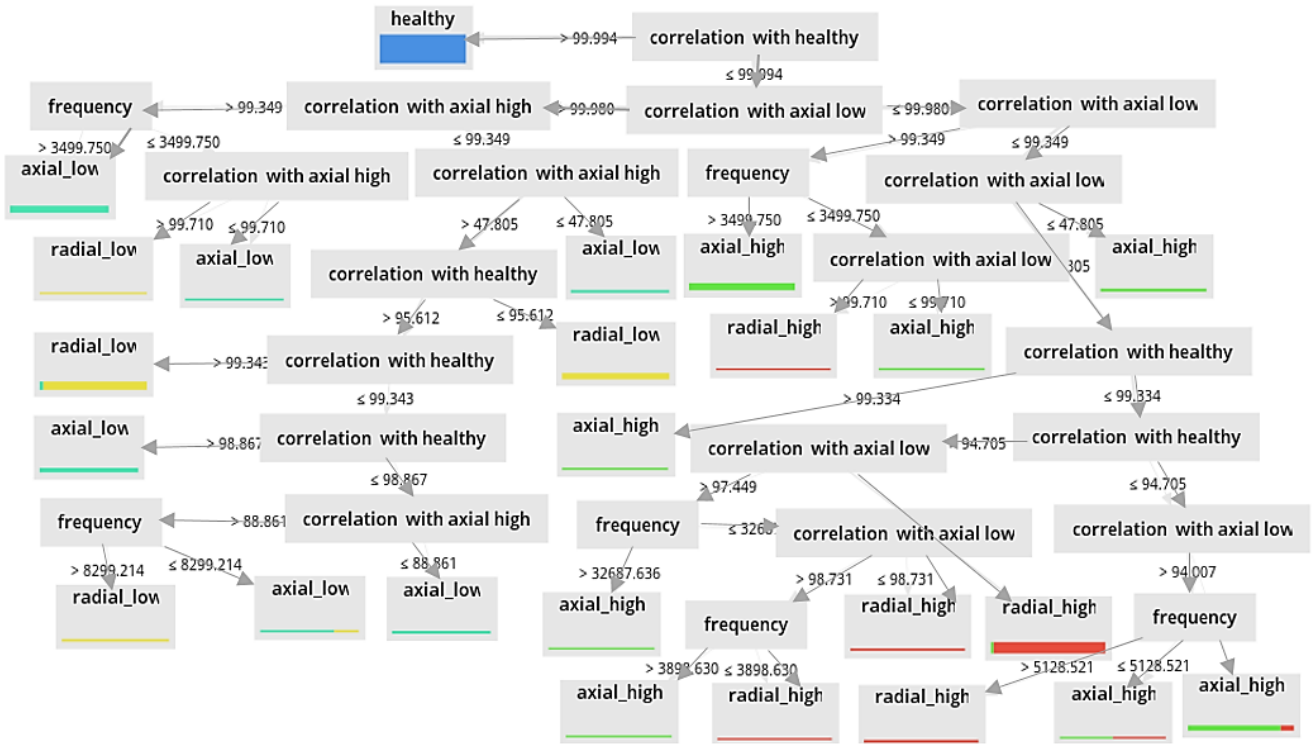


**Fig. 9**. The decision tree model

Figure (9) reports the decision tree model with high accuracy. Most of the reported rules are with higher certainty and probability of occurrence. If the correlation index in the healthy state is more than 99.99, the device is 100% in the healthy condition. The condition of the device is very likely in axial mode(low displacement of the axis).If the correlation index is less than 99.99 in the healthy mode , much more than 99.98 in the low-displacement mode of the coil axis, and more than 99.34 in the high-displacement mode of the winding and the received frequency is more than 34499.7,the condition of the device is very likely in the axial low mode (low axis displacement).

## VI. CONCLUSION

In this study, to discriminate the types of transformer mechanical faults, the transformer behavior with frequency response and correlation indices in five models of device condition (healthy, high axial, low axial, high radial and low radial) was collected with 348 samples in two axial and radial deformation conditions. In the analysis section of the results, it was observed that the properties had outlier values. Therefore, in the preprocessing step by LOF method and threshold of 1.1, 18, outlier data samples were removed.

Decision tree, machine learning techniques, neural network, support vector machines, and ensemble methods of bagging, boosting gradient and random forest were used to classify the type of faults. The frequency responses of the transformer were modeled once without LOF and then by LOF, and the results showed increased accuracy and reduced error when the outlier data removing in all techniques, especially in the tree methods.

The technique of support vector machines with linear kernel reported poor results up to 49% and low accuracy in all types of fault classes. Basic and combined tree methods had a good average accuracy for classifying the type of transformer fault, The best accuracy was more than 92.68% exhibited by decision tree bagging. bagging ensemble methods and boosting gradients improved the results of the base decision tree and proved the need to use ensemble methods to improve the models. Compared to other articles, the presented study focused on generating hidden rules regarding the type of transformer fault and frequency responses with ensemble methods and to constructing a model of classification of fault with ensemble methods that have not been used in other published articles.

## REFERENCES

[1] Lu. Bin. David B Durocher, and Peter Stemper. "*Predictive maintenance techniques*," IEEE Industry Applications Magazine, Vol.15,pp.52-60. 2009.

[2] V.P.Darabad, M. Vakilian, T.R. Blackburn, and B.T. Phung. "*An efficient PD data mining method f or power transformer defect models using SOM technique*", International Journal of Electrical Power & Energy Systems, Vol.71,pp. 373-382. 2015.

[3] Y.Jiang, B. Cukic, and Y.Ma. "*Techniques for evaluating fault prediction models*", Empirical Software Engineering, Vol.13pp. 561-595. 2008.

[4] R.N. Nair, S. M. Drus, and P. S. Krishnan. "*Data*

*Mining Techniques for Transformer Failure Prediction Model: A Systematic Literature Review*." IEEE 9th Symposium on Computer Applications & Industrial Electronics (ISCAIE),pp. 305-309. 2019.

[5] Z. Hanbo, Y. Zhang, J. Liu, Hua Wei, J. Zhao, and R. Liao. "*A novel model based on wavelet LS-SVM integrated improved PSO algorithm for forecasting of dissolved gas contents in power transformers*", Electric Power Systems Research, Vol.155,pp.205, 2018.

[6] W. Ganjun,L. Jingshu ,H. Yufeng , X. Peng, Y. Wu, and Y. Chen. "*Features Selection for Partial Discharge and Interference Recognition of HV Cables based on Random Forest Method*".25th international conference Electricity distribution, 2019.

[7] AJ.Ghanizadeh, and GB. Gharehpetian. "*ANN and cross-correlation based features for discrimination between electrical and mechanical defects and their localization in transformer winding*", IEEE Transactions on Dielectrics and Electrical Insulation,Vol. 21,pp.2374-2382.2014.

[8] S. Bagheri, Z. Moravej, and GB. Gharehpetian. *"Classification and discrimination among winding mechanical defects, internal and external electrical faults, and inrush current of transformer*", IEEE Transactions on Industrial Informatics,Vol.93,pp.484;514, 2017.

[9] O. Ozgonenel and S. Karagol, "*Power transformer protection based on decision tree approach*," IET Electr. Power Appl, vol. 8, no. 7, pp. 251–256, 2014.

[10] H. Balaga, N. Gupta and D. N. Vishwakarma, "*GA trained parallel hidden layered ANN based differential protection of three phase power transformer*," Int. J. Electr. Power Energy Syst, vol. 67, pp. 286–297, 2015.

[11] Zhou, L., Lin, T., Zhou, X., Gao, Sh., Wu, Zh., Zhang, Ch., "*Detection of Winding Faults Using Image Features and Binary Tree Support Vector Machine for Autotransformer*", IEEE Transactions on Transportation Electrification, Vol. 6, No. 2 , pp. 625-634, 2020.

[12] O.Gaderi and M.R.Feyzi"*New method to estimating the remaining life of power transformers using oil DGA*," TJEE,No.1,Vol.39,PP.25-36.1388

[13] N.ghaffarzedeh, "*A New Method for Power Quality Events Detection and Classification using Discrete Wavelet Transform and Correlation Coefficients*,"IECO, V ol. 4, no. 1, pp. 47-57, 2021.

[14] A. Ashrafian, M. Rostami and G.B. Gharehpetian, "*Hyperbolic S-transform-based method for classification of external faults, incipient faults, inrush currents and internal faults in power transformers*," IET Gener. Transm. Distrib, vol. 6, no. 10, pp. 940-950, 2012

[15] A. Ashrafian, M. Rostami and G. B. Gharehpetian, "*Characterization of internal disturbances and external faults in transformers using an S-transform–based algorithm*," Turk. J. Electr. Eng. Comput. Sci, vol. 21, no. 2, pp.330-349, 2013.

[16] A. Ashrafian, B. Vahidi and M. Mirsalim, "*Time–time-transform application to fault diagnosis of power transformers*," IET Gener. Transm. Distrib, vol. 8, no. 6, pp. 1156-1167, 2014.

[17] Jianqiang, Ni., Zhongyong, Zh., Shan, T., Yu, Ch., Chenguo, Y., Chao, T., "*The actual measurement and analysis of transformer winding deformation fault degrees by FRA using mathematical indicators*", Electric Power Systems Research, Vol. 184, pp. 1-11, 2020.

[18] Bigdeli, M., Azizian, D., Gharehpetian, G. B., "*Detection of Probability of Occurrence, Type and Severity of Faults in Transformer Using Frequency Response Analysis Based Numerical Indices*", Measurement, Vol. 168, Art. no.. 108322, 2021.

[19] A. J. Ghanizadeh and G. B. Gharehpetian, "*ANN and Cross-correlation based Features for Discrimination between Electrical and Mechanical Defects and their Localization in Transformer Winding*," IEEE Trans. Dielectr. Electr. Insul, vol. 21, no. 5, pp. 2374-2382, 2014.

[20] Gan, Zongxin, and X. Zhou.. "*Abnormal Network Traffic Detection Based on Improved LOF Algorithm*." In 2018 10th International Conference on Intelligent Human-Machine Systems and Cybernetics (IHMSC), 142-45. IEEE.2018

[21] Schubert, Erich, Arthur Zimek, and Hans-Peter Kriegel. "*Fast and scalable outlier detection with approximate nearest neighbor ensembles*." In International Conference on Database Systems for Advanced Applications,Vol.9050, pp.19-36. Springer2015.

**Zahra Moravej.** Was born in Fras.Iran.1960.(SM'11).she received the B.E and M.E degrees in electrical engineering from Bangalore University, India, in 1985 and 1991, respectively, and, the Ph.D. degree from IIT Banaras Hindu University India, in 2001. Currently, she is Professor with the Electrical and Computer, Engineering Faculty, Semnan University, Semnan Iran. Her areas of research interest include power system protection & Control, the application of artificial intelligence and machine learning in power system protection, power quality, and substation automation systems. She is senior member of IEEE.

**Mahmoud Mortazavi**. Was born in behbahan,Iran.,1979.he received the M.SC in electrical engineering from Semnan University, Semnan, Iran**.** 2017, Now he is Ph.D. Candidate of electrical engineering in Semnan university. His areas of research interest include power system protection & Control.

**Mojtaba Mohseni**. Was born in Fars,Iran,1989. He received the M.Sc. degree in Electrical Engineering from amirkabir university of Technology, Tehran, Iran in 2020. Currently, he is pursuing second M.Sc. degree in economics at the department of GSME, Sharif University of Technology, Tehran, Iran. His research interest includes machine learning, resiliency, optimization and game theory.

International Journal of Industrial Electronics, Control and Optimization © 2021 IECO
Vol. 4, No. 3, pp. 285-297, July (2021)

# A New DC Fault Detector Scheme for Multi-terminal HVDC Transmission lines

Mohammad Reza Noori [1], Seyed Ghodretolah Seifossadat [2, †], Alireza Saffarian [3]

[1, 2, 3] Department of Electrical Engineering, Shahid Chamran University of Ahvaz, Ahvaz, Iran

ABSTRACT

*In this paper, a novel selective DC fault detector approach based on the adaptive cumulative sum method (ACUSUM) is suggested for the protection of high voltage direct current (HVDC) transmission lines. Using a communication channel, the proposed method detects DC fault occurrence and determines faulty lines at a multi-terminal HVDC (MT-HVDC) transmission system in less than 2ms. The suggested approach works in the time domain and employs the ACUSUM method as a mathematical tool to detect abrupt variations in the magnitude of line currents for fault detection. Simulation results confirm the selectivity of the proposed algorithm at different DC fault situations, which enhances the reliability of the power system. Besides the low sampling rate, the ACUSUM calculation burden is very low and its implementation needs no special or complicated hardware. Adaptivity, independence from system parameters, robustness against fault resistance, fault distance and noise are significant advantages of the proposed algorithm in comparison with other methods in addition to its appropriate speed.*

**Article Info**

***Keywords:***
Fault detection, Fault diagnosis, HVDC transmission lines, Power system relaying, Power system protection

***Article History:***
**Received** 2020-11-07
**Accepted** 2021-03-24

## I. INTRODUCTION

Nowadays, because of their undeniable benefits, HVDC systems play a vital role in enhancing power system capability and reliability [1]. It is more difficult to protect an HVDC system than an HVAC one [2]. When a fault occurs in a DC line, just correct DC breakers must be opened to isolate the faulty line. In this situation, opening any AC breaker or healthy DC line breakers will distort the selectivity of the protection scheme and notably decrease the reliability of the power system.

Various approaches have been proposed based-on different ideas for fault detection in multi-terminal HVDC transmission systems. The first category employs the variation pattern of line currents and bus voltages for fault detection. The method introduced by [3] uses the superimposed theory and detects DC faults by monitoring the variation pattern of fault current at line terminals. An approach based on the magnitude and direction of line currents connected to the same bus has been suggested in [4] but it suffers from high sampling frequency (100 kHz). In [5], utilizing the ratio of the transient voltage indices and a fault-blocking converter (FBC), Relays have been coordinated to realize internal fault detection and faulty line location for hybrid MT-HVDC networks.

The approach suggested in [6] uses the voltage gradient and voltage derivative for fault detection and discrimination of AC from DC faults, respectively. Another method employs the monitoring of the calculated rate of change in the current-to-voltage ratio for fault detection. Consequently, the suggested method identifies the faulted section by checking the

[†]**Corresponding Author**: gh.seifossadat@scu.ac.ir
Department of Electrical Engineering, Shahid Chamran University of Ahvaz, Ahvaz, Iran.

summation and direction of all branch currents at each busbar, individually [7].

Because of its capability in pattern recognition and classification, a fault detector based-on the artificial neural network (ANN) is proposed in [8], which uses the voltage waveform measured at the rectifier substation. Regarding the fact that there is no unique routine method for designing ANN layers, different structures may differ in performance.

The traveling wave theory is considered a strong tool in the field of fault detection. Detecting voltage waves at the terminal and comparing them with an appropriate threshold has been used in [9] for fault detection. In [10] a protection scheme based on the energy ratio between backward and forward traveling waves has been proposed which requires a logic signal from the remote end. A single-end protection method using the morphological gradient of DC voltage with predefined thresholds has been proposed in [11] to protect DC cables and overhead lines in voltage source converter-based MTDC grids. This method is based on the effect of series inductors attenuating high-frequency voltage traveling waves transmitted from the fault point to the grid line ends. A centralized protective scheme has been proposed in [12] in which the principles of busbar differential protection and traveling waves are employed. A non-unit line protection scheme is presented in [13], which is based on the initial line-mode voltage traveling waves (ILVTWs). Based on the analysis of the traveling wave (TW) propagation characteristics, the transfer functions of ILVTWs under typical internal and external faults have been derived. By comparing the differences of the transfer functions in the frequency domain, the corresponding protection principles have been developed.

Recently, protective algorithms based on harmonic analysis have been employed for fault diagnosis. Investigations show that monitoring the magnitude of the $12^{th}$ harmonic of fault current can be useful for separating external faults from internal ones [14]. Another approach has used a specific frequency alternating current (SFAC) during fault transient [15]. Faulty zone selection based on harmonic content has been proposed in [16] too.

Presently, TW-based protection and voltage derivative protection are usually used as the main protection for HVDC transmission lines, while backup line protections are composed of DC under voltage and current differential protection [17]. Albeit their fast response (typically less than 1 ms), TW-based protections always suffer from not being supported by the capacitive voltage transformer (CVT) frequency responses, being affected by noise and fault resistance, and needing high sampling frequency devices while complexity and expensive implementation are major problems with TW-based fault detectors, too. On the other hand, voltage derivative protection is sensitive to fault transition impedance and noise. Under voltage protection is lowly reliable (i.e., separating internal from external faults) and current differential protection operates with time delay up to hundreds of milliseconds [17].

Regarding these problems of the aforementioned protection principles, this paper proposes a new highly reliable DC fault detection algorithm based on the ACUSUM method for the protection of MT-HVDC transmission lines. This algorithm increases the detection time to less than 2 ms, which makes it appropriate for backup protection, not main protection. The suggested approach works in the time domain based on the variation patterns of the magnitude of line currents during DC faults. As a mathematical tool, the ACUSUM algorithm provides meaningful indices, which can detect DC faults and determine the faulty line. Appropriate speed (as backup protection), independence from system parameters, adaptivity, low sampling frequency, low computational burden, simplicity, no need for any complicated hardware, robustness against fault resistance, fault distance, and noise are the significant benefits of this method in comparison with others.

The rest of the paper is organized as follows. The proposed method is described in Section 2. Simulations and results are presented in Section 3. Finally, Section 4 concludes the paper.

## II. PROPOSED ALGORITHM DESCRIPTION

The CUSUM test has been employed widely as a technique for detecting abrupt changes in various fields [18]. Considering the helpful variations in current signal amplitude during a fault, a fault detector based on the adaptive CUSUM (ACUSUM) algorithm for AC power transmission systems has been proposed in [19]. To detect and distinguish faults in an MT-HVDC transmission system, a new version of ACUSUM is proposed and used as the basis of the fault detector unit, which is explained below.

### *A. Main Idea*

Fault inception in an HVDC transmission system, either in DC or AC zone, causes deviation of voltage and current signals from their original shapes. A detailed assessment of these variation patterns can be a valuable tool for fault diagnosis. Figure 1 shows a mono-polar meshed 150 kV four terminals VSC-HVDC network, where the points of measurement are on DC lines. The technical details of this simulated network have been explained in section 3, completely. Also, a DC and an AC fault have been shown on this system as F1 and F2 respectively.

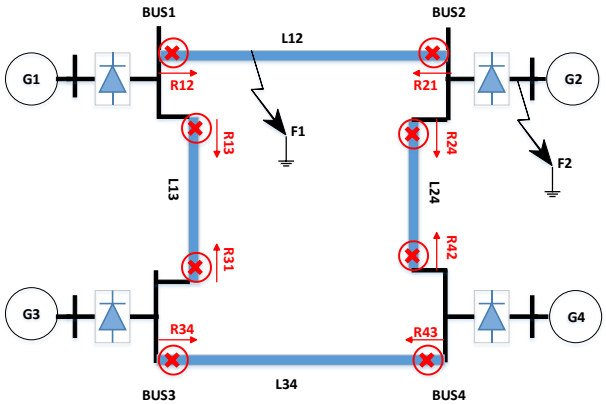


**Fig.1**. Simulated four-terminal meshed VSC-HVDC transmission system

i) Figures 2 and 3 depict measurements by R12 and R21, respectively against fault occurrence on F1 (at the middle of the line at t=0.5 s). It can be seen that the incoming line currents at both ends of the faulted DC line experience an increment just after fault inception; while the bus voltages at both ends show decrements. Figure 4 shows the measurements by R31 for the same fault. It is observable from this figure that the control system of converters can retain line current and bus voltage without significant change. Regardless of voltage decrement at faulted line terminals, it is evident that relays installed at both ends of a faulted DC line experience incremental variations in measured current, simultaneously. This fact provides the basis for a selective protection scheme on the DC side, where an increase in the measured line current at both ends can be an indication of a fault on the DC line where these are observed.

ii) For the fault at F2, Figures 5 to 8 illustrate measurements by R21, R12, R24, and R42, respectively. It can be seen that the bus voltage, with the fault on the AC side (V2), experiences a decrement after fault inception; while outgoing DC line currents from that bus (I21 and I24) show decrements. In this case, measurements by R12 and R42 at the remote ends of the DC lines connected to the bus (with the fault on behind) show an increment in the current signal with the remaining voltage in a controllable manner. These graphs confirm that regardless of voltage variations, based on the predefined positive direction for relays accruing an AC fault cannot lead to simultaneous incremental variation in the current signal of two adjacent buses connected with a line. This fact can make AC faults filterable from DC ones by the proposed method.

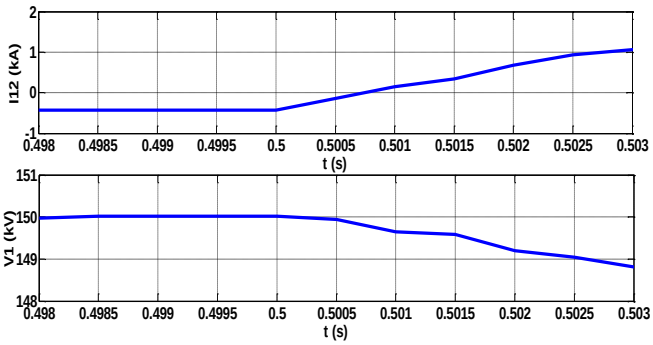


**Fig.2**. Current of L12 (top) and the voltage of bus 1 (bottom) against the fault at F1 seen by R12 (fault inception: t=0.5 s).

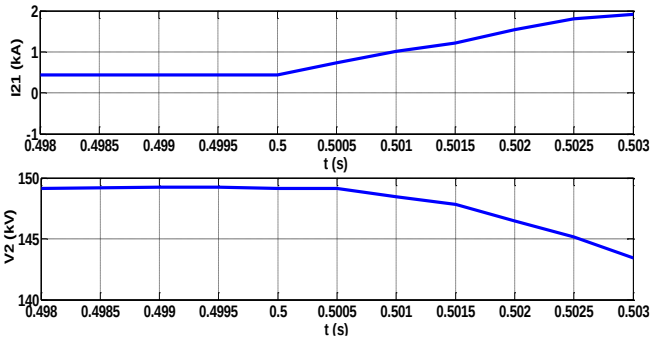


**Fig.3**. Current of L12 (top) and the voltage of bus 2 (bottom) against the fault at F1 seen by R21 (fault inception: t=0.5 s).

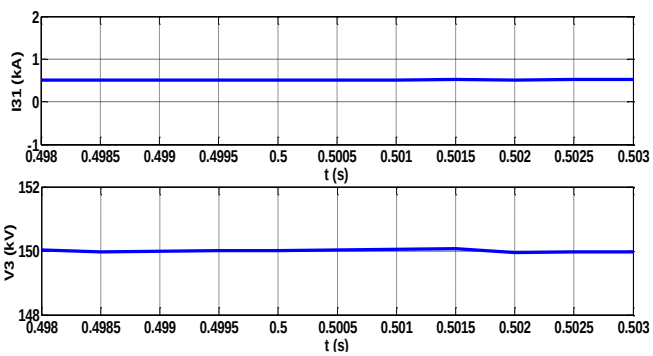


**Fig.4**. Current of L13 (top) and the voltage of bus 3 (bottom) against the fault at F1 seen by R31 (fault inception: t=0.5 s).

### *B. Fault Detection Procedure*

The proposed protective scheme has four steps:

*Step 1: Data Acquisition*

In this step, the corresponding line current at each end of DC lines is sampled with an appropriate sampling frequency (2 kHz). Generally, two main concerns should be considered in selecting a sampling rate:

- Usually, fault detectors with a high sampling rate suffer from not being supported by CVT frequency responses and the need for high sampling frequency devices. Therefore, detector algorithms with low sampling rare are more practicable than other rivals with a high sampling frequency.
- Decreasing the sampling rate of the ACUSUM algorithm increases detection time, which is undesired. On the other hand, increasing the sampling rate can distort the security of the ACUSUM algorithm against the noise, which has been discussed in the next sections.

To sum up the above two factors, 2 kHz is employed as a sampling rate for ACUSUM to carry out the integration.

*Step 2: Detection of Current Increment*

In this step, the increment in current magnitude, as shown in Fig. 2, is detected by ACUSUM as:

$$P1_{(k)} = \max[(P1_{(k-1)} + i_{(k)} - \beta_1 I_{dyn,k}), 0] \quad (1)$$

where $i_{(k)}$ represents the k[th] sample of the corresponding current signal, $P1_{(k)}$ represents output indices for k[th] instants, and $\beta_1 I_{dyn,k}$ is an adaptive current setting of the relay at the k[th] instant where $I_{dyn,k}$ is the average of the corresponding line current from the previous moments. $\beta_1$ is a setting parameter that can take any value. The values less than 1 will provide better dependability and larger than 1 will enhance the security of the proposed approach [19]. In fact, $\beta_1 I_{dyn,k}$ provides a low pass filtering effect. Regarding the max operation in (1), $P1_{(k)}$ is always zero or has a positive value. In other words, while the system is working in normal conditions, no current sample is larger than the adaptive setting of the relay ( $\beta_1 I_{dyn,k}$ ) and the output index ( $P1_{(k)}$ ) remains at zero. When a current increment happens, current samples become bigger than $\beta_1 I_{dyn,k}$ and $P1_{(k)}$ starts growing up. DC Trigger Signal will be switched if the following criterion is fulfilled at, for example, three consecutive samples:

$$DC\,Trigger\ Signal = DCTS = \begin{cases} 1, & if \quad P1_{(k)} > h_1 \\ 0, & else \end{cases} \quad (2)$$

where $h_1$ is an arbitrary constant and should be ideally zero. In fact, $h_1$ determines the permitted increment in the output index of the algorithm when the magnitude of the current signal passes the adaptive setting of the relay.

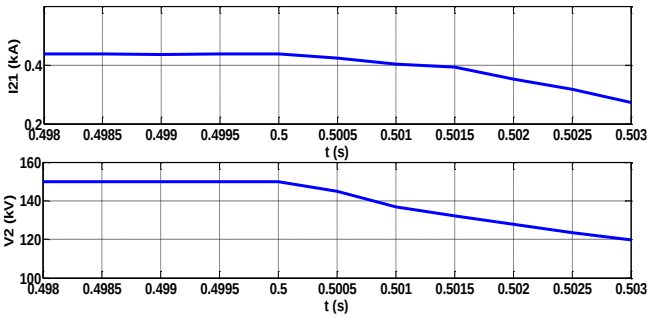


**Fig.5.** Current of L12 (top) and the voltage of bus 2 (bottom) against the fault at F2 seen by R21 (fault inception: t=0.5 s).

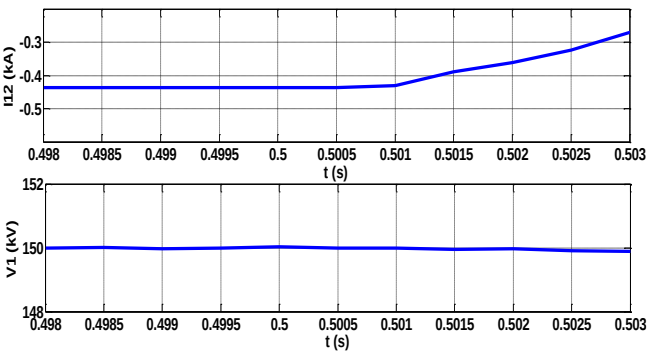


**Fig.6.** Current of L12 (top) and the voltage of bus 1 (bottom) against the fault at F2 seen by R12 (fault inception: t=0.5 s).

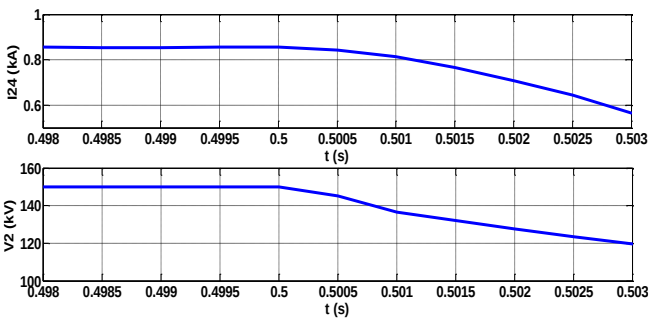


**Fig.7**. Current of L24 (top) and the voltage of bus 2 (bottom) against the fault at F2 seen by R24 (fault inception: t=0.5 s).

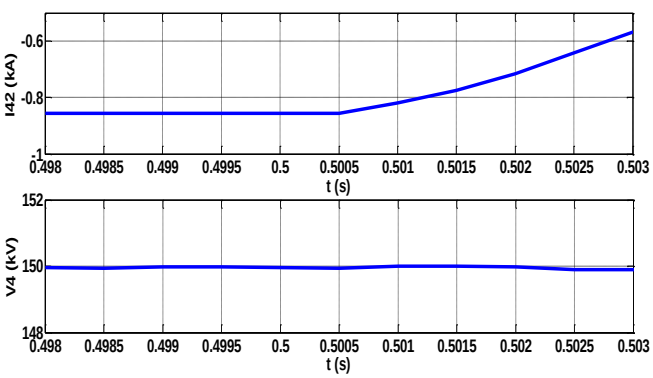


**Fig.8**. Current of L24 (top) and the voltage of bus 4 (bottom) against the fault at F2 seen by R42 (fault inception: t=0.5 s).

*Step 3: State Announcement*

*DCTS* (introduced in step 2) as a primary flag is attached to each installed relay at each terminal that addresses the primitive diagnosis of the relay whose high value proposes the corresponding DC line as a primitive candidate for the faulty line. Regarding what was described in section II-A, since the DC fault detection procedure needs the *DCTS* flag of both line terminals, a communication link should be employed. In other words, by using a communication channel, the adjacent relays share their *DCTS* flag values.

*Step 4: Decision Making*

Finally, the faulted DC line is detected as a connective line between two adjacent relays whose *DCTS* flags have become high, simultaneously. Regarding the proposed logic, *DCTS* changeover neither in one relay nor in two relays with no communication line in between leads to protective operation. After each fault detection, $P1_{(k)}$ is reset.

$$P1_{(k)} = 0, k = k_0 \tag{3}$$

Figure 9 shows the flowchart of the proposed algorithm.

*C. Discussion*

*1) Determination of* $I_{dyn,k}$

For the calculation of $I_{dyn,k}$ , an appropriate data window should be employed. The length of the moving data window is a choice that may be affected by various parameters considering the fault detector's structure and features. Regardless of special issues, two facts are considered when determining data window length (DWL):

- DWL should be short enough to prevent the increase in the computational burden of the algorithm in each time step. This fact becomes essential for those detector algorithms with complicated structure and calculation. Luckily, because of the simplicity of computation and structure, ACUSAM is not affected by this fact.
- Considering the disturbance of extra short time constant phenomena like lightning, DWL should not be less than 3 ms to make these phenomena separable from faults [7].

To sum up the above two factors, a 5 ms moving window (containing 10 samples with 2 kHz sampling frequency) is employed to carry out the integration. In each step, $I_k$ is the average of the current samples of the moving data window ended to $k^{th}$ sample.

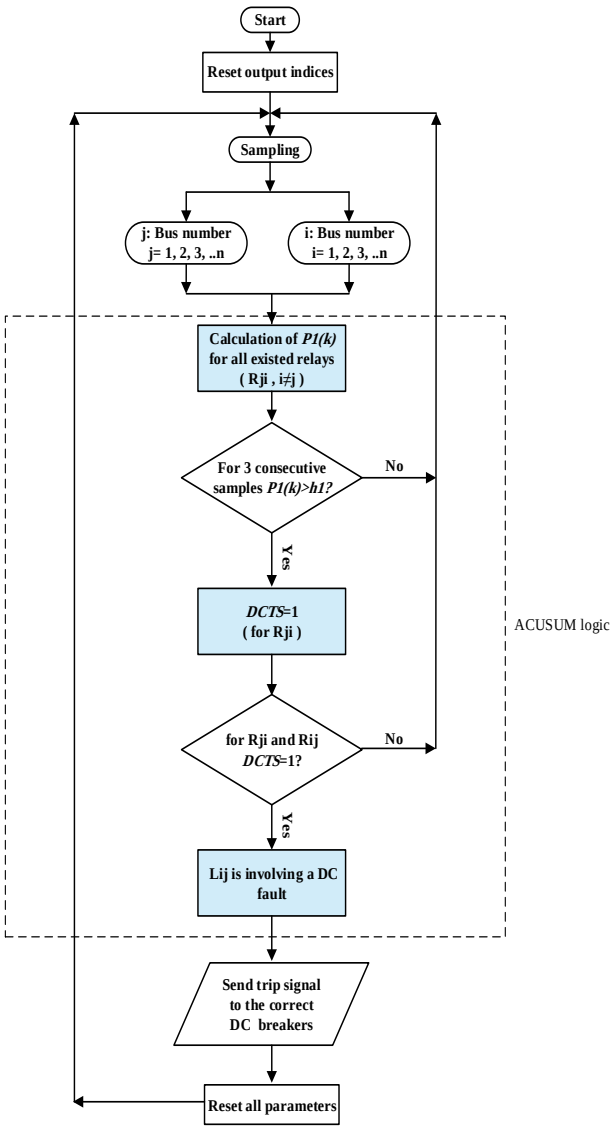


**Fig.9.** Flowchart of the proposed algorithm

$$I_k = \frac{1}{10}\sum_{j=k-9}^{j=k} i_{(j)} \tag{4}$$

While the system is working in a normal situation, extracted $I_k$ has acceptable accuracy and can directly be used as $I_{dyn,k}$ . But, by any sudden variation in the current signal caused by a fault or load switching, because the samples of the moving data window are not homogeneous, $I_k$ does not correspond with the real line current. Luckily, since ACUSUM is capable of separating DC faults from load switching (which has been assessed completely in Subsection 3-B-1), there is no concern about this imprecise estimation, and $I_{dyn,k}$ in (1) can be simply substituted by $I_k$ with an adjustable delay as follows [19]:

$$I_{dyn,k} = I_{(k-\gamma)} \quad (5)$$

where γ is a constant that has no effect on the magnitude and just shifts it by γ steps [19]. Regarding the fact that fault criteria should be satisfied for 3 consecutive samples, γ=3 is a good choice.

*2) Determination of Setting Parameter ($\beta_1$)*

To explain $\beta_1$ employed in *DCTS* calculation for DC fault detection, it should be noted that choosing values greater than 1 for this parameter makes currents with larger magnitudes than existing load current and less than $\beta_1 I_{dyn,k}$ not being detected by ACUSUM. This may be suitable for a forecasted increase in the load where it is desired that the fault detection unit (FDU) remains inactive upon that. But this choice makes high resistance faults (HRFs) with a similar condition on magnitude undetectable by ACUSUM as has been expatiated in [19].

The most important issue in a robust fault detection algorithm is high dependability, which must be 100% with acceptable security [19]. Therefore, no significant current variations should be ignored by FDU. Owing to what was mentioned above, in a DC fault situation, perfect dependability means that for any meaningful increment in the current level, *DCTS* must be issued. This is achievable by selecting $\beta_1 = 1$. It is clear that if this current increment is not related to a DC fault, the *DCTS* flag of the remote end will block FDU and support the security of the protective algorithm.

*3) Determination of Threshold ($h_1$)*

This parameter is arbitrary constant and should be ideally zero. Because of the inherent features of the real application such as noise, the security of the protection system necessitates replacing zero value with an appropriate threshold to prevent mall-operation of relays in normal conditions. Since remote terminal data transmission and setting parameter ($\beta_1$) are respectively assigned to mainly support the security and dependability requirements of FDU, the threshold should be defined to filter just small variations in input signals such as noise. In this study, $h_1$ is set at 0.05. It can be changed by the operator corresponding to the real field operation condition.

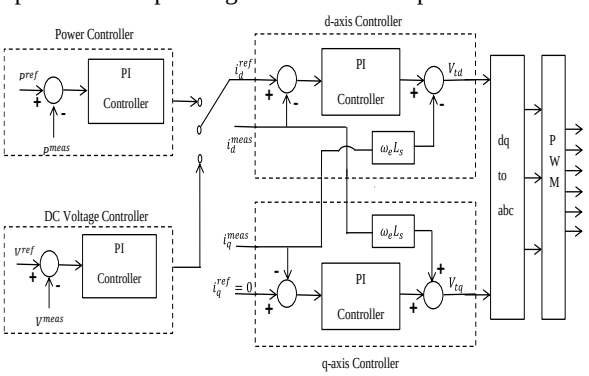


**Fig.10**. VSC control diagram

**TABLE I**
SIMULATED SYSTEM PARAMETERS

| **DC line parameters** | **L12** | **L13** | **L24** | **L34** |
|---|---|---|---|---|
| Distance (km) | 200 | 150 | 100 | 100 |
| Resistance (Ω/km) | $1.27\times10^{-2}$ | | | |
| Inductance (H/km) | $9.3\times10^{-4}$ | | | |
| Capacitance (F/km) | $12.74\times10^{-9}$ | | | |
| **VSC parameters** | **VSC1** | **VSC2** | **VSC3** | **VSC4** |
| Terminal power situation | Receive | Send | Send | Receive |
| AC voltage (kV) | 83 | 83 | 70 | 83 |
| Converter type | Two-level converter | | | |
| AC frequency (Hz) | 50 | | | |
| DC voltage (kV) | 150 | | | |
| Series AC resistance (Ω) | 0.92 | | | |
| Series AC inductance (mH) | 1 | | | |
| DC link capacitor (mF) | 0.4 | | | |

## III. Simulation Results

To evaluate the proposed algorithm, a 150 kV four-terminal meshed VSC-HVDC transmission system, which is an expanded example of the test network in [20] (shown in Fig. 1), was simulated in the Simulink environment of the MATLAB program whose details are summarized in Table 1. The mono-polar test network consists of four remote AC sources, four converter stations, and four transmission lines where both ends are equipped with two directional relays. Figure 10 shows the block diagram of VSC control. Terminals 2 and 3 are under constant active power control and terminals 1 and 4 are in the DC voltage regulator. $V_q$ is considered $V_q = 0$. Additional details about the control system are available in [20]. Because of its more transient resolution than others, a distributed parameter model has been used for transmission lines [21]. Two convertor stations have been grounded solidly [22]. The sampling rate is 2 kHz. Data processing has been done in the MATLAB program. The incoming direction is considered the positive direction for lines current. Different DC faults at different locations with various fault resistances have been simulated and reported in the next section for the evaluation of the suggested algorithm.

*A. Dependability Assessment*

*1) First Simulated Case*

Consider a solid pole to ground (PG) fault at the middle of L12 as shown in Fig. 1 (point F1) at t= 500ms. Figs. 11 and 12 depict the line currents at buses 1 and 2, respectively. Output indices of the corresponding relays have been illustrated, too. According to Fig. 11, *DCTS* is issued by R12 at t=501.5ms. Figure 12 confirms the same scenario for R21. R13 and R24 remain inactive correctly. It means that the proposed algorithm detects L12 as faulted line and the trip signal is sent to the related DC breakers to isolate L12 just 1.5ms after fault inception. As expected and shown in Figs. 13 and 14, the control system of VSCs retains other currents in an acceptable

controlled manner and no protective reactions are permitted for the installed relays at buses 3 and 4.

The effect of fault resistance on the performance of the suggested algorithm was inspected. The results are described in TABLE II. In these cases, the fault resistance for F1 has been varied from 0Ω to 100Ω. The results reveal that for all fault resistance values, the extracted indices are completely sufficient and meaningful to make a correct protective decision, so the algorithm can detect the faulted line in just 1.5ms after fault inception.

The performance of the algorithm in various fault locations has also been investigated. TABLE III presents the results of these simulations, supporting the robustness of the proposed algorithm against fault location. According to the detection time of the relays installed on both terminals of the faulted line, for all tested distances (from bus 1), the algorithm detects the faulty line in less than 2ms after fault initiation.

**TABLE II**
THE OUTPOT INDICES OF R12 AND R21 AND THE DETECTION TIME FOR DIFFERENT FAULT RESISTANCE OF F1

| Fault resistance | | R=0 Ω | R=10 Ω | R=50 Ω | R=100 Ω |
|---|---|---|---|---|---|
| R12 | $P1_{(k)}$ | 2.05 | 1.89 | 1.4 | 0.99 |
| Detection time | | 1.5 ms | | | |
| R21 | $P1_{(k)}$ | 2.55 | 2.39 | 1.9 | 1.5 |
| Detection time | | 1.5 ms | | | |

**TABLE III**
THE OUTPUT INDICES OF R12 AND R21 AND THE DETECTION TIME FOR DIFFERENT FAULT DISTANCES (FROM BUS 1) OF F1

| Fault distance | | 10%L | 50%L | 90%L |
|---|---|---|---|---|
| R12 | $P1_{(k)}$ | 7.77 | 2.05 | 0.79 |
| Detection time | | 1.5 ms | | 2 ms |
| R21 | $P1_{(k)}$ | 1.16 | 2.55 | 8.213 |
| Detection time | | 2 ms | 1.5 ms | |

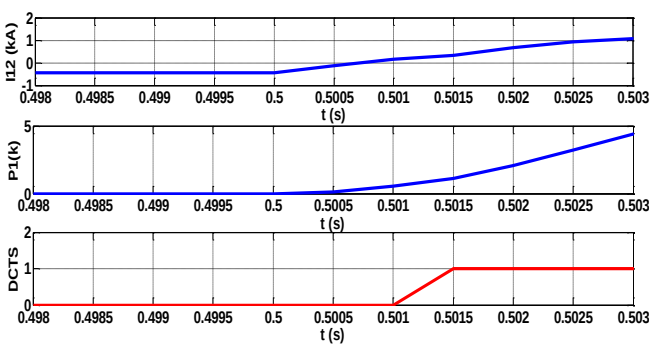


(a)

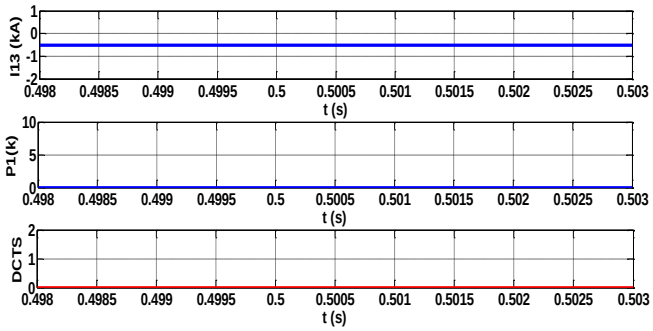


(b)

**Fig.11.** Current signals and detection indices at bus 1 against the fault at F1, (a) I12, (b) I13 (fault initiation: t= 0.5 s).

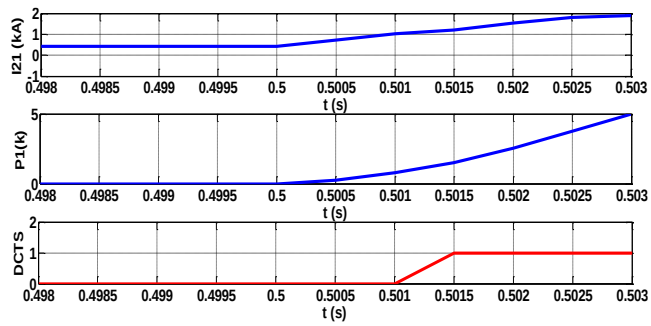


(a)

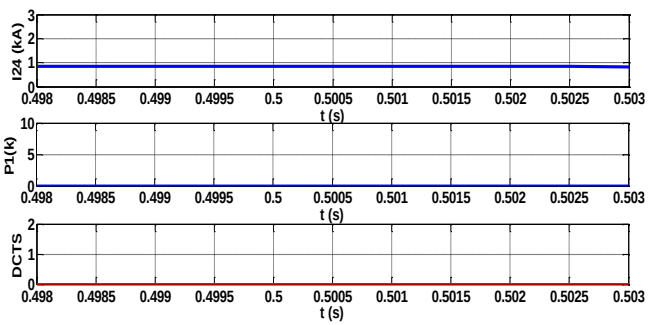


(b)

**Fig.12.** Current signals and detection indices at bus 2 against the fault at F1, (a) I21, (b) I24 (fault initiation: t= 0.5 s).

*2) Second Simulated Case*

An accurate selectivity assessment of the proposed method demands a close-up reverse fault simulation. For this study, F1 is placed at 2.5% of the length of L12 (5 km far from R12). In addition to R12 and R21, which must isolate the line, the correct operation of R13 and R31 are of importance and should be inspected. Evidently, this fault location replacement has no special effect on the measurements by R24, R42, R34, and R43, which have been depicted in Figures 11 to 14. On the other hand, regarding the former simulated case and Table 3, the *DCTS* flag surely becomes high for R12 and R21, so the related

figures are not shown again. The measurements by R13 and R31 are illustrated in Figures 15 and 16, respectively. Two valuable concepts are achievable from these graphs:

- First, there is no concern about R13 mall-operation in reverse close-up faults. Regarding Figure 16, *DCTS* becomes high for R31 at t=503ms, while R13 remains inactive in Figure 15. According to the predefined logic of the algorithm, these couple of flags are completely meaningless and do not start the protection of L13 correctly.
- Secondly, there is no concern about the overreaching of R31 for occurring a close-up/ low-impedance fault at an adjacent line, too. This robustness confirms the selectivity power of ACUSUM.

A question may be introduced as a relay could be designed to detect any increment in the current signal without needing the extra computational burden of ACUSAM. It should be noted that $I_{setting}$ in a simple overcurrent relay is a static parameter that should be changed for different load conditions by the operator whereas $I_{dyn}$ continuously adjusts itself by load conditions. The mall-operation of a simple overcurrent relay becomes worse when a decrease in the line current occurs followed by an HRF whose magnitude falls below $I_{setting}$ . But, in ACUSUM, as $I_{dyn}$ adjusts itself with the load decrease, it can detect HRF in this case as well as other types of faults [19]. Moreover, due to cumulative sum, ACUSUM provides bigger indices with more consistency than the simple over current approach, which is considered an important property in the detection of high-resistance or long-distance faults. Finally, it should not be ignored that all the aforementioned benefits are reachable without any notable extra computational burden regarding the present-day digital technology.

The results of the simulation for over 100 various cases have proven that the proposed algorithm can detect any DC fault in less than 2ms. Table 4 compares the vital features of the proposed method with those published in recent years.

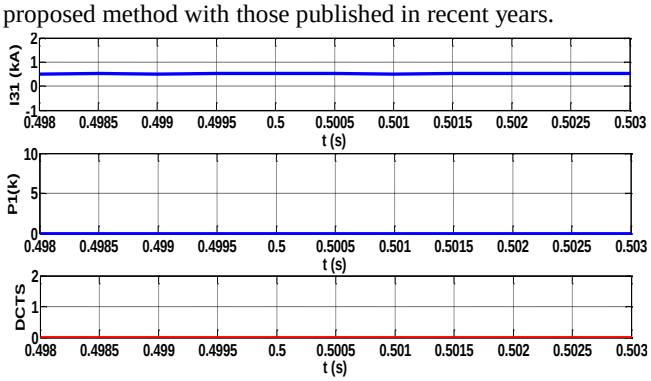


(a)

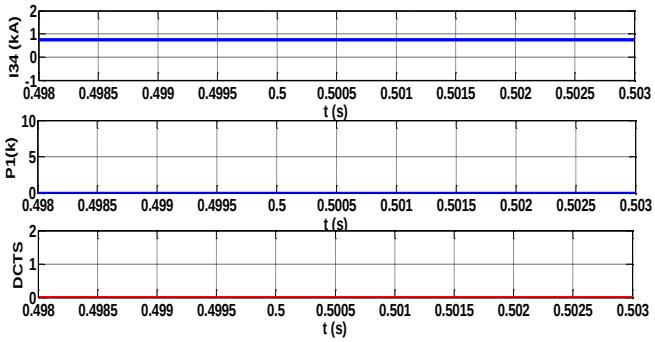


(b)

**Fig.13**. Current signals and detection indices at bus 3 against the fault at F1, (a) I31, (b) I34 (fault initiation: t= 0.5 s).

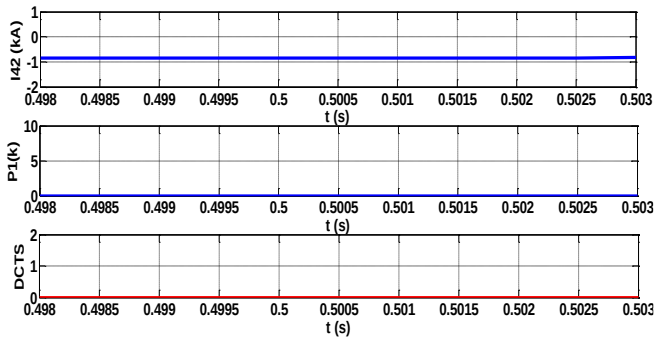


(a)

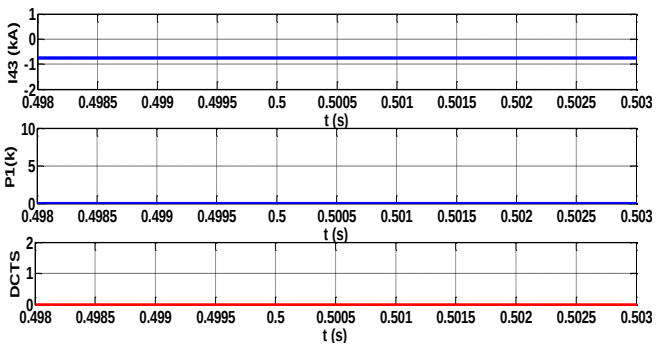


(b)

**Fig.14.** Current signals and detection indices at bus 4 against the fault at F1, (a) I42, (b) I43 (fault initiation: t= 0.5 s).

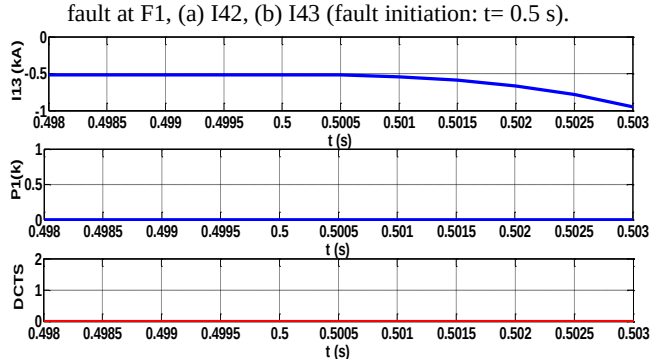


**Fig.15.** Signal and detection indices seen by R13 against the fault at F1 at the beginning of L12 (fault initiation: t= 0.5 s).

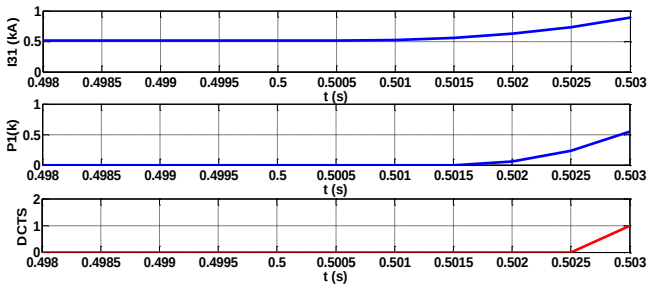


**Fig.16.** Signal and detection indices seen by R31 against the fault at F1 at the beginning of L12 (fault initiation: t= 0.5 s).

*B. Security Assessment*

*1) Load changing*

Since load changing at bus results in variations in the current magnitude of lines, a security assessment should be done to confirm that the proposed algorithm can filter load changing and separate it from DC fault occurrence. For more exact inspection, a load switching in bus 2 at t=0.5 s has been simulated. Figures 17 and 18 show the measurements at both ends of L12 and L24, respectively. The predefined positive direction for relays guarantees that the relays installed at both sides of a line cannot experience increment in measured current signal during a load switching. This fact is perceptible from Figures 17 and 18. According to Figure 17, although the current increment triggers *DCTS* for R12, R21 with remaining at *DCTS=0* blocks any protection on L12 and does not permit the relay to react against this load switching. Figure 18 confirms the same scenario for the relays installed at both ends of L24. The results of the simulation illustrate the robustness of the proposed algorithm in the separation of DC faults from load changing.

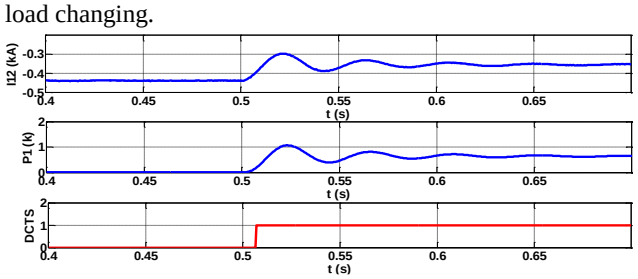


(a)

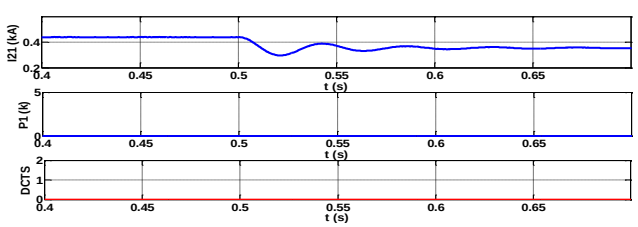


(b)

**Fig. 17.** Signals and detection indices at both sides of L12 against the load switching at bus2, (a) I12, (b) I21 (switching instant: t=0.5 s).

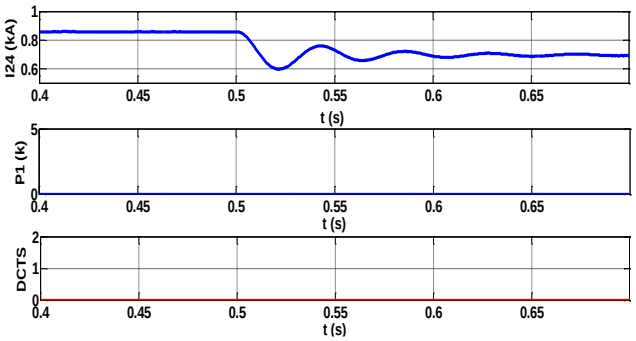


(a)

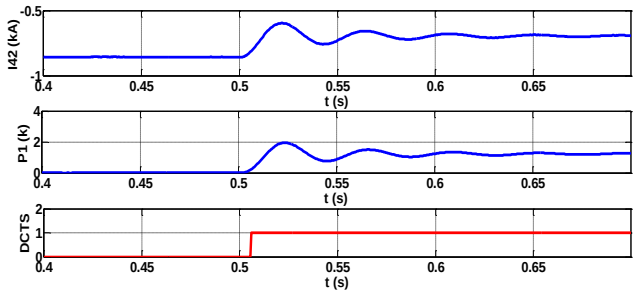


(b)

**Fig. 18.** Signals and detection indices at both sides of L24 against the load switching at bus2, (a) I24, (b) I42 (switching instant: t=0.5 s).

**TABLE IV**
THE COMPARISON OF VITAL FEATURES OF DIFFERENT APPROACHES

| Reference | [4] | [23] | [17] | [24] | [25] | [26] | This paper |
|---|---|---|---|---|---|---|---|
| Sampling rate (kHz) | 100 | 10 | 10 | 20 | 100 | 2 | 2 |
| Detection time (ms) | Var | NI/R | ≤ 6 | ≤ 1 | ≤ 2 | ≤ 10 | ≤ 2 |
| Computation burden | L | H | VH | VH | H | VH | VL |
| Communication based | Yes | Yes | No | No | No | No | Yes |
| Maximum tested fault resistance (Ω) | 350 | 300 | 200 | 0.01 | 50 | 300 | 100 |

Var: Variable with line length and communication speed.
NI/R: Not investigated or reported. L: Low H: High
VH: Very high. VL: Very low

*2) Noise*

This section investigates the performance of the ACUSUM algorithm in presence of noise. For this study, the fault simulated in Section 3.1.1 (F1 in the middle of L12 initiated at t= 0.5 s) is reconsidered while all of the measured signals are polluted with Gaussian noises with SNR=20 dB. Figures 19 to 22 illustrate the results of this part where the effect of noise is observable on the measured signals. In comparison with

Figures 11 to 14, the assessment results reveal that albeit signals have been polluted, the performance of the algorithm remains hale and the algorithm detects L12 as a faulty line in just 1.5 ms after fault initiation while other healthy parts of the system continue power transmission. These results confirm the robustness of the ACUSUM algorithm against noise. Four main points should be mentioned in this part:

- As is observable in Figures 19 to 22, low-magnitude disturbances caused by the noise have been filtered by the setting of an appropriate threshold as described in Subsection 2.3.C. In fact, $h_1$ does not permit $P1_{(k)}$ with values smaller than 0.05 to changeover the *DCTS* flag. Enlarging this threshold can lead to an increase in the security of the ACUSUM and its detection time.
- Applying a consistency check (checking for three consecutive samples) improves the performance of the algorithm against noise and does not permit the low-magnitude disturbances caused by the noise to start any protection. Increasing the number of consecutive samples for the consistency check enhances the security of the ACUSUM and its detection time.

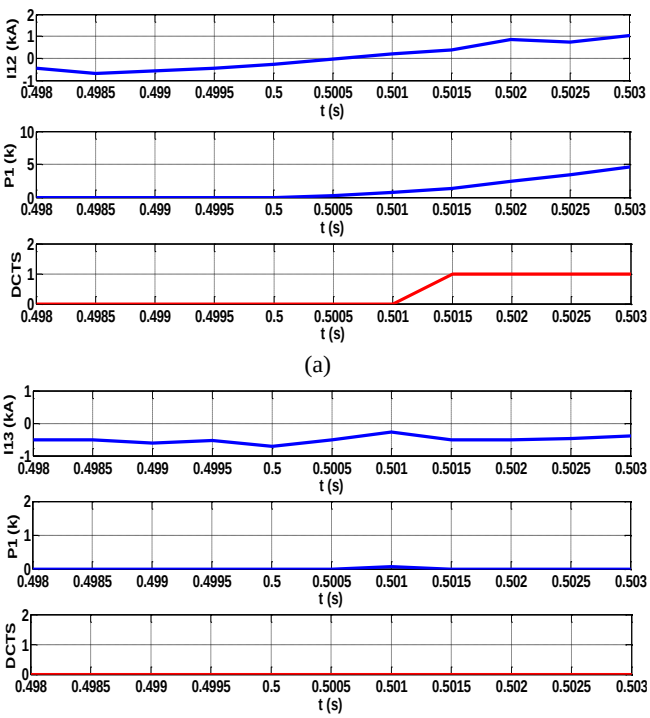


**Fig. 19.** Signals and detection indices at bus 1 against the fault at F1 in presence of Gaussian noise with SNR=20, (a) I12, (b) I13 (fault initiation: t= 0.5 s).

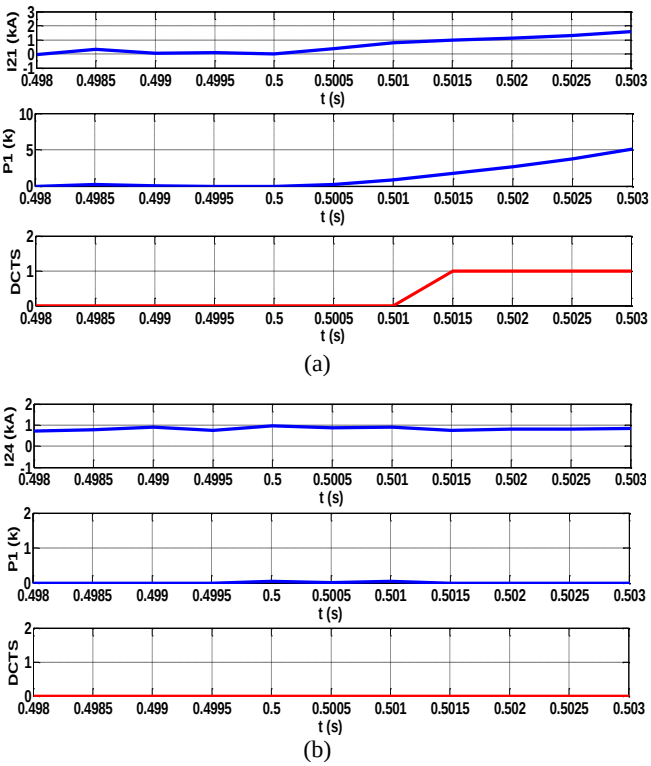


**Fig. 20.** Signals and detection indices at bus 2 against the fault at F1 in presence of Gaussian noise with SNR=20, (a) I21, (b) I24 (fault initiation: t= 0.5 s).

- Regarding the former issue, increasing the sampling rate can reduce the security of the proposed detector in a noisy condition, unlike its detection time.
- In comparison with what was mentioned above, other parameters such as the length of the data window, β, and γ values have no significant effect on the ACUSUM performance in presence of noise.

### *C. Supplementary Augment*

*1) Communication*

Currently, optical ground wires (OPGWs) are widely used in HVDC transmission systems [27]. The signal transfer delay in an optical fiber cable is approximately 4.9 μs/km [28]. In other words, even adding the communication time delay for transferring data between protective relays of the line, the proposed ACUSUM still belongs to the category of fast detectors (as backup protection). Furthermore, this protection can employ existing communication links without additional cost. Regarding the reliability concerns, OPGWs are immune to electromagnetic interference arising from corona on DC wires or faults in the transmission system [27], which ensures high communication reliability.

*2) Independence of the Algorithm*

The proposed algorithm uses the variations in current signal for fault detection, which is an inevitable phenomenon during

permanent faults. Moreover, the auxiliary parameters of the proposed algorithm are flexible and can change due to making the desired compromise between dependability and security (considering the network configuration and operation condition). Therefore, regardless of system parameters, different converter types and configurations, and different control systems, ACUSUM can be used as a fault detector algorithm. In other words, during a permanent fault, different converter types and control systems may result in different variation levels in the current signal, which cannot remain masked from ACUSUM. This sounds the independence of the proposed method performance from the system parameters and configuration.

## IV. Conclusion

In this paper, a novel selective DC fault detector scheme based on the adaptive cumulative sum (ACUSUM) method has been proposed for MT-HVDC transmission lines, which can detect DC faults and discriminate faulted line in less than 2ms. This feature of the proposed algorithm ensures the selectivity of the protection system and enhances the reliability of the HVDC power transmission grid. The assessments have shown that noise, variations in fault location, and fault resistance cannot distort the performance of the algorithm. Appropriate speed (as backup protection), adaptivity, low sampling frequency, low computational burden, independence from system parameters, and the need for no complicated equipment or hardware are notable advantages of the proposed method, which make it applicable for practical applications.

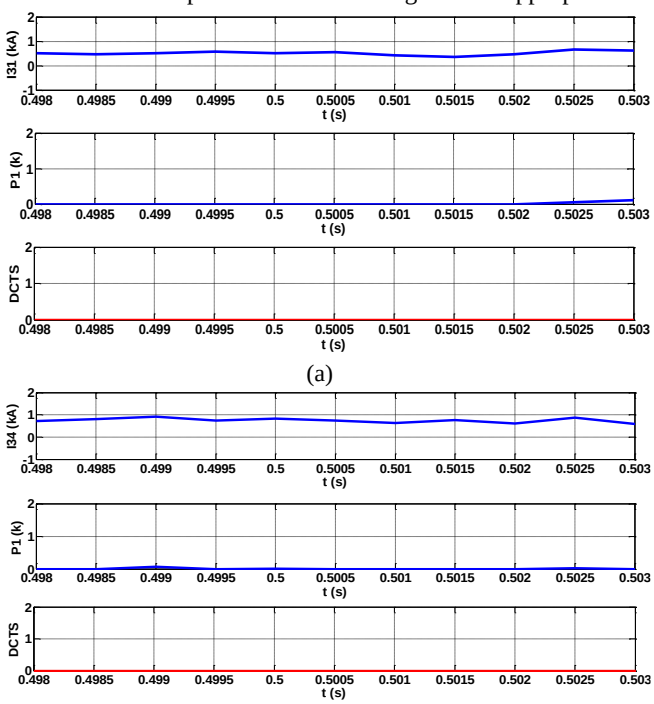


(a)

(b)

**Fig. 21.** Signals and detection indices at bus 3 against the fault at F1 in presence of Gaussian noise with SNR=20, (a) I31, (b) I34 (fault initiation: t= 0.5 s).

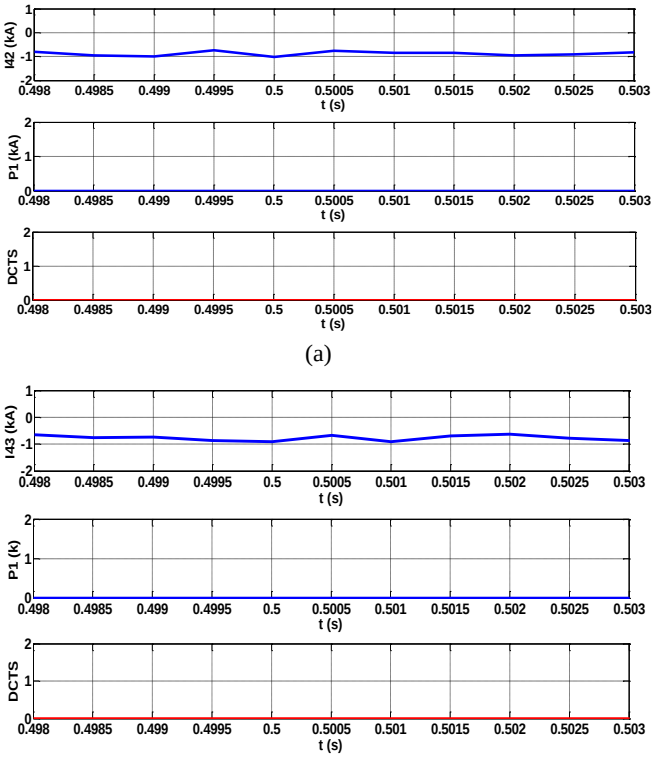


(a)

(b)

**Fig. 22.** Signals and detection indices at bus 4 against the fault at F1 in presence of Gaussian noise with SNR=20, (a) I42, (b) I43 (fault initiation: t= 0.5 s)

## References

[1] Zheng. X, Tal. N, Wu.Zh and Thorp. J, "Harmonic Current Protection Scheme for Voltage Source Converter-based High Voltage Direct Current Transmission System", *IEEE Power & Energy Society General Meeting*, 2015.

[2] Torres. R and Kristian. H, "Inverse time over Current Protection Scheme for Fault Location in Multi Terminal HVDC", *IEEE Eindhoven Power Tech Conference*, 2015.

[3] Jin. X, Ma. Zh, Song. G and Gao. S, "Novel Pilot Protection for High Voltage Direct Current Transmission Lines Based on Fault Component Current Characteristics", *IET Generation, Transmission & Distribution*, Vol. 9, Issue.5, pp. 468-474, 2015.

[4] Samir. A, Elanien. A, Khalik. A, Massoud. A and Ahmed. S, "A Directional Protection Technique for MTDC Networks", *4th International EPECS Conference*, 2015.

[5] X. Chen, H. Li, Y. Liang and G. Wang, "A Protection Scheme for Hybrid Multi-terminal HVDC Networks Utilizing a Time-domain Transient Voltage Based on Fault-blocking Converters", *International Journal of*

*Electrical Power & Energy Systems*, Vol. 118, p. 105825, June, 2020.

[6] Y. Wang, B. Zhang and X. Fan, "The Overhead Transmission Line Protection Scheme for the VSC-based HVDC Grid", *The Journal of Engineering*, October, 2018.

[7] M. Elgeziry, M. Elsadd and N. Elkalashy, "Non-Pilot Protection Scheme for Multi-terminal VSC–HVDC Transmission Systems", *IET Renewable Power Generation*, Vol. 13, Issue. 16, pp. 3033-3042, September, 2019.

[8] V. L. Merlin, R. C. Santos and S. Le Blond, "Efficient and Robust ANN-based Method for an Improved Protection of VSC-HVDC Systems", *IET Renewable Power Generation*, Vol. 12, No. 13, pp. 1555-1562, September, 2018.

[9] W. Leterme, J. Beerten and D. Van, "Non-Unit Protection of HVDC Grid with Inductive DC Cable Termination", *IEEE Transaction on Power Delivery*, Vol.31, Issue. 2, pp. 820-828, April, 2016.

[10] N. Tong, X. Lin and C. Li, "Permissive Pilot Protection Adaptive to DC Fault Interruption for VSC-MTDC", *International Journal of Electrical Power & Energy Systems*, Vol. 123, p. 106234, December, 2020.

[11] S. Jamali and S. S. Mirhosseini, "Protection of Transmission Lines in Multi-terminal HVDC Grids Using Travelling Waves Morphological Gradient", *International Journal of Electrical Power & Energy Systems*, Vol. 108, pp. 125-134, June, 2019.

[12] D. Tzelepis, A. Dysko and S. Blair, "Centralized Busbar Differential and Wavelet-based Line Protection System for Multi-terminal Direct Current Grids, with Practical IEC-61869-Compliant Measurements", *IET Generation, Transmission & Distribution*, Vol. 12, Issue. 14, pp. 3578-3586, August, 2018.

[13] S. Zhang, G. Zou and C. Wang, "A Non-unit Boundary Protection of DC Line for MMC-MTDC Grids", *International Journal of Electrical Power & Energy Systems*, Vol. 116, p. 105538, March, 2020.

[14] Song. G, Chu. X, Gao. S, Kang. X and Jiao. Z, "A New Whole-Line Quick Action Protection Principle for HVDC Transmission Lines Using One-End Current", *IEEE Transaction on Power Delivery*, Vol.30, No.2, PP. 599-607, 2015.

[15] Liu. J, Tai. N, Fan. C and Huang. W, "Protection Scheme for High Voltage Direct Current Transmission Lines Based on Transient AC Current", *IET Generation, Transmission & Distribution*, Vol.9, No.16, PP.2633-2643, 2015.

[16] Dong. Z, Ling. T, Thorp. J and Liang. Y, "A Transient Harmonic Current Protection Scheme for HVDC Transmission Line", *IEEE Transaction on Power Delivery*, Vol. 27, No. 4, PP. 2278-2285, 2012.

[17] Kong. F, Hao. Z, Zhang. S and Zhang. B, "Development of Novel Protection Device for Bipolar HVDC Transmission Lines", *IEEE Transaction on Power Delivery*, Vol. 29, No.5, pp. 2270-2278, 2014.

[18] S. R. Mohanty,A. K. Pradhn,and A. Routray, "A Cumulative Sum-based Fault Detector for Power System Relaying Application, *"IEEE Transaction on Power Delivery*, Vol. 23, No. 1, pp. 79–86, Jan, 2008.

[19] Noori. M. R and Shahrtash. S. M, "Combined Fault Detector and Faulted Phase Selector for Transmission Lines Based on Adaptive Cumulative Sum Method", *IEEE Transaction on Power Delivery*, Vol. 28, No. 3, PP. 1779-1787, 2013.

[20] E. Veilleux and B. Ooi, "Multi-terminal HVDC Thyristor Power-Flow Controller", *IEEE Transaction on Power Delivery*, Vol. 27, No. 3, pp. 1205-1212, July, 2012.

[21] Khatir. M, Zidi. S. A and Fellah. M, "HVDC Transmission Line Models for Steady State and Transient Analysis in Simulink Environment", *32nd Annual Conference on IEEE Industrial Electronics (IECON)*, November, 2006.

[22] W. Leterme, P. Tielens and S. Boeck, "Overview of Grounding and Configuration Options for Meshed HVDC Grids", *IEEE Transaction on Power Delivery*, Vol. 29, No. 6, pp. 2467-2475, December, 2014.

[23] G. Zou, B. Tong and Z. Li, "A Novel Directional Protection Based on Transient Energy for HVDC Line", *IEEE Power & Energy Society General Meeting*, 2015.

[24] K. Karf, K. Srivastava and M. Reza, "Wavelet-based Protection Strategy for DC Fault in Multi-terminal VSC HVDC Systems", *IET Generation, Transmission & Distribution*, Vol. 5, Issue. 4, pp. 496-503, March, 2015.

[25] J. Descloux, B. Raison and J. B. CUris, "Protection Algorithm Based on Differential Voltage Measurement for MTDC Grid", *12th IET International Conference on Developments in Power System Protection (DPSP)*, April, 2014.

[26] X. Jin and G. Song," A Novel Pilot Protection for VSC HVDC Transmission Lines Based on Correlation Analysis", *Energy and Power Engineering (EPE) Journal*, Vol. 5, No. 48, pp. 1182- 1186, July, 2013.

[27] S. Luo, X. Dong and S. Shi, "A Directional Protection Scheme for HVDC Transmission Lines Based on Reactive Energy", *IEEE Transaction on Power Delivery*, Vol. 31, pp. 559-567, April, 2016.

[28] IEEE Guide for Power System Protective Relay Applications over Digital Communication Channels, *IEEE Standard C37.236*, 2013.

**Mohammadreza Noori** was born in Kermanshah, Iran in 1984. He received his B.Sc. degree in Electrical Engineering from Kordestan University, Sanandaj, Iran in 2007 and his M.Sc. degree in Electrical Engineering from the Iran University of Science and Technology (IUST), Tehran, Iran in 2011. He is presently a Ph.D. candidate at Shahid Chamran University, Ahvaz, Iran. His main research areas are condition monitoring and power system protection.

**S. G.h Seifossadat** was born in Ahvaz, Iran on August 28, 1963. He received his B.Sc. degree in Electrical Engineering from the Iran University of Science and Technology (IUST), Tehran in 1989, his M.Sc. degree in Electrical Engineering from the Ferdowsi University of Mashhad, Mashhad, Iran in 1992 and his Ph.D. degree from the IUST in 2006. Currently, he is a Professor with the Department of Electrical Engineering, Shahid Chamran University of Ahvaz, Iran, where he has been since 1992. His research interests are power system protection, and power quality.

**Alireza Saffarian** was born in Ahvaz, Iran in 1981. He received his B.Sc. and M.Sc. degrees in Electrical Engineering from the Amirkabir University of Technology, Tehran, Iran in 2003 and 2005, respectively and his Ph.D. degree from the University of Tehran, Tehran, Iran. Currently, he is an Assistant Professor with the Department of Electrical Engineering, Shahid Chamran University of Ahvaz, Ahvaz, Iran. His research interests include power system protection, power system stability, and power quality assessment.

**IECO**

**This page intentionally left blank.**

International Journal of Industrial Electronics, Control and Optimization © 2021 IECO
Vol. 4, No. 3, pp. 299-311, July (2021)

# Hybrid Functions to Solve Fractional Optimal Control Problems Using the Collocation Method

Seyed Mehdi Shafiof[1,†], Javad Askari[2] , Maryam Shams Solary[3]

[1,3] Department of Mathematics, Payame Noor University, Tehran, Iran
[2]Department of Electrical and Computer Engineering, Isfahan University of Technology, Isfahan, Iran.

**ABSTRACT**

*This article aims to introduce a modern numerical method based on the hybrid functions, consisting of the Bernoulli polynomials and Block-Pulse functions. An indirect approach is proposed for solving the fractional optimal control problems (FOCPs). Firstly, the two-point boundary value problem (TPBVP) is calculated for a class of FOCPs, including integer-fractional derivatives, leading to a system of fractional differential equations (FDEs), which have the left and right-sided Caputo fractional derivatives (CFD). Therefore, a new approach is proposing to achieve the left Riemann-Liouville fractional integral (LRLFI) and right Riemann-Liouville fractional integral (RRLFI) operators for Bernoulli hybrid functions. Then, hybrid functions approximation, LRLFI and RRLFI operators, and the collocation method are used to solve the TPBVP. The error bounds for the hybrid function and LRLFI and RRLFI operators are also presented. Moreover, the convergence of the proposed method is proved. Finally, the simplicity and accuracy of the method are illustrated using some numerical examples.*

**Article Info**

***Keywords:***
Bernoulli polynomials, Block-Pulse functions, Collocation method, Fractional optimal control, Hybrid functions, Riemann-Liouville fractional integral operators

***Article History:***
**Received** 2021-01-14
**Accepted** 2021-05-02

## I. INTRODUCTION

In 1695, the idea of fractional calculus was firstly discussed in some correspondence between Leibniz and Hopital. Leibniz predicted that "one day, the useful consequences would be drawn," although his vision has been realized during the following years. Later, fractional calculus became a fascinating area for mathematicians, and many forms of fractional differential operators were proposed. The most popular ones are the Riemann-Liouville and Caputo fractional derivatives [1]-[4]. Fractional calculus is an effective modeling tool that displays the behavior of many mechanical and biological dynamics better than the integer models [5]. Recently, fractional calculus has been widely used in different fields of applied sciences such as physics, engineering, and bioengineering [6], stochastic systems [7], and the theory of diffusion [8]. One of the latest applications of fractional models is to investigate and analyze the complex transmission pattern of COVID-19 disease [9], [10].

The optimal control problems have been studied in almost many fields to provide broad background knowledge. These problems minimize an objective function, subject to dynamic constraints on the state and control variables [11], [12]. FOCPs are a subclass of optimal control problems, which objective function or constraint equation governed by FDE [13]. Since the dynamic constraints of these problems involve FDE, finding the exact solution is very complicated, so numerical methods must be utilized to solve FOCPs. These numerical methods can be divided into two major classes, including direct and indirect methods. The indirect methods are based on Pontryagin's maximum principle and the necessary optimality conditions for FOCPs. These conditions lead to a TPBVP that can analytically or numerically be solved using widely known methods for differential equations. For this purpose, Agrawal used the calculus of variation to specify the optimality conditions for FOCPs, based on the Riemann-Liouville fractional derivatives (RLFD) [14]. He also set the optimality conditions for FOCPs containing CFD [15]. The TPBVP,

[†]**Corresponding Author**: smshafiof@pnu.ac.ir , Tel: +98-3135328134, Department of Mathematics, Payame Noor University, Tehran, Iran

including left and right fractional derivatives, have approximately been solved by the Legendre multiwavelet collocation method [16], variational iteration and Adomian decomposition methods [17], and fractional power series neural network method [18]. The advantages of indirect methods are explained in [19], [20]. In the direct methods, FOCP is solved by minimizing the objective function, using the approximation or discretization of unknown functions, according to the problem constraints, and without deriving the Hamiltonian equations. Some examples of this method are as follows: Hybrid of Block-Pulse functions and orthonormal Taylor polynomials [21], Bernoulli polynomials with the operational matrix of fractional integration [22], Genocchi operational matrix of integration [23], Fractional-order Bessel wavelet functions [24].

In recent years, many authors have applied hybrid functions to solve different problems because hybrid functions are a mathematical power tool to approximate the functions defined on the distinct subintervals. Hybrid functions have consisted of the combination of a polynomial with piecewise constant basis functions such as Block-Pulse. For more details about this topic, can refer to [25]-[27].

In the current article, we focus on the FOCP characterized by integer-fractional dynamical system as follows:

$$\min J = \int_{t_0}^{t_f} f\big(t, x(t), u(t)\big)dt, \tag{1}$$

subject to

$$K_1\dot{x}(t) + K_2\, {}_{t_0}^{C}D_t^{\alpha}x(t) = g\big(t, x(t)\big) + b(t)u(t), \tag{2}$$

with initial condition

$$x(t_0) = x_0, \qquad 0 < \alpha < 1, \tag{3}$$

where $f\big(t, x(t), u(t)\big)$, $g\big(t, x(t)\big)$ and $b(t)$ are smooth, $b(t)$ is non-zero and, $K_1$ and $K_2$ are scalar numbers. As a practical example, the dynamical system of light amplification in Erbium-doped fiber amplifier, one of the most commonly applied types of fiber amplifiers in metro optical networks, contains the integer-fractional derivatives [28].

This article presents a new method to obtain the LRLFI, and RRLFI operators for the hybrid of Bernoulli polynomials and Block-Pulse functions directly and without any approximation. The accuracy of these operators is effective in increasing the accuracy of the proposed method for solving FOCPs. We employ the following steps to solve the stated FOCP using the suggested indirect method.

First, TPBVP based on the left and right CFD is obtained from the necessary optimality conditions of the FOCP. Then, in the obtained FDEs, the highest order derivatives of the state $x(t)$ and costate $\lambda(t)$ functions are approximated by using the Bernoulli hybrid functions with unknown coefficients. Afterward, by applying the LRLFI, RRLFI operators, and Legendre-Gauss collocation method, the problem is converted to a system of algebraic equations, by the solution of which the unknown coefficients are obtained. Besides, estimation errors and convergence analysis are brought. The existing results demonstrate that by increasing the number of hybrid functions basis, the approximate solutions converge to the exact solutions.

The organization of this paper is as follows: In Section II, we provide some necessary definitions and properties of fractional calculus and hybrid functions. Section III, introduces LRLFI and RRLFI operators for hybrid functions. In Section IV, we obtain the necessary optimality conditions and describe the numerical method for solving FOCPs. We provide error bound and convergence analysis for the proposed method in Section V. In Section VI, test problems are used to verify the accuracy of the suggested approach. The final section of this article is the conclusion.

## II. PRELIMINARIES AND NOTATIONS

We present some basic definitions and some required properties of the fractional calculus and hybrid functions used in this article.

### A. *Fractional Calculus*

In this part, we briefly provide some definitions of the fractional derivative and integral, and their properties [1]-[4], [29]. Let $f: [a, b] \to R$ be a function, and $\alpha > 0$ be the order of fractional derivative and integral, and $m = [\alpha] + 1$.

**Definition 1** The LRLFI and RRLFI operators of order $\alpha$ are respectively defined as follows:

$${}_aI_t^{\alpha}f(t) = \frac{1}{\Gamma(\alpha)}\int_a^t (t-\tau)^{\alpha-1} f(\tau)d\tau, \tag{4}$$

$${}_tI_b^{\alpha}f(t) = \frac{1}{\Gamma(\alpha)}\int_t^b (\tau-t)^{\alpha-1} f(\tau)d\tau, \tag{5}$$

where $\Gamma(\alpha)$ is the Gamma function.

**Definition 2** The left and right RLFD operators of order $\alpha$ are given by:

$${}_a^{RL}D_t^{\alpha}f(t) = \frac{1}{\Gamma(m-\alpha)}\frac{d^m}{dt^m}\int_a^t (t-\tau)^{m-\alpha-1} f(\tau)\, d\tau, \tag{6}$$

$${}_t^{RL}D_b^{\alpha}f(t) = \frac{(-1)^m}{\Gamma(m-\alpha)}\frac{d^m}{dt^m}\int_t^b (\tau-t)^{m-\alpha-1} f(\tau)\, d\tau. \tag{7}$$

**Definition 3** The left and right CFD operators are defined by:

$${}_a^{C}D_t^{\alpha}f(t) = \frac{1}{\Gamma(m-\alpha)}\int_a^t (t-\tau)^{m-\alpha-1} f^{(m)}(\tau)d\tau, \tag{8}$$

$${}_t^{C}D_b^{\alpha}f(t) = \frac{(-1)^m}{\Gamma(m-\alpha)}\int_t^b (\tau-t)^{m-\alpha-1} f^{(m)}(\tau)d\tau. \tag{9}$$

Some properties of the Caputo derivative are as follows:

$${}_a^{C}D_t^{\alpha}\ {}_aI_t^{\alpha}f(t) = f(t),\ {}_t^{C}D_b^{\beta}\ {}_tI_b^{\beta}f(t) = f(t),\ 0 < \beta < 1. \tag{10}$$

$${}_aI_t^{\alpha}\,{}_a^{C}D_t^{\alpha}f(t) = f(t) - \sum_{i=0}^{m-1} f^{(i)}(a)\frac{(t-a)^i}{i!}. \tag{11}$$

$${}_a^{C}D_t^{\alpha}K = 0,\ (K \text{ is constant.}) \tag{12}$$

$$\begin{cases} {}_a^{C}D_t^{m}f(t) = f^{(m)}(t), \\ {}_t^{C}D_b^{m}f(t) = (-1)^m f^{(m)}(t), \quad m \in N, \\ {}_a^{C}D_t^{\alpha}f(t) = {}_aI_t^{m-\alpha}D^m f(t), \\ {}_t^{C}D_b^{\alpha}f(t) = (-1)^m\ {}_tI_b^{m-\alpha}D^m f(t), \qquad \alpha \notin N_0. \end{cases} \tag{13}$$

The relation between RCFD and RRLFD is as follows:

$$ {}_t^C D_b^\alpha f(t) = {}^{RL}_t D_b^\alpha f(t) - \sum_{k=0}^{m-1} \frac{f^{(k)}(b)}{\Gamma(k+1-\alpha)} (b-t)^{k-\alpha}. \quad (14) $$

The following relations are established:

$$ {}_a I_t^\alpha \; {}_a I_t^\beta f(t) = {}_a I_t^{\alpha+\beta} f(t), \; {}_t I_b^\alpha \; {}_t I_b^\beta f(t) = {}_t I_b^{\alpha+\beta} f(t), \alpha, \beta > 0 \quad (15) $$

$$ {}_t I_b^\alpha \; {}_t^C D_b^\alpha f(t) = f(t) - \sum_{i=0}^{m-1} (-1)^i f^{(i)}(b) \frac{(b-t)^i}{i!}. \quad (16) $$

$$ {}_t I_b^\alpha (b-t)^{B-1} = \frac{\Gamma(B)}{\Gamma(B+\alpha)} (b-t)^{B+\alpha-1}, \quad \alpha, B > 0. \quad (17) $$

$$ {}_0 I_t^\alpha t^r = \frac{\Gamma(r+1)}{\Gamma(r+1+\alpha)} t^{r+\alpha}, \quad r \in N_0, \quad t > 0. \quad (18) $$

$$ \| {}_a I_t^\alpha f(t) \|_{L^2(a,b)} \le \frac{(b-a)^\alpha}{\Gamma(\alpha+1)} \| f(t) \|_{L^2(a,b)}, \quad 0 < \alpha \le 1. \quad (19) $$

$$ \| {}_t I_b^\alpha f(t) \|_{L^2(a,b)} \le \frac{(b-a)^\alpha}{\Gamma(\alpha+1)} \| f(t) \|_{L^2(a,b)}, \quad 0 < \alpha \le 1. \quad (20) $$

LRLFI operator satisfies the following formula:

$$ \frac{1}{\Gamma(\alpha)} \int_0^t (t-\tau)^{\alpha-1} f(\tau) d\tau = \frac{1}{\Gamma(\alpha)} t^{\alpha-1} * f(t), \quad (21) $$

where $t^{\alpha-1} * f(t)$ is the convolution of $t^{\alpha-1}$ and $f(t)$. Also, RLFI and CFD operators are linear operations.

### B. Bernoulli Polynomials

Bernoulli polynomials of order $m$ can be defined as [30]:

$$ \beta_m(t) = \sum_{k=0}^{m} \binom{m}{k} \alpha_{m-k} t^k, \quad (22) $$

where $\alpha_k = \beta_k(0), k = 0,1,2,\dots,m,$ are Bernoulli numbers. The Bernoulli polynomials satisfy the following formula:

$$ \beta_m(1-t) = (-1)^m \beta_m(t) \quad (23) $$

### C. Hybrid of Block-Pulse Functions and Bernoulli Polynomials

Hybrid functions $b_{nm}(t)$ for $n = 1,2,\dots,N, m = 0,1,2,\dots,M$ are given over the interval $[0,1)$ as:

$$ b_{nm}(t) = \begin{cases} \beta_m(Nt-n+1), & t \in \left[\frac{n-1}{N}, \frac{n}{N}\right), \\ 0, & otherwise, \end{cases} \quad (24) $$

where $n$ and $m$ are the orders of the Block-Pulse functions and Bernoulli polynomials, respectively. It is clear that

$$ Y = span\{b_{10}(t), b_{20}(t), \dots, b_{N0}(t), b_{11}(t), \dots, b_{N1}(t), \dots, b_{1M}(t), \dots, b_{NM}(t)\}, \quad (25) $$

is a finite dimensional and closed subspace of the Hilbert space $H = L^2[0,1]$. Therefore, $Y$ is a complete subspace, and there is a unique best approximation out of $Y$, such as $f_{NM} \in Y$ for each $f \in H$, that is $\forall y \in Y, \|f - f_{NM}\| \le \|f - y\|$. Since $f_{NM} \in Y$, there exist unique coefficients $c_{10}, c_{20}, \dots, c_{NM}$, so that [31]

$$ f(t) \simeq f_{NM}(t) = \sum_{n=1}^{N} \sum_{m=0}^{M} c_{nm} b_{nm}(t) = C^T B(t), \quad (26) $$

where $C$ and $B(t)$ are the following vectors:

$$ B^T(t) = [b_{10}(t), b_{20}(t), \dots, b_{N0}(t), b_{11}(t), \dots, b_{N1}(t), \dots, b_{1M}(t), \dots, b_{NM}(t)], $$
$$ C^T = [c_{10}, c_{20}, \dots, c_{N0}, c_{11}, \dots, c_{N1}, \dots, c_{1M}, \dots, c_{NM}]. \quad (27) $$

## III. LRLFI AND RRLFI OPERATORS FOR BERNOULLI HYBRID FUNCTIONS

In this section, LRLFI and RRLFI operators, are obtained for hybrid functions which, are shown with $I_L^\alpha$ and $I_R^\alpha$, respectively. We divide the interval $[0,1]$ into three subintervals including $\left[0, \frac{n-1}{N}\right), \left[\frac{n-1}{N}, \frac{n}{N}\right)$ and $\left[\frac{n}{N}, 1\right)$ according to the properties of the hybrid functions.

### A. LRLFI Operator

In this part, we use the new method to obtain the LRLFI operator for hybrid functions. Suppose ${}_0 I_t^\alpha B(t) = I_L^\alpha B(t)$, where

$$ I_L^\alpha B(t) = [I_L^\alpha b_{10}(t), \dots, I_L^\alpha b_{N0}(t), I_L^\alpha b_{11}(t), \dots, I_L^\alpha b_{N1}(t), \dots, I_L^\alpha b_{1M}(t), \dots, I_L^\alpha b_{NM}(t)]^T. $$

We obtain $I_L^\alpha b_{nm}(t)$ for $t \in \left[\frac{n-1}{N}, \frac{n}{N}\right), n = 1,2,\dots,N, m = 0,1,2,\dots,M$. So from Equs. (4) and (21), and by applying the definition of the convolution, we have

$$ I_L^\alpha b_{nm}(t) = \frac{1}{\Gamma(\alpha)} \int_0^t (t-\tau)^{\alpha-1} b_{nm}(\tau) d\tau = \frac{1}{\Gamma(\alpha)} \int_0^t \tau^{\alpha-1} b_{nm}(t-\tau) d\tau. \quad (28) $$

By using the Equs. (24) and (28), and introducing the change of variable $T = t - \frac{n-1}{N}$, we have

$$ I_L^\alpha b_{nm}(t) = \frac{1}{\Gamma(\alpha)} \int_0^t \tau^{\alpha-1} b_{nm}(t-\tau) d\tau $$
$$ = \frac{1}{\Gamma(\alpha)} \int_0^{t-\frac{n-1}{N}} \tau^{\alpha-1} \beta_m(N(t-\tau)-n+1) d\tau $$
$$ = \frac{1}{\Gamma(\alpha)} \int_0^{t-\frac{n-1}{N}} \tau^{\alpha-1} \beta_m\left(N\left(\left(t-\frac{n-1}{N}\right)-\tau\right)\right) d\tau $$
$$ = \frac{1}{\Gamma(\alpha)} \int_0^T \tau^{\alpha-1} \beta_m(N(T-\tau)) d\tau = {}_0 I_T^\alpha \beta_m(NT). \quad (29) $$

From the Equs. (18) and (29), and by using the definition of Bernoulli polynomials (22), we get

$$ {}_0 I_T^\alpha \beta_m(NT) = \sum_{k=0}^{m} \binom{m}{k} N^k \alpha_{m-k} \; {}_0 I_T^\alpha (T^k) = \sum_{k=0}^{m} \binom{m}{k} N^k \alpha_{m-k} \frac{\Gamma(k+1)}{\Gamma(k+\alpha+1)} \mathrm{T}^{k+\alpha}. \quad (30) $$

Then, the Equ. (30) yields

$$ \frac{1}{\Gamma(\alpha)} \int_0^{t-\frac{n-1}{N}} \tau^{\alpha-1} \beta_m(N(t-\tau)-n+1) d\tau = \sum_{k=0}^{m} \binom{m}{k} N^k \alpha_{m-k} \frac{\Gamma(k+1)}{\Gamma(k+\alpha+1)} \left(t - \frac{n-1}{N}\right)^{k+\alpha}. \quad (31) $$

In addition, for $t \in [\frac{n}{N}, 1)$, by using the Equs. (24) and (28), we have

$$I_L^{\alpha} b_{nm}(t) = \frac{1}{\Gamma(\alpha)} \int_0^t \tau^{\alpha-1} b_{nm}(t-\tau) d\tau$$
$$= \frac{1}{\Gamma(\alpha)} \int_{t-\frac{n}{N}}^{t-\frac{n-1}{N}} \tau^{\alpha-1} \beta_m(N(t-\tau)-n+1) d\tau$$
$$= \frac{1}{\Gamma(\alpha)} \left( \int_0^{t-\frac{n-1}{N}} \tau^{\alpha-1} \beta_m(N(t-\tau)-n+1) d\tau - \int_0^{t-\frac{n}{N}} \tau^{\alpha-1} \beta_m(N(t-\tau)-n+1) d\tau \right). \quad (32)$$

The first integral in relation (32) is equal to Equ. (31) and the second integral is calculated using the Equ. (23) as follows:

$$\frac{1}{\Gamma(\alpha)} \int_0^{t-\frac{n}{N}} \tau^{\alpha-1} \beta_m(N(t-\tau)-n+1)$$
$$= \frac{1}{\Gamma(\alpha)} \int_0^{t-\frac{n}{N}} \tau^{\alpha-1} \beta_m\big(1-(-N(t-\tau)+n)\big) d\tau$$
$$= \frac{(-1)^m}{\Gamma(\alpha)} \int_0^{t-\frac{n}{N}} \tau^{\alpha-1} \beta_m\left(-N\left(\left(t-\frac{n}{N}\right)-\tau\right)\right) d\tau, \quad (33)$$

by substituting $Z = t - \frac{n}{N}$ into Equ. (33), we have

$$\frac{(-1)^m}{\Gamma(\alpha)} \int_0^Z \tau^{\alpha-1} \beta_m\big(-N(Z-\tau)\big) d\tau = (-1)^m \, {}_0I_Z^{\alpha} \beta_m(-NZ). \quad (34)$$

Following a similar approach to the one used in Equ. (30), the Equs. (32) to (34) yield

$$\frac{1}{\Gamma(\alpha)} \int_0^{t-\frac{n}{N}} \tau^{\alpha-1} \beta_m(N(t-\tau)-n+1) d\tau$$
$$= (-1)^m \sum_{k=0}^{m} \binom{m}{k} (-N)^k \alpha_{m-k} \frac{\Gamma(k+1)}{\Gamma(k+\alpha+1)} \left(t-\frac{n}{N}\right)^{k+\alpha}. \quad (35)$$

Finally, using the preceding results, we can write

$$I_L^{\alpha} b_{nm}(t) = \begin{cases} 0, & t \in \left[0, \frac{n-1}{N}\right), \\ R_{nm}(t), & t \in \left[\frac{n-1}{N}, \frac{n}{N}\right), \\ R_{nm}(t) - S_{nm}(t), & t \in \left[\frac{n}{N}, 1\right), \end{cases} \quad (36)$$

Where $R_{nm}(t)$ and $S_{nm}(t)$ are the relations (31) and (35), respectively.

### *B. RRLFI Operator*

Now, we obtain the RRLFI operator for hybrid functions. Suppose $t \in \left[\frac{n-1}{N}, \frac{n}{N}\right), n = 1,2,\dots,N$, and ${}_tI_1^{\alpha} B(t) = I_R^{\alpha} B(t)$, from Equ. (5) and Bernoulli hybrid functions (24), we have

$$I_R^{\alpha} b_{nm}(t) = \frac{1}{\Gamma(\alpha)} \int_t^1 (\tau-t)^{\alpha-1} b_{nm}(\tau) d\tau$$
$$= \frac{1}{\Gamma(\alpha)} \int_t^{\frac{n}{N}} (\tau-t)^{\alpha-1} \beta_m(N\tau-n+1) d\tau$$
$$= {}_tI_{\frac{n}{N}}^{\alpha} \beta_m(Nt-n+1) = {}_tI_{\frac{n}{N}}^{\alpha} \beta_m\left(1-N\left(\frac{n}{N}-t\right)\right).$$

From Equs. (17), (22), and (23), we get

$${}_tI_{\frac{n}{N}}^{\alpha} \beta_m(Nt-n+1) = (-1)^m \, {}_tI_{\frac{n}{N}}^{\alpha} \beta_m\left(N\left(\frac{n}{N}-t\right)\right)$$
$$= (-1)^m \, {}_tI_{\frac{n}{N}}^{\alpha} \left( \sum_{k=0}^{m} \binom{m}{k} N^k \alpha_{m-k} \left(\frac{n}{N}-t\right)^k \right)$$
$$= (-1)^m \sum_{k=0}^{m} \binom{m}{k} N^k \alpha_{m-k} \, {}_tI_{\frac{n}{N}}^{\alpha} \left(\frac{n}{N}-t\right)^k$$
$$= (-1)^m \sum_{k=0}^{m} \binom{m}{k} N^k \alpha_{m-k} \frac{\Gamma(k+1)}{\Gamma(k+\alpha+1)} \left(\frac{n}{N}-t\right)^{k+\alpha}.$$

So, we conclude

$${}_tI_{\frac{n}{N}}^{\alpha} \beta_m(Nt-n+1)$$
$$= (-1)^m \sum_{k=0}^{m} \binom{m}{k} N^k \alpha_{m-k} \frac{\Gamma(k+1)}{\Gamma(k+\alpha+1)} \left(\frac{n}{N}-t\right)^{k+\alpha}. \quad (37)$$

For $t \in \left[0, \frac{n-1}{N}\right)$, from Equs. (5) and (24), the RRLFI operator is obtained as follows:

$$I_R^{\alpha} b_{nm}(t) = \frac{1}{\Gamma(\alpha)} \int_t^1 (\tau-t)^{\alpha-1} b_{nm}(\tau) d\tau$$
$$= \frac{1}{\Gamma(\alpha)} \int_t^{\frac{n-1}{N}} (\tau-t)^{\alpha-1} b_{nm}(\tau) d\tau$$
$$+ \frac{1}{\Gamma(\alpha)} \int_{\frac{n-1}{N}}^{\frac{n}{N}} (\tau-t)^{\alpha-1} b_{nm}(\tau) d\tau$$
$$+ \frac{1}{\Gamma(\alpha)} \int_{\frac{n}{N}}^{1} (\tau-t)^{\alpha-1} b_{nm}(\tau) d\tau$$
$$= \frac{1}{\Gamma(\alpha)} \int_{\frac{n-1}{N}}^{\frac{n}{N}} (\tau-t)^{\alpha-1} \beta_m(N\tau-n+1) d\tau$$
$$= \frac{1}{\Gamma(\alpha)} \int_t^{\frac{n}{N}} (\tau-t)^{\alpha-1} \beta_m(N\tau-n+1) d\tau$$
$$- \frac{1}{\Gamma(\alpha)} \int_t^{\frac{n-1}{N}} (\tau-t)^{\alpha-1} \beta_m(N\tau-n+1) d\tau$$
$$= {}_tI_{\frac{n}{N}}^{\alpha} \beta_m(Nt-n+1) - {}_tI_{\frac{n-1}{N}}^{\alpha} \beta_m(Nt-n+1).$$

${}_tI_{\frac{n}{N}}^{\alpha} \beta_m(Nt-n+1)$ is equal to Equ. (37), and ${}_tI_{\frac{n-1}{N}}^{\alpha} \beta_m(Nt-n+1)$ is calculated as follows:

$${}_tI_{\frac{n-1}{N}}^{\alpha} \beta_m(Nt-n+1) = {}_tI_{\frac{n-1}{N}}^{\alpha} \beta_m\left(-N\left(\frac{n-1}{N}-\mathrm{t}\right)\right)$$
$$= \sum_{k=0}^{m} \binom{m}{k} (-N)^k \alpha_{m-k} \, {}_tI_{\frac{n-1}{N}}^{\alpha} \left(\frac{n-1}{N}-t\right)^k,$$

By using Equ. (17), we get

$${}_tI_{\frac{n-1}{N}}^{\alpha} \beta_m(Nt-n+1)$$
$$= \sum_{k=0}^{m} \binom{m}{k} (-N)^k \alpha_{m-k} \frac{\Gamma(k+1)}{\Gamma(k+\alpha+1)} \left(\frac{n-1}{N}-t\right)^{k+\alpha}. \quad (38)$$

By applying the Equs. (37) and (38), we deduce that

$I_R^{\alpha} b_{nm}(t) =$

$$\begin{cases} {}_tI_{\frac{n}{N}}^{\alpha}\beta_m(Nt-n+1) - {}_tI_{\frac{n-1}{N}}^{\alpha}\beta_m(Nt-n+1), & t\in\left[0,\frac{n-1}{N}\right), \\ {}_tI_{\frac{n}{N}}^{\alpha}\beta_m(Nt-n+1) & t\in\left[\frac{n-1}{N},\frac{n}{N}\right), \\ 0, & t\in\left[\frac{n}{N},1\right). \end{cases} \quad (39)$$

## IV. DESCRIPTION OF THE PROPOSED METHOD

In this section, we find $x(t)$ and $u(t)$ such that the constraint (2) and the initial condition (3) are satisfied and the objective function (1) of the problem becomes minimum. To this end, we transform the necessary optimality conditions of the FOCP into an equivalent fractional TPBVP. Then, using fractional operators and the collocation method, TPBVP is converted to a system of algebraic equations. By solving this system, the state variable$x(t)$, the costate variable$\lambda(t)$, and finally the control variable $u(t)$, are determined.

### A. *Necessary Optimality Conditions*

In this part, we obtain the necessary optimality conditions for FOCP in the form of fractional TPBVP according to the proposed method based on the LCFD and RCFD operators.

**Theorem 1** If $\big(x(t),\ u(t)\big)$ be the optimal solution of FOCP expressed in Equs. (1) to (3), there will be a costate function $\lambda(t)$, such that

$$\begin{cases} K_2\,{}_t^{C}D_{t_f}^{\alpha}\lambda(t) - K_1\dot{\lambda}(t) = P\big(t,x(t),\lambda(t)\big), \\ K_1\dot{x}(t) + K_2\,{}_{t_0}^{C}D_t^{\alpha}x(t) = Q\big(t,x(t),\lambda(t)\big), \\ x(t_0)=x_0,\ \ \lambda\big(t_f\big)=0, \end{cases} \quad (40)$$

Where $P$ and $Q$ are the known functions in terms of $x(t)$ and $\lambda(t)$.

**Proof** This theorem is stated in reference [32] based on RRLFD. For compatibility with the proposed method, we replace RRLFD with RCFD. For this purpose, from Equ. (14), RRLFD of the costate function can be written in the following form:

$${}_t^{RL}D_{t_f}^{\alpha}\lambda(t) = {}_t^{C}D_{t_f}^{\alpha}\lambda(t) + \frac{\lambda(t_f)}{\Gamma(1-\alpha)}(t_f-t)^{-\alpha},$$

since$\lambda\big(t_f\big)=0$, we apply ${}_t^{C}D_{t_f}^{\alpha}\lambda(t)$, in the first Equ. (40) instead of the RRLFD. Also, using the necessary optimality conditions, the control variable can be represented in terms of costate and state variables. □

### B. *Solving the Fractional TPBVP*

In this part, the Bernoulli hybrid functions, LRLFI and RRLFI operators, and Legendre collocation method are used to approximate the solution of the mentioned fractional TPBVP. For solving the fractional differential equations (40) without loss of generality, let $t_0=0$ and $t_f=1$. Then, we expand the first-order derivative of the state function $\dot{x}(t)$ and costate function $\dot{\lambda}(t)$ by the hybrid function as follows:

$$\dot{x}(t) = A^T B(t), \quad (41)$$

$$\dot{\lambda}(t) = C^T \bar{B}(t), \quad (42)$$

where

$$B^T(t) = [b_{10}(t), b_{20}(t), \dots, b_{N0}(t), b_{11}(t), \dots, b_{N1}(t), \dots, b_{1M}(t), \dots, b_{NM}(t)], \quad (43)$$

$$A^T = [a_{10}, a_{20}, \dots, a_{N0}, a_{11}, \dots, a_{N1}, \dots, a_{1M}, \dots, a_{NM}], \quad (44)$$

$$\bar{B}^T(t) = [b_{10}(t), b_{20}(t), \dots, b_{\acute{N}0}(t), b_{11}(t), \dots, b_{\acute{N}1}(t), \dots, b_{1\acute{M}}(t), \dots, b_{\acute{N}\acute{M}}(t)], \quad (45)$$

$$C^T = [c_{10}, c_{20}, \dots, c_{\acute{N}0}, c_{11}, \dots, c_{\acute{N}1}, \dots, c_{1\acute{M}}, \dots, c_{\acute{N}\acute{M}}]. \quad (46)$$

If $\alpha=0, \alpha=1,$ Equs. (4) and (41) yield

$$x(t) = A^T I_L^1 B(t) + x_0, \quad (47)$$

By applying properties (10), (12), and (15) in Equ. (47), we obtain

$${}_0^{C}D_t^{\alpha}x(t) = A^T I_L^{1-\alpha}B(t). \quad (48)$$

Let $\alpha=1, b=1,$ from the Equs. (5), (42), and boundary conditions (40), we get

$$\lambda(t) = -C^T I_R^1 \bar{B}(t), \quad (49)$$

By using Equs. (10) and (15), the Equ. (49) yields

$${}_t^{C}D_1^{\alpha}\lambda(t) = -C^T I_R^{1-\alpha}\bar{B}(t). \quad (50)$$

Substituting relations (41), (42), and (47) to (50) into Equs. (40) implies that

$$\begin{aligned} &-K_1 C^T \bar{B}(t) - K_2 C^T I_R^{1-\alpha}\bar{B}(t) \\ &\quad = P\big(t, A^T I_L^1 B(t) + x_0, -C^T I_R^1 \bar{B}(t)\big), \\ &K_1 A^T B(t) + K_2 A^T I_L^{1-\alpha} B(t) \\ &\quad = Q\big(t, A^T I_L^1 B(t) + x_0, -C^T I_R^1 \bar{B}(t)\big). \end{aligned} \quad (51)$$

After simplifying the Equs. (51), if possible, now we collocate them in the Legendre-Gauss collocation points $\{t_i\}_{i=0}^{k}, k = N(M+1) + \acute{N}\big(\acute{M}+1\big) - 1$, on the interval $[0,1]$ which are the roots of Legendre polynomial $p_{k+1}$. The system of Equs. (51) is reduced to that of algebraic equations as follows:

$$\begin{aligned} &-K_1 C^T \bar{B}(t_i) - K_2 C^T I_R^{1-\alpha}\bar{B}(t_i) \\ &\quad = P\big(t_i, A^T I_L^1 B(t_i) + x_0, -C^T I_R^1 \bar{B}(t_i)\big), \\ &K_1 A^T B\big(t_j\big) + K_2 A^T I_L^{1-\alpha} B\big(t_j\big) \\ &\quad = Q\left(t_j, A^T I_L^1 B\big(t_j\big) + x_0, -C^T I_R^1 \bar{B}\big(t_j\big)\right), \end{aligned} \quad (52)$$

Where $i = 0,1,\dots,\acute{N}\big(\acute{M}+1\big)-1$ and $j = \acute{N}\big(\acute{M}+1\big), \dots, k$. By solving Equs. (52) via a standard numerical method, the unknown coefficient $A^T$ and $C^T$ will be determined.

**Remark 1** In the dynamic constraint of the system, if $K_1=0$, the approximate functions of the problem-solving process are considered as follows:

$${}_0^{C}D_t^{\alpha}x(t) = A^T B(t), \quad (53)$$

$${}_t^{C}D_1^{\alpha}\lambda(t) = C^T \bar{B}(t). \quad (54)$$

By using Equs. (11), (16), and LRLFI and RRLFI operators, from Equs. (53) and (54), $x(t)$ and $\lambda(t)$ can be written as:

$$x(t) = A^T I_L^{\alpha} B(t) + x(0) = A^T I_L^{\alpha} B(t) + x_0, \quad (55)$$

$$\lambda(t) = C^T I_R^{\alpha}\bar{B}(t) + \lambda(1) = C^T I_R^{\alpha}\bar{B}(t). \quad (56)$$

## V. ERROR BOUNDS

In this section, the error bounds for the hybrid functions approximation, LRLFI and RRLFI operators, and the proposed method are presented.

### A. Error Bound for Hybrid Functions Approximation

In the following theorem, the upper bound for the error and the convergence of Bernoulli hybrid functions approximation are investigated.

**Theorem 2** Suppose that $f(t) \in C^{(M+1)}[0,1]$ and $f_{NM}(t) = \sum_{n=1}^{N}\sum_{m=0}^{M} c_{nm} b_{nm}(t)$, be the best approximation $f(t)$ out of $Y$ given in (25) and (26), the following inequality is satisfied:

$$\|f(t) - f_{NM}(t)\|_2 \le \frac{L}{(M+1)!N^{(M+1)}\sqrt{2M+3}}, \quad (57)$$

where

$$L = max\left|f^{(M+1)}(t)\right|, t \in [0,1]. \quad (58)$$

**Proof** We divide interval [0,1] into subintervals $\left[\frac{n-1}{N}, \frac{n}{N}\right], n = 1,2,\dots,N$, with the limitation that $f_n$ approximates $f$ over the subinterval $\left[\frac{n-1}{N}, \frac{n}{N}\right], n = 1,2,\dots,N$ and $f(t) \simeq \sum_{n=1}^{N} f_n(t)$. Let the Taylor polynomials

$$f_n(t) = \sum_{k=0}^{M} f^{(k)}\left(\frac{n-1}{N}\right)\frac{(t-\frac{n-1}{N})^k}{k!},$$

We know that

$$|f(t) - f_n(t)| \le \left|f^{(M+1)}(\xi)\right|\frac{\left(t-\frac{n-1}{N}\right)^{M+1}}{(M+1)!}, \xi \in \left[\frac{n-1}{N}, \frac{n}{N}\right]. \quad (59)$$

Assume that $f_{nM}(t) = \sum_{m=0}^{M} c_{nm} b_{nm}(t)$, from Equs. (24), (58), and (59), we have

$$\begin{aligned}
\|f(t) - f_{NM}\|_2^2 &= \int_0^1 |f(t) - f_{NM}(t)|^2 dt \\
&= \sum_{n=1}^{N}\int_{\frac{n-1}{N}}^{\frac{n}{N}} |f(t) - f_{nM}(t)|^2 dt \\
&\le \sum_{n=1}^{N}\int_{\frac{n-1}{N}}^{\frac{n}{N}} |f(t) - f_n(t)|^2 dt \\
&\le \sum_{n=1}^{N}\int_{\frac{n-1}{N}}^{\frac{n}{N}} \left|f^{(M+1)}(\xi)\right|^2 \left(\frac{\left(t-\frac{n-1}{N}\right)^{M+1}}{(M+1)!}\right)^2 dt \\
&\le \frac{L^2}{(2M+3)\left((M+1)!\right)^2 N^{2(M+1)}},
\end{aligned}$$

And by taking square roots, the proof is finished. This theorem shows that the Bernoulli hybrid functions approximation error tends to zero if M and N are sufficiently increased. This result confirms that $f_{NM}$ converges to $f$. □

### B. Error Bound for the LRLFI Operator

**Theorem 3** Suppose $f(t) \in C^{(M+1)}[0,1]$ and $0 < \alpha \le 1$, the error bound for the LRLFI operator is achieved as follows:

$$\|I_L^{\alpha} f(t) - I_L^{\alpha} f_{NM}(t)\|_2 \le \frac{L}{\Gamma(\alpha+1)(M+1)!N^{(M+1)}\sqrt{2M+3}}. \quad (60)$$

**Proof** This theorem is proved by using inequalities (19) and (57). □

### C. Error Bound for the RRLFI Operator

**Theorem 4** Assume $f(t) \in C^{(M+1)}[0,1]$. For $0 < \alpha \le 1$, the error bound for the RRLFI operator is defined by:

$$\|I_R^{\alpha} f(t) - I_R^{\alpha} f_{NM}(t)\|_2 \le \frac{L}{\Gamma(\alpha+1)(M+1)!N^{(M+1)}\sqrt{2M+3}}. \quad (61)$$

**Proof** By using relations (20) and (57), inequality (61) is resulted. □

### D. Error Bound for the Proposed Method

In this section, we estimate the error of the proposed method with respect to the hybrid functions order $N, M, \acute{N}$, and $\acute{M}$. This theorem shows while the dimensions of the basis functions are increased, the error bounds tend to zero, consequently the state and control approximate variables converge to the exact values.

**Theorem 5** Suppose $x(t)$ and $\lambda(t)$ are the exact solutions of the TPBVP (40), $x(t)$ and $\lambda(t) \in C^{(M+2)}[0,1]$. $x_{NM}(t) = A^T I_L^1 B(t) + x_0$ and $\lambda_{\acute{N}\acute{M}}(t) = -C^T I_R^1 \bar{B}(t)$ are the approximate solutions of $x(t)$ and $\lambda(t)$ where achieved from Equs. (47) and (49). Also $P\big(t, x(t), \lambda(t)\big)$ and $Q\big(t, x(t), \lambda(t)\big)$ are Lipschitz functions, with the Lipschitz constants $P_i, Q_i$, for $i = 1, 2$, respectively. The error bounds of (40) showing with $E_1$ and $E_2$, for the proposed method are obtained as follows:

$$\begin{aligned}
\|E_1\|_2 &\le \frac{P_1 L_1}{(M+1)!N^{(M+1)}\sqrt{2M+3}} + \frac{\left(K_1 + \frac{K_2}{\Gamma(2-\alpha)} + P_2\right)L_2}{(\acute{M}+1)!\acute{N}^{(\acute{M}+1)}\sqrt{2\acute{M}+3}}, \\
\|E_2\|_2 &\le \frac{\left(K_1 + \frac{K_2}{\Gamma(2-\alpha)} + Q_1\right)L_1}{(M+1)!N^{(M+1)}\sqrt{2M+3}} + \frac{Q_2 L_2}{(\acute{M}+1)!\acute{N}^{(\acute{M}+1)}\sqrt{2\acute{M}+3}},
\end{aligned} \quad (62)$$

Where

$L_1 = max\left|x^{(M+2)}(t)\right|, t \in [0,1]$ and $L_2 = max\left|\lambda^{(M+2)}(t)\right|$, $t \in [0,1]$.

**Proof** We define

$$\begin{aligned}
\|E_1\|_2 &= \Big\|K_2\, {}_t^C D_1^{\alpha}\lambda(t) - K_1\dot{\lambda}(t) - P\big(t, x(t), \lambda(t)\big) \\
&\quad -\big(K_2\, {}_t^C D_1^{\alpha}\lambda_{\acute{N}\acute{M}}(t) - K_1\dot{\lambda}_{\acute{N}\acute{M}}(t) - P\big(t, x_{NM}(t), \lambda_{\acute{N}\acute{M}}(t)\big)\big)\Big\|_2,
\end{aligned}$$

according to the method outlined in Section IV, we get

$$\begin{aligned}
\|E_1\|_2 &= \Big\|K_2\, {}_t^C D_1^{\alpha}\lambda(t) - K_1\dot{\lambda}(t) - P\big(t, x(t), \lambda(t)\big) \\
&\quad + K_2 C^T I_R^{1-\alpha}\bar{B}(t) + K_1 C^T \bar{B}(t) \\
&\quad + P\big(t, A^T I_L^1 B(t) + x_0, -C^T I_R^1 \bar{B}(t)\big)\Big\|_2,
\end{aligned}$$

from the Lipschitz condition and Equs. (13), we have

$$\begin{aligned}
\|E_1\|_2 &\le K_1\left\|\dot{\lambda}(t) - C^T\bar{B}(t)\right\|_2 \\
&\quad + K_2\|{}_t^C D_1^{\alpha}\lambda(t) + C^T I_R^{1-\alpha}\bar{B}(t)\|_2 \\
&\quad + \left\|P\big(t, x(t), \lambda(t)\big) - P\big(t, A^T I_L^1 B(t) + x_0, -C^T I_R^1\bar{B}(t)\big)\right\|_2 \\
&\le K_1\left\|\dot{\lambda}(t) - C^T\bar{B}(t)\right\|_2 + K_2\left\|-I_R^{1-\alpha}\dot{\lambda}(t) + C^T I_R^{1-\alpha}\bar{B}(t)\right\|_2 \\
&\quad + P_1\|x(t) - (A^T I_L^1 B(t) + x_0)\|_2 + P_2\|\lambda(t) + C^T I_R^1\bar{B}(t)\|_2.
\end{aligned} \quad (63)$$

From definitions (4) and (5), we have $x(t) = I_L^1\dot{x}(t) + x_0$ and $\lambda(t) = -I_R^1\dot{\lambda}(t)$. By substituting these equations into Equ. (63) and using error bounds (57), (60) and (61), we have

$$\begin{aligned}
\|E_1\|_2 &\le K_1\left\|\dot{\lambda}(t) - C^T\bar{B}(t)\right\|_2 \\
&\quad + K_2\left\|-I_R^{1-\alpha}\dot{\lambda}(t) + C^T I_R^{1-\alpha}\bar{B}(t)\right\|_2 \\
&\quad + P_1\|I_L^1\dot{x}(t) - A^T I_L^1 B(t)\|_2 + P_2\left\|-I_R^1\dot{\lambda}(t) + C^T I_R^1\bar{B}(t)\right\|_2 \\
&\le K_1\left\|\dot{\lambda}(t) - C^T\bar{B}(t)\right\|_2 + \frac{K_2}{\Gamma(2-\alpha)}\left\|\dot{\lambda}(t) - C^T\bar{B}(t)\right\|_2
\end{aligned}$$

$$+P_1\|\dot{x}(t)-A^TB(t)\|_2+P_2\left\|\dot{\lambda}(t)-C^T\bar{B}(t)\right\|_2$$
$$=P_1\|\dot{x}(t)-A^TB(t)\|_2$$
$$+\left(K_1+\frac{K_2}{\Gamma(2-\alpha)}+P_2\right)\left\|\dot{\lambda}(t)-C^T\bar{B}(t)\right\|_2$$
$$\leq\frac{P_1L_1}{(M+1)!N^{(M+1)}\sqrt{2M+3}}+\frac{\left(K_1+\frac{K_2}{\Gamma(2-\alpha)}+P_2\right)L_2}{(\acute{M}+1)!\acute{N}^{(\acute{M}+1)}\sqrt{2\acute{M}+3}}.$$

Now we define $\|E_2\|_2$ as follows:

$$\|E_2\|_2=\left\|K_1\dot{x}(t)+K_2{}_0^CD_t^\alpha x(t)-Q\left(t,x(t),\lambda(t)\right)\right.$$
$$\left.-\left(K_1\dot{x}_{NM}(t)+K_2{}_0^CD_t^\alpha x_{NM}(t)-Q\left(t,x_{NM}(t),\lambda_{\acute{N}\acute{M}}(t)\right)\right)\right\|_2,$$

similarly, we can obtain the following relation

$$\|E_2\|_2\leq\frac{\left(K_1+\frac{K_2}{\Gamma(2-\alpha)}+Q_1\right)L_1}{(M+1)!N^{(M+1)}\sqrt{2M+3}}+\frac{Q_2L_2}{(\acute{M}+1)!\acute{N}^{(\acute{M}+1)}\sqrt{2\acute{M}+3}}.\quad\square$$

## VI. ILLUSTRATIVE EXAMPLES

In this section, some examples are presented to illustrate the efficiency and accuracy of the proposed method. The obtained results have been compared with those reported by using other methods.

**Example** 1 Consider the following two-dimensional FOCP [34]

$$\min J=\int_0^1\left((x_1(t)-1-t^{1.5})^2+(x_2(t)-t^{2.5})^2+\left(u(t)-\frac{3\sqrt{\pi}}{4}t+t^{2.5}\right)^2\right)dt,$$

subject to:

$${}_0^CD_t^{0.5}x_1(t)=x_2(t)+u(t),$$
$${}_0^CD_t^{0.5}x_2(t)=x_1(t)+\frac{15\sqrt{\pi}}{16}t^2-t^{1.5}-1,$$
$$x_1(0)=1,x_2(0)=0.$$

For this problem, $x_1(t)=1+t^{1.5}$, $x_2(t)=t^{2.5}$, and $u(t)=\frac{3\sqrt{\pi}}{4}t-t^{2.5}$ minimize the cost function and the minimum value is $J=0$. The necessary optimality conditions are as follows:

$$\begin{aligned}
&{}_0^CD_t^{0.5}x_1(t)=x_2(t)+\tfrac{3\sqrt{\pi}}{4}t-t^{2.5}-\tfrac{1}{2}\lambda_1(t),\\
&{}_0^CD_t^{0.5}x_2(t)=x_1(t)+\tfrac{15\sqrt{\pi}}{16}t^2-t^{1.5}-1,\\
&{}_t^CD_1^{0.5}\lambda_1(t)=\lambda_2(t)-2t^{1.5}+2x_1(t)-2,\\
&{}_t^CD_1^{0.5}\lambda_2(t)=\lambda_1(t)-2t^{2.5}+2x_2(t),\\
&u(t)+\tfrac{1}{2}\lambda_1(t)-\tfrac{3\sqrt{\pi}}{4}t+t^{2.5}=0,\\
&x_1(0)=1,x_2(0)=0,\lambda_1(1)=0,\lambda_2(1)=0.
\end{aligned}\quad(64)$$

By applying the proposed approach and Equs. (53) and (54), for $N=1,M=2$ and $\acute{N}=1,\acute{M}=1$, we obtain

$$\begin{aligned}
&{}_0^CD_t^{0.5}x_1(t)=A^TB(t)=a_{10}b_{10}(t)+a_{11}b_{11}(t)+a_{12}b_{12}(t),\\
&{}_0^CD_t^{0.5}x_2(t)=C^TB(t)=c_{10}b_{10}(t)+c_{11}b_{11}(t)+c_{12}b_{12}(t),\\
&{}_t^CD_1^{0.5}\lambda_1(t)=d_{10}b_{10}(t)+d_{11}b_{11}(t),\\
&{}_t^CD_1^{0.5}\lambda_2(t)=e_{10}b_{10}(t)+e_{11}b_{11}(t).
\end{aligned}\quad(65)$$

Using the Equs. (55) and (56) yield

$$\begin{aligned}
x_1(t)&=A^TI_L^{0.5}B(t)+x_1(0)\\
&=a_{10}I_L^{0.5}b_{10}(t)+a_{11}I_L^{0.5}b_{11}(t)+a_{12}I_L^{0.5}b_{12}(t)+1,\\
x_2(t)&=C^TI_L^{0.5}B(t)+x_2(0)\\
&=c_{10}I_L^{0.5}b_{10}(t)+c_{11}I_L^{0.5}b_{11}(t)+c_{12}I_L^{0.5}b_{12}(t),\\
\lambda_1(t)&=d_{10}I_R^{0.5}b_{10}(t)+d_{11}I_R^{0.5}b_{11}(t),\ \text{and}\\
\lambda_2(t)&=e_{10}I_R^{0.5}b_{10}(t)+e_{11}I_R^{0.5}b_{11}(t).
\end{aligned}\quad(66)$$

By substituting Equs. (65) to (66) into Equs. (64), and using the collocation method, we obtain a system of algebraic equations. By solving this system, the unknown coefficients are determined as follows:

$$\begin{aligned}
c_{10}&=0.55389182840797393036362224115202,\\
c_{11}&=1.66167548522392145371809335507 86,\\
c_{12}&=1.66167548522392137565553693612 23,\\
d_{10}&=0.00000000000000001646518398466862,\\
d_{11}&=-0.00000000000000009879110390801123,\\
a_{10}&=0.66467019408956860353341674532566,\\
a_{11}&=1.32934038817913725095654228919 59,\\
a_{12}&=0.00000000000000004463398968873306.\\
e_{10}&=0.00000000000000019409327747612383,\\
e_{11}&=0.00000000000000036094262159047331.
\end{aligned}$$

**TABLE I**
COMPARISON OF THE OPTIMAL VALUE $J$ WITH METHODS IN [28], [33], AND [34] FOR EXAMPLE 1

| Method | Optimal cost function $J$ | Approximation order |
|---|---|---|
| Bernoulli operational matrix [28] | $9.4157\times10^{-8}$ | $m=8$ |
| Epsilon-Ritz [33] | $8.0027\times10^{-6}$ | $k=8$ |
| MADM [34] | $8.4738\times10^{-17}$ | $N=30$ |
| Present method | $1.9636\times10^{-32}$ | $N=1,M=2$ |

The optimal cost function $J$ obtained of the proposed method and Bernoulli fractional derivative operational matrix compatible with the spectral Ritz method in the direct approach [28], Epsilon-Ritz method in [33], and modified Adomian decomposition method (MADM) in [34], are displayed in Table I. This comparison shows that the hybrid functions proposed method provides a more accurate solution than the mentioned methods by taking a small number of basis functions. Compared to the method [28], the suggested method using the exact fractional operators versus the approximate operational matrix and applying the fractional calculus to impose initial conditions against the Ritz method, leading to a better solution**.** The graphs of the exact and approximate state and control variables are shown in Figs. 1 and 2, demonstrating the approximate solution matches the exact solution.

**Example 2** We consider the following FOCP with variable fractional order [32]

$$\min J=\int_0^1\left(tu(t)-(\alpha+2)x(t)\right)^2dt,$$

subject to the dynamical system

$$\dot{x}(t)+{}_0^CD_t^\alpha x(t)=u(t)+t^2,\ x(0)=0,\ x(1)=\frac{2}{\Gamma(\alpha+3)}.$$

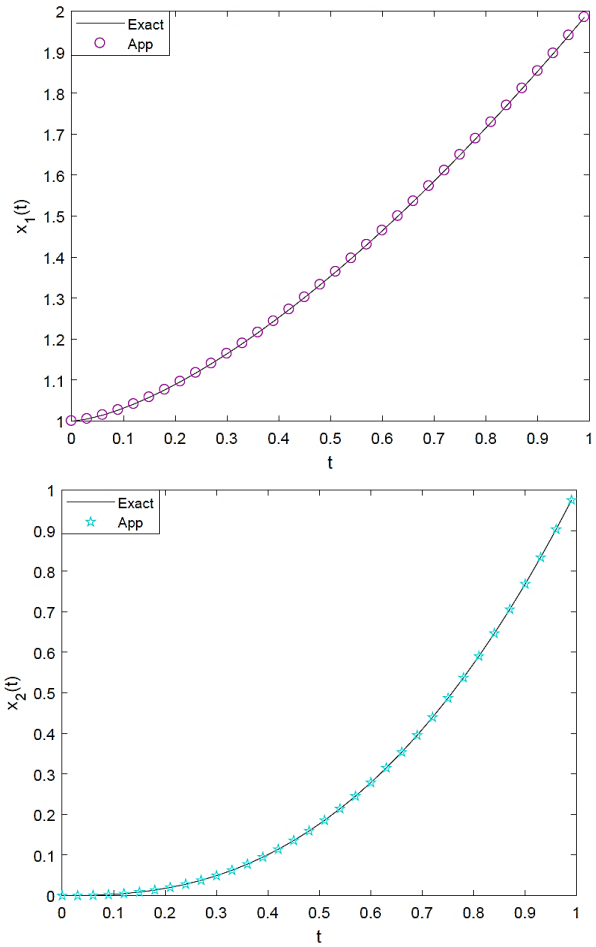


**Fig. 1.** The exact and approximate state variable $x_1(t)$ and $x_2(t)$ for Example 1.

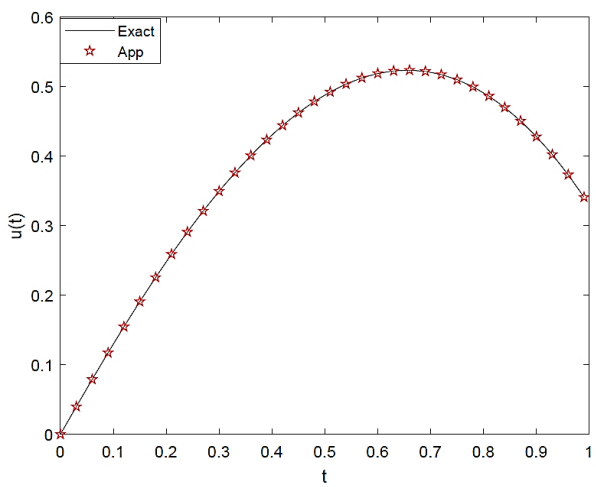


**Fig. 2.** The exact and approximate control variable $u(t)$ for Example 1.

For this problem, the exact solution is $\big(x(t),u(t)\big)=\left(\frac{2t^{\alpha+2}}{\Gamma(\alpha+3)},\frac{2t^{\alpha+1}}{\Gamma(\alpha+2)}\right)$. The necessary optimality conditions are as follows:

$$2t\big(tu(t)-(\alpha+2)x(t)\big)+\lambda(t)=0, \tag{67}$$

$$\dot{\lambda}(t)-{}_t^C D_1^{\alpha}\lambda(t)=-\lambda(t)\frac{(\alpha+2)}{t},$$
$$\dot{x}(t)+{}_0^C D_t^{\alpha}x(t)=u(t)+t^2,\quad x(0)=0,\lambda(1)=0.$$

From Equ. (67), we have

$$u(t)=\frac{(\alpha+2)}{t}x(t)-\frac{\lambda(t)}{2t^2}. \tag{68}$$

Here, we approximate the unknown functions by the hybrid functions as follows:

$$\dot{\lambda}(t)=d_{10}b_{10}(t)+d_{11}b_{11}(t),$$
$$\lambda(t)=-d_{10}I_R^1 b_{10}(t)-d_{11}I_R^1 b_{11}(t), \tag{69}$$
$${}_t^C D_1^{\alpha}\lambda(t)=-d_{10}I_R^{1-\alpha}b_{10}(t)-d_{11}I_R^{1-\alpha}b_{11}(t).$$
$$\dot{x}(t)=A^T B(t)\ ,\ x(t)=A^T I_L^1 B(t),$$
$${}_0^C D_t^{\alpha}x(t)=A^T I_L^{1-\alpha}B(t).$$

We replaced Equs. (68) and (69) in necessary optimality conditions (67) and solved the resulting equations. This problem was solved in [32] by two algorithms (Alg.1 and Alg.2). The Alg.1 is based on calculating the necessary optimality conditions and solves the resulted equations using the spectral method. In Alg.2 the state function was firstly discretized using the numerical integration, followed by the Rayleigh-Ritz method to evaluate state and control functions.

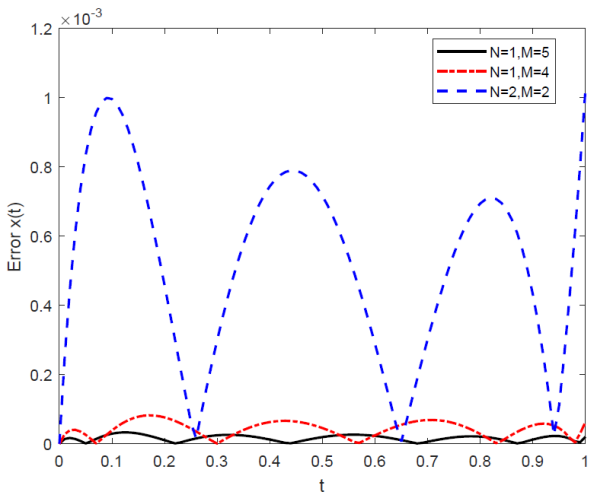


**Fig. 3.** Comparison of the errors $x(t)$ at $\alpha=0.5$ for different values of $N$ and $M$ for Example 2.

A direct approach based on Chebyshev polynomials and the Legendre-Gauss quadrature formula is employed to solve this FOCP [35]. The comparison of maximum absolute errors in the state and control variables of the present method with those of proposed numerical schemes in [32] and [35] is shown in Tables II and III. Figs. 3 and 4 display the absolute errors of $x(t)$ and $u(t)$ by selecting the different values of $N$ and $M$ at $\alpha=0.5$. These graphs show that the error of the solutions is decreased by increasing the number of basis functions. The exact and approximate solutions of state and control variables for different values of $\alpha$ are depicted in Fig. 5.

**Example 3** As a practical and nonlinear example, consider the optimal maneuvers of a rigid asymmetric spacecraft. The Euler equations for the angular velocities $x_1(\tau)$, $x_2(\tau)$, and $x_3(\tau)$

of spacecraft are given by

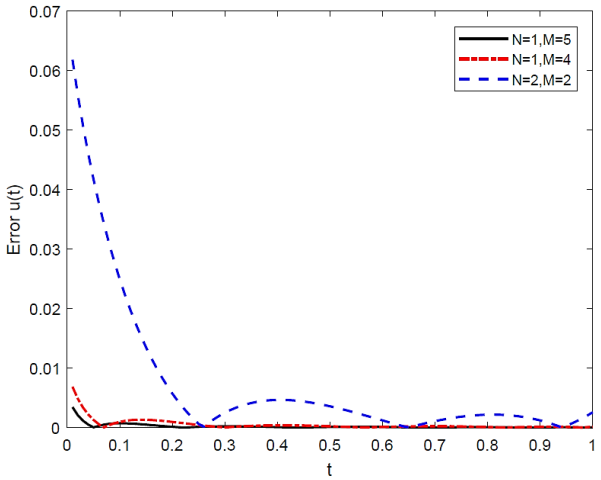


**Fig. 4.** Comparison of the errors $u(t)$ at $\alpha = 0.5$ for different values of $N$ and $M$ for Example 2.

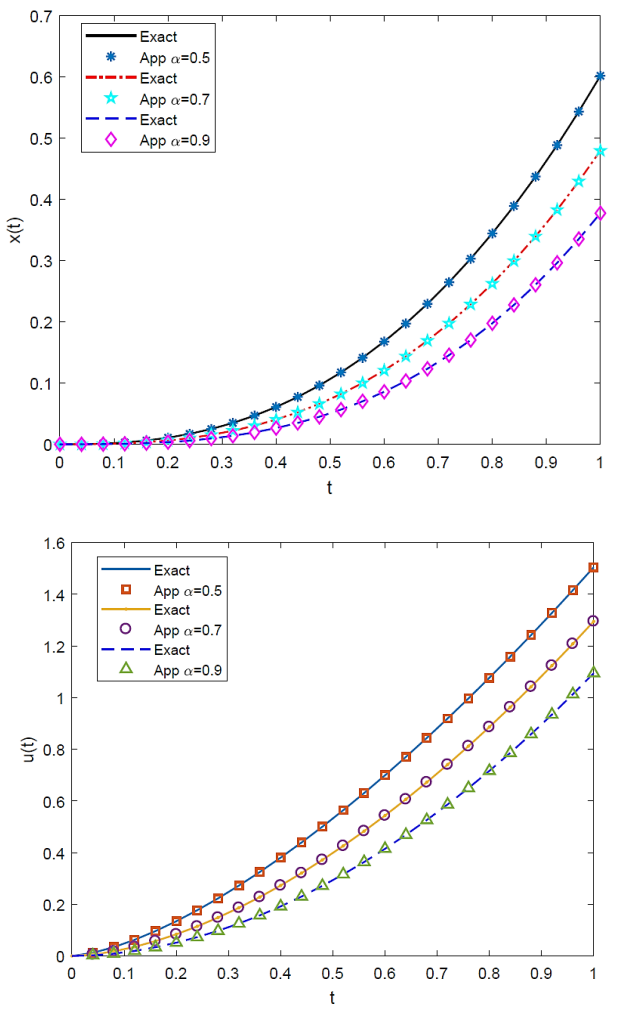


**Fig. 5.** The exact and approximate state and control variables for different values of $\alpha$ with $N = 1, M = 5$ for Example 2.

$$\dot{x_1}(\tau) = -\frac{I_3-I_2}{I_1}x_2(\tau)x_3(\tau) + \frac{u_1(\tau)}{I_1},$$
$$\dot{x_2}(\tau) = -\frac{I_1-I_3}{I_2}x_1(\tau)x_3(\tau) + \frac{u_2(\tau)}{I_2},$$
$$\dot{x_3}(\tau) = -\frac{I_2-I_1}{I_3}x_1(\tau)x_2(\tau) + \frac{u_3(\tau)}{I_3},$$

where $u_1$, $u_2$, and $u_3$ are control the torques. The spacecraft principle inertia are $I_1 = 86.24\ Kg\ m^2$, $I_2 = 85.07 Kg\ m^2$, and $I_3 = 113.59\ Kg\ m^2$. Also, $\frac{I_3-I_2}{I_1}$, $\frac{I_1-I_3}{I_2}$, and $\frac{I_2-I_1}{I_3}$ are the inertia difference ratios. The performance index to be minimized is expressed by

$$\min J = \frac{1}{2}\int_0^{100}\left(u_1^2(\tau) + u_2^2(\tau) + u_3^2(\tau)\right)d\tau,$$

The boundary conditions are as follows:

$x_1(0) = 0.01\ \frac{r}{s}$, $x_2(0) = 0.005\ \frac{r}{s}$, $x_3(0) = 0.001\ \frac{r}{s}$, and $x_1(100) = x_2(100) = x_3(100) = 0\ \frac{r}{s}$. According to the proposed method, the following TPBVP should be solved:

$$\dot{x_1}(\tau) = -\frac{I_3-I_2}{I_1}x_2(\tau)x_3(\tau) - \frac{\lambda_1(\tau)}{I_1^2},$$
$$\dot{x_2}(\tau) = -\frac{I_1-I_3}{I_2}x_1(\tau)x_3(\tau) - \frac{\lambda_2(\tau)}{I_2^2},$$
$$\dot{x_3}(\tau) = -\frac{I_2-I_1}{I_3}x_1(\tau)x_2(\tau) - \frac{\lambda_3(\tau)}{I_3^2},$$
$$\dot{\lambda_1}(\tau) = \frac{I_1-I_3}{I_2}x_3(\tau)\lambda_2(\tau) + \frac{I_2-I_1}{I_3}x_2(\tau)\lambda_3(\tau),$$
$$\dot{\lambda_2}(\tau) = \frac{I_3-I_2}{I_1}x_3(\tau)\lambda_1(\tau) + \frac{I_2-I_1}{I_3}x_1(\tau)\lambda_3(\tau),$$
$$\dot{\lambda_3}(\tau) = \frac{I_3-I_2}{I_1}x_2(\tau)\lambda_1(\tau) + \frac{I_1-I_3}{I_2}x_1(\tau)\lambda_2(\tau).$$

Also, the optimal control variables are obtained as follows:

$$u_1(\tau) = -\frac{\lambda_1(\tau)}{I_1}, u_2(\tau) = -\frac{\lambda_2(\tau)}{I_2}, and\ u_3(\tau) = -\frac{\lambda_3(\tau)}{I_3}.$$

We use transformation $\tau = 100t, t \in [0,1]$ to apply the proposed method. By using this method with $N = 1, M = 7$, we get:

$$x_1(t) = -2.468260116060948 \times 10^{-16}t^8 - 3.823003555219281 \times 10^{-14}t^7 + 2.722028451181812 \times 10^{-13}t^6 + 2.386478651140519 \times 10^{-10}t^5 - 1.195968612517397 \times 10^{-9}t^4 - 8.248480368393749 \times 10^{-7}t^3 + 2.479330170240148 \times 10^{-6}t^2 - 0.010001653525046t + 0.01,$$

$$x_2(t) = 3.957240843616689 \times 10^{-16}t^8 - 8.933546050793784 \times 10^{-15}t^7 + 5.561002887595278 \times 10^{-14}t^6 - 1.406589411719365 \times 10^{-10}t^5 + 7.027484806347674 \times 10^{-10}t^4 + 1.606375494884975 \times 10^{-6}t^3 - 4.821937043751208 \times 10^{-6}t^2 - 0.004996785000588t + 0.005,$$

$$x_3(t) = 1.707020832761955 \times 10^{-12}t^8 - 6.071238553944105 \times 10^{-12}t^7 + 7.687249774825881 \times 10^{-12}t^6 - 3.529343339794504 \times 10^{-11}t^5 + 1.550767918419068 \times 10^{-10}t^4 + 2.572588863294985 \times 10^{-7}t^3 - 7.7239218234617 \times 10^{-7}t^2 - 9.99484989810374 \times 10^{-4}t + 0.001.$$

By substituting $t = 0$ and $t = 1$, boundary conditions are obtained. In Table IV, a comparison is created among the numerical results of the cost function $J$, generated by the

proposed hybrid functions method by taking $N = 1$, $M = 7$ with the reported results in [36] by applying fractional order Chebyshev functions, [37] by using a quasilinearization technique based on the Chebyshev polynomials, and [38] by adopting Fibonacci wavelets and the Galerkin method. These results demonstrate the accuracy and efficiency of the proposed approach in comparison with mentioned methods. State and control approximate variables are shown in Figs. 6 and 7.

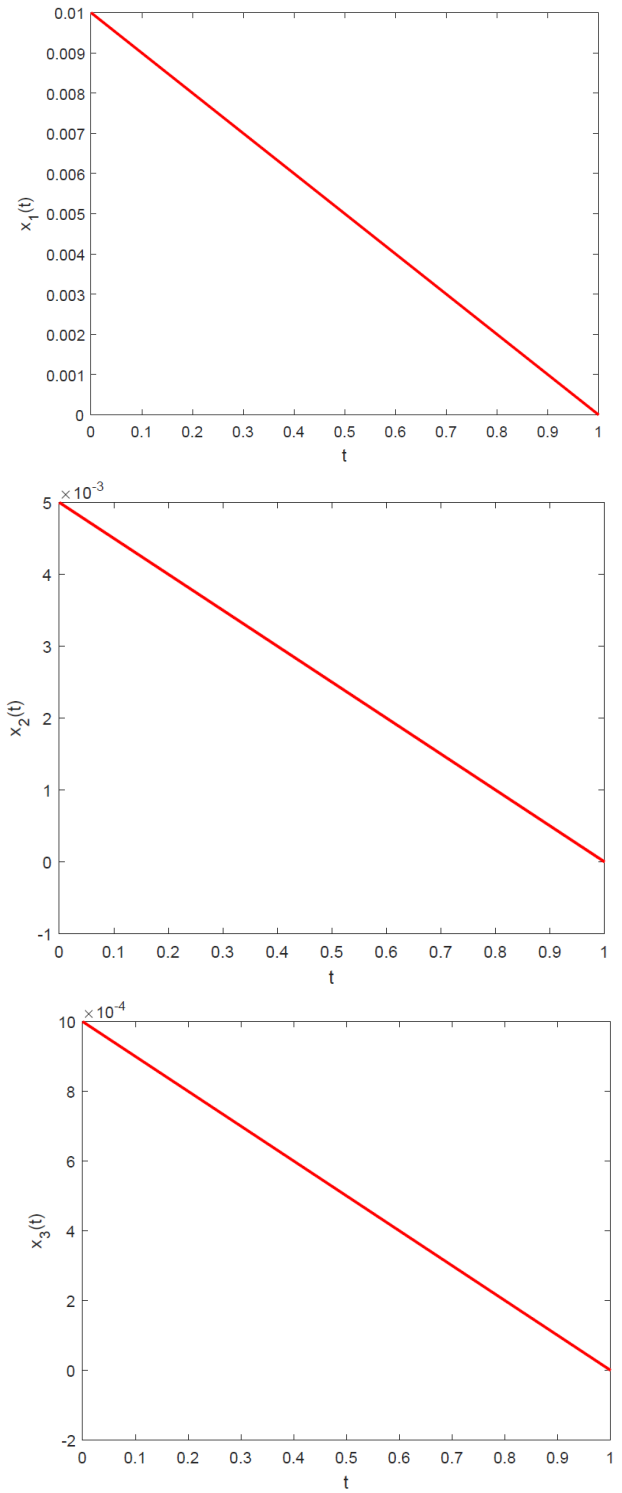


**Fig. 6.** The numerical values of state variables for Example 3.

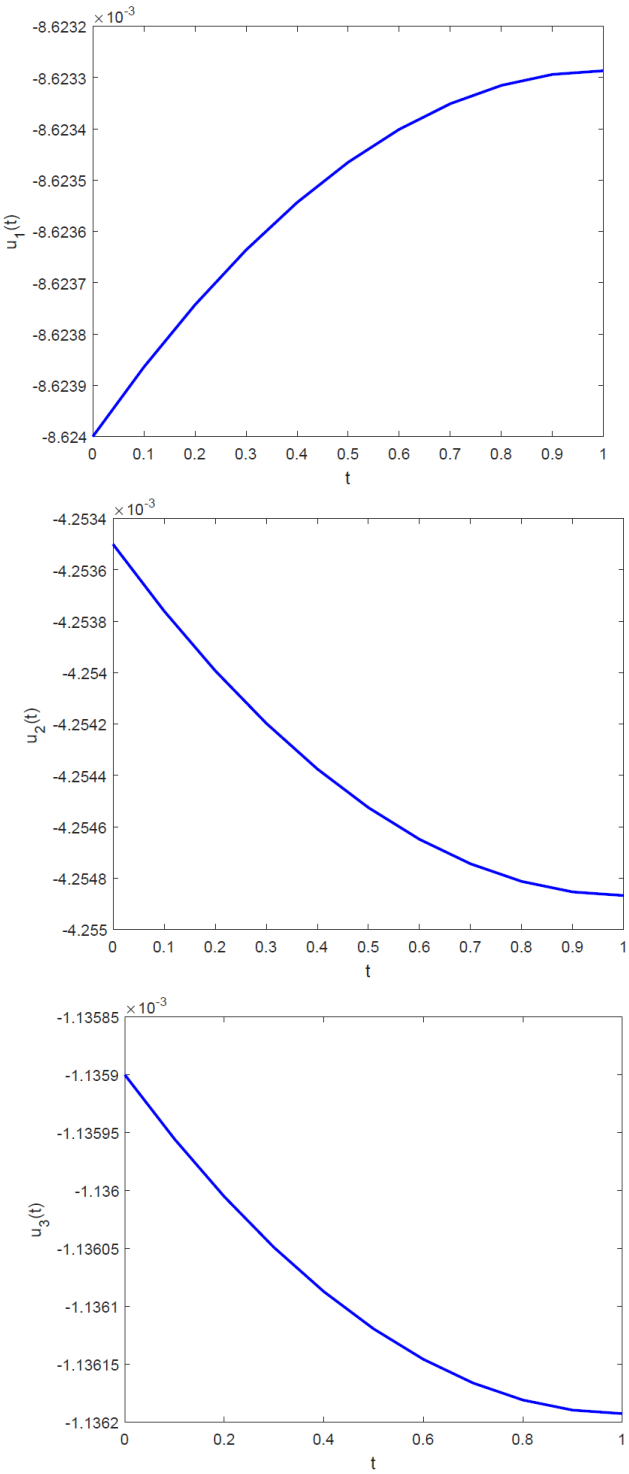


**Fig. 7.** The estimate values of control variables in Example 3.

**TABLE II**
THE MAXIMUM ERROR OF $x(t)$ AT $\alpha = 0.5$ AND COMPARISON WITH OTHER METHODS FOR EXAMPLE 2

| | Alg.1[32] | Alg.2 [32] | Chebyshev polynomials [35] | Present method |
|---|---|---|---|---|
| $N = 2$ | $3.10 \times 10^{-2}$ | $2.73 \times 10^{-2}$ | $2.16 \times 10^{-2}$ | $1.02 \times 10^{-3}$ $(N = 2, M = 2)$ |
| $N = 5$ | $3.55 \times 10^{-4}$ | $1.60 \times 10^{-4}$ | $1.72 \times 10^{-4}$ | $3.26 \times 10^{-5}$ $(N = 1, M = 5)$ |

**TABLE III**
THE MAXIMUM ERROR OF $u(t)$ AT $\alpha = 0.5$ AND COMPARISON WITH OTHER METHODS FOR EXAMPLE 2

| | Alg.1[32] | Alg.2 [32] | Chebyshev polynomials [35] | Present method |
|---|---|---|---|---|
| $N = 2$ | $2.04 \times 10^{-1}$ | $2.56 \times 10^{-1}$ | $2.44 \times 10^{-1}$ | $6.18 \times 10^{-2}$ $(N = 2, M = 2)$ |
| $N = 5$ | $9.13 \times 10^{-3}$ | $8.22 \times 10^{-3}$ | $6.26 \times 10^{-3}$ | $3.44 \times 10^{-3}$ $(N = 1, M = 5)$ |

**TABLE IV**
COMPARISON OF THE OPTIMAL VALUE $J$ WITH METHODS IN [36], [37], AND [38] FOR EXAMPLE 3

| Method | Optimal cost function $J$ | Approximation order |
|---|---|---|
| Fractional Chebyshev functions [36] | 0.004687795 | $m = 10$ |
| Quasi linearization [37] | 0.00534063 | $N = 10$ |
| Fibonacci wavelets and Galerkin [38] | 0.00526040 | $k = 2, M = 4$ |
| Present method | 0.004687795353 | $N = 1, M = 7$ |

## VII. CONCLUSION

In this paper, the Bernoulli hybrid functions indirect method is presented to solve integer-fractional OCPs. Here, the LRLFI and RRLFI operators are computed for mentioned hybrid functions directly and without any approximation. By determining the necessary optimality conditions, the solution of the FOCP is transformed into solving TPBVP, including a system of FDEs. Then, the resulted system is solved, using the hybrid functions approximation and LRLFI and RRLFI operators as well as the collocation method. The error bounds and convergence of the proposed method are investigated. Finally, the method is illustrated by some test problems. The obtained numerical results are compared with the exact solutions and some of the ones available to display the accuracy and proficiency of the proposed method. As can be seen, with a few numbers of the hybrid basis functions, satisfactory results are obtained.

## REFERENCES


[1] R. Hilfer, *Applications of Fractional Calculus in Physics*, World Scientific Publishing, River Edge, NJ, USA, 2000.

[2] A. A. Kilbas, H. M. Srivastava, and J. J. Trujillo, *Theory and Applications of Fractional Differential Equations*, Vol. 204, (North-Holland Mathematics Studies), Elsevier Science Inc. New York, NY, 2006.

[3] I. Podlubny, *Fractional Differential Equations: An Introduction to Fractional Derivatives, Fractional Differential Equations, to Methods of their Solution and some of their Applications*, Academic Press, 1999.

[4] S. G. Samko, A. A. Kilbas, and O. I. Marichev, *Fractional Integrals and Derivatives: Theory and Applications*, Switzerland: Gordon and Breach Science Publishers, 1993.

[5] Y. A. Rossikhin and M. V. Shitikova, "Applications of fractional calculus to dynamic problems of linear and nonlinear hereditary mechanics of solids," *Appl. Mech. Rev*, Vol. 50, No. 1, pp. 15-67, 1997.

[6] R. L. Magin, "Fractional calculus in Bioengineering," *Crit. Rev. Biomed. Eng*, Vol. 32, No. 1, pp. 1-104, 2004.

[7] G. Jumarie, "Modelling fractional stochastic systems as non-random fractional dynamics driven by Brownian motions," *APPL. Math. Model*, Vol. 32, No. 5, pp. 836-859, 2008.

[8] B. Alkahtani, V. Gulati, and A. Kalman, "Application of sumudu transform in generalized fractional reaction diffusion equation," *Int. J. Appl. Comput. Math*, Vol. 2, pp. 387-394, 2016.

[9] A. S. Shaikh, I. N. Shaikh, and K. S. Nisar, "A mathematical model of COVID-19 using fractional derivative: outbreak in India with dynamics of transmission and control," *Adv. Differ. Equ*, Vol. 373, 2020.

[10] A. Atangana, "Modelling the spread of COVID-19 with new fractal-fractional operators: Can the lockdown save mankind before vaccination?," *Chaos Solitons Fractals*, Vol. 136, 2020.

[11] Z. Shabani and H. Tajadodi, "A numerical scheme for constrained optimal control problems," *International Journal of Industrial Electronics, Control and Optimization*, Vol. 2, No. 3, pp. 233-238, 2019.

[12] M. Alipour and P. Omidiniya, "A Semi-Analytic Method for Solving a Class of Non-Linear Optimal Control Problems," *International Journal of Industrial*

*Electronics, Control and Optimization*, Vol. 3, No. 4, pp. 415-429, 2020.

[13] O. P. Agrawal, "A general formulation and solution scheme for fractional optimal control problems," *Nonlinear Dyn*, Vol. 38, No. (1-4), pp. 323-337, 2004.

[14] O. P. Agrawal and D. Baleanu, "A Hamiltonian Formulation and a Direct Numerical Scheme for Fractional Optimal Control Problems," *Journal of Vibration and Control*, Vol. 13, No. (9-10), pp. 1269–1281. 2007.

[15] O. P. Agrawal, "A quadratic numerical scheme for fractional optimal control problem," *J. Dyn. Sys. Meas. Control*, Vol. 130, No. 1, pp. 011010-011010-6, 2008.

[16] S. A. Yusefi, A. Lotfi, and M. Dehghan, "The use of a Legendre multiwavelet collocation method for solving the fractional optimal control problem," *Journal of Vibration and Control*, Vol. 17, No. 13, pp. 2059-2065, 2011.

[17] A. Alizadeh, S. Effati, and A. Heidari, "Numerical schemes for fractional optimal control problems," *J. Dyn. Sys. Meas. Control*, Vol. 139, No. 8, pp. 1-17, 2017.

[18] S. Ghasemi and A. Nazemi, "A fractional power series neural network for solving a class of fractional optimal control problems with equality and inequality constraints," *Network: Computation in Neural Systems*, Vol. 30, No. (1-4), pp. 148-175, 2019.

[19] S. S. Zeid, S. Effati, and A. V. Kamyad, "Approximation methods for solving fractional optimal control problems," *Comp. Appl. Math*, Vol. 37, pp. 158-182, 2017.

[20] S. Soradi-Zeid, "Efficient radial basis functions approaches for solving a class of fractional optimal control problems," *Computational and Applied Mathematics*, Vol. 39, No. 1, 2020.

[21] H. R. Marzban and F. Malakoutikhah, "Solution of delay fractional optimal control problems using a hybrid of Block-Pulse functions and orthonormal Taylor polynomials," *Journal of the Franklin Institute*, vol. 356, No. 15, pp. 8182–8215, 2019.

[22] E. Keshavarz, Y. Ordokhani, and M. Razzaghi, "A numerical solution for fractional optimal control problems via Bernoulli polynomial," *Journal of Vibration and Control*, Vol. 22, No. 18, pp. 3889-3903, 2015.

[23] C. Phang, N. F. Ismail, A. Isah, and J. R. Loh, "A new efficient numerical scheme for solving fractional optimal control problems via a Genocchi operational matrix of integration," *Journal of Vibration and Control*, Vol. 24, No. 14, pp. 3036-3048, 2017.

[24] H. Dehestani, Y. Ordokhani, and M. Razzaghi, "Fractional-order Bessel wavelet functions for solving variable order fractional optimal control problems with estimation error," *Int J Syst Sci*, Vol. 51, No. 6, pp. 1032–1052, 2020.

[25] K. Maleknejad and E. Saeedpoor, "An efficient method based on hybrid functions for Fredholm integral equation of the first kind with convergence analysis," *Applied Mathematics and Computation*, Vol. 304, pp. 93-102, 2017.

[26] S. Mashayekhi and M. Razzaghi, "An approximate method for solving fractional optimal control problems by hybrid functions," *Journal of Vibration and Control*, Vol. 24, No. 9, pp. 1621-1631, 2018.

[27] F. Mohammadi, L. Moradi, D. Baleanu, and A. Jajarmi, "A hybrid functions numerical scheme for fractional optimal control problem: Application to nonanalytic dynamic systems," *Journal of Vibration and Control*, Vol. 24, No. 21, pp. 5030-5043, 2018.

[28] V. Taherpour, M. Nazari, and A. Nemati, "A new numerical Bernoulli polynomial method for solving fractional optimal control problems with vector components," *Computational Methods for Differential Equations*, Vol. 9, No. 2, pp. 446-466, 2021.

[29] Y. Zhou, *Basic Theory of Fractional Differential Equations*, World Scientific Publishing, Co. Pte. Ltd, 2014.

[30] C. Viola, *An Introduction to Special Functions*, Springer International Publishing, Switzerland, 2016.

[31] E. Kreyszig, *Introductory Functional Analysis with Applications*, Vol. 81, John Wiley & Sons, New York, NY, USA, 1989.

[32] N. H. Sweilam and T. M. Alajmi, "Legendre spectral collocation method for solving some type of fractional optimal control problem," *J. Adv. Res*, Vol. 6, No. 3, pp. 393-403, 2015.

[33] A. Lotfi and S. A. Yusefi, "Epsilon-Ritz method for solving a class of fractional constrained optimization problems," *J. Optim. Theory Appl*, Vol. 163, No. 3, pp. 884-899, 2014.

[34] A. Alizadeh and S. Effati, "Modified Adomian decomposition method for solving fractional optimal control problems," *Transactions of the Institute of Measurement and Control*, Vol. 40, No. 6, pp. 2054–2061, 2017.

[35] A. H. Bhrawy, S. S. Ezz-Eliden, E. H. Doha, M. A. Abdelkawy, and D. Baleanu, "Solving fractional optimal control problems with in Chebyshev-Legendre operational technique," *Internat. J. Control*, Vol. 90, No. 6, pp. 1230-1244, 2017.

[36] K. Rabiei and K. Parand, "Collocation method to solve inequality-constrained optimal control problems of arbitrary order," *Engineering with Computers*, Vol. 36, pp. 115–125, 2020.

[37] H. Jaddu, "Direct solution of nonlinear optimal control problems using quasilinearization and Chebyshev polynomials," *Journal of the Franklin Institute*, Vol. 339, pp. 479–498, 2002.

[38] S. Sabermahani and Y. Ordokhani, "Fibonacci wavelets and Galerkin method to investigate fractional optimal control problems with bibliometric analysis," *Journal of Vibration and Control*, pp. 1-15, 2020.

**Seyed Mehdi Shafiof** was born in 1980 in Isfahan, Iran. He received the B.S. degree in Applied Mathematics from K.N. Toosi University of Technology (KNTU), Tehran, Iran, in 2004 and M.S. degree in Applied Mathematics from the Guilan University, Rasht, Iran, in 2006, and the Ph.D. degree in Control and Optimization from the Payame Noor University, Tehran, Iran, in 2020. In 2008, he joined the Payame Noor University as an Instructor in the Department of Mathematics. His current research interests include fractional optimal control problems and fractional differential equations.

**Javad Askari-Marnani** was born in 1964 in Isfahan, Iran. He received the B.Sc. and M.Sc. degrees in electrical engineering from the Isfahan University of Technology in 1987 and the University of Tehran in 1993, respectively. He received also Ph.D. degree in electrical engineering from the University of Tehran in 2001 and under the supervision of Professor Jabedar. From 1988 to 1990 he worked at Isfahan Petrochemical Company in Isfahan. From 1999 to 2001, he received a grant from DAAD and joined the Control Engineering department at Technical University Hamburg, Hamburg, Germany, where he completes his Ph.D. with Professor Lunze's research group. He is currently an associate professor at the control engineering department of the Isfahan University of Technology. His current research interests are in control theory, particularly in the field of fault diagnosis and fault-tolerant control, adaptive control of time-delay systems, multi-agent systems, identification, and electrical engineering curriculum.

**Maryam Shams Solary** was born in Tehran, Iran, in 1978. She received the B.S. degree from the Faculty of Mathematics, Isfahan University of Technology, Isfahan, Iran, in 2000. She received her M.S. and Ph.D. degrees in Applied Mathematics from the Guilan University, Iran, in 2002 and 2009, respectively. In 2010, she joined the Payame Noor University as an Assistant Professor in the Department of Mathematics. From September 2008 to April 2009, she was a Visiting Student at the Hamburg University of Technology, Hamburg, Germany that she worked by Siegfried M. Rump (Head of the Institute for Reliable Computing, Hamburg University of Technology). Her current research interests include Applied Mathematics, Numerical Analysis, Numerical Linear Algebra, Matrix Theory.

IECO

This page intentionally left blank.

International Journal of Industrial Electronics, Control and Optimization © 2021 IECO
Vol. 4, No. 3, pp.313-320, July (2021)

# Methods and Criteria for Evaluating Controllability of Video Bit Rate in HEVC-SCC

Hadi Esmaeeli[1], Mehdi Rezaei[2,†]

[1,2] Department of Electrical and Computer Engineering, University of Sistan and Baluchestan, Zahedan, Iran

ABSTRACT

*Videos directly captured from a computer or smartphone screen have certain characteristics that differentiate them from camera-captured (CC) ones. These videos are called screen content (SC) videos whose specific encoder has been introduced as a new extension of the HEVC standard called screen content coding (SCC). Most screen content applications are real-time with low delay requiring an accurate rate control. The difference in the characteristics and use of special coding tools such as palette mode, intra block copy, and adaptive color transform in this standard, have affected the mechanism of bit rate generation and control. This paper presents methods and criteria to evaluate the controllability of the bit rate of SC videos and compare it with that of CC counterparts. Furthermore, the requirements of SC video rate control are studied. The experimental results indicate that the bit rate of SC videos is much less controllable than the conventional ones so that the conventional rate-distortion models and bit rate control algorithms are not effective in coding the SC videos.*

**Article Info**

***Keywords:*** Bit rate, Control, HEVC standard, Screen content, Video coding

***Article History:***

**Received** 2021-03-06

**Accepted** 2021-06-04

## I. INTRODUCTION

The focus of all video coding standards up to the first version of the HEVC standard has been on the camera-captured (CC) videos. However, in recent years, screen content (SC) videos, which are known as the content type due to a computer or mobile screen, have become a popular video type. This is driven partly by recent advances in mobile, cloud, and display technologies, such as wireless displays, screen sharing and remote collaboration, cloud computing, and gaming [1]. However, unlike CC videos, the SC is a set of images with a large number of uniformly flat areas, repeated patterns, a limited number of colors, and numerically identical blocks without sensor noise [2]. Given these characteristics, the SC has been considered during the development of the HEVC standard, and SC coding tools were gradually expanded. The first draft of SCC was published in July 2014 and was officially introduced as one of the HEVC extensions called HEVC-SCC.

The most important techniques and tools used in the HEVC SCC extension, which have originated from the SC characteristics, include the palette mode, intra block copy, adaptive color-space transform, and adaptive motion vector resolution [3]. These techniques are briefly introduced below:

- The palette mode is characterized by the use of a limited number of colors of the SC. All pixels in a block are classified into a list of major colors. For each coding unit, a color index table is created and all pixels in that unit are converted into the indices corresponding to each color, except for some rarely used ones that can not be quantized to any of the major colors and are called escape pixels [4]. The palette mode is a new coding path in the encoder block diagram [1].
- Intra block copy is a very effective technique in terms of improving the coding performance, which takes advantage of the repeated patterns in the SC. It is a block matching technique in which the current predictor block is predicted from a reference block located in the previously reconstructed regions of the same image [5].
- Adaptive color-space transform is used to identify the redundancy between color components, i.e., statistical redundancy between the different color components [6].
- Adaptive motion vector resolution is inferred from the

[†]**Corresponding Author**: mehdi.rezaei@ece.usb.ac.ir,
Tel: +98-5431132628, Fax: +98-5433447908, Faculty of Electrical and Computer Engineering, University of Sistan and Baluchestan, Zahedan, Iran

fact that in the SC, unlike the continuous CC content, the amount of motion from one image to another is often an integer value. If this mode is enabled, all motion vectors are expressed in integer-pixel resolutions and the additional overhead is avoided [7].

Most of the SC applications require a low delay and constant bit rate. For this purpose, more accurate rate controls (RCs) are needed whose design requires accurate evaluation of their rate controllability. There is no algorithm for controlling the rate in the video coding standard.

So far, several RC algorithms have been proposed for different applications of different standards [8]. For example, an RC algorithm is proposed in [9] for the HEVC standard to keep the consistent objective quality. In the presented algorithm, the probability density function of transformed coefficients is modeled based on a Laplacian function that considers the quad-tree coding unit structure. A frame-level rate control scheme based on a new ρ-domain Rate-GOP[1] based rate-distortion (RD) model is proposed in [10]. Another frame-level RC scheme is proposed in [11] based on texture and non-textured rate models, which is capable of maintaining stable buffer status levels. Authors in [12] found that there existed a more robust correspondence between rate and the Lagrange multiplier λ and proposed a novel λ-domain RC algorithm. An efficient distortion-based Lagrange multiplier approach in low-latency video communications is introduced in [13]. Based on the proposed distortion model, a computationally feasible λ is obtained in the minimization of the total distortion subject to a given bit rate. A proportional, integral, and derivative (PID)-fuzzy RC algorithm is proposed in [14] to reach a higher visual quality in high-delay applications with the buffering constraint. A new RC scheme is proposed in [15] for a region of interest mode coding based on the DCT coefficient model. A joint framework of machine learning and game theory modeling is presented in [16] for inter frame coding tree unit (CTU) level bit allocation and RC optimization.

All of the above-mentioned algorithms well control the bit rate of CC videos and their various applications such as low or high delay. However, they are ineffective for SC videos due to their specific features and new coding tools proposed, which affect the generating mechanism of bit rate in the encoder and its control as a consequence.

Some RC schemes for SC videos have recently been put forward [17-24]. Guo et al. [17] proposed an RC algorithm based on the R-λ model in which the complexity of every picture in the sliding window was estimated and bits were allocated according to the estimated prediction errors. The model parameter λ was dynamically adjusted according to the real consumed bits to achieve the goal of bitrate control. In other work [18], they proposed another RC scheme based on picture classification. The pictures were classified based on their complexity. Meanwhile, the proper bit allocation and parameter updating strategies were selected to control buffer occupancy. Xiao et al. [19] designed a pre-analyzer to collect coding information of the next few frames before encoding the current frame. After acquiring this information, a bit allocation strategy was adopted to prevent buffer overflow and underflow. The proposed RC model was based on the R-λ model. An RC scheme based on video content was proposed by Yang et al. in [20]. The proposed scheme uses different R-λ models of different video contents to characterize the relationships between R and D and update their parameters. Also, a scene change is checked out to accomplish bit allocation for regions with different contents. Wang et al. [21] proposed a frame-level RC scheme for SC in which inter frame correlation was used to classify the frames into key-frames and non-key frames. Then, an efficient bit rate allocation scheme was proposed based on the frame type and Hypothetical Reference Decoder (HRD) to ensure RD performance. Finally, based on the characteristics of the two types of frames, two rate quantization (R-Q) models were established. Tang and Li [22] proposed a low delay RC method for SC coding. In the proposed method, the picture type and buffer status are considered in the bit allocation scheme. A linear R−MAD (Rate-Mean Absolute Difference) model is utilized to estimate frame QP (Quantization Parameter) in the RC scheme. A down-sampling-based RC algorithm aimed at the mobile screen video was presented by Tang et al. [23]. In this RC, the source video is down-sampled and is then encoded twice and the coding information is stored. The real encoding process is optimized at bit allocation and bit control based on the stored coding information. Yang et al. in [24] proposed a very similar content-based RC as in [20] based on the R-λ model.

The whole articles reviewed above are based on the inter frames and do not provide any real solution for intra frames which is required for low-delay applications of SC videos. In this paper, we do not intend to propose an RC algorithm for SC videos. The main contribution of this paper is to compare the controllability of the bit rate of SC videos with that of CC videos from different aspects and then to study the requirements of SC video RC algorithms, especially for low-delay applications.

The rest of this paper is organized as follows. Section II proposes methods to evaluate the controllability of SC videos. Section III presents the experimental results of the methods proposed in Section II, and Section IV gives the conclusions.

## II. METHODS AND CRITERIA FOR EVALUATING THE CONTROLLABILITY OF SC VIDEOS

To distinguish the difference between SC and CC videos,

[1] Group of pictures

several methods and criteria have been employed. The corresponding experiments are illustrated in the results section. These methods and criteria are examined in more detail in the following subsections.

### A. Consecutive Frame Changes

In CC videos, all consecutive frames have gradual changes, so RD models used for RC are well suited for them, and the model parameters can be updated based on the results of previously encoded frames [25, 26]. As a result, the RC algorithm can provide accurate control over bit rate. On the other hand, in SC videos, abrupt changes in consecutive frames prevent effective control. MAD and SAD (Sum Absolute Difference) can be used as criteria to compare the SC and CC videos in terms of changes in consecutive frames. The results provided are relevant to the rate controllability.

### B. Peak-to-Average Bit Ratio

In low delay applications, all frames should be encoded with approximately equal bits, and the video for which the peak-to-average bit ratio tends to one meets the best controllability. Thus, controlling the bit rate of a video for this purpose means reducing the number of bits for the frames having a large number of bits without control and vice versa to push the bit rate peak close to the average bit rate. The higher the value of the peak-to-average ratio in a video is, the harder its RC will be. Therefore, this metric is proposed for comparing the rate controllability of SC and CC videos.

### C. Multi-Pass Rate Control Performance

To further compare the rate controllability of SC videos with CC ones in practice, a multi-pass RC algorithm is proposed. It has been attempted to convert the bit rate of several videos to a fixed bit rate by multi-pass encoding. In other words, their peak-to-average bit ratios should approach one. This algorithm is designed in such a way that at each pass, the QP of the frames whose bit rate in the previous pass is far from the average bit with a threshold is modified. The pseudocode of this algorithm can be observed as below. The performance of the proposed multi-pass RC algorithm over the SC and CC videos can be used to compare their controllability.

MULTI-PASS RC ALGORITHM PSEUDO CODE

Step 1: Encode all video frames with a constant *QP*.
Step 2: Calculate the mean of the frame bits.
Step 3: *for* each video frame with index *n*:
Step 4: *If* (frame bits> α*mean of the frame bits)
*QPn = QPn + 1*
*Else If* (frame bits < β*mean of the frame bits)
*QPn = QPn – 1*
*Otherwise*
*QPn = QPn*
Step 5: Encode the video frame with the new *QP* value
Step 6: Repeat from Step 2 several times

### D. Accuracy of the Standard Model RC Algorithm

In this method, the CC and SC videos have been encoded and compared to control the bit rate with the existing RC of the HM standard model software, which is based on the R-λ model. This RC algorithm has shown good performance for CC videos. Investigation of the performance of this RC algorithm over the SC videos can show the controllability of the SC video bit rate.

### E. Content-Based RD Modelling Capability

A content-based RD model is needed for intra-frame RC. However, it can be useful even for inter-frame RC. To compare the RD modeling capability of SC videos with that of CC videos, a set of SC and CC videos are encoded. Then, the fitness of their provided results to a simple content-based RD model is compared. For this purpose, the following simple RD model has been selected from [14].

$$Q = \frac{X_I}{B_I}, \tag{1}$$

where $X_I$ and $B_I$ represent the coding complexity and the consumed bits of intra frame, respectively. Q denotes the quantization step, which is related to the QP as [14]

$$Q = 0.85 \times \left(2^{\frac{QP-12}{6}}\right). \tag{2}$$

It should be noted that several criteria can be used for the coding complexity measurement. The criterion in [27] that has been validated for the AVC/H.264 and previous standards is used here.

$$X = (\bar{V} + \bar{T}_V + \bar{T}_H), \tag{3}$$

in which

$$V = \frac{1}{s^2}\sum_{x=1}^{s}\sum_{y=1}^{s}(P(x,y) - \overline{P(x,y)})^2, \tag{4}$$

$$T_V = \frac{1}{s^2}\sum_{x=1}^{s}\sum_{y=1}^{s}\left|P(x,y) - P(x,y-1)\right|, \tag{5}$$

$$T_H = \frac{1}{s^2}\sum_{x=1}^{s}\sum_{y=1}^{s}\left|P(x,y) - P(x-1,y)\right|, \tag{6}$$

where $X$ denotes the complexity measure, $V$ is the variance of luminance pixels $P(x, y)$ in one CTU of size $s$, $T_V$ and $T_H$ denote the vertical and the horizontal texture measures on the luminance pixels, respectively, $\bar{V}$, $\bar{T}_V$, and $\bar{T}_H$ are average values of $V$, $T_V$, and $T_H$, on all CTUs in the frame, respectively.

### F. Relative Coding Complexity of Intra to Inter Frames

The intra frames usually consume more bits than the inter

ones and they thus have a big impact on the video quality and their RC is of high importance [25,28,29,30]. A higher portion of the bit budget consumed by the intra frames means a higher degree of importance for intra frame RC. To compare the SC and CC videos from this point of view, the relative coding complexity of intra to inter frames in the two mentioned video types has been examined. Given a low-delay GOP structure with periodic IDR (Instantaneous Decoder Refresh) pictures, the average relative coding complexity is defined as

$$X_{IP} = \frac{\frac{1}{N}\sum_{i=1}^{N} X_{Ii}}{\frac{1}{M}\sum_{j=1}^{M} X_{Pj}} = \frac{\frac{1}{N}\sum_{i=1}^{N} QP_{Ii} \times B_{Ii}}{\frac{1}{M}\sum_{j=1}^{M} QP_{Pj} \times B_{Pj}}, \quad (7)$$

where $i$ and $j$ denote the index of intra and inter frames, respectively, $N$ and $M$ are the numbers of encoded intra and inter frames, respectively, $X_{Ii}$ and $X_{Pj}$ represent the coding complexity of intra and inter frames, respectively, $QP_{Ii}$ and $QP_{Pj}$ are QP used for encoding intra and inter frames, respectively, and $B_{Ii}$ and $B_{Pj}$ show the consumed bits by the intra and inter frames, receptively. These metrics reveal the importance of intra frames RC in SC videos.

## III. EXPERIMENTAL RESULTS

The HEVC-SCC test model in HM-16.16+SCM8.5 software has been used for all experiments. Six experiments corresponding to the proposed methods and criteria in section II are executed, and the results of the experiments are presented in the following subsections. For the first three experiments, the All-INTRA coding structure has been used for encoding, QP offset values have been set to zero, and the intra period has been set to half of GOP.

### *A. Results of Consecutive Frame Changes*

The consecutive frame changes in two test video sequences including Basketball and Web Browsing sequences, as samples of CC and SC videos, are computed in terms of MAD, and the comparison results are displayed in Fig. 1. As can be seen, the MAD of the CC sequence has gradual changes with good continuity and a strong correlation between the sequential frames. On the other hand, in the SC sequence, most frames have a very low MAD over long periods, and very sharp changes are observed in very short periods. Assuming a correlation between the bit rate and MAD, these results show that the rate control task is very difficult in SC videos, especially for low-delay applications.

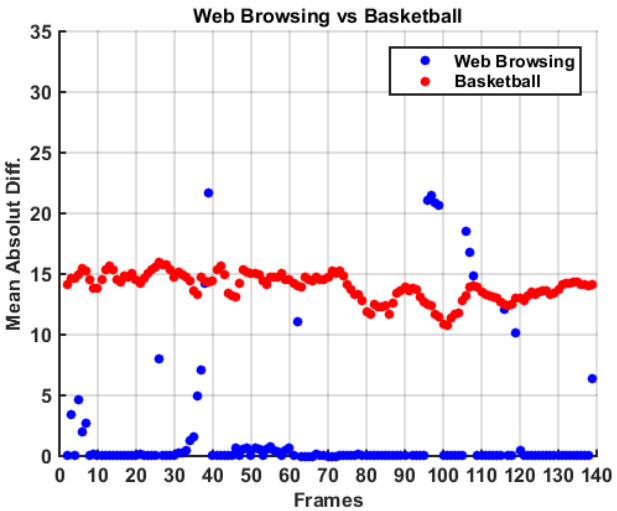


**Fig. 1**. A comparison of the complexity of consecutive frames in the Web Browsing and Basketball Sequences.

### *B. Results of Peak-to-Average Bit Ratio Criterion*

Four videos of each type have been selected and coded with different QPs and their corresponding peak-to-average (P/A) curves have been plotted in Fig. 2. As shown in this figure, all the CC videos (Park, Kimono, Basket, and 4People) are at the bottom (low P/A), and all SC ones (Map, PCB, Web, and Word) are at the top (high P/A). Table I presents the numerical results and the average values obtained via these experiments. The average values have been obtained as 39.55 and 4.37 for the SC and CC videos, respectively, which indicates a significant difference. So, the controllability of the bit rate of SC videos is more difficult than those of CC videos, especially for high bit rates or low QP values.

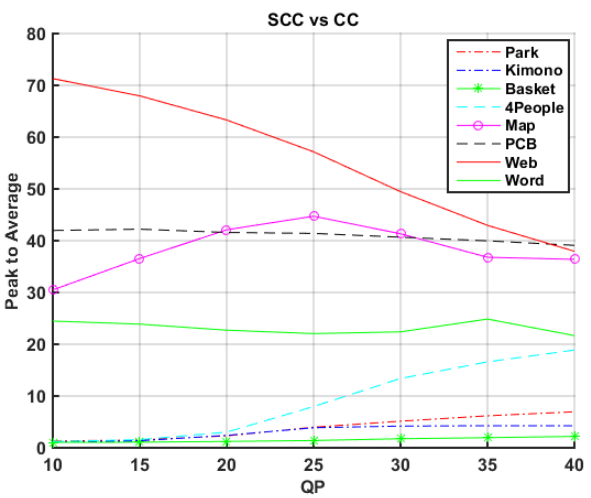


**Fig. 2.** Variations in the peak-to-average ratios for the CC and SC videos.

**Table I**
The Numerical Values Of The Peak-To-Average Ratios Associated With The Cc And Sc Videos.

| | | Peak to Average ratio | | | | | | | |
|---|---|---|---|---|---|---|---|---|---|
| Video type | Sequence name | Qp=10 | Qp=15 | Qp=20 | Qp=25 | Qp=30 | Qp=35 | Qp=40 | Average |
| CC | ParkScene | 1.309 | 1.519 | 2.304 | 3.978 | 5.139 | 6.181 | 6.957 | 3.912 |
| | Kimono | 1.187 | 1.355 | 2.404 | 3.880 | 4.192 | 4.267 | 4.262 | 3.078 |
| | Basketball | 1.060 | 1.082 | 1.231 | 1.407 | 1.753 | 1.958 | 2.199 | 1.527 |
| | 4People | 1.213 | 1.570 | 3.024 | 7.971 | 13.390 | 16.598 | 18.878 | 8.949 |
| Total Average | | | | | | | | | 4.367 |
| SC | Map | 30.4959 | 36.5519 | 42.1037 | 44.7242 | 41.3380 | 36.8037 | 36.3917 | 38.344 |
| | PCB | 41.9714 | 42.2193 | 41.5911 | 41.4042 | 40.6735 | 39.9720 | 39.1007 | 40.990 |
| | Web | 71.2969 | 67.9695 | 63.3051 | 57.1676 | 49.471 | 42.9627 | 37.9547 | 55.732 |
| | WordEditing | 24.4814 | 23.8815 | 22.7150 | 22.0587 | 22.3924 | 24.8658 | 21.6759 | 23.153 |
| Total Average | | | | | | | | | 39.55 |

### *C. Results of Proposed Multi-Pass Rate Control*

To check the bit rate controllability with the proposed multi-pass RC algorithm, four CC and four SC videos have been selected and encoded with a fixed QP of 20, as the first step of the algorithm. Then, the next steps of the algorithm were executed and repeated for 20 passes for each test sequence. After each pass, the *Peak-to-Average* criterion is computed for the resulting bitstream. The results of implementing the proposed algorithm for eight videos are shown in Fig. 3. As shown in the figure, all four CC videos at the bottom of the chart approached 1 very quickly, indicating that the bit rate has moved toward a fixed value and has been well controlled. On the other hand, the behavior is different for the four SC videos at the top of the chart. The P/A values of the above three videos approach about 4 or 5 after eleven passes, but in the next passes, they meet an increase in the P/A criterion, and next, they show some fluctuations. In the best cases, their P/A values are about 4 and 5, which are far from 1. Thus, more control over their bit rate is impossible. It can be seen that the fourth SC video from above has a behavior between these two types of videos. The content of

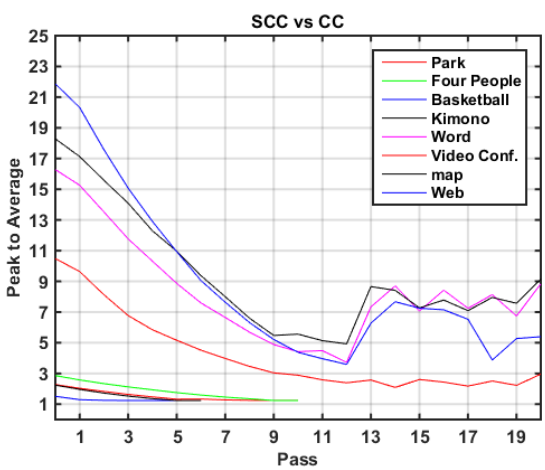


**Fig. 3**. Video comparison using the proposed multi-pass rate control.

this video (Web Conference) includes a combination of CC and SC videos, so it shows such intermediate behavior.

### *D. Results of Standard Model RC Algorithms*

For this purpose, four videos from each type (CC and SC) have been concatenated to make long test sequences with different scenes. The concatenated videos are coded in three different modes: (intra period =32 and GOP = 4),

1) With a constant QP (CQP) of 25
2) RC of HM software for CC and that of HM-SCM for SC videos without any buffer.
3) Similar to mode 2 with enabling HRD (Hypothetical Reference Decoder) constraint.

The variations in the buffer status versus the number of frames are plotted in Figs. 4 and 5 for the CC and SC videos, respectively.

The results indicate that in comparison with the constant QP mode, the bit rate of CC videos is controlled with the RC algorithms to some extent. On the other hand, the RC algorithms fail to control the SC video both with and without buffer. In these scenarios, the RC algorithm should prevent buffer overflow and underflow. The buffer size is shown by the orange color lines in the figures. The graphical results show that the encoded SC videos are far from the buffer constraint and have a low degree of controllability.

### *E. Results of Content-Based RD Modelling*

Using the simple RD model in formula (1) and complexity measure in formula (3), the content complexity diagram has been plotted versus the number of coding tree unit (CTU) bits for four CC and SC videos in Figs. 6 and 7, respectively. As can be seen in Fig. 6, the results are very close to each other and almost in the bisector direction, and the relationship is relatively linear. The closer the results are to the straight line, the more accurate the RD model will be. On the other hand, the results are scattered for the SC videos in Fig. 7 and there is no specific correlation between the complexity measure and bits. The results show a low capability of content-based RD modeling for SC videos.

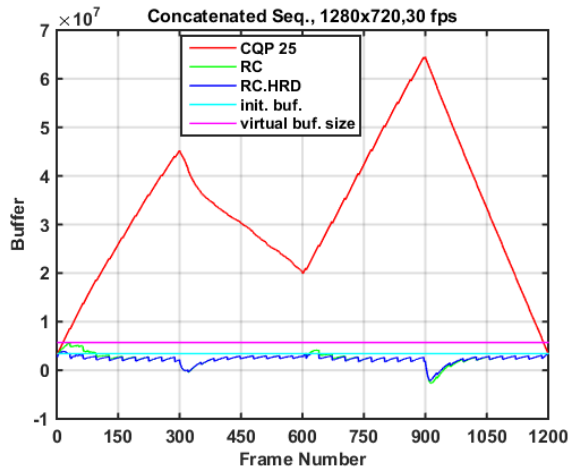


**Fig. 4**. The buffer status variation with the number of frames in the CC videos.

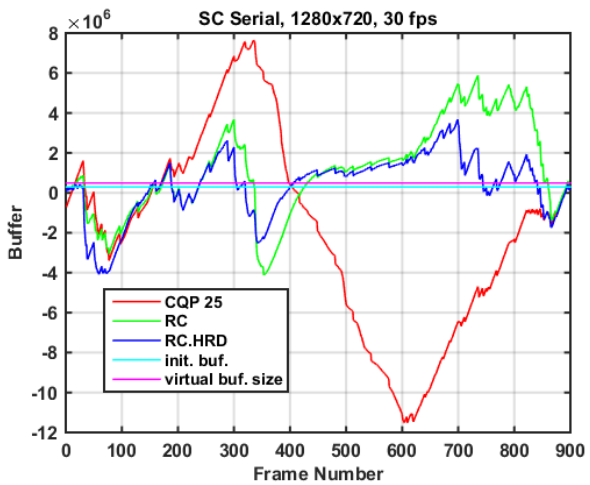


**Fig. 5**. The buffer status variation with the number of frames in the SC videos.

### *F. Results of Relative Coding Complexity of Intra to Inter Frames*

Three CC (4People, Kristen, and Vidyo) and three SC (Map, Web, and Video Conference) test video sequences with the size of 1280×720 and the chroma format 4:2:0 have been used for this experiment. The test sequences are encoded with low-delay coding structure, IntraPeriod = 8, GOP = 4, QP = 10, 15, …, 40, and default QP offset values. The average relative coding complexity values for all sequences are presented in Table II for different QPs. An average on all QPs is also presented for each sequence. According to this table, the relative coding complexity in SC videos is much higher than that in the CC ones, especially for the QPs smaller than

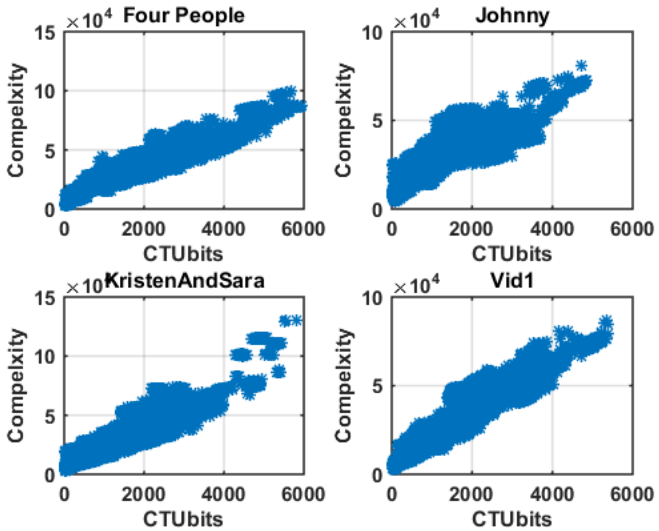


**Fig. 6**. Content complexity to CTU bits for CC videos.

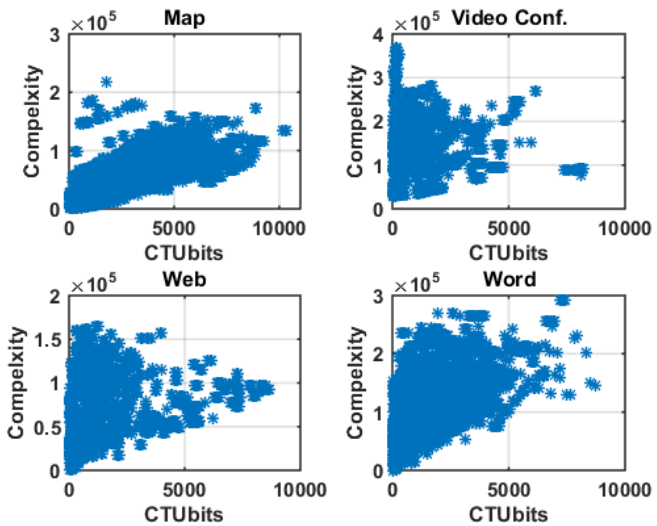


**Fig. 7**. Content complexity to CTU bits for SC videos.

25. A value larger than 100 for the Video Conference sequence demonstrates that, on average, an intra frame consumes a hundred times more bits than an inter frame. Therefore, a larger portion of the bit budget is consumed by the intra frames in SC than in CC videos. As a result, the intra frame rate control in SC videos is more important than in CC videos. Therefore, the bit rate of intra frames in SC must be controlled with a high degree of accuracy, and a proper accurate intra RD model is required.

**Table II**
Average relative coding complexity of the intra to inter frames.

| QP | SC Video Sequences | | | CC Video Sequences | | |
|---|---|---|---|---|---|---|
| | Map | Web | Video Conf. | 4People | Kirsten | Vidyo |
| 10 | 15.27 | 63.81 | 24.67 | 3.17 | 3.17 | 3.19 |
| 20 | 20.23 | 64.62 | 49.31 | 11.47 | 9.42 | 9.30 |
| 30 | 27.21 | 62.43 | 107.95 | 26.29 | 25.03 | 21.21 |
| 40 | 33.61 | 59.44 | 107.55 | 35.81 | 34.08 | 27.25 |
| **Average** | **24.08** | **62.57** | **72.37** | **19.18** | **17.92** | **15.24** |

## IV. CONCLUSIONS

In this paper, methods and criteria are proposed to examine the controllability of the bit rate of SC videos for the low delay applications and to study the requirements of SC video RC algorithms. The results of experiments showed that the bit rate controllability of this type of video is low and it is very difficult to achieve a fixed bit rate, especially for low-delay applications in which all video frames should consume a near fixed bit budget. It was also found that the used RD model and the RC algorithm in the standard model software are not suitable for this type of video and a more appropriate RD model should be found and a proper RC algorithm should be designed. This model must support new SC coding tools. On the other hand, since the relative coding complexity of intra to inter frames in this type of content is too high, the accuracy of intra RD modeling and RC is very important while the intra RD model must be content-based.

## REFERENCES


[1].W. Peng, F. Walls, R. Cohen, J Xu, J. Ostermann, A. MacInnis, and T. Lin, “Overview of Screen Content Video Coding: Technologies, Standards, and Beyond,” IEEE Journal on Emerging and Selected Topics in Circuits and Systems, vol. 6, No.4, pp. 393 – 408, 2016.

[2]J. Xu, R. Joshi and R. A. Cohen, "Overview of the Emerging HEVC Screen Content Coding Extension," in IEEE Transactions on Circuits and Systems for Video Technology, vol. 26, no. 1, pp. 50-62, Jan. 2016, doi: 10.1109/TCSVT.2015.2478706.

[3].S. Liu, X. Xu, S. Lei, & K. Jou, (2015). Overview of HEVC extensions on screen content coding. APSIPA Transactions on Signal and Information Processing, 4, E10. doi:10.1017/ATSIP.2015.11.

[4].Y. Sun et al., "Improvements of HEVC SCC Palette Mode and Intra Block Copy," in IEEE Journal on Emerging and Selected Topics in Circuits and Systems, vol. 6, no. 4, pp. 433-445, Dec. 2016, doi: 10.1109/JETCAS.2016.2598193.

[5].X. Xu et al., "Intra Block Copy in HEVC Screen Content Coding Extensions," in IEEE Journal on Emerging and Selected Topics in Circuits and Systems, vol. 6, no. 4, pp. 409-419, Dec. 2016, doi: 10.1109/JETCAS.2016.2597645.

[6].L. Zhang et al., "Adaptive Color-Space Transform in HEVC Screen Content Coding," in IEEE Journal on Emerging and Selected Topics in Circuits and Systems, vol. 6, no. 4, pp. 446-459, Dec. 2016, doi: 10.1109/JETCAS.2016.2599860.

[7].B. Li et al, "Adaptive Motion Vector Resolution for Screen Content, document", JCTVC-S0085, Joint Collaborative Team Video Coding, Strasbourg, France, Oct. 2014.

[8] H. Guo, C. Zhu, S. Li and Y. Gao, "Optimal Bit Allocation at Frame Level for Rate Control in HEVC," in IEEE Transactions on Broadcasting, vol. 65, no. 2, pp. 270-281, June 2019.

[9].Ch. W. Seo, J. H. Moon, J. K. Han, “Rate control for consistent objective quality in high efficiency video coding,” IEEE Trans. Image Process. vol. 22, no. 6, pp. 2442–2454, 2013.

[10].Sh. Wang, S. Ma, Sh. Wang, D. Zhao and W. Gao,” Rate-GOP Based Rate Control for High Efficiency Video Coding,” IEEE Journal of Selected Topics in Signal Processing. vol. 7, No. 6, pp. 1101-1111, 2013.

[11].B. Lee, M. Kim, and T. Q. Nguyen,” A Frame-Level Rate Control Scheme Based on Texture and Nontexture Rate Models for High Efficiency Video Coding,” IEEE Transactions on Circuits and Systems for Video Technology, vol. 24, No. 3, pp. 465 – 479, 2014.

[12].B. Li, H. Li, L. Li, and J. Zhang,” λ Domain Rate Control Algorithm for High Efficiency Video Coding,” IEEE Transactions on Image Processing, vol. 23, No. 9, pp. 3841-3854, 2014.

[13].M. Wang, K. N. Ngan and H. Li,” Low-Delay Rate Control for Consistent Quality Using Distortion-Based Lagrange Multiplier,” IEEE Transactions on Image Processing, vol. 25, No. 7, pp. 2943-2955, 2016.

[14].D. Fani and M. Rezaei,” A Novel PID-Fuzzy Video Rate Controller for High-Delay Applications of HEVC Standard,” IEEE Transactions on Circuits and Systems for Video Technology, vol. PP, No. 99, p. 1, 2017.

[15].Z. Zhang, T. Jing, J. Han, Y. Xu, and F. Zhang,” A New Rate Control Scheme for Video Coding Based On Region of Interest,” IEEE Access, vol. 5, pp. 13677-13688, 2017.

[16].W. Gao, S. Kwong, and Y. Jia,” Joint Machine Learning and Game Theory for Rate Control in High Efficiency Video Coding,” IEEE Transactions on Image Processing, vol. 26, No.12, pp. 6074-6089, 2017.

[17] Y. Guo, B. Li, S. Sun, and J. Xu, “Rate control for screen content coding in HEVC,” Circuits and Systems (ISCAS), 2015 IEEE International Symposium on, Lisbon, 2015.

[18] Y. Guo, B. Li, S. Sun, and J. Xu, “Rate control for screen content coding based on picture classification,” Visual Communications and Image Processing (VCIP), Singapore,

2015.
[19].J. Xiao, B. Li, S. Sun and J. Xu, "Rate control with delay constraint for screen content coding," 2017 IEEE Visual Communications and Image Processing (VCIP), St. Petersburg, FL, 2017, pp. 1-4, doi: 10.1109/VCIP.2017.8305100.
[20].Y. Yang, L. Shen, H. Yang, & P. An (2019). "A content-based rate control algorithm for screen content video coding". Journal of Visual Communication and Image Representation, 60, 328–338.
[21].S. Wang, J. Li, S. Wang, S. Ma and W. Gao, "A Frame Level Rate Control Algorithm for Screen Content Coding," 2018 IEEE International Symposium on Circuits and Systems (ISCAS), Florence, 2018, pp. 1-4, doi: 10.1109/ISCAS.2018.8351596.
[22].T. Tang, & L. Li (2019). "A low delay rate control method for screen content coding". Multimedia Tools and Applications, 78(19), 28231–28256.
[23].T. Tang, J. Yang, B. Du and L. Tang, "Down-Sampling Based Rate Control for Mobile Screen Video Coding," in IEEE Access, vol. 7, pp. 139560-139570, 2019, doi: 10.1109/ACCESS.2019.2943887.
[24].H. Yang, L. Shen, Y. Yang and W. Lin, "A Novel Rate Control Scheme for Video Coding in HEVC-SCC," in IEEE Transactions on Broadcasting, vol. 66, no. 2, pp. 333-345, June 2020, doi: 10.1109/TBC.2019.2954062.
[25].Y. Li, B. Li, D. Liu and Z. Chen, "A convolutional neural network-based approach to rate control in HEVC intra coding," 2017 IEEE Visual Communications and Image Processing (VCIP), St. Petersburg, FL, 2017, pp. 1-4, doi: 10.1109/VCIP.2017.8305050.
[26].X. Lu, B. Zhou, X. Jin and G. Martin, "A Rate Control Scheme for HEVC Intra Coding Using Convolution Neural Network (CNN)," 2020 Data Compression Conference (DCC), Snowbird, UT, USA, 2020, pp. 382-382, doi: 10.1109/DCC47342.2020.00055.
[27].M. Rezaei et al., "Analyzed Rate Distortion Model in Standard Video Codecs for Rate Control", IEEE Workshop on Signal Processing Systems Design and Implementation, Athens, Greece, Nov. 2005.
[28].M. Wang, K. N. Ngan and H. Li, "An Efficient Frame-Content Based Intra Frame Rate Control for High Efficiency Video Coding," in IEEE Signal Processing Letters, vol. 22, no. 7, pp. 896-900, July 2015, doi: 10.1109/LSP.2014.2377032.
[29].L. Sun, O. C. Au, W. Dai, Y. Guo and R. Zou, "An adaptive frame complexity based rate quantization model for intra-frame rate control of High Efficiency Video Coding (HEVC)," Proceedings of The 2012 Asia Pacific Signal and Information Processing Association Annual Summit and Conference, Hollywood, CA, 2012, pp. 1-6.
[30].W. Li, P. Ren, E. Zhang, and F. Zhao, "Rate control for HEVC intra-coding with a CTU-dependent distorti jfv,mhngn xyon model,". SIViP 13, 17–25 (2019). https://doi.org/10.1007/s11760-018-1323-8.

**Hadi Esmaeeli** received the B.S. degree in electronics engineering from the University of Sistan and Baluchestan (USB), Iran in 1997 and M.Sc. degree in information technology engineering from the Amir Kabir University of Technology (Polytechnic of Tehran), Tehran, Iran in 2007. He was the head of the E-learning Center at the USB from 2011 to 2016. He is currently pursuing the Ph.D. degree in communications systems engineering and is a lecturer in the Department of Information Technology Engineering, USB, Iran. His research interests include multimedia signal processing and communications.

**Mehdi Rezaei (M'04)** received the B.S. and M.Sc. degrees in electronics engineering from the Amir Kabir University of Technology (Polytechnic of Tehran) and Tarbiat Modares University, Tehran, Iran in 1992 and 1996, respectively, and also Ph.D. degree in Signal Processing from the Tampere University of Technology (TUT), Finland in 2008. His research interests include multimedia signal processing and communications. He has published several papers in these fields. During his Ph.D. program, he had a close collaboration with the Nokia Research Center and he filled several patents. He also received the Nokia Foundation Award in 2005 and 2006. Between 2015, he worked as Deputy Dean for Education and Postgraduate Studies and as Deputy Dean for Research in Faculty of Electrical and Computer Engineering, and also Dean of Education at the University of Sistan and Baluchestan, Iran. Now, he is an Associate Professor of Communications Engineering Department, University of Sistan and Baluchestan, Iran.

International Journal of Industrial Electronics, Control and Optimization © 2021 IECO
Vol. 4, No. 3, pp. 321-331, July (2021)

# Reconfiguring Distribution Networks by Minimizing Power Loss and Considering Overcurrent Protection

Elham Khoshbakht Sangkar[1], Farhad Namdari[2, †], Meysam Doostizadeh [3]

[1, 2, 3] Department of Electrical Power Engineering, Engineering Faculty, Lorestan University, Khorram Abad, Iran.

**ABSTRACT**

*This paper studies the reciprocal of distribution network protection and reconfiguration of an active distribution network (AND). Accordingly, a distribution network reconfiguration is carried out to find the optimal switching operations. Since the switching operations will change the network topology and the short circuit level of the buses, the protection coordination may be invalid. To address this issue, constraints of the coordination of the protection relays and fuses are formulated and added to the reconfiguration problem. Moreover, the nonlinear equations of the problem are linearized and transform the reconfiguration problem into Mixed-Integer Linear Programming (MILP) to achieve the global optimal solution. The proposed method was implemented on a 33-bus distribution network. The results clearly show the effectiveness of active and reactive power management in an intelligent distribution network considering protection concepts.*

**Article Info**

***Keywords:***
Active distribution network, Mixed-integer linear programming, Protection coordination, Reconfiguration.

***Article History:***
**Received** 2020-10-29
**Accepted** 2021-04-05

## I. INTRODUCTION

The smartness of distribution grids has significantly grown in recent years. This smart view will improve the operation of the grids in cases like reducing the level of blackouts at the distribution level, developing the use of renewable energy, random loads, and presenting solutions for the control and management of electrical energy consumption. Incorporating smartness into distribution grids makes them flexible to use renewable energy resources in low or medium voltage levels. One of the most effective techniques in smart power systems is a reconfiguration strategy [1]. With this respect, the open/close operation of breakers will be done by using operational improvements. It is clear, in this case, that configuration and reconfiguration will be changed. In distribution networks, reconfiguration changes the grid topology to improve the network operation, which will maintain the radial structure of the grid [2]. The resulting topology depends on different input parameters, where reconfiguration is based on changes in the operating conditions of the system in an hour, day, or season. Reconfiguration of distribution grids to reduce losses is reorganizing it; somewhere by reduction of losses, the grid radial structure is maintained, done by proper changes in the status of the breakers [3].

Reconfiguration is a combined nonlinear optimization problem with integer numbers [4], which is solved considering grid operation constraints to reach various purposes such as reducing losses [5], load balances [6], etc.

The reconfiguration of distribution grids to reduce losses was firstly introduced by Marilyn and Beck [7] in 1975, where after closing all the breakers, the breakers with the least current were opened one after the other, which was obtained from a DC load flow to reduce losses under various load conditions. Gosuami and Basu [8] presented a heuristic algorithm for reconfiguration by using a load flow program. Talesky and Rajisik [9] presented an optimization technique to determine the structure of a distribution system with minimum energy losses for a given period. Applied aspects of the optimal reconfiguration of the distribution systems were introduced by Brazen and Rajkovich [10]. Indeed, the reconfiguration is similar to the problem of optimal load flow. Various methods have been used to solve the reconfiguration problem, which can be divided into four general categories:

1. Heuristic methods [11]
2. Mathematical optimization methods [12]

† **Corresponding Author** : namdari.f@lu.ac.ir
Tel/Fax: +98-6633120005, Department of Electrical Power Engineering, Engineering Faculty, Lorestan University, Khorram Abad, Iran.

3. Metaheuristic or smart optimization methods [1], [13]
4. Combined methods [14], [15]

Load flow and short circuit calculations show that by changing grid configuration, the load currents and short circuit levels are changed, which may cause problems with the coordination of protection elements [6]. Thus, it is possible that by reconfiguring the grid topology, the designed protection system loses its efficiency, and the distribution grid is exploited in an unprotected state or the normal performance of the grid is disrupted [16].

To maintain the coordination between the protective elements and their correct functioning, the system can be classified into two categories [12]:

• A fully automatic distribution system that allows online changes in the relay settings after reconfiguration. In this case, using the design of the new protection system in the modified configuration, protection system settings are adopted in the new configuration [13].

• The distribution system has a semi-automatic control so that only the operator can change the relay settings.

The smart grid brings the ability to use different technologies for energy production and storage easily. Research studies on the reconfiguration of distribution systems have pursued various purposes, but most of them have not considered grid protection. In these studies, the researchers have mostly focused on whether the studied distribution system is equipped with a fully automatic system, so they have considered that the protection system will adapt itself to the new configuration [6]. An algorithm has been presented in [6] and [17] for designing a protection system for several different configurations. In this algorithm, besides coordinating the relays in the feed bus and determining the nominal value of the re-closers and fuses, the proper location of their installation is specified as well. After designing the protection system with these features, the authorized switching area of the automation system is defined and the protection system will function properly and desirably. The same approach was considered in [18]. The technique is referred to as the virtual microgrid system. Several factors are considered in the study, including the maximum load demand, the available power supply, and the operation cost. The restoration problem is posed as a MILP problem [19].

In [20], the genetic algorithm is used with a slight change in composition and mutation operators using a competition mechanism to solve the reconfiguration problem. The MILP problem is the problem of optimizing the value of a linear objective function of some integer/real-valued variables, which satisfy some linear (in) equality constraints. MILP solvers can contribute to finding the best differential characteristic of a cipher if the problem of finding the optimal differential characteristic of a cipher can be translated into a (not too large) MILP problem. To that end, the objective function should be set to an adequate strictly monotonic function of the characteristic probability, and the linear constraints should be configured to express the propagation of the differing values in the cipher. Therefore, to the modeled cryptosystem, the optimum differential characteristic probability would be returned by solving the model with an adequate MILP solver [21]. The linearization method is introduced to model the day-ahead scheduling of ADN as a MILP problem, in which the electricity purchasing cost, line switch operation cost, and responsive load subsidy cost of the power systems with wind power integrated are simultaneously optimized. The results under different uncertainties of loads and DGs, which are handled by the combined scenario and Monte-Carlo method, further verify the feasibility of the MILP model [22].

The necessity of this paper is modeled in randomized optimization problems, non-deterministic and random variables with a suitable distribution function so that the behavioral pattern of these variables can be expressed with different probabilities. It is necessary to increase the installation of these types of resources on grids to use the environmental benefits and low cost of distributed renewable energy resources. The thermal rating of the lines, voltage increase, and protection difficulties could be mentioned as some of the most important barriers to installing distributed generations (DGs) in grids. DG placement and installation methods are generally used to get the best location and the maximum active power to be installed in a particular configuration in the worst scenario. The solution to this problem has recently been discussed in [22].

In Table I, a comparison is made between this work and the previous research, and the comprehensiveness of the design of the reconfiguration distribution system protection (RDSP) proposed in this paper is demonstrated. Accordingly, the effect of reconfiguration on the network protection plan has not been studied in previous research. Neglecting the receptacle impact of network reconfiguration and protection may lead to missing the operation of protective devices. Therefore, to cover this research gap, the effects of distribution network reconfiguration on its protective coordination are considered in the proposed model. Also, the uncertainties and variations in the output power of the DG, photovoltaic (PV), and wind turbine (WT) are considered in this study. Moreover, an MILP formulation is presented to solve the proposed model. According to the contents of this paper, a two-step algorithm is proposed to establish coordination between the protection system and the network configuration. The first step is to determine the optimal reconfiguration to reduce system-wide losses. This is achieved by shortening the flow through the optimal feeders and exploiting the existing distributed renewable generation. In the second stage, the obtained makeup is examined from a protective point of view. At this stage, by determining the possibility of resetting all or several protection relays, the protective function of the network is feasible. Otherwise, if it is infeasible, the fault signal is sent to the first stage and another optimal reconfiguration is determined, which certainly has a higher loss rate. The details of the iteration

loop are fully explained in the simulation section.

In this paper, a new RDSP scheme is presented based on mathematical formulations. The contributions of the paper are highlighted below.

- Determining optimal reconfiguration of the distribution network considering fault occurrences so that the maximum possible value is retrieved and the new network reconfiguration has a minimum of active power losses.
- Coordinating the problem of overcurrent relays, and proper network switching.
- Linearization of the models, and comparison of the proposed model MILP with the nonlinear heuristic methods.
- Coordination modeling of protective elements taking into account the uncertainty of uncertainties of DG, PV, and WT in the reconfiguration distribution system.

**TABLE I**

COMPARISON OF THE PROPOSED MODEL WITH RECENT RESEARCHES.

| Reference | Uncertainty Resource | | | Reconfiguration | Protection | Solving Strategy | | | | Optimized Linearization of the model |
|---|---|---|---|---|---|---|---|---|---|---|
| | Wind | PV | DG | | | CSA | GA | ICA | MILP | |
| [14] | | | ✓ | ✓ | | ✓ | | | | |
| [15] | | | ✓ | | ✓ | | | ✓ | | |
| [23] | | | ✓ | ✓ | ✓ | | | | | |
| [24] | | | ✓ | ✓ | | | ✓ | | | |
| [27] | | | ✓ | | ✓ | | | | | |
| [19] | | | ✓ | | | | | | ✓ | ✓ |
| [22] | | | ✓ | ✓ | | | | | ✓ | ✓ |
| This Paper | ✓ | ✓ | ✓ | ✓ | ✓ | | | | ✓ | ✓ |

The structure of the papers is as follows. Section II discusses the reconfiguration and protection characteristics of the distribution grid. The constraints related to the operation and relay coordination are then formulated. The 33-bus test grid has been used to develop reconfiguration, design, and adjustment of the protection system according to the proposed concepts. Finally, the effects of protective constraints and considering the presented uncertainty for studying networks will be presented.

## II. RECONFIGURATION OF DISTRIBUTION GRIDS

Reconfiguration in distribution grids to find the best switching using smart techniques is one of the vital issues in power distribution companies. Due to the appropriate protection coordination, limiting the grid's short circuit, and the problems of interconnected grids, operation of distribution grids is done in radial form. Moreover, there are several disconnecting switches in the grid with significant roles in managing the grid structure to reach the optimal form [2], [3], [23].

## III. PROTECTION OF DISTRIBUTION SYSTEM

Protection is one of the most important needs for the acceptable operation of distribution grids. Security concepts of power system protection depend on parameters like sensitivity, selectivity, speed, and reliability. The protection system detects specific faults and limits any damage to power equipment. Each protection device installed in the distribution grid shall only detect faults on its downstream due to the radial property of the grid. A widespread protection philosophy is used to protect distribution grids, without any specific standard for overall protection [6], [13], [17], [18], [22].

## IV. FORMULATION OF THE PROBLEM

The purpose of the optimization is the reconfiguration of the grid by reducing losses and enhancing the voltage profile while the security system works properly. In this paper, the objective function is optimized using the meta-heuristic optimization method.

$$F = \frac{\mathrm{F_{loss}}}{\mathrm{F_m}} + \sum_{j \in V,I,F} penalty - R \tag{1}$$

Where $F_{loss}$ is the loss objective function, $F_m$ is the total network loss in the initial settings, and *Penalty-R* is a permitted function of the problem constraint, including the usual constraints of the reconfiguration problem and the security constraints.

### *A. Loss of Objective Function*

The main objective of the proposed model is to find the optimal configuration of the distribution network through the minimization of total system losses. Total system losses include total losses of all system branches that can be formulated as follows:

$$MinJ = \sum_t \sum_{nm \in \Omega_H} \sum_{s=1}^{N_S} \psi_s \; h_t \, r_{nm} (p^2_{nm,t,s} + q^2_{nm,t,s}) \tag{2}$$

Equation (2) is subjected to the following constraints. The $\Psi_s$ index in the relationship indicates the probability of each scenario.

### *B. Power Flow Constraint*

Constraints (3) and (4) present the active and reactive nodal power balance, respectively. Equations (5) and (6) describe the net nodal demand and line flow formulations, respectively. Constraints (7) and (8) present maximum active and reactive transmitted powers of connected lines, respectively. Equations (9) and (10) define the active and reactive power transferred through the substation, respectively.

$$\sum_{nm\in\Omega_H}\sum_{s=1}^{N_S}\Psi_s p_{nm,t,s}-\sum_{mn\in\Omega_H}\sum_{s=1}^{N_S}\Psi_s p_{mn,t,s}=L_{pn,t,s} \quad (3)$$

$$\sum_{nm\in\Omega_H}\sum_{s=1}^{N_S}\Psi_s q_{nm,t,s}-\sum_{mn\in\Omega_H}\sum_{s=1}^{N_S}\Psi_s q_{mn,t,s}=L_{qn,t,s} \quad (4)$$

$$L_{pn,t,s}=d_{pn,t,s}-P_{gn,t,s}, L_{qn,t,s}=d_{qn,t,s}-F(pf_{gn})P_{gn,t,s} \quad (5)$$

$$P_{nm,t,s}=F(v,i), Q_{nm,t,s}=G(v,i) \quad (6)$$

$$-y_{nm}p_{nm}^{\max}\le p_{nm,t}\le y_{nm}p_{nm}^{\max} \quad (7)$$

$$-y_{nm}q_{nm}^{\max}\le q_{nm,t}\le y_{nm}q_{nm}^{\max} \quad (8)$$

$$P_{sn,t,s}=\sum_{nm\in\Omega_H}\sum_{s=1}^{N_S}\Psi_s p_{nm,t,s} \quad (9)$$

$$Q_{sn,t,s}=\sum_{nm\in\Omega_H}\sum_{s=1}^{N_S}\Psi_s q_{nm,t,s} \quad (10)$$

*1) Voltage limits:* For each configuration operation of the grid, the value of the voltages in all the buses should remain in their pre-specified values:

$$V_{\min}\le|V_i|\le V_{\max} \quad (11)$$

Where $V_{min}$ and $V_{max}$ are the minimum and maximum bus voltages, respectively. To function, the permitted voltage ranges of the grid bus interface (18) are used as follows:

$$penalty-V=W\times(\sum_{i=1}^{Nbus}\max(V_i-V_{\max},0)+\sum_{i=1}^{Nbus}\max(V_i-V_{\min},0)) \quad (12)$$

Where $W$ is the penalty coefficient assigned to the constraint in the distribution grid.

*2) Lines capacity constraint:* Given the thermal limit of line currents, overloading of any of the grid lines is not allowed:

$$|I_i|\le I_{\max,i} \quad (13)$$

where $I_{max,i}$ is related to the current of the lines. The penalty functions presented in Equation (20) are used for the proper functioning of the constraint of the current passing through the lines:

$$penalty-I=W\times(\sum_{i=1}^{Nb}\max(|I_i|-I_{\max,i},0) \quad (14)$$

*3) Topology constraints:* Reconfiguration of the distribution grid is a change in the grid topology, done by maintaining the radial structure of the grid to improve the system operation. This means that there is no loop in a distribution grid, and all buses must be connected to one of the main feeder buses. Regarding this, to remain in the radial direction of the grid, any restoration of the configuration should have the following equations:

$$z_{nm,b}=0 \quad (15)$$

$$z_{nm,b}+z_{mn,b}=y_{nm} \qquad \forall b,\forall nm\in\Omega_H \quad (16)$$

$$\sum_{b,nm\in\Omega_H}z_{nm,b}=1 \quad (17)$$

$$\sum_{nm,b\in\Omega_H}(y_{nm}-y_{nm}^0)^2\le N_{sw} \quad (18)$$

$$z_{nm,b},y_{nm}\in\{0,1\} \quad (19)$$

*4) Constraints of protecting the distribution grid:* At the beginning of each branch, there must be an overcurrent relay whose pickup current is greater than the maximum through-load current, considering the overload, and should be able to cut off the short-circuit current of the desired branch:

$$I_{pickup}=OLF\times I_{nom} \quad (20)$$

Where *OLF* is the overload factor, $I_{nom}$ is the nominal current passing through the relay location, and *OLF* has different values for different protected types of equipment.

*5) Protective constraints:* The coordination of the protective equipment that should be considered in the formulation of constraints after reconfiguration. Warrington model relates to the time of the relay operation with the parameters TDS and $I_b$ as follows:

$$t=c+\frac{k}{\left(\frac{I}{I_b}\right)^n-1}\times TDS \quad (21)$$

Where *TDS* represents the timing dial setting, *I* represents the current passing through the relay, $I_b$ is the relay regulating current, *k* is the constant coefficient depending on the type of relay, *n* is a constant number depending on the type of relay reduction characteristic and *c* is a constant coefficient to consider the effect of friction and hysteresis. Various types of relays can be modeled using this equation.

*6) Functional constraints and fuse coordination:* The constraints related to fuse function and coordination are considered as follows:

$$Penalty-F=W_{1,1}\times\sum_{i=1}^{N_F}\max(1.25\times I_{i,IF},0)+W_{1,2}\times\sum_{i=1}^{N_{CF}}\max(MCT_{i,m}-0.75\times MMT_{i,b},0) \quad (22)$$

According to [26], to achieve the fuse-fuse coordination for the same short-circuit connection, the maximum cut time (MCT) of the fuse must not exceed 75% of the time required for melting the fusing element. One can examine the coordination of two or more fuses by plotting time-current characteristic of them in the logarithmic diagram.

The constraints related to the grid fuses are composed of two parts: the first part is intended to prevent the operation of the fuse under load, where a maximum of 25% of the overload is predicted for the grid in the new reconfiguration. The second part intended for reconfiguration of the primary/backup fuses is in coordination with the new conditions and the property of selectivity is observed.

The features of the conventional protection system in distribution grids show that the coordination constraints and the functionality of the equipment are formulated in the normal way and added to the reconfiguration problem. In this study, as the studied grid is balanced, three-phase, short-circuit and the three-phase fault are symmetric, it should be noted that the load current is ignored in the state of the fault.

### *A. Linearized Model*

In the proposed model, equations have a nonlinear structure. This causes the nonlinear problem, so using conventional nonlinear programming (NLP) solver engines with the general algebraic modeling system (GAMS) software produces two major faults that are [24]:

Due to the nonlinear constraints of the area, the probability is non-convex, so it is possible to stop the solution after finding the local optimum with the NLP solution engine.

- Given the numerical solution methods for repetition for nonlinear problems, the problem-solving process is long considering time; therefore, the problem implementation speed is low.
- In this paper, the use of linear equations corresponding to nonlinear equations is proposed as an alternative to nonlinear equations to have an optimal global response and high implementation speed. Thus, the problem presented in Section I is rewritten as a linear problem with integer numbers. The second-order function of Equation (2) can be compared with the piecewise-linear function of the first-order loss function. In doing so, assume that we put linear sections $l$ for the powerful currents $p_{nm,t,s}$,$q_{nmt,s}$, and lets them as follows:

$$J = \sum_t \sum_{nm\in\Omega_H} \sum_{s=1}^{N_s} \Psi_s h_t r_{nm} \left(\sum_{l=1}^{N_l} \alpha^l_{nm,t,s} p^l_{nm,t,s} + \beta^l_{nm,t,s} q^l_{nm,t,s}\right) \quad (23)$$

If:

$$p_{nm,t,s} = \sum_{l=1}^{N_l} p^l_{nm,t,s} \quad \forall t, nm \in \Omega_H \quad (24)$$

$$q_{nm,t,s} = \sum_{l=1}^{N_l} q^l_{nm,t,s} \quad \forall t, nm \in \Omega_H \quad (25)$$

$$0 \le p^l_{nm,t,s} \le p^{l_{\max}}_{nm,s} \quad \forall t, nm \in \Omega_H, l = 1,\ldots,N_l \quad (26)$$

$$0 \le q^l_{nm,t,s} \le q^{l_{\max}}_{nm,s} \quad \forall t, nm \in \Omega_H, l = 1,\ldots,N_l \quad (27)$$

Equation (23) shows the objective function of the problem, which corresponds to the objective function of the nonlinear problem. The losses are shown by the piecewise-linear method in Figure 1, and Equations (24) and (25) included linear-piecewise load-distribution equations. Thus, with the coefficients of the line slope $\propto^l_{nm,t,s}$ and$\beta^l_{nm,t,s}$, we express the piecewise-linear $I$. The remaining constraints of the proposed model are linear and the flowchart of the proposed model is presented in Figure 2.

According to the above description and the mathematical modeling of various programming sections, this section presents the steps of implementing the proposed algorithm as follows:

Initially, basic information, including the basic structure of the network, is determined by using the data of the primary lines, specifications of system equipment, and load curves.

Then, reconfiguration is performed according to the objective function in GAMS software and a set of new structures are provided. The first solution has the least loss. The second, pay attention to the network's new structure, including the original and the reconfigured structures, programming is performed in MATLAB to minimize the loss with protection coordination optimal.

The flowchart of the proposed algorithm is illustrated in Figure 2 to indicate the implementation.

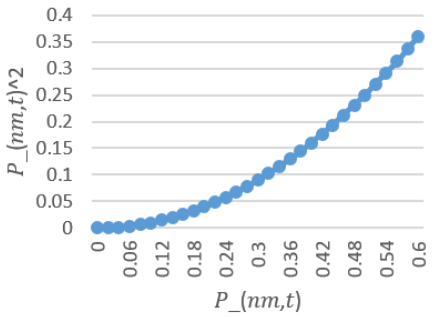


**Fig. 1.** Piecewise-linear approximations of the second-order equation.

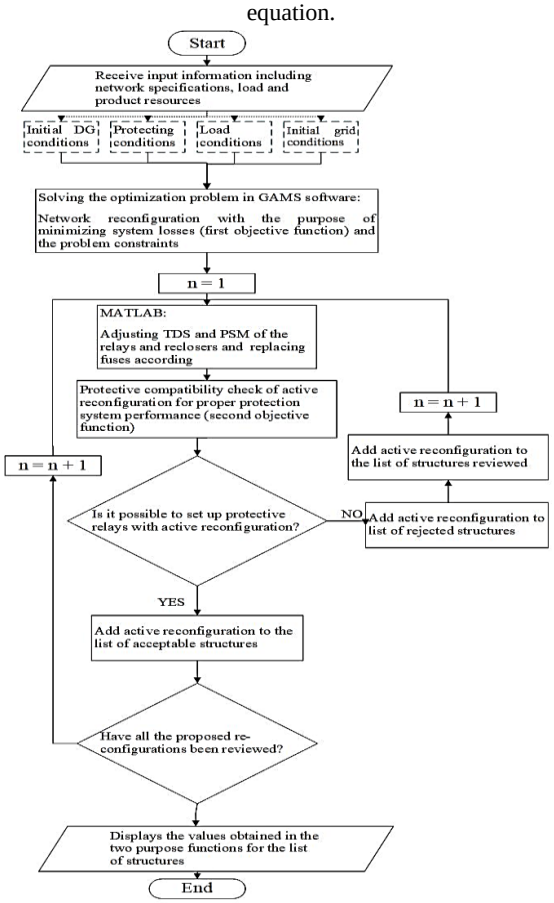


**Fig. 2.** The flowchart of the suggested method.

## V. Simulation Results

In this paper, two MATLAB and GAMS software packages were used together for simulation, where GAMS was used to perform optimization and protection requirements of the load flow. The proposed problem is implemented in a 33-bus radial distribution grid displayed in Figure 3. The active and reactive loads of peak momentum are presented in [25]. The base power and voltage are 1 MW and 12.66 kV, respectively. The base curve for the predicted daily charge demand in Figure 4 and the prediction of wind turbine and photovoltaic power is evaluated. In this grid, there are 33 closed normal keys and 5 normal open keys that should be controlled during optimization. The proposed grid includes both active and reactive loads [26]. According to the grid's basic information, there are 3 or 4 distribution lines connected to some of the

buses that could be switched. Also, the total number of switchings is limited. Therefore, the best times and lines that should happen are selected. As the number of switchings is limited and only allows the power to be received at any point on one side, the lines are disconnected in the studied intervals. Moreover, by providing the load distribution equations for the linearization and definition of the switching of the grid similar to the other methods stated, the optimal overall point is obtained. In the proposed model, the parameters with uncertainty are quantified according to the probability distribution functions. The Weibull distribution function is used for the wind turbine, and the normal distribution function is used for the photovoltaic. All load, photovoltaic, and wind speed input information, as shown in Figure 4 for 24 hours a day, is also examined in a few stochastic samples in demand Figure (a-5), photovoltaic Figure (b-5), and wind turbine Figure (c-5). Finally, by reviewing the grid reconfiguration and considering the uncertainty scenarios of the active distribution grid, the best mode for interconnecting the branches in 1-hour and load the current diagram is shown in the figure6; for the rated current line is selected and is designated as $I\_n$.

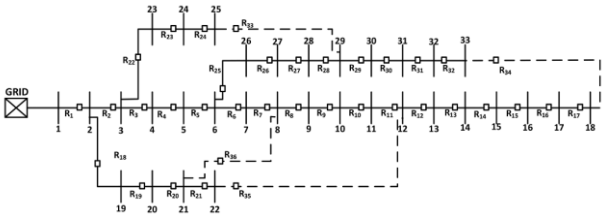


**Fig. 3.** The 33-bus distribution grid.

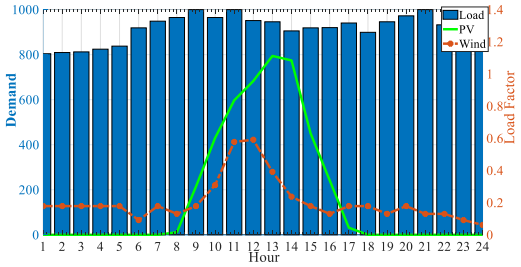


**Fig. 4.** Estimated grid demand and produced power [27].

In the present paper, a relay is considered in the main supply bus as the primary protection of the entire grid, dispersed products in bus 22 and 30, two wind turbines in buses 10 and 14, and a solar cell in bus 19. The relays are used as main protection and backup in switching buses. A genetic algorithm (GA) is used as an optimization tool, and the objective functions are to satisfy formulated constraints. Generally, depending on the position of the connection point and the primary switch, the switching and protection settings are specified based on the primary and backup protection for all lines. Two approaches are defined by linear and nonlinear optimization methods based on artificial intelligence to show the performance of the proposed model. In the first case, the formulated reconfiguration is solved without any protective restrictions. In the second case, the reconfiguration problem is solved considering protective constraints.

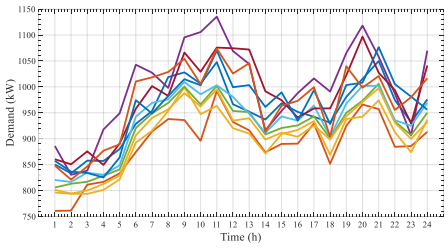


(a) Demand

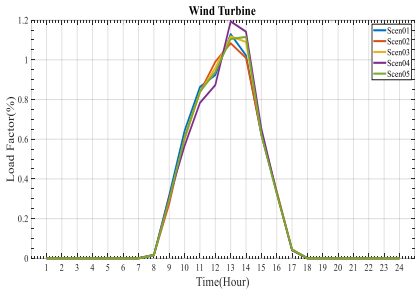


(b) Wind Turbine

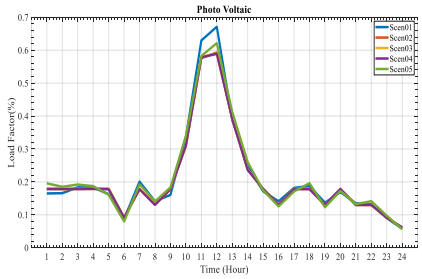


(c) Photo Voltaic

**Fig. 5.** Predicting demand, wind turbine, and photovoltaic production capacity in 5 stochastic samples.

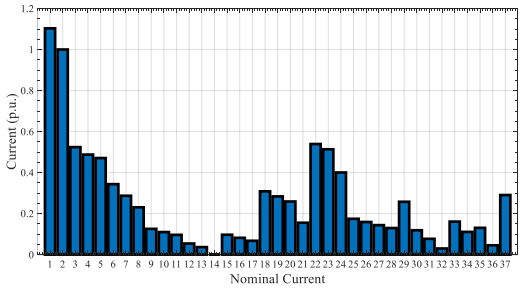


**Fig. 6.** The load current diagram at hour 1.

*1) The first case*

In this section, the reconfiguration problem of reducing losses and improving the voltage profile of the 33-bus grid is solved regardless of the protective constraints. Table II shows the keys obtained from the solution of the nonlinear optimization problem, according to the meta-heuristic algorithms, compared with the results obtained in the scientific references [28]. This algorithm has the necessary efficiency in solving the problem of reconfiguration in the grid. Figure 7 shows the process of minimizing the voltage profile by the algorithms, without the presence of protection utilizing backward-forward sweep load flow for this case. Comparing the voltage profiles in the three samples of the studied algorithm shows that in the first iterations, the value of the objective function is not less than one; in subsequent

iterations, the value of the objective function decreases dramatically. The minimization process continues until it is repeated until the objective function reaches its optimal value.

In repetitive numerical solution methods for nonlinear problems, the problem-solving process is time-consuming [24], so the speed of execution of the problem decreases. In this research, to have the optimal global solution and high execution speed, it is suggested to use linear equations instead of nonlinear equations. Hence, the proposed problem is rewritten as a linear problem mixed with integers.

**TABLE II**

RESULTS OF NONLINEAR AND LINEAR OPTIMAL RECONFIGURATION FOR REDUCING LOSSES, REGARDLESS OF PROTECTIVE CONSTRAINTS.

| Problem Solving Method | Maneuvered Switched | Real Power loss(kW) | $V_{min}(p.u.)$ |
|---|---|---|---|
| Genetic Algorithm | 6-13-17-35-37 | 158.3641 | 0.9312 |
| Imperialist Competitive Algorithm | 7-9-13-28-32 | 143.5327 | 0.9404 |
| Crow Search Algorithm | 7-9-14-28-32 | 139.9814 | 0.9413 |
| The proposed Model | 14-28-33-35-36 | 139.5384 | 0.9240 |

As can be seen, each of these objective functions has been able to have positive effects on improving the state of the network from a unique perspective. However, the problem here is that each of these objective functions, after single-objective optimization, reaches a different and optimal keying pattern. In other words, if it certainly does not happen for all objective functions, the optimal switching patterns found in this objective function will likely be different. However, it is ultimately required to provide an optimal switching pattern for the entire network so that all the objective functions of the problem are performed to a large extent. One way to respond to this need is to provide a multi-objective optimization framework.

*2) Second case*

In this case, the optimal reconfiguration problem for a 33-bus grid has been solved for optimizing the total losses of this grid and considers the protection constraints.

The proposed model considers grid configuration protective problems online with the presence of any distributed products for using a reactive-active distribution network. By solving optimization problems in the studied system, there is a series of switching operations. This switching is done due to a change in the graph and a change in the power of the short-circuit connections. Changes in the short circuit power due to load discharges cause key switching. It is impossible to change the settings of all the relays in a microgrid or distribution network. Our study period is a short-term system operation and a limited number of keys have this feature. Measurements are made to protect at the maneuvering points, and then the protection relays are placed at the same points to indicate the configuration. Other protection architecture is based on using fuses.

After calculating the nominal current, we dealt with the grid fault, which is the first step in applying the fault on the grid. To apply faults on the grid in a bus, for example, in bus 4, faults are generated, and according to the loop and node rules, the currents passing through the branches are obtained.

Now, with the current lines in the event of a fault in the grid and having the nominal current obtained in the previous step, one can express protection based on the Warrington equation (16). This equation expresses the fuses coordination in the event of a fault so that when a fault occurs on a line or a student bus, the closest fuses act to the fault location at a specific time if these fuses have a functional disruption. In the next few moments, the fuses of the higher lines are involved.

Finally, the result of the nominal flow fault can be seen in Table III and Figure 8. As expected, the value of the objective function is increased by considering the new constraints. Then, considering the protection constraints causes a reduction in grid losses that leads to more constraints on the optimization problem. However, in this configuration, the network losses are reduced by about 30 kW compared to the initial case of the network. The use of protective and coordination devices should be examined to confirm the proper functioning of the protective system in this case.

As there is the necessary time interval (margin = 0.3 s) between their performance, one can conclude that the coordination of its protected elements is low.

**TABLE III**

COMPARING RECONFIGURATION RESULTS TO REDUCE THE LOSSES WITH OTHER REFERENCES, CONSIDERING THE PROTECTIVE CONSTRAINT.

| Problem Solving Method | Maneuvered Switched | Real Power loss(kW) | $V_{min}(p.u.)$ |
|---|---|---|---|
| Crow Search Algorithm | 6-13-21-32-37 | 165.0138 | 0.9218 |
| Genetic Algorithm | 7-13-17-21-28 | 158.8401 | 0.9327 |
| Imperialist Competitive Algorithm | 6-11-34-36-37 | 145.4154 | 0.9373 |
| Fault in the fourth bus OF the proposed model | 3-14-28-33-36 | 139.98 | 0.9413 |

Table IV shows the backup relays of each relay and Table V shows the settings of each relay.

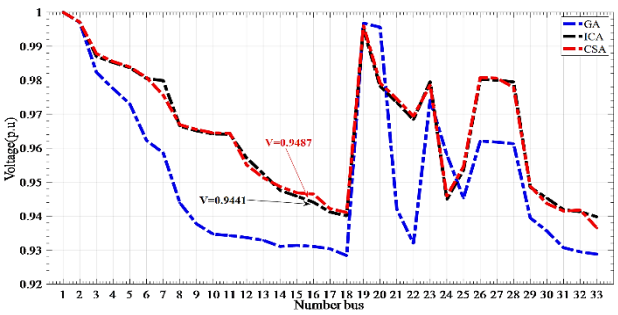


**Fig. 7.** Comparing the voltage profile with multi-objective reconfiguration regardless of protective constraints.

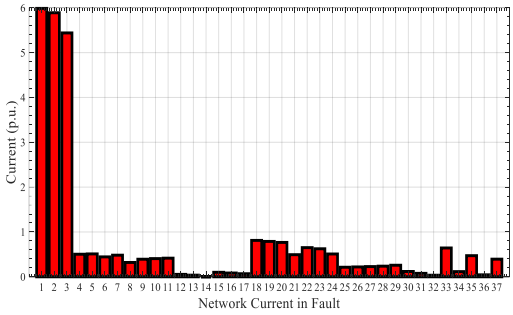


**Fig. 8.** Nominal current fault in the bus4, 1-hour interval.

*Setting the Priority and Short Circuit Level:* To determine the path of current flow to energize the network busses, the radial diagram of the existing structure is first plotted and the corresponding graph is drafted. Table IV shows optimal structures.

Considering the radial structure of the DN, the obtained graph is a tree graph, based on which the current flow. Path to supply electricity to each bus can be determined. Given the existence of a protection relay on all lines, the short circuit in each line is calculated and the binary priority of the relays is determined relative to each other. According to the structure shown in Figure 3, the short circuit level at the installation site of the protection relays is shown in Table IV, which introduces the line numbers, the beginning and end buses, the short circuit current level, and the line number in which the backup relay of each line is contracted. As it turns out, except for the line 1 relay, the backup relay number of each line is determined by the current path.

**TABLE IV**
SHORT CIRCUIT CURRENT AND BACKUP RELAYS IN BASIC.

| Line Number | Bus Send | Bus Receiver | Short Circuit Current | Line Number With Backup Relay | Line Number | Bus Send | Bus Receiver | Short Circuit Current | Line Number With Backup Relay |
|---|---|---|---|---|---|---|---|---|---|
| 1 | 1 | 2 | 4140.855 | NaN | 17 | 17 | 18 | 3920.999 | 16 |
| 2 | 2 | 3 | 4134.487 | 1 | 18 | 2 | 19 | 4138.065 | 1 |
| 3 | 3 | 4 | 4125.173 | 2 | 19 | 19 | 20 | 4119.985 | 18 |
| 4 | 4 | 5 | 4117.107 | 3 | 20 | 20 | 21 | 4099.439 | 19 |
| 5 | 5 | 6 | 4104.216 | 4 | 21 | 21 | 22 | 4087.526 | 20 |
| 6 | 6 | 7 | 4093.47 | 5 | 22 | 3 | 23 | 4124.252 | 2 |
| 7 | 7 | 8 | 4083.921 | 6 | 23 | 23 | 24 | 4109.715 | 22 |
| 8 | 8 | 9 | 4065.541 | 7 | 24 | 24 | 25 | 4090.543 | 23 |
| 9 | 9 | 10 | 4043.866 | 8 | 25 | 6 | 26 | 4093.302 | 5 |
| 10 | 10 | 11 | 4031.01 | 9 | 26 | 26 | 27 | 4088.119 | 25 |
| 11 | 11 | 12 | 4025.121 | 10 | 27 | 27 | 28 | 4073.899 | 26 |
| 12 | 12 | 13 | 4006.235 | 11 | 28 | 28 | 29 | 4054.336 | 27 |
| 13 | 13 | 14 | 3985.836 | 12 | 29 | 29 | 30 | 4040.676 | 28 |
| 14 | 14 | 15 | 3974.43 | 13 | 30 | 30 | 31 | 4025.354 | 29 |
| 15 | 15 | 16 | 3961.047 | 14 | 31 | 31 | 32 | 4012.162 | 30 |
| 16 | 16 | 17 | 3940.851 | 15 | 32 | 32 | 33 | 4005.506 | 31 |

It is clear in Table IV that both structures have 32 lines and the difference in the short circuit current level is reduced by moving away from the transformer. According to Table IV, the maximum short circuit level in the above network is 4140.855 A. This value can be calculated according to the transformer specifications and main voltage. The amount of system losses, in this case, is equal to 207.759 kW. In this case, how to coordinate protection relays, according to the second objective function, is shown in Table V. According to Table V, it is clear that the maximum operating time in the main line relay is equal to 4.2 seconds. It should be noted that the minimum operating time for the relay is 0.9 seconds. The duration of operation of the whole protection system, in this case, is equal to 66.6.

In this case, planning has been done according to the possibility of resetting all protection relays. Due to the above conditions, in this case, there is no more performance error among the relays due to the change in structure. The reason for this is the reprogramming of all relays according to the new structure. The results obtained in this case are presented in Table VI. The system loss is equal to 139.98 kW in this case. The table presents the optimization results for the second case. By comparing the two tables, it is revealed that the operating time of the main relay, in this case, is equal to 3, implying a decrease of 28.57% versus the first case. The reason for this is a reduction in the strength of the network tree branches so that all branches have almost the same resistance. In this case, the total operating time of the system is 53. Overall, at each stage after the coordination of the protection devices, the graph corresponding to the new grid configuration is checked. If the previous configuration loading is declared infeasible in the grid, it will be done with feedback to the reconfiguration of the linear optimization that is the link between MATLAB and GAMS. According to the objective function and the problem constraints, a new topology is suggested at each step of the reconfiguration according to the observations.

**TABLE V**
COORDINATE PROTECTION RELAYS IN THE BASE STRUCTURE.

| Line Number | Relay Operation Time | TDS | PS | CTR | Line Number | Relay Operation Time | TDS | PS | CTR |
|---|---|---|---|---|---|---|---|---|---|
| 1 | 4.2 | 0.786 | 1.815 | 626.419 | 17 | 1 | 0.277 | 1.191 | 491.262 |
| 2 | 4 | 0.865 | 1.366 | 681.885 | 18 | 1.6 | 0.754 | 1.8 | 94.201 |
| 3 | 3.8 | 0.759 | 1.657 | 626.679 | 19 | 1.4 | 0.755 | 0.5 | 216.925 |
| 4 | 3.6 | 0.566 | 1.961 | 707.351 | 20 | 1.2 | 0.287 | 1.19 | 663.032 |
| 5 | 3.4 | 0.84 | 1.701 | 441.119 | 21 | 1 | 0.303 | 1.265 | 405.568 |
| 6 | 3.2 | 0.593 | 1.588 | 715.556 | 22 | 1.4 | 0.235 | 1.962 | 657.492 |
| 7 | 3 | 0.382 | 1.689 | 1000 | 23 | 1.2 | 0.354 | 1.158 | 470.24 |
| 8 | 2.8 | 0.613 | 1.526 | 588.678 | 24 | 1 | 0.247 | 1.503 | 498.168 |
| 9 | 2.6 | 0.565 | 1.155 | 781.96 | 25 | 2.4 | 0.486 | 1.784 | 567.813 |
| 10 | 2.4 | 0.601 | 1.951 | 369.373 | 26 | 2.2 | 0.602 | 1.357 | 460.237 |
| 11 | 2.2 | 0.615 | 1.581 | 373.665 | 27 | 2 | 0.313 | 1.882 | 732.259 |
| 12 | 2 | 0.498 | 1.949 | 370.346 | 28 | 1.8 | 0.752 | 1.363 | 173.173 |
| 13 | 1.8 | 0.565 | 0.626 | 740.865 | 29 | 1.6 | 0.6 | 1.424 | 219.323 |
| 14 | 1.6 | 0.543 | 1.252 | 312.454 | 30 | 1.4 | 0.517 | 0.687 | 470.774 |
| 15 | 1.4 | 0.406 | 1.326 | 408.215 | 31 | 1.2 | 0.566 | 1.581 | 103.796 |
| 16 | 1.2 | 0.256 | 1.464 | 616.525 | 32 | 1 | 0.256 | 1.126 | 611.838 |

**TABLE VI**
COORDINATE PROTECTION RELAYS IN THE OPTIMAL STRUCTURE.

| Line Number | Relay Operation Time | TDS | PS | CTR | Line Number | Relay Operation Time | TDS | PS | CTR |
|---|---|---|---|---|---|---|---|---|---|
| 1 | 3 | 0.696 | 1.693 | 494.69 | 20 | 2.459 | 0.669 | 0.991 | 611.2 |
| 2 | 2.4 | 0.478 | 1.728 | 605.16 | 21 | 1.591 | 0.557 | 0.753 | 503.225 |
| 3 | 2 | 0.471 | 1.774 | 459.577 | 22 | 2.206 | 0.469 | 1.554 | 611.088 |
| 4 | 1.8 | 0.309 | 2.496 | 503.696 | 23 | 2.001 | 0.624 | 0.997 | 485.658 |
| 5 | 1.6 | 0.607 | 1.491 | 206.918 | 24 | 1.8 | 0.496 | 1.948 | 316.715 |
| 6 | 1 | 0.404 | 1.692 | 154.607 | 25 | 1.395 | 0.44 | 0.805 | 590.828 |
| 8 | 1.989 | 0.593 | 1.138 | 464.608 | 26 | 1.198 | 0.328 | 1.157 | 541.405 |
| 10 | 0.995 | 0.213 | 1.613 | 575.984 | 27 | 0.997 | 0.255 | 1.613 | 438.261 |
| 11 | 1.2 | 0.321 | 1.03 | 623.814 | 29 | 1.394 | 0.364 | 1.734 | 391.982 |
| 12 | 1.198 | 0.487 | 1.573 | 160.602 | 30 | 1.194 | 0.401 | 0.948 | 434.428 |
| 13 | 0.995 | 0.167 | 2.115 | 594.246 | 31 | 0.997 | 0.341 | 1.385 | 284.506 |
| 15 | 1.598 | 0.651 | 0.762 | 327.788 | 33 | 2.202 | 0.559 | 2.192 | 322.19 |
| 16 | 1.396 | 0.506 | 1.28 | 262.097 | 34 | 1.789 | 0.494 | 1.279 | 473.377 |
| 17 | 1.197 | 0.535 | 1.534 | 124.286 | 35 | 1.403 | 0.589 | 0.949 | 244.231 |
| 18 | 2.906 | 0.507 | 1.653 | 716.845 | 36 | 0.989 | 0.287 | 1.106 | 496.125 |
| 19 | 2.673 | 0.619 | 1.665 | 480.295 | 37 | 1.614 | 0.472 | 1.143 | 472.016 |

The results of the surveys conducted in the sample distribution network are as follows:

- The main problem that occurs in reconfiguring without considering the protective restrictions and in most cases is related to the operation of the fuses. In solving the reconfiguration without considering the protection constraints, we can pay attention to several scenarios in which, in all cases, several network fuses operate under load and cut off the load. Discrepancies are not shown.
- Although studies have shown that the displacement of short circuit levels depends on different reconfigurations and also depends on the protection system in the network, there is a possibility of disruption in the coordination of this equipment, but by examining the simulation results of the proposed model in different scenarios of relay, inconsistency or recloser was not observed with fuses.
- Therefore, by using the proposed method, it is possible to ensure the correct operation of the protection system by performing reconfiguration in addition to using the advantages of this method in the operation of distribution networks.
- The proposed method is a method that will allow changing the makeup without prior planning. Also, if the network layout is changed with prior planning, the network can be used more efficiently and economically than the proposed method.
- Other features of the MILP method with the above problems include (1) very low solution execution time, (2) having an absolute optimum solution, (3) ability to run on a large network, and (4) providing a solid model with simple equations and methods.
- In the studied systems, the operating time is improved compared to another reference [11-15], which indicates the efficiency of the linear programming method developed in the

- GAMS environment because of applying a more accurate approach to solving coordination of overcurrent relays problem by exact mathematical methods developed in the GAMS environment.

## VI. CONCLUSIONS

This paper analyzed the coordination of network structure with two approaches to minimizing losses and reducing the operating time of protection relays. A new method is proposed according to the branch switch optimization algorithms and sequential branch opening to solve reconfiguration. Using advanced technologies for data collection, the implementation of decision-making algorithms, and dynamic load distribution control, power outages in smart grids are minimized. By comparing the simulation results, one can understand that the mentioned linearization method has a good efficiency in solving the reconfiguration problem. Protective constraints include equipment performance and coordination of protective tools and formulation added to the reconfiguration problem. By examining the simulation results in the study of the sample grid and different scenarios, there was no lack of coordination among the elements. Studies show that despite short-circuit surface displacement that depends on different configurations and grid protection, there is a potential disruption in the coordination of the equipment. By presenting the optimal settings of the sample testing system, this paper accurately performs minimum active power loss and optimal voltage characteristics with protective devices and renewable energies.

According to research carried out in this paper, it is suggested to study the effect of unbalanced loads and the associated uncertainties and to include reliability evaluation in the proposed model in future research.

## References


[1] A. Kavousi-Fard, et al, "Multi-objective probabilistic reconfiguration considering uncertainty and multi-level load model," *IET Science, Measurement & Technology*, vol. 9, no. 1, pp. 44-55, 2014.

[2] I. Ben Hamida, et al, "Optimal integration of distributed generations with network reconfiguration using a pareto algorithm," *International Journal of Renewable Energy Research*, Vol. 8, No. 1, pp. 345-356, 2018.

[3] M. Mohammadi, et al, "Distribution automation planning and operation considering optimized switch placement and feeder reconfiguration strategies from reliability enhancement perspective," *IOS Press*, vol. 35, pp. 3493-3506, 2018.

[4] F. Xinming, et al, "Application of discrete learning optimization algorithm to distribution netwrk reconfiguration considering distrebuted generation[J]," *Power System Protection and Control*, vol. 46, no. 8, pp. 156-163, 2018.

[5] S. P. Ghanegaonkar, V. N. Pande, "Optimal hourly scheduling of distributed generation and capacitors for minimisation of energy loss and reduction in capacitors switching operations," *IET Generation, Transmission & Distribution*, vol. 11, no. 9, pp. 2244-2250, 2017.

[6] S. Mohanty, et al, "A novel meta-heuristic approach for load balancing in cloud computing," *IGI Global*, vol. 8, no. 1, pp. 29-49, 2018.

[7] A. Merlin, "Search for a minimal-loss operating spanning tree configuration for an urban power distribution system. *Proc. of 5th PSCC*, vol. 1, pp. 1-18, 1975.

[8] S. K. Goswami, S. K. Basu, "A new algorithm for the reconfiguration of distribution feeders for loss minimization," *IEEE Transactions on Power Delivery*, vol. 7, no. 3, pp. 1484-1491, 1992.

[9] R. Taleski, D. Rajicic, "Distribution network reconfiguration for energy loss reduction," *IEEE Transactions on Power Systems*, vol. 12, no. 1, pp. 398-406, 1997.

[10] V. Borozan, N. Rajakovic, "Application assessments of distribution network minimum loss reconfiguration," *IEEE Transactions on Power Delivery*, vol. 12, no. 4, pp. 1786-1792, 1997.

[11] F. Ding, K. A. Loparo, "Hierarchical decentralized network reconfiguration for smart distribution systems—Part I: Problem formulation and algorithm development," *IEEE Transactions on Power Systems*, vol. 30, no. 2, pp. 734-743, 2014.

[12] P. Mariaraja, T. Manigandan and S. Thiruvenkadam, "An expert system for distribution system reconfiguration through fuzzy logic and flower pollination algorithm," *SAGE Publications*, vol. 51, pp. 371-382, 2018.

[13] S. S. F. Souza, R. Romero and J. F. Franco, "Artificial immune networks copt-ainet and opt-ainet applied to the reconfiguration problem of radial electrical distribution systems," *Electric Power Systems Research*, vol. 119, pp. 304-312, 2015.

[14] K. S. Kumar, T. Javabarathi, "Power system reconfiguration and loss minimization for a distribution systems using bacterial foraging optimization algorithm," *International Journal of Electrical Power & Energy Systems*, vol. 36, pp. 13-17, 2012.

[15] X. Xiaoqin, et al, "Reconfiguration of two-voltage distribution network based on cuckoo srarch and simulated annealing algorithm," *Power System Protection and Control*, vol. 48, pp. 11, 2018.

[16] G. J. Peponis, M. P. Papadopulos and N. D. Hatziargyriou, "Optimal operation of distribution networks," *IEEE Transactions on Power Systems*, vol. 11, no. 1, pp. 59-67, 1996.

[17] F. Capitanescu, et al, "Assessing the potential of network reconfiguration to improve distributed generation hosting capacity in active distribution systems," *IEEE Transactions on Power Systems*, vol. 30, no. 1, pp. 346-356, 2014.

[18] S. M. Hadad Baygi, J. Farzane, "Application of artificial intelligence techniques for optimum design of hybrid grid-independent PV/WT/battery power system," *International Journal of Industrial Electronics, Control and Optimization*, Vol.3, no. 3, pp. 275-289, 2020.

[19] A. Bu Jubarah, M. Al-Muhaini and I. M. Elamin, "A MILP-based approach for virtual microgrid restoration," *IEEE Access*, vol. 8, pp. 116695-116703, 2020.

[20] S. K. Bhattacharya, S. K. Goswami, "Distribution network reconfiguration considering protection coordination constraint," *Electric Power Components and Systems*, vol. 36, no. 11, pp. 1150-1165, 2008.

[21] E. Bagherzadeh, Z. Ahmadian, "MILP-based automatic differential search for LEA and HIGHT block ciphers," *IET Information Security*, vol. 14, no. 5, pp. 595-603, 2020.

[22] X. Qiao, et al, "Optimal scheduling of distribution network incorporating topology reconfiguration, BES and load response: A MILP model," *CSEE Journal of Power and Energy Systems*, pp. 1-12, 2020.

[23] R. P. Broadwater, et. Al, "An expert system for integrated protection design with configurable distribution circuits. I, " *IEEE Transactions on Power Delivery*, vol. 9, no. 2, pp. 1115-1121, 1994.

[24] W.-M. Lin, F.-S. Cheng and M.-T. Tsay, "Distribution feeder reconfiguration with refined genetic algorithm," *IEE Proceedings-Generation, Transmission and Distribution*, vol. 147, no. 6, pp. 349-354, 2000.

[25] D. Zhang, Z. Fu and L. Zhang, "An improved TS algorithm for loss-minimum reconfiguration in large-scale distribution systems," *Electric Power Systems Research*, vol. 77, no. 5-6, pp. 685-694, 2007.

[26] J. S. Savier, D. Das, "Impact of network reconfiguration on loss allocation of radial distribution systems," *IEEE Transactions on Power Delivery*, vol. 22, no. 4, pp. 2473-2480, 2007.

[27] J. J. Shea, "Protection of electricity distribution networks, 2nd ed," *IEEE Electrical Insulation Magazine*, vol. 21, no. 2, pp. 55–55, 2005.

[28] GAMS, 2011. [Online]. Available: http://www.gams.com.

**Abbreviations:**

$W_{1,1}$ : Fine factor related to fuse performance under normal conditions.

$N_F$ : A total number of grid fuses.

$I_{i,nf}$ : The nominal current of the $i$-th fuse and $I_{i,If}$ , the passing current from the same fuse.

$W_{1,2}$ : The penalty factor is related to the lack of coordination between fuses in tandem.

$N_{CF}$ : The number of pairs of tandem fuses.

$MCT_{i,m}$ : Maximum time needed for a downstream fuse or main protection.

$MMT_{i,b}$ : Minimum time required for melting the fuse element of the upstream or the backup fuse.

$t_{margin}$ : The security margin of time.

Variables: Variables based on pre-unit (p.u).

$n, m, P_{nm,t,s}, Q_{nm,t,s}$ : The active and reactive power passing through the line at the two ends of the bus.

$p^{l}_{nm,t,s}, q^{l}_{nm,t,s}$ : Active and reactive power linear approximation.

$P_{sn,t,s}, Q_{sn,t,s}$ : The active and reactive power of the reference bus.

$d_{pn,t}, d_{qn,t}$ : Injection of active and reactive power.

$y_{nm}, z_{nm}$ : The binary variable in the feeder connection status: 1 if connected and zero if disconnected.

Parameters: Parameters are based on pre-unit

$h_b$ : Number of hours of time period.

$r_{nm}$ : Resistance of each branch.

$N_{sw}$ : Number of switching operations.

$PD, QD$: Active and reactive power consumed.

$V_{\min}, V_{\max}$ : The minimum and maximum voltage range.

Collections and indices:

$\phi_n, \phi_t, \phi_l, \phi_k$ : Bus set, time, line, and linearization.

$n, m$: Bas counter.

$t$ : Time.

$l, k$: Line, Number of Linearization

**Elham Khoshbakht** received the BSc and MSc degrees in Electrical Power Engineering from Lorestan University in 2015 and 2018, respectively. She started her Ph.D. in Electrical Power Engineering in 2019 at Lorestan University. She has published 6 technical papers at international conferences. Her fields of interest are Active Distribution Networks, Smart Grids, Power System Protection, and Power System Reconfiguration.

**Farhad Namdari** received the BSc from Iran University of Science and Technology (IUST) in 1995 and the MSc from Tarbiat Modarres University (TMU), Iran in 1998, and the Ph.D. from IUST in 2006 all in Electrical Power Engineering. He is currently working as an Associate Professor with the Lorestan University. Dr. Namdari has published more than 100 technical papers in valuable journals and conferences. His fields of interest are Power System Protection, Power System Transients, Smart Grids, and Artificial Intelligent (AI) Applications in Power Systems, Power System Optimization, and Wide Area Monitoring, Protection, and Control of Power Systems.

**Meysam Doostizadeh** received the MSc and Ph.D. degrees in Electrical Engineering from the University of Tehran, Tehran, Iran, in 2012 and 2016, respectively. He is currently an Assistant Professor with the Engineering Faculty, Lorestan University, Iran. His research interests include electricity markets, smart grid technologies, and integration of renewable energy into power systems.

IECO
This page intentionally left blank.

International Journal of Industrial Electronics, Control and Optimization © 2021 IECO
Vol. 4, No. 3, pp. 333-340, July (2021)

# A Discussion on the Existence of Smooth Lyapunov Functions for Continuous Stable Systems

Majid Akbarian[1,†], Naser Pariz [2]

[1,2] Department of Electrical Engineering, Ferdowsi University of Mashhad, Mashhad, Iran

ABSTRACT

*Lyapunov's theorem is the basic criteria to establish the stability properties of the nonlinear dynamical systems. In this method, it is a necessity to find the positive definite functions with negative definite or negative semi-definite derivative. These functions that named Lyapunov functions, form the core of this criterion. The existence of the Lyapunov functions for asymptotically stable equilibrium points is guaranteed by converse Lyapunov theorems. On the other hand, for the cases where the equilibrium point is stable in the sense of Lyapunov, converse Lyapunov theorems only ensure non-smooth Lyapunov functions. In this paper, it is proved that there exist some autonomous nonlinear systems with stable equilibrium points that despite stability don't admit convex Lyapunov functions. In addition, it is also shown that there exist some nonlinear systems that despite the fact that they are stable at the origin, but do not admit smooth Lyapunov functions in the form of $V(x)$ or $V(t,x)$ even locally. Finally, a class of non-autonomous dynamical systems with uniform stable equilibrium points, is introduced. It is also proven that this class do not admit any continuous Lyapunov functions in the form of $V(x)$ to establish stability.*

**Article Info**

***Keywords:***
Stability, Smooth Lyapunov functions, Stable equilibrium points, Limit cycles.
***Article History:***
**Received** 2020-08-17
**Accepted** 2021-04-12

## I. INTRODUCTION

In this paper, we focus on two main classes of continuous time nonlinear dynamical systems (NDSs). The first class is described by [1]

$$\dot{x} = f(x), \quad x(0) = x_0 \tag{1}$$

where $D \subset \mathbb{R}^n$, and $f: D \to \mathbb{R}^n$ is a locally Lipschitz function with origin being the equilibrium point (i.e,. $f(0) = 0$).

The second class is described by

$$\dot{x} = f(t,x), \quad x(t_0) = x_0 \tag{2}$$

where $D \subset \mathbb{R}^n$, and $f: [0,\infty] \times D \to \mathbb{R}^n$ is locally Lipschitz in $x$ on $[0,\infty] \times D$ and piecewise continuous in $t$. Again, the origin is the equilibrium point of (2) (i.e., $f(t,0) = 0$).

Nonlinear dynamical systems appear in many practical applications including control engineering [2], biological systems [3] and population dynamics [1]. Therefore, the study of stability properties of equilibrium points has always been a crucial issue for mathematicians and control scientists. Among all of this application, stability analysis has attached more attention due to its essential role in real world application including controller design [4], estimation domain of attraction [5] and hybrid systems [6].

It is well known that the origin of (1) is stable in the sense of Lyapunov if

$$\text{for all } \varepsilon > 0, \text{ there exist } \delta = \delta(\varepsilon) > 0, \; s.t. \; \|x_0\| < \delta \Rightarrow \|x(t)\| < \varepsilon \tag{3}$$

In addition, for the nonlinear system in (2), the equilibrium point ($x = 0$), is stable if

$$\text{for all } \varepsilon > 0, \text{ there exist } \delta = \delta(t_0,\varepsilon) > 0, \; s.t. \; \|x_0\| < \delta \Rightarrow \|x(t)\| < \varepsilon \;\; t \geq t_0 \tag{4}$$

† **Corresponding Author**: n-pariz@um.ac.ir, Faculty of Electrical Engineering, Ferdowsi University of Mashhad, Mashhad, Iran

and it is uniformly stable when

$$\text{for all } \varepsilon > 0, \text{ there exist } \delta = \delta(\varepsilon) > 0, \; s.t. \; \|x_0\| < \delta \Rightarrow \|x(t)\| < \varepsilon \quad t \geq t_0 \tag{5}$$

In fact, if the nonlinear system is uniformly stable, then $\delta$ does not explicitly depend on $t_0$.

It should be mentioned that the nonlinear system (2) in its domain $D \subset \mathbb{R}^n$ including origin $x = 0$, is stable in the sense of Lyapunov if there exist a continuously differentiable function $V(t,x): [0,\infty] \times D \to \mathbb{R}$ that satisfies the following conditions for all $t \geq t_0$ and for all $x \in D$

$$V(t,0)=0, \quad V(t,x) \geq \eta_1(x) \tag{6}$$

$$\frac{\partial V}{\partial x} f(t,x) + \frac{\partial V}{\partial t} \leq 0 \tag{7}$$

where, $\eta_1(x)$ is a continuous positive definite function. Also, if $V(t,x)$ satisfies the following inequality

$$V(t,x) \leq \eta_2(x) \tag{8}$$

Then, $x = 0$ is a uniformly stable equilibrium point [7].

It is well known that finding these scalar positive definite functions forms the core of Lyapunov's method. Introducing and computing such suitable Lyapunov functions for NDSs has been one of the main challenges in the literature of NDSs [8-10] and has attracted much attention [11]. In addition, Lyapunov functions are applied in various controller designs [12],[13].

For stable nonlinear systems, it is natural to search for Lyapunov functions to infer stability properties. In fact, the existence of Lyapunov functions are guaranteed by *converse Lyapunov theorems (CLT)* [14, 15]. The study of Lyapunov functions and their properties has become widely popular for researchers in the fields of dynamical systems. For example, for the nonlinear system (1) it is proved in [16] that if the origin is stable in the sense of Lyapunov, and $f(x)$ admits the assumptions in [16] then it is possible to construct some semi-continuous weak Lyapunov functions. The necessary and sufficient conditions for the existence continuous Lyapunov functions can be found in [17].

Recently, special attention has been given to prove the existence of Lyapunov functions for the conditions that the nonlinear system is globally asymptotically stable. For instance, Ahmadi and Kristic in [18] proposed a globally asymptotically stable polynomial vector field with no polynomial Lyapunov functions. Also, Ahmadi and Khadir in [19] investigated a two-dimensional polynomial vector field with no analytic Lyapunov functions. Although in [20], it is proved for the homogeneous vector field of a nonlinear dynamical system that asymptotic stability ensures the existence of a rational Lyapunov function.

Due to the great importance of finding Lyapunov functions with proper analytic properties, this paper has been dedicated to the investigation of stable systems that do not admit smooth Lyapunov functions.

To the best of the author's knowledge, no further results have been available in the context of stable systems. The main contributions of this paper are as follows:

- As a first result, it is proved that if the equilibrium point of (1) is stable, then application of convex Lyapunov functions may fail to satisfy Lyapunov's theorem.
- It is also proved that using smooth Lyapunov functions for the equilibrium point of (1) fails to infer stability properties.
- Finally, it is shown that there exist no smooth Lyapunov functions to establish stability properties of (2).

The continuation of this paper is organized as follows. In Section II, the existence of smooth Lyapunov functions for autonomous stable systems is investigated. Section III is dedicated to some examples of non-autonomous systems that do not admit smooth Lyapunov functions. Simulation results are given in section IV, and section VI concludes the paper.

## II. Existence of Smooth Lyapunov Functions for Autonomous Stable Systems

In this section, we propose some examples of autonomous nonlinear dynamical systems and prove that despite stability, they do not admit smooth Lyapunov functions.

**Lemma 1.** Suppose $V(t,x)$ is a convex Lyapunov function candidate. Then, in the neighborhood of origin, $\nabla V(t,x)^T x$ is positive definite.

**Proof.** Obviously, for any convex function it holds that

$$V(t, \lambda x + (1-\lambda)y) \leq \lambda V(t,x) + (1-\lambda)(t,y) \tag{9}$$

Rewriting above equation as $\lambda \to 0$ and $y = 0$, implies that $\nabla V^T(t,x) \;\; x$ is positive definite.

**Theorem 1.** There exist some nonlinear autonomous systems that despite stability do not admit any convex Lyapunov functions.

**Proof .** Let the function $f(x)$ in (1) be defined by

$$f(x) = Ax + x\|x\|^{2k} sin^{2m+1}\left(\frac{1}{\|x\|}\right) \tag{10}$$

where $x = [x_1 \; x_2]^T$ and all the eigenvalues lie on the imaginary axis $(\pm j\omega_1)$.

This system is stable; however, there are no convex Lyapunov functions in the form $V(x)$ or $V(t,x)$ in order to infer stability.

Due to the fact that all of the eigenvalues of $A$ lie on the imaginary axis, according to linear systems theory, the linear system $\dot{x} = Ax$ is stable in the sense of Lyapunov. Therefore, there exist the positive definite matrix $P$ such that $A^T P +$

$PA = 0$. In order to prove stability of (10), consider $V(x) = x^T Px$ , the time derivative of this function along the trajectories of system implies that

$$\dot{V} = 2x^T Px\|x\|^{2k} sin^{2m+1}(\frac{1}{\|x\|}) \quad (11)$$

It is clear that the origin is surrounded by a countable set of limit cycles. To satisfy the condition $\| x \| \leq \varepsilon$, it is sufficient to choose $\delta \leq \frac{1}{n\pi}$ with large enough values of $n$.

Now, suppose for the sake of contradiction that there exist a convex Lyapunov function in the form of $V(t,x)$ that satisfies the condition of Lyapunov's theorem.

According to Lyapunov's theorem,

$$\dot{V} = \frac{\partial V}{\partial x}\dot{x} + \frac{\partial V}{\partial t} \leq 0 \quad (12)$$

On the other hand, for any square matrix $A$, there exist a similarity transformation $T$ such that $T^{-1}AT$ is diagonal. Substitution of $x = Tz$, in (10) leads to

$$\dot{z} = T^{-1}ATz + z\|Tz\|^{2k}\sin(\frac{1}{\|Tz\|})^{2m+1} \quad (13)$$

Now, equation (12) can be written as follows

$$\dot{V} = \frac{\partial V}{\partial z}\frac{\partial z}{\partial x}\dot{x} + \frac{\partial V}{\partial t} = \frac{\partial V}{\partial z}T^{-1}\dot{x} + \frac{\partial V}{\partial t} = \frac{\partial V}{\partial z}\dot{z} + \frac{\partial V}{\partial t} \leq 0 \quad (14)$$

Since (14) is held in the region $D$ including origin, it is easy to choose $n$ large enough such that $U = \{r| \frac{1}{n\pi+\frac{3\pi}{4}} \leq \|Tz\| \leq \frac{1}{n\pi+\frac{\pi}{4}} (n = 2k)\}$ is situated in $D$. Also, due to the fact that $\dot{V}$ is negative definite, $\int_U \dot{V}$ must be negative in this region.

Integrating $\dot{V}$ implies that

$$\int_U \dot{V} = \int_U \left(\frac{\partial V}{\partial z_1}\omega_1 z_2 - \frac{\partial V}{\partial z_2}\omega_1 z_1\right)$$

$$+ \int_U \nabla V^T(t,z)z\|Tz\|^{2k}\sin(\frac{1}{\|Tz\|})^{2m+1} \quad (15)$$

$$\int_U \frac{\partial V}{\partial t}$$

Let

$$\mathrm{I}_1 = \int_U \left(\frac{\partial V}{\partial z_1}\omega_1 z_2 - \frac{\partial V}{\partial z_2}\omega_1 z_1\right) dS$$

$$\mathrm{I}_2 = \int_U \nabla V^T(t,z)z\|Tz\|^{2k}\sin(\frac{1}{\|Tz\|})^{2m+1} \quad (16)$$

$$\mathrm{I}_3 = \int_U \frac{\partial V}{\partial t}$$

According to Lemma 1, $\nabla V^T(t,z)z$ is positive; as a result, $\mathrm{I}_2 > 0$

Application of divergence theorem implies that

$$\mathrm{I}_1 = \int_U \left(\frac{\partial(V\omega_1 z_2)}{\partial z_1} + \frac{\partial(-V\omega_1 z_1)}{\partial z_2}\right) dS = \int_{\partial U} \left([V\omega_1 z_2 - V\omega_1 z_1].\begin{bmatrix}\frac{z_1}{\sqrt{z_1^2+z_2^2}}\\ \frac{z_2}{\sqrt{z_1^2+z_2^2}}\end{bmatrix}\right) dS = 0 \quad (17)$$

Because of the fact that $\int_U \dot{V} \leq 0$ and $I_2 > 0$ in the region $U$, there exist a region $S_1 \subseteq U$ such that

$$\nabla V^T(t,z)z\|Tz\|^{2k}\sin(\frac{1}{\|Tz\|})^{2m+1} + \frac{\partial V}{\partial t} < 0 \text{ in } S_1 \quad (18)$$

On the other hand, according to Lemma 1, $\nabla V^T(t,z)z$ is positive-definite. Without loss of generality, assume that

$$\nabla V^T(t,z)z \geq V_1(z) \quad (19)$$

Where $V_1(z)$ is positive definite. Substitution of (19) in equation (18) infers that

$$V_1(z)\|Tz\|^{2k}\sin(\frac{1}{\|Tz\|})^{2m+1} + \frac{\partial V}{\partial t} < 0 \text{ in } S_1 \quad (20)$$

This implies that

$$V(t,z) < -V_1(z)\|Tz\|^{2k}\sin\left(\frac{1}{\|Tz\|}\right)^{2m+1} t + V(0,z) \text{ in } S_1 \quad (21)$$

Since $S_1$ is bounded and the functions $V_1(z)\|Tz\|^{2k}\sin\left(\frac{1}{\|Tz\|}\right)^{2m+1}$ and $V(0,z)$ are continuous in $S_1$, let

$$\varepsilon_1 = \inf_{S_1} V_1(z)\|Tz\|^{2k}\sin\left(\frac{1}{\|Tz\|}\right)^{2m+1} \quad (22)$$

$$\varepsilon_2 = \sup_{S_1} V(0,z) \quad (23)$$

Then the inequality in (21) can be written follows

$$V(t,z) < -\varepsilon_1 t + \varepsilon_2 \text{ for all } t > 0 \quad (24)$$

Now, to prove that there are no convex Lyapunov functions in the form of $V(t,z)$, choose $t > \frac{\varepsilon_2}{\varepsilon_1}$. This implies that $V(t,z) < 0$, which is a contradiction because $V(t,z) > 0$ for all $z \neq 0$. With a similar reasoning, it is easy to show that there are no convex Lyapunov functions in the form $V(z)$ to establish stability.

**Theorem 2** There exist some nonlinear autonomous systems that despite stability do not admit smooth Lyapunov functions.

**Proof.** Let $f(.)$, in system (1) be defined by

$$f(x)=\begin{cases} x_2+x_1(x_1^2+x_2^2)^2\ \sin^2(\frac{1}{\sqrt{x_1^2+x_2^2}}) \\ -x_1+x_2(x_1^2+x_2^2)^2\ \sin^2(\frac{1}{\sqrt{x_1^2+x_2^2}}) \end{cases} \quad (25)$$

This system is stable in the sense of Lyapunov; however, smooth Lyapunov functions fail to establish stability.

In order to prove stability, consider $V(x)=x_1^2+x_2^2$, the time derivative of this function along the trajectories yields

$$\dot{V}=2(x_1^2+x_2^2)^3 sin^2(\frac{1}{\sqrt{x_1^2+x_2^2}}) \quad (26)$$

It is clear that the origin is surrounded by a countable set of limit cycles and all of the limit cycles are semi-stable. To ensure that $\| x \| \leq \varepsilon$, it is sufficient to choose $\delta \leq \frac{1}{n\pi}$ with large enough values of *n*.

For the sake of contradiction, suppose that there exists a smooth Lyapunov function in the form of $V(t,x)$ which satisfies the Lyapunov's theorem. According to (7),

$$V(t,x(t)) \leq V(t_0,x_0) \quad (27)$$

In order to complete the proof, it is sufficient to determine and compare the values of Lyapunov function on the limit cycles.

It is noticeable that all trajectories starting from the inside of a limit cycle return to the same cycle whereas the outer trajectories approach to the next one. In fact, if the system starts from the outside of $r=\sqrt{x_1^2+x_2^2}=\frac{1}{n\pi}$, it eventually converges to $r=\frac{1}{(n-1)\pi}$, thereby causing the value of Lyapunov function on the surface $r=\frac{1}{(n-1)\pi}$ to be less or equal to the value of Lyapunov function on the surface $r=\frac{1}{n\pi}$. This follows from the fact that by starting (25) from the outside of $\frac{1}{n\pi}$, the system remains bounded. Since $V(t,x(t))$ is a decreasing continuous function, it has a limit *c* as $t \to \infty$. In other words, the value of $V(t,x(t))$ on the surface of limit cycles is constant and $V(t,x_n(t)) \leq V(t_0,x_{n-1}(t_0))$ where $r_n=\|x_n\| =\frac{1}{n^2\pi^2}$ and $r_{n-1}=\|x_{n-1}\| =\frac{1}{(n-1)^2\pi^2}$. Consider $a_n$ as a sequence defined by

$$a_n=V(t,r_n) \text{ where } r_n=\frac{1}{n^2\pi^2} \quad (28)$$

In other words, $a_n$ is a sequence for which its value is computed on the surface of limit cycles.

Let $\gamma_1=\sup V(t,x) \leq \sup V_2(x)$, it is clear that the regions described by $r_n \leq \frac{1}{n\pi}$ are bounded and $V_2(x)$ is continuous; consequently, $\gamma_1$ must be bounded. This implies that $a_n$ is a bounded sequence.

Due to the fact that the value of Lyapunov function on the surface $r_{n-1}=\frac{1}{(n-1)\pi}$ must be less or equal to the value of Lyapunov function on the surface $r_n=\frac{1}{n\pi}$, $a_n$ is an increasing sequence. This means that

$$a_1 \leq a_2 \ldots . \leq a_{n-1} \leq a_n \quad (29)$$

Because of the fact that $a_n$ is a bounded and increasing sequence, $\lim_{n\to\infty} a_n$exists. Assuming $n \to \infty$ implies that $a_n \to 0$ because $x_n \to 0$.

According to (29), $a_1 \leq a_2 \ldots . \leq a_{n-1} \leq 0$ and this yields that $a_1 \leq 0$, which contradicts the fact that $V(t,x_1)=a_1$ must be positive for all $x \neq 0$. This shows that there are no smooth Lyapunov functions in the form of $V(t,x)$ to infer stability of (25) .

It is worth noting that for the system (25) , the results of Theorem 2 do not contradict with CLT, because they guarantee non-smooth Lyapunov functions in general. For more explanations, please see [21],[22]. Although there are no smooth Lyapunov functions in the form of $V(x)$ or $V(t,x)$ for (25), there might exist some lower semi-continuous Lyapunov functions according to [23]. In addition, Theorem 2 confirms the results in [24] through presenting some examples to show that the existence of a continuous Lyapunov function for (1) does not infer the existence of a locally Lipschitz Lyapunov function. Also, it shows that the existence of a Lipschitz Lyapunov function does not infer the existence of a continuously differentiable Lyapunov function in general.

The results of Theorem 2 can be extended to another class of nonlinear systems. Theorem 3 is devoted to this topic.

**Theorem 3** There exist some $n$ dimensional nonlinear autonomous systems that despite stability do not admit smooth Lyapunov functions.

**Proof**. For proving this theorem, consider the following nonlinear system which is described by:

$$\begin{aligned} \dot{x_1} &= x_2+x_1(x_1^2+x_2^2)^2\ \sin^2(\frac{1}{\sqrt{x_1^2+x_2^2}}), \\ \dot{x_2} &= -x_1+x_2(x_1^2+x_2^2)^2\ \sin^2(\frac{1}{\sqrt{x_1^2+x_2^2}}), \\ \dot{y} &= f(y) \end{aligned} \quad (30)$$

Where the nonlinear system $\dot{y}=f(y)$ is stable in the sense of Lyapunov.

The trajectories of this system i.e., $\eta=[x_1\ x_2\ y^T]^T$are stable in the sense of Lyapunov; however, the task of establishing stability through smooth Lyapunov function fails.

Suppose for the sake of contradiction that there exist a smooth Lyapunov function in the form of $V(t,x,y)$ for which it satisfies the condition of Lyapunov's theorem. Application of Lyapunov's theorem, infers that

$$V(t,x(t),y(t)) \le V(t_0,x_0,y_0) \quad (31)$$

The relation (31) must hold for all $\eta \neq 0$. Suppose $y = 0$, then (31) turns to

$$V(t,x(t),0) \le V(t_0,x_0,0) \quad (32)$$

This implies that for the nonlinear system discussed in Theorem 2, there exist a smooth Lyapunov function in the form of $V(t,x)$ which satisfies the conditions of Lyapunov's theorem and this is a contradiction because it is shown that there are no smooth Lyapunov functions to establish the stability of this system.

During the next theorem it is shown that Theorem 2 could be generalized for proving the existence of the smooth functions, used in LaSalle's invariance principle [25].

**Theorem 4** There exist some nonlinear autonomous systems that despite having an infinite number of limit cycles, do not admit continuous functions in the form $V(x)$ to establish LaSalle's invariance principle.

**Proof.** In the proof of Theorem 2, it is illustrated that there exist numerous limit cycles for (25).

Consider a continuous function $V(x)$ with a minimum at $x_p$, that satisfies LaSalle's invariance principle [25]. Then, $V$ must be decreasing in the region $\psi$ described by $V(x) \le c$. Since $\psi$ is compact, consider $a_1$ as follows:

$$a_1 = \min_{\psi} V(x) \quad (33)$$

Suppose that the function $V(x)$ has a global minimum point at $x_p$, let $a_1 = V(x_p)$, and define

$$W(x) = V(x) - a_1 \quad (34)$$

It is clear that $W(x) \ge 0$. In addition, $W(x)$ and $V(x)$ have the same trend of monotonicity. This means that for the nonlinear system (25) there exist a decreasing continuous positive function $W(x)$ which is not essentially positive definite. The remainder of proof could be followed from the proof of Theorem 2.

In the continuation of this paper, it is proved that there exist a similar criterion for non-autonomous dynamical systems.

## III. Existence of Smooth Lyapunov Functions for Nonautonomous Stable Systems

The motivation of this section is to show that the results of Theorem 2 can be generalized for non-autonomous systems.

**Theorem 5** There exist some two dimensional nonlinear non-autonomous systems that despite stability do not admit smooth Lyapunov functions in the form of $V(x)$.

**Proof.** Let the nonlinear system (2) be defined by

$$f(t,x) = \begin{cases} \dfrac{f(t)x_1}{1+{x_1}^2} \\ \dfrac{f(t)x_2}{1+{x_2}^2} \end{cases} \quad (35)$$

Where $f(t) > 0$ and $\int_{t_0}^{\infty} f(\tau)d\tau = M_1 < \infty$. This system is stable but there are no continuous Lyapunov functions in the form of $V(x)$ in order to prove its stability.

Rewriting (35) implies that

$$\frac{dx_1}{x_1} = \frac{f(t)dt}{1+{x_1}^2} \Rightarrow \int_{x_1(0)}^{x_1(t)} \frac{dx_1}{x_1} = \int_{t_0}^{t} \frac{f(\tau)d\tau}{1+{x_1}^2} \le \int_{t_0}^{t} f(\tau)d\tau = M_1 \Rightarrow \ln(|x_1(t)|) - \ln(|x_1(0)|) \le M_1 \Rightarrow \quad (36)$$

$$\ln\left(\frac{|x_1(t)|}{|x_1(0)|}\right) \le M_1 \Rightarrow \sup(|x_1(t)|) < |x_1(0)|e^{M_1} \quad (37)$$

With a similar reasoning, it is easy to see that $\sup(|x_2(t)|) < |x_2(0)|e^{M_1}$. Application of (36) and (37) leads to

$$\|x\|^2 \le x_1(0)^2 e^{2M_1} + x_2(0)^2 e^{2M_1} = \|x_0\|^2 e^{2M_1} \quad (38)$$

For any given $\varepsilon$, in order to satisfy (4), it is sufficient to choose $\delta \le \varepsilon e^{-M_1}$, because

$$\sup(\|x(t)\|) \le \|x_0\| \; e^{M_1} \Rightarrow \sup(\|x(t)\|) \le \varepsilon e^{-M_1} e^{M_1} = \varepsilon \Rightarrow \|x(t)\| \le \varepsilon \quad (39)$$

Equation (39) infers that, the system (35) is stable in the sense of Lyapunov. Due to the fact that $\delta$ does not depend on $t_0$ explicitly, (35) is uniformly stable (please see equation (5)).

To prove that there are no continuous Lyapunov functions to establish stability, it is sufficient to rewrite (35) in the form of

$$\left(\frac{1}{x_1} + x_1\right) dx_1 = f(t)dt \Rightarrow \ln(|x_1(t)|) - \ln(|x_1(0)|) + \frac{x_1(t)^2}{2} - \frac{x_1(0)^2}{2} = \int_{t_0}^{t} f(\tau)d\tau. \quad (40)$$

If $x_1(0) > 0$, (40) can be written as follows

$$x_1(t)e^{\frac{x_1(t)^2}{2}} = x_1(0)e^{\frac{x_1(0)^2}{2}} e^{\int_{t_0}^{t} f(\tau)d\tau} \quad (41)$$

Suppose $\lim_{t\to\infty} x_1(t) = y_1$, this ensures that

$$y_1 e^{\frac{{y_1}^2}{2}} = x_1(0)e^{\frac{x_1(0)^2}{2}} e^{M_1} \quad (42)$$

Equation (42) implies that $y_1$ is a function of $x_1(0)$. In addition, since $y_1$ is an invertible function; for any final state $y_1$ there exist an initial condition $x_1(0)$ that satisfies (42). In general, for any final state $y_1(n-1)$ there exist the initial condition $y_1(n)$ such that it satisfies (42). Similar reasoning could be applied to derive (42) for $x_2$.

For the sake of contradiction, suppose that there exist a smooth Lyapunov function which satisfies the condition of Lyapunov's theorem, then a ,mccording to Lyapunov's theorem, there must

exist a decreasing positive definite function in the region $D$. Consider $\bar{x} = [x_1\ x_2]^T \epsilon D$ where $x_i > 0$ . According to previous explanations, there exist the final state $y_1 = \begin{pmatrix} y_1(1) \\ y_2(1) \end{pmatrix}$ which satisfies (42). In general, for any final state $y_{n-1}$ there exists an initial condition $y_n$ that satisfies (42). Due to the fact that $V(x)$ is a decreasing function $V(y_{n-1}) \leq V(y_n)$ . This relation says that

$$V(y_1) \leq V(y_2) \ldots \leq V(y_{n-1}) \leq V(y_n) \quad (43)$$

Let $\lim_{n\to\infty} y_1(n) = L_1$, according to (42),

$$L_1 e^{\frac{L_1^2}{2}} = L_1 e^{\frac{L_1^2}{2}} e^{M_1} \quad (44)$$

Equation (44) infers that $L_1 = 0$ . Due to the fact that $V(x)$ is continuous,

$$\lim_{n\to\infty} V(y_n) = V\left(\lim_{n\to\infty} y_n\right) = V(0) = 0 \quad (45)$$

Rewriting (43) implies that

$$V(y_1) \leq V(y_2) \ldots \leq V(y_{n-1}) \leq 0 \quad (46)$$

According to (46), $V(y_1) \leq 0$, and this is a contradiction because $V(x)$ must be positive for all $x \neq 0$.

## IV. SIMULATION RESULTS

In this section, we present some results to demonstrate the effectiveness of the proposed theorems. In fact, some nonlinear systems are investigated, all of them being stable in the sense of Lyapunov, that do not admit smooth Lyapunov functions.

**Example 1** Consider the nonlinear system (10), with $A = \begin{pmatrix} -4 & 17 \\ -1 & 4 \end{pmatrix}$. It is easy to see that the positive definite matrix $P = \begin{pmatrix} 1 & -4 \\ -4 & 17 \end{pmatrix}$ satisfies $A^T P + PA = 0$. The trajectories of this system for the initial value $(0.03,0)$ are illustrated in Figure 1.

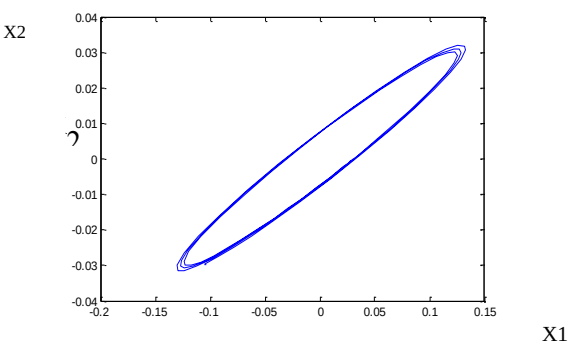


**Fig. 1:** The trajectories of (10) for initial value $(0.03,0)$.

Fig. **1** shows that the system is stable, although in Theorem 1 it was proved t hat it does not admit convex Lyapunov functions.

**Example 2.** Consider the nonlinear system (25) with the initial condition $(0, \frac{-1}{\pi} + 0.1)$ .

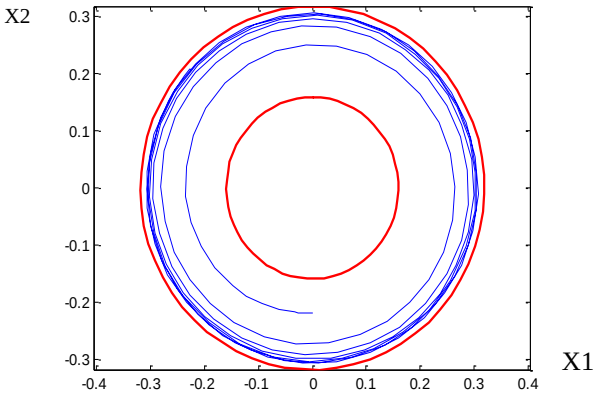


**Fig.2**: The trajectories of (25) for initial value $\left(0, \frac{-1}{\pi} + 0.1\right)$.

The simulation results confirm that all of the limit cycles for the system are semi-stable. As shown in Figure 2, the innermost curve is a limit cycle described by $\frac{1}{2\pi}$ and the outermost curve is a limit cycle described by $\frac{1}{\pi}$.

**Example 3.** The purpose of this example is to show the simulation results for the case of non-autonomous dynamical systems. Consider the nonlinear system (35) for $(t) = \frac{1}{t^4+1}$ . To satisfy (3) with $\varepsilon = 0.01$, choosing $\delta \leq 0.01 e^{-\frac{\pi}{2\sqrt{2}}} = 0.003$ confirms that $\|x\| \leq \varepsilon$. The results are depicted in Figure 3.

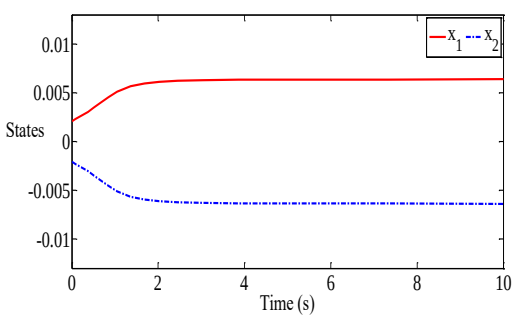


**Fig. 3:** The trajectories of (35) for the initial condition (0.0021,-0.0021)

## V. CONCLUSIONS

This paper studies the stable NDSs that do not admit smooth Lyapunov functions. It is proved that the existence of smooth Lyapunov functions is not necessary for the case that NDSs are stable in the sense of Lyapunov. In fact, the stability analysis of two different classes of nonlinear dynamical systems is discussed and it is shown that their stability cannot be

established by any convex differentiable Lyapunov functions or smooth Lyapunov functions.

As a first result, we discussed a NDS which is stable; however, investigating the stability of this system through convex Lyapunov functions is impossible. Subsequently, we introduced a class of NDS and proved that there are no smooth Lyapunov functions to establish the stability through classical Lyapunov method. In addition, a general class of NDSs were investigated and it is shown that they not admit continuous Lyapunov functions in the form $V(x)$ or $V(t,x)$. Furthermore, it is proved that LaSalle's invariance principle is unable to infer the convergence of trajectories towards the invariant sets. Finally, we present a stable non-autonomous dynamical system and prove that there are no smooth Lyapunov functions in the form of $V(x)$ to establish stability. From the second part of this paper, it can be inferred that existence of smooth Lyapunov function in the form of $V(x)$ or $V(t,x)$ is not necessary for stable equilibrium points and third part states that there exist some non-autonomous systems with uniformly stable equilibrium point that don't admit continuous Lyapunov function in the form of $V(x)$.

## REFERENCES


[1] H. K. Khalil and J. Grizzle, "Nonlinear systems, vol. 3," *Prentice hall Upper Saddle River*, 2002.

[2] S. Jafari Fesharaki, F. Sheikholeslam, M. Kamali, and A. Talebi, "Tractable robust model predictive control with adaptive sliding mode for uncertain nonlinear systems," *International Journal of Systems Science*, vol. 51, no. 12, pp. 2204-2216, 2020.

[3] T. S. Gardner, C. R. Cantor, and J. J. Collins, "Construction of a genetic toggle switch in Escherichia coli," *Nature*, vol. 403, no. 6767, pp. 339-342, 2000.

[4] L. Li, H. Zhang, and Y. Wang, "Stabilization and optimal control of discrete-time systems with multiplicative noise and multiple input delays," *Systems & Control Letters*, vol. 147, p. 104833, 2021.

[5] Z. Shen, C. Li, H. Li, and Z. Cao, "Estimation of the domain of attraction for discrete-time linear impulsive control systems with input saturation," *Applied Mathematics and Computation*, vol. 362, p. 124502, 2019.

[6] X.-F. Wang, A. R. Teel, K.-Z. Liu, and X.-M. Sun, "Stability analysis of distributed convex optimization under persistent attacks: A hybrid systems approach," *Automatica*, vol. 111, p. 108607, 2020.

[7] J.J. E. Slotine and W. Li, *Applied nonlinear control* (no. 1). Prentice hall Englewood Cliffs, NJ, 1991.

[8] A. I. Doban and M. Lazar, "Computation of Lyapunov functions for nonlinear differential equations via a Yoshizawa—type construction," *IFAC-PapersOnLine*, vol. 49, no. 18, pp. 29-34, 2016.

[9] A. I. Doban and M. Lazar, "Computation of Lyapunov functions for nonlinear differential equations via a Massera-type construction," *IEEE Transactions on Automatic Control*, vol. 63, no. 5, pp. 1259-1272, 2017.

[10] P. Giesl and S. Hafstein, "Review on computational methods for Lyapunov functions," *Discrete and Continuous Dynamical Systems-Series B*, vol. 20, no. 8, pp. 2291-2331, 2015.

[11] G. Bidari, N. Pariz, and A. Karimpour, "Sufficient conditions for stabilization of interval uncertain LTI switched systems with unstable subsystems," *International Journal of Industrial Electronics, Control and Optimization*, vol. 2, no. 1, pp. 1-6, 2019.

[12] M. Akbarian, N. Eghbal, and N. Pariz, "A Novel Method for Optimal Control of Piecewise Affine Systems Using Semi-Definite Programming," *International Journal of Industrial Electronics, Control and Optimization*, vol. 3, no. 1, pp. 59-68, 2020.

[13] S. S. S. Farahani and S. Fakhimi Derakhshan, "LMI-based congestion control algorithms for a delayed network," vol. 2, no. 2, pp. 91-98, 2019.

[14] K. Persidskii, "On a theorem of Liapunov," in *CR (Dokl.) Acad. Sci. URSS*, 1937, vol. 14, pp. 541-543.

[15] C. M. Kellett, "Classical converse theorems in Lyapunov's second method," *arXiv preprint arXiv:1502.04809*, 2015.

[16] A. Bacciotti, L. Rosier, and Z. Lin, "Liapunov Functions and Stability in Control Theory. Lecture Notes in Control and Information Sciences 267," *Appl. Mech. Rev.*, vol. 55, no. 5, pp. B88-B89, 2002.

[17] J. Auslander and P. Seibert, "Prolongations and stability in dynamical systems," in *Annales de l'institut Fourier*, 1964, vol. 14, no. 2, pp. 237-267.

[18] A. A. Ahmadi, M. Krstic, and P. A. Parrilo, "A globally asymptotically stable polynomial vector field with no polynomial Lyapunov function," in *2011 50th IEEE Conference on Decision and Control and European Control Conference*, 2011, pp. 7579-7580: IEEE.

[19] A. A. Ahmadi and B. El Khadir, "A globally asymptotically stable polynomial vector field with rational coefficients and no local polynomial Lyapunov function," *Systems & Control Letters*, vol. 121, pp. 50-53, 2018.

[20] A. A. Ahmadi and B. El Khadir, "On algebraic proofs of stability for homogeneous vector fields," *IEEE Transactions on Automatic Control*, 2019.

[21] W. Hahn, *Stability of motion*. Springer, 1967.

[22] F. H. Clarke, Y. S. Ledyaev, R. J. Stern, and P. R. Wolenski, *Nonsmooth analysis and control theory*. Springer Science & Business Media, 2008.

[23] A. Bacciotti and L. Rosier, *Liapunov functions and stability in control theory*. Springer Science & Business Media, 2006.

[24] A. Bacciotti and L. Rosier, "Regularity of Liapunov functions for stable systems," *Systems & control letters*, vol. 41, no. 4, pp. 265-270, 2000.

[25] J. LaSalle, "Some extensions of Liapunov's second method," *IRE Transactions on circuit theory*, vol. 7, no. 4, pp. 520-527, 1960.


**Majid Akbarian** received the B.S. degree in Electrical Engineering from Hakim Sabzevari University, sabzevar, Iran, in 2013 and M.S. degree in Electrical Engineering from the Ferdowsi University of Mashhad, Mashhad, Iran in 2015, where he is currently pursuing Ph.D degree in Electrical Engineering.
His current research interests include optimal control, nonlinear control, stability, and dynamical systems.

**Naser Pariz** received the B.S. and M.Sc .degree in Electrical Engineering from Ferdowsi University of Mashhad, Iran, in 1988 and 1991 respectively. He received his Ph.D. from the Department of Electrical Engineering at Ferdowsi University of Mashhad in 2001. He is a Professor at Ferdowsi University. His research interests are nonlinear and control systems

International Journal of Industrial Electronics, Control and Optimization © 2021 IECO
Vol. 4, No.3, pp. 341-353, July (2021)

# Dynamic Stability Improvement of Power System with Simultaneous and Coordinated Control of DFIG and UPFC using LMI

Masoud Maleki Rizi[1], Saeed Abazari[2†], Nima Mahdian[3]

[1,2]Department of Engineering, University of Shahrekord, Shahrekord, Iran
[3] Shahid Rajaee Teacher training University, Tehran, Iran.

**ABSTRACT**

*This paper presents an enhancement of the dynamic stability of a power system equipped with both a unified power flow controller (UPFC) and a doubly-fed induction generator (DFIG) by using the LMI technique. We use all UPFC main basic PI controllers and its power oscillation damping (POD) supplementary controller. A more complete model of DFIG and both rotor-side converter (RSC) and grid-side converter (GSC) dynamics with their controllers are considered, too. These two devices controllers are simultaneously coordinated and optimized with compromising between their control variables parameters. The particle swarm optimization (PSO) algorithm is used to optimize the objective function based on eigenvalues and damping ratio to reach the best parameters and variables of controllers of both UPFC and DFIG. Linear matrix inequality (LMI) is applied to the whole system linearized model to reach optimally modified eigenvalues. Within the steady state and dynamic study, we consider practical line thermal capacity and UPFC power rating, too. Simulation results in 39-bus 10-machine New-England power systems illustrate the capability of the applied method. The results demonstrate that coordinated control of these two devices besides using LMI results in more damping of system modes oscillations and more stability in the power* system.

**Article Info**

***Keywords:***
Dynamic stability, Doubly-fed induction generator, Linear Matrix Inequality, Optimization, Unified power flow controller.

*Article History:*
**Received** 2021-02-12
**Accepted** 2021-06-01

## I. INTRODUCTION

The unified power flow controller (UPFC) is an effective flexible alternating current transmission system (FACTS) device that helps overcome some of existing power system operation limitations. It is the most important and comprehensive device that helps stability improvement in power systems. UPFC is equipped with a power oscillation damping (POD), and the damping effect of this POD is better than the power system stabilizer (PSS).

On the other hand, wind energy conversion systems (WECS) are growing fast due to environmental issues and the limitations of natural resources. The application of wind energy to produce electrical energy using doubly-fed induction generators (DFIGs) is growing in power systems because DFIGs allow a larger portion of the wind energy to be absorbed. The interaction of DFIG controllers will occur with both electrical and mechanical system modes leading to electrical and mechanical oscillations [1]. Then, the effect of these devices on power system oscillations and stability is an important issue.

The stability enhancement of a three-machine system by using the coordinated application of the UPFC and the PSS designed employing the Firefly algorithm was already

[†]**Corresponding Author:** abazari-s@eng.sku.ac.ir
Tel: +98-9133144539, Faculty of Electrical Engineering, Shahrekord University, Shahrekord, Iran.

compared with the genetic search algorithm approach [2]. To UPFC POD controller design in MMPS, in three-machine system, with selecting damping ratio based objective function LQR (Linear Quadratic Regulation) have used under different loading condition and better result demonstrated [3]. The improved grey wolf optimizer (IGWO) was compared with differential evolution (DE) and particle swarm optimization(PSO) to optimize UPFC POD controller with integral of time-weighted absolute error (ITAE) criteria too and the results demonstrated the stability enhancement of MMPS in the three-machine system while comparing using either $m_B$ or $\delta_E$ [4].

On the other hand, the effect of DFIG controllers and system parameters in linear modal analysis of DFIG torsional interaction was investigated and the results showed that the DFIG controllers should be adjusted, otherwise, an interaction may occur and the system oscillations may increase, which may even make the system unstable. The damping mechanisms of power systems were analytically compared with induction generator-based wind power generation by Bu in a multi-machine power system in which a model with rotor-side converter (RSC) dynamics and a model without RSC dynamics with fixed rotor speed and with offset rotor voltage only and with constant rotor voltage were investigated [5].

Today, power systems may consist of both of these two important devices because of their operational, economic, and environmental advantages. Beside these advantages, they have interactions and influence the stability of power systems. So, many studies have recently focused on the effects of each of these two devices on the other device or the overall power system.

UPFC can be used to improve the overall performance of WECS through the development of an appropriate control algorithm. The application of a UPFC control algorithm is also investigated in one research to overcome some problems associated with the internal faults associated with WECS [6]. Based on power control and speed error minimization objectives, wind turbines were utilized in a research study,and to improve reactive and real power, IEEE-9 and 14 bus systems were investigated by installing UPFC in the transmission line. [7]. The simulation results show that UPFC can improve the low voltage ride-through (LVRT) of DFIG-based WECS, reduce machine oscillations, and finally maintain wind turbine connection to the grid during certain levels of voltage fluctuations on the grid side and fault conditions [8]-[10]. UPFC can noticeably improve the fault ride-through (FRT) capability of WECS, so it can support the grid during fault conditions [11]. UPFC has been used in a DFIG-based wind turbine system to provide dynamic reactive power support at the PCC in the occurrence of three-phase fault conditions [12]. In a transient stability study, a control proposed for the admittance model of the UPFC was validated in a DFIG wind farm penetrated power system. The power output of the DFIG was stabilized, which helped recover rotor angular deviation of the respective generators, which significantly stabilized the network [13]. Performance of wind power and UPFC to increase the fault critical clearing time of power system using MATLAB/SIMULINK software simulated the IEEE 3 machines 9 buses verified and showed that the better result will be obtained while these two devices are in the optimum location [14].

Linear matrix inequality (LMI)-based techniques have already been used for the stability of power systems that are equipped with UPFC to have optimal control while the LMI approach is used for optimal pole placement [15]. This approach has been used in the robust adaptive model predictive control of DFIG [16]. But, it has not been employed in multi- machine power systems consisting of both of these two devices. Then, we applied LMI in order to optimize pole placement more optimally and improve the robustness of this large power system linear system model.

Then, it is important to study and improve this stability in the systems in which both UPFC and DFIG are installed. Here, we have studied more complete small signal models of UPFC and DFIG to investigate the damping effects of UPFC and DFIG in multi-machine power systems considering all dynamic states of both of them in comparison with previous studies. We have considered practical constraints too while using PSO (its detail algorithm can be found in [17]). To optimize the control parameters of each of them, LMI was applied to the system to have optimal eigenvalues, too.

The main contributions of the study are the application of all classic controllers of UPFC together, the application of practical constraints of line and UPFC capacities, the use of DFIG complete electrical model and all of its converters controllers, the use of PSO to optimize simultaneously and coordinated UPFC and DFIG controllers, the use of LMI approach to more optimization in eigenvalues of the whole system, and increasing the whole control system robustness.

The following sections introduce UPFC and its small signal model and control aspects. Then, DFIG small signal modeling and control are reviewed. Then, the combined power system model with UPFC installed and DFIG connected models are presented. PSO algorithm and LMI technique, which have been used, are briefly described too. In the last section, the simulation results of these two devices that are applied to dynamic stability individually and together are demonstrated and compared.

## II. UNIFIED POWER FLOW CONTROLLER

As is seen in Figure 1, UPFC consists of two converters coupled through a common DC link. Eq. (1) expresses the UPFC terminals voltages.

$$\bar{V}_E = \frac{m_E V dc}{2} e^{j\delta_E}, \bar{V}_B = \frac{m_B V dc}{2} e^{j\delta_B} \quad (1)$$

Where

$m_B$ is the pulse width modulation index of the series(boosting) inverter, $m_E$ is the pulse width modulation index of the shunt (exciting) inverter, $\delta_B$ is the phase angle of the series injected voltage, and $\delta_E$ is the voltage phase angle of the shunt inverter.

The series branch of the UPFC injects an AC voltage with controllable magnitude and phase angle at the power frequency. Then, it can exchange real and reactive power with the installed line. The shunt converter is primarily used to provide active power demand of the series converter through a common DC link and can exchange reactive power to adjust the voltage of the bus, which is connected. So, due to these capabilities, UPFC is an excellent choice for damping power system oscillations. This damping can be obtained by regulating the abovementioned controllable parameters by controlling the decoupled variables of the UPFC by the following four controllers:

$$\delta_B = \left(\frac{1}{1+T_{\delta B}S}\right)\left(K_{Pp} + \frac{K_{Pi}}{s}\right)\left(P_{Ref} - P\right) \quad (2)$$

$$m_B = \left(\frac{1}{1+T_{mB}S}\right)\left(K_{Qp} + \frac{K_{Qi}}{s}\right)\left(Q_{Ref} - Q\right) \quad (3)$$

$$m_E = \left(\frac{1}{1+T_{mE}S}\right)\left(K_{Vp} + \frac{K_{Vi}}{s}\right)\left(V_{Ref} - V\right) \quad (4)$$

$$\delta_E = \left(\frac{1}{1+T_{\delta E}S}\right)\left(K_{DCp} + \frac{K_{DCi}}{s}\right)\left(V_{DC,Ref} - V_{DC}\right) \quad (5)$$

Where

$T_x$ is delay time constants, and $K_{xp}$ and $K_{xi}$ are PI controllers proportional and integral gains, respectively, $P, Q, V$ and $V_{DC}$ are active and reactive power flow through line and bus voltage to which UPFC is connected and UPFC dc link voltage, respectively.

Comprehensive models of UPFC for steady-state, transient stability and dynamic stability studies and also a dynamic model of the system installed with UPFC are presented in [18] and [19]. A unified model of a multi-machine power system and developed UPFC models is proposed that has been linearized and incorporated into the Heffron-Phillips model [19]. The conflict between UPFC multiple control functions and their interactions was investigated and it was shown that the application of all four control functions may sometimes decrease the accuracy of the results [20]. We used all of these four controllers simultaneously and made a compromise between four control variables. Due to technical and economical restrictions, the rating of the UPFC power is limited and this leads to applying limits of its real and reactive power by additional limiter blocks and then modifying the UPFC related parameters in each of iteration.

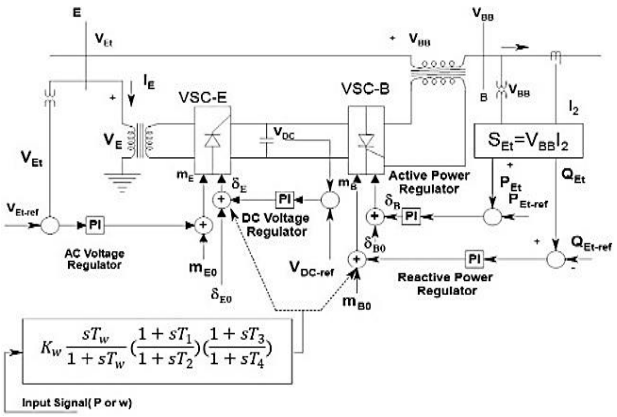


**Fig. 1.** The UPFC power and control flow diagram

A supplementary controller, known as POD, is designed in UPFC to enhance the transient stability of the entire electric power system. Inverse interaction between PSS and series part control is compensated by providing a UPFC-based damping controller [21]. As shown in Figure 1, POD controllers have a lead-lag controller structure transfer function consisting of gain, a washout function, and two lead-lag blocks, which should be adjusted. Fixed parameter classical controller is not suitable for the UPFC damping control design. Then, a flexible controller should be developed. Several approaches have been proposed for it, such as root locus and sensitivity analysis, pole placement, and robust control. The conventional techniques require heavy computation and have slow convergence. The search methods may also be trapped in a local minimum and the solution obtained may not be the finest. In addition, it is necessary that the designed controller provide some robustness to the variations of parameters, conditions, and configurations. Also, the controller parameters, which have stabilized the system in a certain operating condition, may no longer have acceptable results in case of large disturbances [22].

To improve its dynamic performance, its parameters can be optimized by using an optimization problem. Based on eigenvalues, a multi-objective function related to the damping factor and damping ratio is considered as:

$$J = \sum_{j=1}^{NP}\sum_{\sigma_i \geq \sigma_0}\left(\sigma_0 - \sigma_{ij}\right)^2 + \alpha\sum_{j=1}^{NP}\sum_{\zeta_i \geq \zeta_0}\left(\zeta_0 - \zeta_{ij}\right)^2$$

$$f(x) = \min J \quad (6)$$

$$K^{\min} \leq K \leq K^{\max}$$

$$T_1^{\min} \leq T_1 \leq T_1^{\max}$$

$$T_2^{\min} \leq T_2 \leq T_2^{\max}$$

$$T_3^{\min} \leq T_3 \leq T_3^{\max}$$

$$T_4^{\min} \leq T_4 \leq T_4^{\max}$$

Where $\sigma_{ij}$ is the real parts of system eigenvalues, $\sigma_0$ is

desired real part of eigenvalue, $\zeta_{ij}$ is the damping ratios of system variables, and $\zeta_0$ is the desired damping ratio. This optimization problem can use a numerical technique, such as PSO.

## III. An Introduction to DFIG Study

In DFIG, two converters are included in the rotor circuit. The power electronic converters ratio is a fraction of the total power. Therefore, the losses in the power electronic converter can be reduced compared to a system where the converter has to handle the entire power, and the system cost is lower due to the partially rated power electronics. DFIG operates in both sub-synchronous and super-synchronous modes with a rotor speed range around the synchronous speed. For variable-speed systems, DFIG offers adequate performance [23]. Figure 2 shows a DFIG-based wind farm connected to a power system.

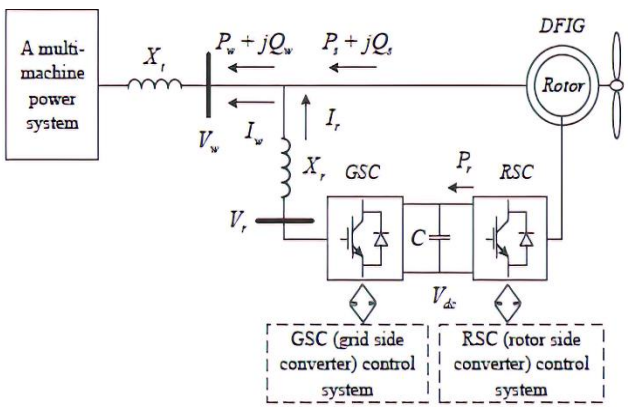


**Fig. 2**. DFIG connected to a multi-machine power system

In [24], different state space models of DFIG for power system study have been compared. The modeling details of the turbine, drive train**,** pitch controller, induction machine, and the controllers of both RSC and the grid-side converter (GSC) of DFIG have been introduced.

DFIG state equations in dynamic stability studies are mentioned below.

Eq. (7)-(10) are related to two-mass model turbine drive dynamic, Eq. (11)-(13) are for the three-degree model of the machine, Eq. (14)-(17) are related to for GSC controller, and Eq. (18)-(21) are for RSC controller as follows:

$$2H_t \frac{d\omega_t}{dt} = T_m - T_{sh} \tag{7}$$

$$2H_g \frac{d\omega_g}{dt} = T_{sh} - T_e \tag{8}$$

$$\frac{1}{\omega_b}\frac{d\theta_{tw}}{dt} = \omega_t - \omega_g \tag{9}$$

$$T_{sh} = D\frac{d\theta_{tw}}{dt} + K\theta_{tw} \tag{10}$$

$$T_0' \frac{dE_{qD}'}{dt} = -\left(E_{qD}' + (X_s - X_s')I_{ds}\right) + T_0'\left(\omega_s \frac{X_m}{X_r} V_{dr} - (\omega_s - \omega_r)E_{dD}'\right) \tag{11}$$

$$T_0' \frac{dE_{dD}'}{dt} = -\left(E_{dD}' + (X_s - X_s')I_{qs}\right) + T_0'\left(\omega_s \frac{X_m}{X_r} V_{qr} - (\omega_s - \omega_r)E_{qD}'\right) \tag{12}$$

$$2\frac{H_D}{\omega_s}\frac{d\omega_r}{dt} = T_m - E_{dD}' I_{ds} - E_{qD}' I_{qs} \tag{13}$$

*While:*

$$V_{qs} = -R_s I_{qs} - X_s' I_{ds} + E_{qD}'$$

$$V_{ds} = -R_s I_{ds} + X_s' I_{qs} + E_{dD}'$$

$$I_{dr} = \frac{E_{qD}'}{X_m} + \frac{X_m}{X_r} I_{ds} \quad , \quad I_{qr} = -\frac{E_{dD}'}{X_m} + \frac{X_m}{X_r} I_{qs}$$

$$T_0' = \frac{X_r}{\omega_s R_r} \quad , \quad X_s' = X_s - \frac{X_m^2}{X_r}$$

$$E_{qD}' = \frac{X_m}{X_r}\varphi_{qr} \quad , \quad E_{dD}' = -\frac{X_m}{X_r}\varphi_{qr}$$

Considering RSC and GSC dynamic via defining auxiliary variables, $x_1$ to $x_8$, which are displayed in Figure 3, are as follows:

$$dx_1 = \frac{1}{K_{I1}}(\omega_{ref} - \omega_r) \tag{14}$$

$$dx_2 = \frac{1}{K_{I2}}(i_{qr} - (-x_1 + K_{P1}((\omega_{ref} - \omega_r)))) \tag{15}$$

$$dx_3 = \frac{1}{K_{I3}}(Q_{sref} - Q_s) \tag{16}$$

$$dx_4 = \frac{1}{K_{I4}}(i_{dr} - (-x_3 + K_{P3}((Q_{sref} - Q_s)))) \tag{17}$$

$$dx_5 = \frac{1}{K_{I5}}(V_{DCref} - V_{DC}) \tag{18}$$

$$dx_6 = \frac{1}{K_{I6}}(i_{qg} - (-x_5 + K_{P5}((V_{DCref} - V_{DC})))) \tag{19}$$

$$dx_7 = \frac{1}{K_{I7}}(V_s - V_{sref}) \tag{20}$$

$$dx_8 = \frac{1}{K_{I8}}(i_{dg} - (-x_7 + K_{P7}((V_s - V_{sref})))) \tag{21}$$

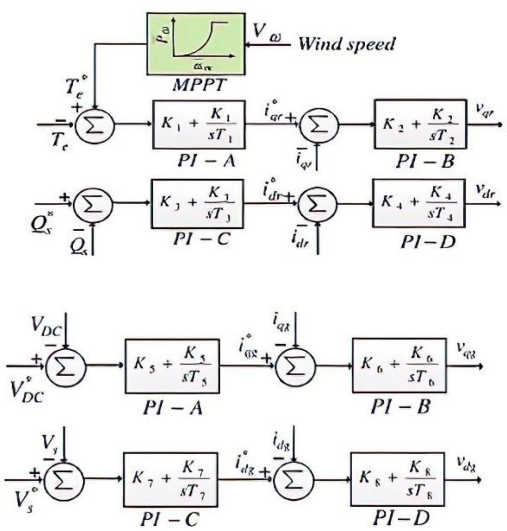


**Fig. 3.** DFIG RSC and GCS PI controllers

The equation, which represents DC link capacitor between two converters dynamic, is as follows:

$$C_D V_{DC} \frac{dV_{DC}}{dt} = \left(v_{dr} i_{dr} + v_{qr} i_{qr}\right) - \left(v_{dg} i_{dg} + v_{qg} i_{qg}\right) \quad (22)$$

## IV. Modeling Power System with UPFC Installed

The performance analysis of UPFC requires its steady-state and dynamic models. Figure 4 shows UPFC in a multi-machine power system:

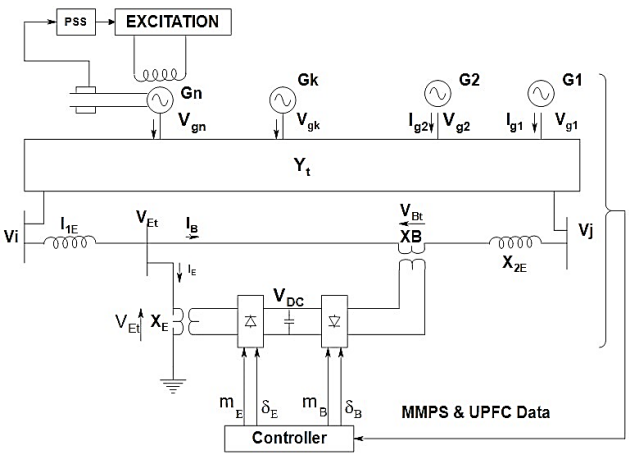


**Fig. 4.** UPFC in the multi-machine power system

With reducing the bus admittance matrices to generator internal buses and UPFC terminal buses, the following equation can be written:

$$\overline{YE} = \bar{I}\ ,\ \overline{Y} = \begin{bmatrix} Y_{GG} & Y_{GU} \\ Y_{UG} & Y_{UU} \end{bmatrix},\ \overline{E} = \begin{bmatrix} \overline{E}_G \\ \overline{V}_U \end{bmatrix},\ \bar{I} = \begin{bmatrix} \bar{I}_G \\ \bar{I}_U \end{bmatrix} \quad (23)$$

While $Y_{GG}$ is the reduced admittance matrices connecting the generator current injection to the internal generator voltages. $Y_{GU}$ is the admittance matric component, which gives the generator currents due to the voltages at UPFC buses, $Y_{UG}$ is the admittance matrices component, which gives UPFC currents in terms of the generator internal voltages, $Y_{UU}$ is the admittance matrices connecting UPFC currents to the voltages at UPFC buses, $\overline{E}_G$ is the vector of generator internal bus voltages, $\overline{V}_U$ is the vector of UPFC ac bus voltages, $\bar{I}_G$ is the vector of generators' currents injection, $\bar{I}_U$ is the vector of UPFC currents injected to the power network. Then these parameters values will incorporate in deriving matrices equation of multi machine power system with UPFC installed which is essential in dynamic stability analysis.

For the small signal stability studies of the power system, the linear model of Heffron-Phillips is used, which provides reliable and enough accurate results [25]. The nonlinear dynamic model of the system installed with the UPFC equations is as follows:

$$\dot{\delta} = \omega_b(\omega - 1) \quad (24)$$

$$\dot{\omega} = M^{-1}\left(T_m - T_e - D(\omega - 1)\right) \quad (25)$$

$$\dot{E}'_q = T'_{do}\left(E_{fd} - E'_q + (X_d - X'_d)I_d\right) \quad (26)$$

$$\dot{E}_{fd} = \left(K_A\left(V_{Ref} - V_t\right) - E_{fd}\right)/T_A \quad (27)$$

$$\dot{V}_{DC} = \frac{3m_E}{4C_{dc}}\left(sin\delta_E I_{Ed} + cos\delta_E I_{Eq}\right) + \frac{3m_B}{4C_{dc}}\left(sin\delta_B I_{Bd} + cos\delta_B I_{Bq}\right) \quad (28)$$

These equations can be re-written and after linearization in following matrix format and detail value calculation of K coefficients firstly introduced in [18]:

$$\begin{bmatrix} \Delta\dot{\delta} \\ \Delta\dot{\omega} \\ \Delta\dot{E}'_q \\ \Delta\dot{E}_{fd} \\ \Delta\dot{V}_{DC} \end{bmatrix} = \begin{bmatrix} 0 & \omega_0 I & 0 & 0 & 0 \\ -M^{-1}K_1 & -M^{-1}D & -M^{-1}K_2 & 0 & -M^{-1}K_{pd} \\ -T_{do}^{-1}K_4 & 0 & -T_{do}^{-1}K_3 & T_{do}^{-1} & -T_{do}^{-1}K_{qd} \\ -T_A^{-1}K_5K_A & 0 & -T_A^{-1}K_6K_A & -T_A^{-1} & -T_A^{-1}K_6K_{vd} \\ K_7 & 0 & K_8 & 0 & -K_9 \end{bmatrix} \begin{bmatrix} \Delta\delta \\ \Delta\omega \\ \Delta E'_q \\ \Delta E_{fd} \\ \Delta V_{DC} \end{bmatrix}$$

$$+ \begin{bmatrix} 0 & 0 & 0 & 0 \\ -M^{-1}K_{pe} & -M^{-1}K_{pde} & -M^{-1}K_{pb} & -M^{-1}K_{pdb} \\ -T_{do}^{-1}K_{qe} & -T_{do}^{-1}K_{qde} & -T_{do}^{-1}K_{qb} & -T_{do}^{-1}K_{qdb} \\ -T_A^{-1}K_AK_5 & -T_A^{-1}K_AK_{vde} & -T_A^{-1}K_AK_{vb} & -T_A^{-1}K_AK_{vdb} \\ K_{ce} & K_{cde} & K_{cb} & K_{cdb} \end{bmatrix} \begin{bmatrix} \Delta m_E \\ \Delta\delta_E \\ \Delta m_B \\ \Delta\delta_B \end{bmatrix} \quad (29)$$

As we can see, the above equation is the standard form of the linear system as below:

$$\Delta\dot{X}_g = A_g\Delta X_g + B_g\Delta U \quad (30)$$

This matrix equation is suitable for classical linear control and numerical solving of the system equations as well as analysis such as eigenvalues-related techniques.

## V. Modelling of DFIG Connected to Power System

Recently researchers have shown that in a modal study if wind farm is replaced by an equal dynamic DFIG, it will have acceptable result [26]. A comprehensive model of DFIG connected to a power system is similar to Wang' [19] idea that was conducted before FACTS devices were developed [27]. Multi-machine power system linearized model considering DFIG connections (e.g., Figure 2) may be extracted as follows:

$$\frac{d}{dt}\begin{bmatrix} \Delta\delta \\ \Delta\omega \\ \Delta E'_q \\ \Delta E_{fd} \end{bmatrix} = \begin{bmatrix} 0 & \omega_0 I & 0 & 0 \\ -M^{-1}K_1 & -M^{-1}D & -M^{-1}K_2 & 0 \\ -T_{do}^{-1}K_4 & 0 & -T_{do}^{-1}K_3 & T_{do}^{-1} \\ -T_A^{-1}K_5K_A & 0 & -T_A^{-1}K_6K_A & -T_A^{-1} \end{bmatrix} \begin{bmatrix} \Delta\delta \\ \Delta\omega \\ \Delta E'_q \\ \Delta E_{fd} \end{bmatrix} +$$

$$\begin{bmatrix} 0 \\ -M^{-1}k_{PP} \\ -T_{do}^{-1}k_{EP} \\ T_A^{-1}K_Ak_{VP} \end{bmatrix}\Delta P_W + \begin{bmatrix} 0 \\ -M^{-1}k_{PQ} \\ -T_{do}^{-1}k_{EQ} \\ T_A^{-1}K_Ak_{VQ} \end{bmatrix}\Delta Q_W \quad (31)$$

The state vector of the whole grid, $\boldsymbol{X_g}$, in the matrix format while DFIG is connected is as follows:

$$\frac{d}{dt}\Delta \boldsymbol{X}_g = \boldsymbol{A}_g \Delta \boldsymbol{X}_g + \boldsymbol{b}_P \Delta P_w + \boldsymbol{b}_Q \Delta Q_w \quad (32)$$

Where $V_W$ is the bus by which DFIG is connected to power system voltage amplitude that can be represented as below:

$$\Delta V_W = C_g \Delta X_g + d_{g1}\Delta P_W + d_{g2}\Delta Q_W \quad (33)$$

DFIG linearized model can be used in the following format:

$$\frac{d}{dt}\Delta \Psi_{wsd} = K_{wd1}\Delta \Psi_{wsd} + K_{wq1}\Delta \Psi_{wsq} + \cdots + K_{1V}V_w \quad (34)$$

$$\frac{d}{dt}\Delta \Psi_{wsq} = K_{wd2}\Delta \Psi_{wsd} + K_{wq2}\Delta \Psi_{wsq} + \cdots + K_{2V}V_w \quad (35)$$

For any other selected state variable of DFIG:

$$\frac{d}{dt}\Delta x_j = K_{wdj}\Delta \Psi_{wsd} + K_{wqj}\Delta \Psi_{wsq} + \cdots + K_{jV}V_w \quad (36)$$

In matrix format:

$$\frac{d}{dt}\Delta \boldsymbol{X}_w = \boldsymbol{A}_w(p)\Delta \boldsymbol{X}_w + \boldsymbol{b}_w(p)\Delta V_w \quad (37)$$

Output power of DFIG in linear form can be shown as:

$$\begin{bmatrix}\Delta P_w \\ \Delta Q_w\end{bmatrix} = \begin{bmatrix}\boldsymbol{c}_{Pw}^T \\ \boldsymbol{c}_{Qw}^T\end{bmatrix}\Delta \boldsymbol{X}_w + \begin{bmatrix}c_{PV} \\ c_{QV}\end{bmatrix}\Delta V_w \quad (38)$$

We can replace them in Heffron-Philips equations to form matrix format equations containing both power system and DFIG variables:

Here, we have used a more complete model of DFIG so that the state variable vector of DFIG is:

$$\Delta X_w = [\Delta \Psi_{wsd}\ \Delta \Psi_{wsq}\ \Delta \Psi_{wrd}\ \Delta \Psi_{wrq}\ \Delta \omega_{r1}\ \Delta \omega_{r2}\ \Delta \theta_{wr}\ \Delta x_{w1}\ \Delta x_{w2}\ \Delta x_{w3}\ \Delta x_{w4}\ \Delta I_{dcd}\ \Delta I_{dcq}\ \Delta V_{wdc} \Delta x_{w5}\ \Delta x_{w6}\ \Delta x_{w7}]^T \quad (39)$$

Where w index refers to wind (DFIG) parameters, s represents the stator, r is the rotor, d to d axis, q to q axis and dc to dc link. $\Delta x_{w1}$ to $\Delta x_{w7}$ are linearized auxiliary variables to consider RSC and GSC dynamics.

Combining Eq. (32), (33), and (38) will form a dynamic equation for both systems as follows:

$$\begin{bmatrix}\Delta \dot{X}_g \\ \Delta \dot{X}_w \\ \Delta \dot{X}_c\end{bmatrix} = A\begin{bmatrix}\Delta X_g \\ \Delta X_w \\ \Delta X_c\end{bmatrix} \quad (40)$$

Where $X_c$ is the state variables related to PIs of DFIG control system.

For the dynamic stability study of the whole system, we should combine Eq. (30) and (40) to reach Eq. (41), which explains multi-machine power system simultaneously contains UPFC and DFIG and we can use it to investigate small signal issues of the whole system.

$$\Delta \dot{X} = A\Delta X + B\Delta U \quad (41)$$

While:

$$\Delta X = \begin{bmatrix}\Delta X_g \\ \Delta X_W \\ \Delta X_c \\ \Delta V_{DC}\end{bmatrix} \quad (42)$$

Dimension of this state vector is *4n+1+17*. n is the number of synchronous generators, 1 state for UPFC and 17 state for DFIG while 7 of them are auxiliary to express PI controllers.

We use Eq. (41) to design control system and, if required, we can do compromising, co-ordination, and optimization using this last overall matrix linear equation.

## VI. PARTICLE SWARM OPTIMIZATION ALGORITHM

PSO is a population-based optimization technique to solve optimization problems with constraints. In the PSO system, multiple solutions are candidate and cooperate simultaneously. Each candidate, named a particle, flies in the problem search space looking to land on the optimal position. During the generations, particles adjust their own positions according to their own experience and the experience of particles located in the neighborhood. This algorithm attempts to balance exploitation and exploration by combining global and local search methods, and new velocity and position of each particle will be updated according to the following equations [17]:

$$V_i[k+1] = wV_i[k] + c_1 r_1(pbest_i[k] - X_i[k]) + c_2 r_2(gbest[k] - X_i[k])\ , i = 1,2, \ldots, \quad (42)$$

$$X_i[k+1] = X_i[k] + V_i[k+1] \quad (43)$$

where $N$ is the number of particles, $k$ is the current iteration, $w$ is an inertia weight, $r_1$ and $r_2$ are random variables between 0 and 1, $c_1$ and $c_2$ are acceleration coefficients, $V_i$ and $X_i$ are the velocity and position of the particle $i$, respectively, $pbest_i$ are the local best position of particle $i$, And $gbest_i$ is the global- best position of all particles.

In this study, PSO was used three times; (a) Optimizing J function mentioned above with PSO, the lead-lag controller parameters, $T_1$ to $T_4$, and wash-out gain K are adjusted while only UPFC have used in power system. (b); To optimize similar J function (based on Eigen values) to optimize the values of 7 PIs of RSC and GSC of DFIG while only DFIG is connected to the power system. (c) To optimize the same function for the whole system in order to optimize UPFC POD parameters and DFIG PIs parameters simultaneously.

## VII. AN INTRODUCTION TO LMI TECHNIQUE APPLICATION

LMIs are matrix inequalities that are linear or affine in a set of matrix variables. They are basically convex constraints, so many optimization problems with convex objective functions and LMI constraints can easily be solved efficiently. Many control problems can be formulated as LMI problems. An LMI has the following form:

$$F(x) = F_0 + \sum_{i=1}^{n} x_i F_i > 0 \quad (44)$$

where $x \in \mathcal{R}^m$ is the vector of decision variables and $F_0, F_1, \ldots, F_n$ are the constant symmetric real matrices, i.e.,

$F_i = F_i^T$ ,$i = 0, \ldots m$ . The inequality symbol in the equation means that $F(x)$ is positive definite, i.e., $u^T F(x)u > 0$ for all nonzero $u \in \mathcal{R}^n$ . This matrix inequality is linear in the variables $x_i$.

In the analysis of the state feedback controller, the objective is to determine a matrix $F \in \mathcal{R}^{m\times n}$ such that all the eigenvalues of the matrix $A + BF \in \mathcal{R}^{n\times n}$ lie in the open left-half of the complex plane. Using Lyapunov theory, it can be shown that this is equivalent to finding a matrix $F$ and a positive definite matrix $P \in \mathcal{R}^{n\times n}$ such that the following inequality holds:

$$(A + BF)^T P + P(A + BF) < 0 \quad (45)$$

or

$$A^T P + PA + F^T B^T P + PBF < 0 \quad (46)$$

Note that the terms with products of $F$ and $P$ are nonlinear or bilinear. Let us multiply either side of the above equation by $Q = P - 1$. This gives:

$$QA^T + AQ + QF^T B^T + BFQ < 0 \quad (47)$$

This is a new matrix inequality in the variables $Q > 0$ . But it is nonlinear too. By defining a second new variable$= FQ$, we have:

$$QA^T + AQ + L^T B^T + BL < 0 \quad (48)$$

This gives an LMI feasibility problem in the new variables $Q > 0$ and $L \in \mathcal{R}^{m\times n}$. After solving this LMI, the feedback matrices $F$ and Lyapunov variable $P$ can be recovered from $F = LQ - 1$ and $P = Q - 1$. This shows that by making a change in the variables, we can obtain an LMI from a nonlinear matrix inequality [28]. While LMI solvers are concerned to resolve stability issues, we used LMI to achieve a more acceptable result [29].

## VIII. SYSTEM SIMULATION

### *A. Implementation algorithm*

We applied this simulation method to several power systems and we report the results of one of them here. Figure 5 shows the studied power system, which is a 10-machine 39-bus New England network whose data can be found in [30]. For small signal analysis, the sampling time was selected as 0.1 msec, thus the frequency of the two UPFC and DFIG inverters' parameters updating is 10 kHz, which is consistent with the existing switches' speeds. In this study, a PSS was used only for the generator that is installed on the slack bus. We simulated four scenarios: power system without UPFC and without DFIG, power system using UPFC controller only, power system while connected DFIG (wind farm) controller acts, power system while both UPFC and DFIG controllers are simultaneously designed and used.

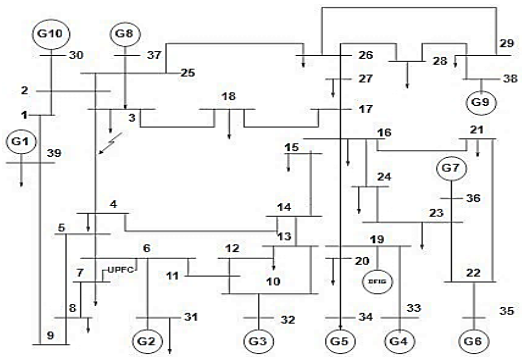


**Fig. 5.** The New England power system network schematic single line

### *B. Power system simulation results*

In this study, MATLAB program was used to simulate the model. Within the load flow solution, the thermal limits of lines capacity are considered. A 3-phase earth fault is applied to the line between bus 3 and 4 and its duration to clear is 0.1 sec which is short enough for small signal analysis. Oscillations are demonstrated by extracting $\Delta\delta$ and $\Delta\omega$ of all machines.

Figure 6 depicts the results while DFIG is not connected and UPFC is not installed. As we can see, the system states are oscillating or have weak damping while UPFC is not installed. (We see in next section that after using UPFC, the system will be more stable after fault clearing.). The results of load flow implementation are used to find UPFC placement to improve voltage profile.

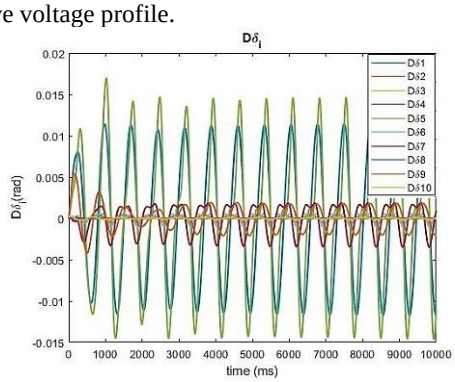


(a) All machines load angle deviations

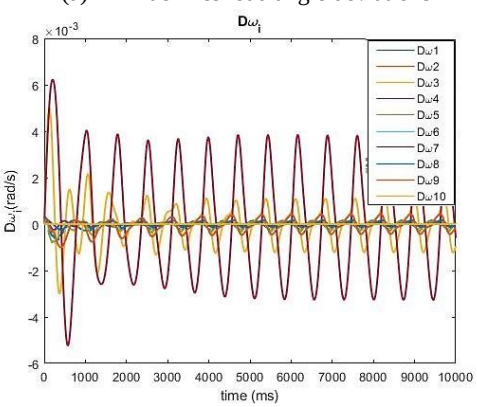


(b) All machines speed deviations

**Fig.6.** System oscillations without UPFC and DFIG

*C. power system using UPFC controller*

The results of load flow implementation are used to find UPFC placement to improve voltage profile and load flow of the power system. Within load flow solution, the thermal limits of lines capacity are considered. After UPFC insertion in the power network, the load flow is executed again. When UPFC is installed between 6 and 7 buses in the system, the active and reactive power loses are reduced. It is also verified that not only the power losses are reduced, the voltage profile of the buses is improved after incorporating UPFC. This simulation is carried out according to flowchart in Figure 7.

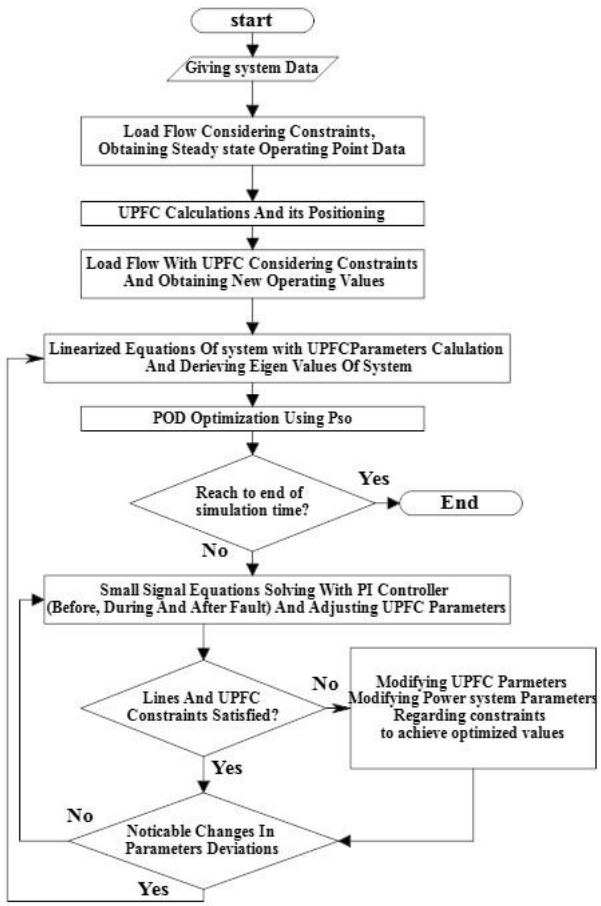


**Fig. 7.** The flowchart of the simulation of the power system with UPFC installed

For small signal and dynamic stability study, we used UPFC dynamic model and interfacing with power system as described in Section IV. All four basic controllers of UPFC are considered. Eigenvalues and damping ratios of the linearized system are derived and, based on these values, the PSO algorithm is used to optimize damping oscillations controller. Figure 8 demonstrate the eigenvalues of the system with and without UPFC in a complex plane. As we can see, some of eigenvalues have a little more negative real part. Some of critical eigenvalues are shown in Table I.

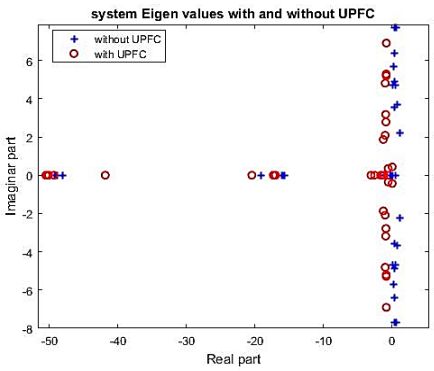


**Fig.8.** A comparison of the system eigenvalues with and without UPFC

**Table I**

SOME CRITICAL EIGENVALUES BEFORE AND AFTER USING UPFC

| Related state | Without UPFC | With UPFC |
|---|---|---|
| Machine no. 1 load angle deviation | 0.638 + 7.701i | -0.849 - 6.908i |
| Machine no. 3 load angle deviation | 0.292 + 7.707i | -0.871 - 5.203i |
| Machine no. 1 angular speed deviation | 0.286 + 4.887i | -0.948 - 3.181i |
| Machine no. 3 angular speed deviation | 0.478 + 4.702i | -1.287 - 1.866i |

To investigate the enhancement of the power system stability by a UPFC, we studied the results and responses of three-phase earth fault scenarios, too. Figures 9(a)-(d) show four UPFC parameters, faulted bus voltage, the variation of all machines load angle variations, and all machines speed variations with three-phase earth fault applied, respectively.

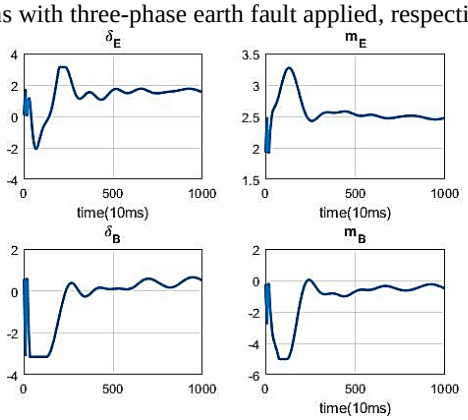


(a) four UPFC parameters

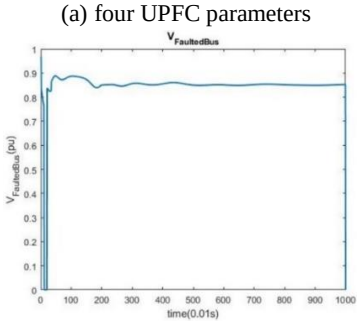


(b) faulted bus voltage

**Fig.9** Continued

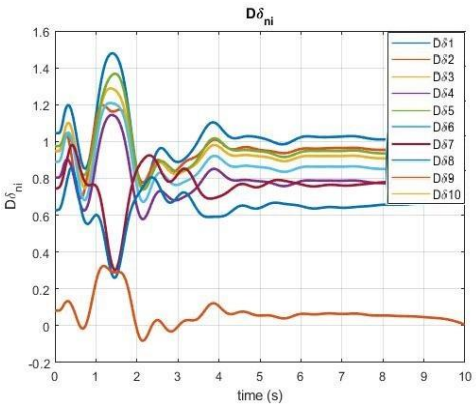


(c) All machines load angle deviations

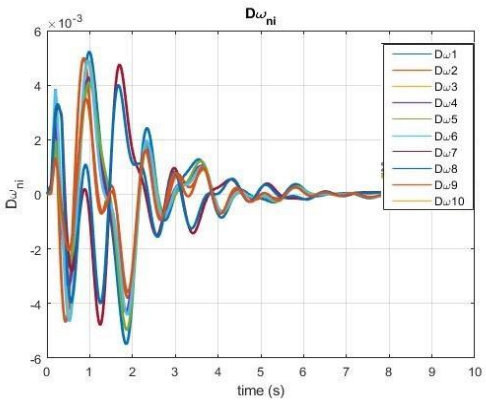


(d) All machines speed deviations

**Fig.9.** Damping performance and effect of UPFC in three-phase earth fault

*D. Power system using connected DFIG controller*

While DFIG (connected to bus 19 with a short line) controller is used to damp oscillations, we can see that its effect is less than when we used UPFC. But, we found that when we increased the capacity of the wind farm (equal DFIG), its effect on oscillation damping increased too. This simulation was carried out according to the flowchart in Figure 10. Figures 11(a)-(c) depict the variations of all machines load angle, all machines speed variations, and DFIG states as assigned in (39), respectively.

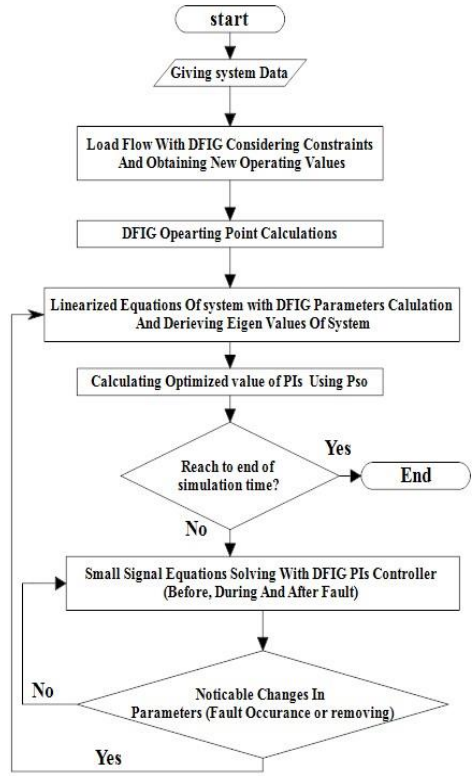


**Fig.10.** The flowchart of the simulation and power system with DFIG connected

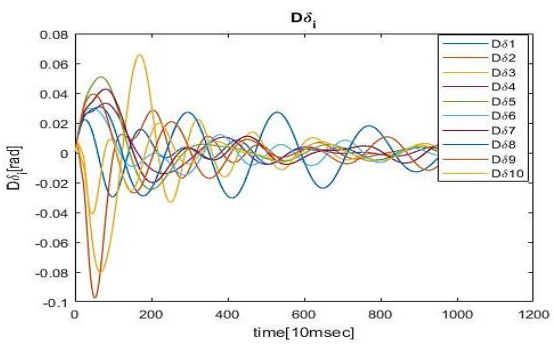


(a) All machines load angle deviations

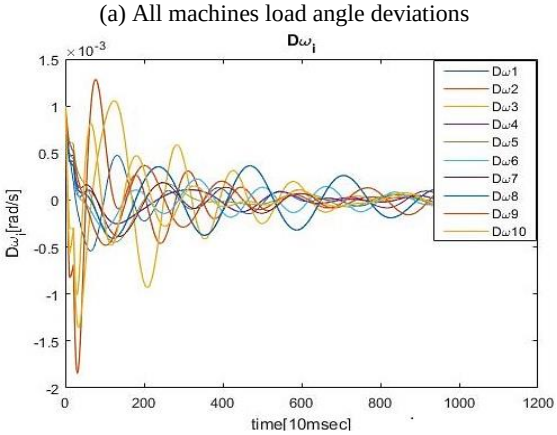


(b) All machines speed deviations

**Fig.11** Continued

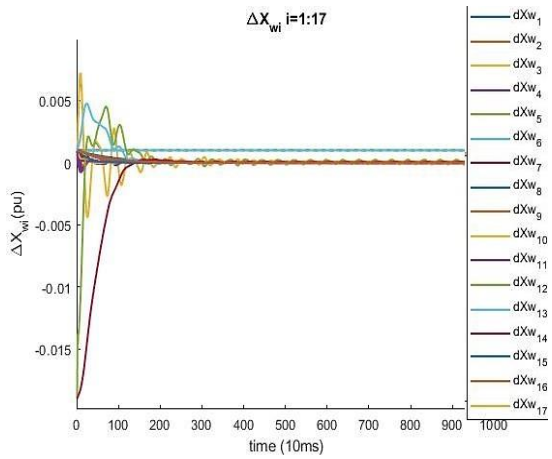


(c) DFIG states deviations

**Fig.11.** Damping effect of DFIG in three phase earth fault

*E. Power system using both UPFC and DFIG controller*

According to the flowchart in Figure 12, the whole system linearized equation, shown in (42), is used to optimize parameters of both UPFC and DFIG and solve and extract the deviation of the variables. While there are both UPFC and DFIG in power system, and we simultaneously and coordinately designed them in one state matrix, damping effect of them is better than when we used their controller with individual design of them. Figures 13(a)-(c) display the variations of all machines load angle, all machines speed variations, and DFIG states as assigned in equation (39), respectively.

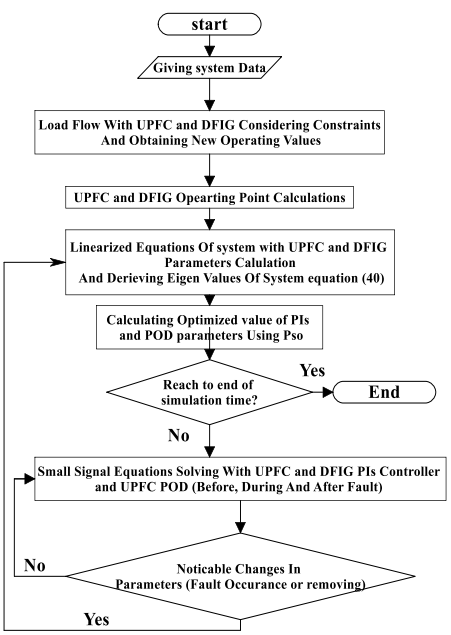


**Fig. 12.** The flowchart of the simulation and power system with DFIG connected and UPFC installed

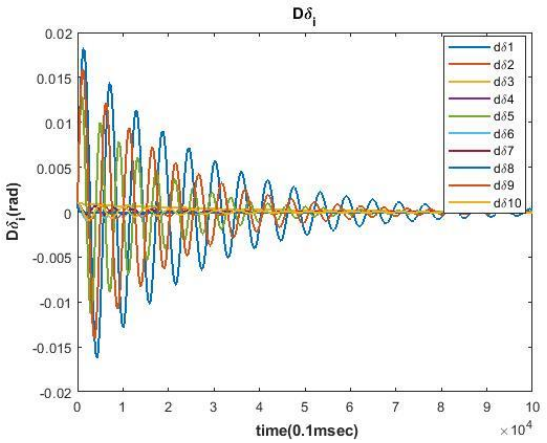


(a) All machines load angle deviations

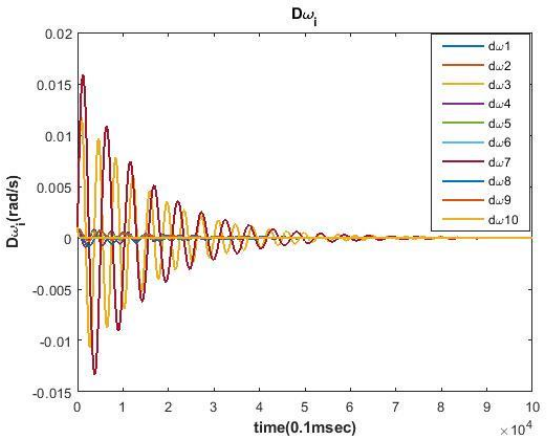


(b) All machines speed deviations

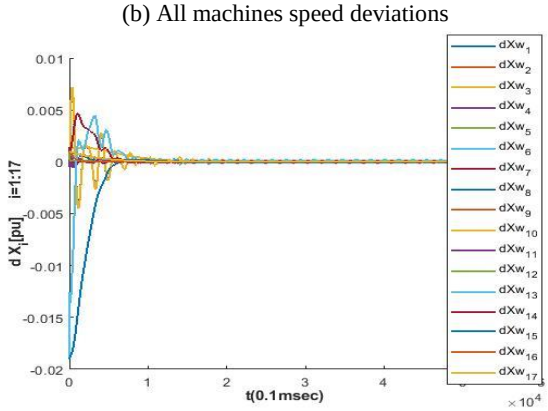


(c) DFIG states variables deviations defined in (39)

**Fig.13.** Damping effect of both UPFC and DFIG in earth fault while coordinately designed

*F. Power system using both UPFC and DFIG controller while LMI has used*

The system and all situations, described in Section E, were used again to simulate and solve whole system linearized state space model using state feedback control and application of LMI technique, described in Section VI. Figures 14(a)-(c) depict the variation of all machines load angle, all machines speed variations, and DFIG states as assigned in Eq. (39), respectively. While comparing them

with Figure 13, faster damping and lower overshoots and then more acceptable result is clear. The results of this more complete models' simulation with both UPFC and DFIG controllers by using LMI has more acceptable damping effects versus [1],[2] and [3] which have used only UPFC with classic controller, only DFIG with classic controller, and using LQR, respectively.

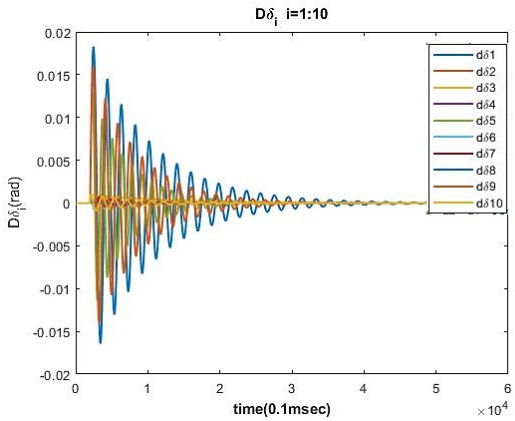


(a)All machines load angle deviations

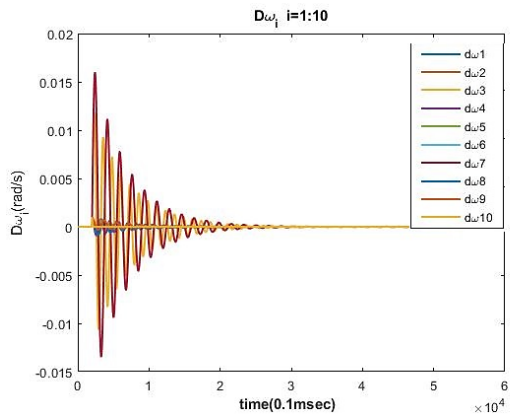


(b) All machines speed deviations

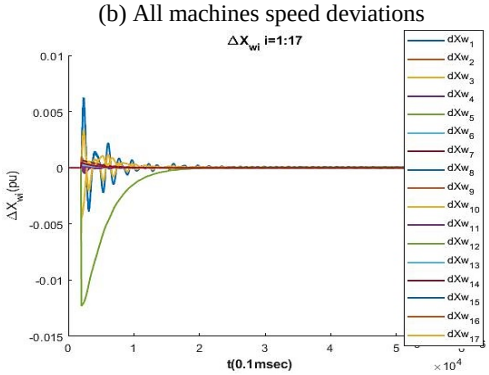


(c) DFIG state variables deviations defined in (39)

**Fig. 14.** Damping effect of both UPFC and DFIG in earth fault while coordinated designed and LMI used

## IX. CONCLUSIONS

In this study, the power system with UPFC and its main and damping controls and its POD here modeled based on the Heffron-Philips model. DFIG small signal modeling was carried out considering its 17 non-mechanical and control state variables. The individual effect of UPFC and DFIG on dynamic stability was also studied. Then, their linearized model was added to the power system model and the modal analysis and dynamic stability of the power system was studied in a 10-machine 39-bus New England multi-machine power system. The results show that UPFC can noticeably improve dynamic stability of the whole power system. The control of DFIG in power system helps the system to improve the dynamic stability of DFIG and the power system. While there are both of these two devices in the multi-machine power system, by coordinating and making some optimization in UPFC parameters and controllers and optimized adjustment in DFIG controllers, the dynamic stability of DFIG and the power system can be improved. The result is better when LMI is used versus when only classic described controllers are used. When using LMI, after 4 seconds oscillations are acceptably damped while before using LMI, near 9 seconds was required to damp oscillations acceptably.

## APPENDIX

*A: UPFC used Data:*

In 39-bus New England network: UPFC Rating=190 MW=1.9 pu, xE= 0.0725 pu, xB=0.0725 pu, C=1 pu, Sb=100MW.

*B: DFIG used Data*:

Mw=3.4, Dwm=0, Rwr=0.0007, Kwm=3.95,
Jwr1=8, Jwr2=8, Dwr1=0.0, Dwr2=0.0,
Xws=0.0878, Xwr=0.0373, Xwm=1.3246, Xwr3=0.05,
Xwf=0.05, sw0=-0.01, Cw=13.29, Rws=0, DFIG rating power=56MW=0.56 pu

## REFERENCES

[1] A. Ziaei , R. Ghazi , R. Zeinali davarani, "Linear Modal Analysis of Doubly-Fed Induction Generator (DFIG) Torsional Interaction: Effect of DFIG Controllers and System Parameters", *Advances in Electrical and Electronic Engineering*, pp. 388-401, 2018.

[2] M. Ravindrababu, G. Saraswathi, K.R. Sudha, "Design of UPFC-PSS using Firefly Algorithm for Stability Improvement of Multi Machine System under Contingency", *Majlesi Journal of Electrical Engineering* , vol. 13, No. 2, pp. 21-39, June 2019.

[3] B. K. Dubey, N.K. Singh, "Multimachine Power System Stability Enhancement with UPFC Using Linear QUADRATIC Regulator Techniques", *International Journal of Advanced Research in Engineering and Technology (IJARET)*, vol. 11, Issue 4, pp. 219-229, April 2020.

[4] N. Nahak, R. K. Mallick, S. P. Muni, "Stability Enhancement of Multi machine System by Improved GWO Optimized UPFC based controller", *International Journal of Pure and Applied Mathematics*, vol. 114 no. 9, pp. 63-72, 2017.

[5] S.Q. Bu, X. Zhang, J.B. Zhu, X. Liu, "Comparison analysis on damping mechanisms of power systems with induction generator based wind power generation", *Electrical Power and Energy Systems*, pp. 250–261, 2018.

[6] Y. Mohammed, R. Alharbi, Application of Unified Power Flow Controller to Improve the Performance of Wind Energy Conversion System, Phd thesis, Department of Electrical and Computer Engineering, Curtin University, March 2016.

[7] S. Vig, B. S. Surjan, Advances in Smart Grid and Renewable Energy , in chapter: Analysis of UPFC Controller Connected with Multiple Wind Turbines by Using IEEE Bus System, Springer ,Singapore, 2021.

[8] P. Khandelwal, B. Modi, S. S. Sharma, "DFIG based WECS Connected Power System Using UPFC for Improvement of Stability", International Journal of Research and Scientific Innovation, vol. I, Issue IV, pp. 10-15, September 2014.

[9] A. Ganesan, R. Rajamoort, "Modeling of FUZZY Controlled UPFC for LVRT Improvement in DFIG Based Grid Connected Wind Farm", *Journal of Electronic Design Engineering*, vol. 5 Issue 1, pp. 29-38, MAT Journals 2019.

[10] M. Ferdosian, H. Abdi, A. Bazaei , "Improving the Wind Energy Conversion System Dynamics during Fault Ride through: UPFC versus STATCOM", *IEEE 2015 IEEE International Conference on Industrial Technology (ICIT)*, pp. 2721-2726, 2015.

[11] Y. M. Alharbi, A. M. S.Yunus, A. Abu-Siada, "Application of UPFC to Improve the FRT Capability of Wind Turbine Generator", *International Journal of Electrical Energy*, vol. 1, No. 4, pp. 188-193, December 2013.

[12] Nidhi Vaishnava Amit Verma , Performance Analysis of DFIG based Wind Turbine System using FACTS Devices , *International Journal of Science Technology & Engineering*, Volume 4, Issue 1, pp. 178-183, July 2017.

[13] P. K. Dash, R. K. Patnaik, S. P. Mishra, Adaptive fractional integral terminal sliding mode power control of UPFC in DFIG wind farm penetrated multimachine power system, *Protection and Control of Modern Power* Systems (2018) 3:8, pp. 1-14,2018 https://doi.org/10.1186/s41601-018-0079-z.

[14] D. E. Tourqui, M. Benakcha, T. Allaoui, "Improving the Electrical Stability by Wind Turbine and UPFC, Improving the Electrical Stability by Wind Turbine and UPFC", *Artificial Intelligence in Renewable Energetic Systems*, Springer International Publishing AG 2018. https://doi.org/10.1007/978-3-319-73192-6_13.

[15] H. R. Koofigar, G. Isazadeh, "Optimal robust stabilizer design based on UPFC for interconnected power systems considering time delay", Archives of Electrical Engineering vol. 66(3), pp. 459-474, 2017.

[16] H. Zhang, J. Hao, C. Wu, Y. Li, A. Sahab, "A novel LMI-based robust adaptive model predictive control for DFIG-based wind energy conversion system", system science & control engineering, vol. 7, pp. 311-320, 2019.

[17] Y. Shi, R. Eberhart, "A modified particle swarm optimizer", *IEEE international conference on evolutionary computation proceedings*, Anchorage, AK, USA, pp. 69–73, 1998.

[18] A. Nabavi-Niaki, M.R. Iravani, "Steady-state and dynamic models of unified power flow controller for power system studies", *IEEE Transactions on Power System*, vol. 11, no. 4, pp. 1937-1950, 1996.

[19] H.F. Wang, "A unified model for the analysis of FACTS devices in damping power system oscillations –Part III: unified power flow controller', *IEEE Transaction on Power Delivery*, vol. 15, no. 3, pp. 978–983, 2000.

[20] H.F. Wang, M. Jazaeri, Y.J. Cao, ¨Analysis of control conflict between UPFC multiple control functions and their interaction indicator", *International Journal of Control, Automation and Systems*, vol. 3, no. 2(special edition), pp. 315-321, 2005.

[21] K. Madhuri, M.V. Srikant, "Modeling and analysis of power flow controller in the presence of power system stabilizer for a multi-machine system", *International Journal of Engineering Research & Technology (IJERT)*, vol. 1, no. 6, pp. 1-7, 2012.

[22] M. Eslami, H. Shareef, M.R. Taha, M. Khajezadeh," Adaptive particle swarm optimization for simultaneous design of UPFC damping controllers", *ELSEVIER Electrical Power and Energy Systems*, vol. 57, pp. 116-128, 2014.

[23] J. Fletcher, J. Yang, "Introduction to the Doubly-Fed Induction Generator for Wind Power Applications", *D. A. Ng, Ed.*, InTech, pp. 259-279, 2010.

[24] H. *Jiang*, H. Liu, L. Wu, Y. Li, "*Comparisons* on State Space Models of Doubly Fed Induction Generators (*DFIG*) for Power System Research", *State Grid Jibei Electric Power Research Institute. Beijing, China. IEEE PES Asia-Pacific Power and Energy Conference* - Xi'an – China, 2016. DOI: 10.1109/APPEEC.2016.7779624.

[25] P. Kundur, "Power System Stability and Control", Electric Power Research Institute, Power System Engineering Series, McGraw-Hill, New York, 1994.

[26] W. Du, X. Chen, H.F. Wang, "Impact of dynamic interactions introduced by the DFIGs on power system electromechanical oscillation modes", *IEEE, 0885-8950 (c)*, 2016.

[27] W. Du, J. Bi, C. Ly, T. Littler, "Damping torque analysis of power systems with DFIGs for wind power generation", *IET Proceedings on Renewable Power Generation*, on-line early view, 2016.

[28] Z. Jian**,** S**.** Akshya**,** N**.S.** Kiong, Robust Observer based Fault Diagnosis for nonlinear systems using MATLAB, springer,

**Masoud Maleki rizi** received his B.Sc. degree in Electrical Engineering from Tabriz University, Tabriz, Iran in 1997 and his M.Sc. degree in Electrical Engineering from Isfahan University of Technology, Isfahan, Iran in 2001. He is currently a Ph.D. candidate in Electrical Engineering at Shahrekord University, shahrekord, Iran. His research interests are power system dynamic stability, FACTS devices impact on power system stability, power system control and stability optimization, and renewable energy systems.

**Saeed Abazari** received his B.Sc. degree in electrical engineering from Isfahan University of Technology, Isfahan, Iran, in 1989, the M.Sc. degree from Ferdowsi University, Mashhad, Iran, in 1992 and the Ph.D. degree from Sharif University of Technology, Tehran, Iran, in 2002. Currently, He is a Professor of the Electrical Engineering Department at the Shahrekord University, Shahrekord, Iran. His research interests are electric power distribution system, smart grid, power system operation and control and FACTS controllers.

**Nima Mahdian Dehkordi** received the M.Sc. and Ph.D. degrees from Sharif University of Technology, Tehran, Iran, in 2012 and 2016, respectively, both in electrical engineering. He joined the the Department of Electrical Engineering, Science and Research Branch, Islamic Azad University, Tehran, Iran, in2017, where he is currently an Assistant Professor. His research interests include control systems, applications of control theory in power electronics, microgrid control, distributed and cooperative control, internet of things, nonlinear control, and network control.

**IECO**

**This page intentionally left blank.**

International Journal of Industrial Electronics, Control and Optimization © 2021 IECO
Vol. 4, No. 3, pp. 355-366, July (2021)

# Chaos Synchronization in Josephson Junction Using a Nonlinear Model Predictive Controller Based on Particle Filter: Processor in the Loop Implementation

Aylar Khooshehmehri [1†], Saeed Nasrollahi [2], Morteza Aliyari[3]
[1, 2, 3]Faculty of Electrical and Computer Engineering, Malek-Ashtar University of Technology, Iran.

ABSTRACT

*In this paper, a model predictive control approach based on a generic particle filter is proposed to synchronize two Josephson junction models with different parameters. For this purpose, an appropriate objective function is defined to assess the particles within the state space. This objective function minimizes simultaneously the tracking error, control effort, and control smoothness. The dynamic optimization problem is solved using a generic particle filter. Here, Josephson junction is described with Resistive Capacitive Inductive Shunted Josephson model, and the synchronization is obtained using the slave–master technique. Moreover, to verify the implementation capability of the proposed algorithm, a processor in loop experiment is performed. The results show that the open-loop system, without the controller, has a chaotic behavior. Numerical simulations are conducted to assess the performance of the proposed algorithm. The results show that the proposed approach can be implemented in a real-time application. Also, the performance of the suggested controller is compared with the proportional integral derivative controller and sliding mode controller.*

**Article Info**

***Keywords:*** Chaos dynamic, Generic particle filter, Josephson junction, Model predictive control, Synchronization.

***Article History:***
**Received** 2020-12-24
**Accepted** 2021-06-29

## I. INTRODUCTION

The Josephson junction is a device consisting of two superconducting electrodes connected by a weak junction such as a thin insulation coating. If the intermediate insulation coating is sufficiently thin, the pair of electrons will tunnel from one superconducting electrode to another; This phenomenon is called the Josephson effect [1]. Like many mechanical and electronic systems, the Josephson junction can exhibit chaotic behavior. Researchers have studied chaos in different structures of the Josephson junction [2–4]. Since chaos is an unpredictable phenomenon and may lead to unwanted behavior in the system, it must be suppressed in many cases [5–7]. For example, in the application of Josephson junction such as Josephson parametric amplifiers [8], voltage standard [9], high-frequency oscillators [10], squid magnetometer [11], soliton transistors [12], pulse generators [13], and the biophysical function of neural the circuit [14,15], it is necessary to prevent chaos, and therefore, the chaos will be controlled in Josephson junction. Several studies are conducted to control and synchronize the chaotic behavior of the junction, which will be discussed below.

In [16], an active control method has been used to control and synchronize two coupled Josephson junction models such that the frequency of oscillation of the slave system has been following the master system; here, a linear model has been used to design the controller. In [17], a nonlinear backstepping controller has been considered to control bifurcation as well as chaos in the RCLSJ Josephson junction. A Lyapunov function has been proposed to analyze the stability of the close loop system. In [18], backstepping control theory has been

[†]**Corresponding Author**: khooshehmehri@mut.ac.ir
Tel: +98-02122945141, Fax: +98-02122959233,
Faculty of Electrical and Computer Engineering, Malek-Ashtar University of Technology, Iran.

used to control and synchronization of chaotic dynamics in RCLSJ. The recursive approach has been employed to eliminate the chaotic behavior of the RCLSJ as well as to attain global asymptotic synchronization. In [19], an active backstepping method has been used to control chaos in RCLSJ model. In the proposed approach the number of control functions has been reduced from three to one that was reduced controller complexity. In [20], a nonlinear recursive method has been used to control the bifurcation as well as chaotic behavior of the Josephson junction. Here, a control signal based on the master and slave concept has been designed. In [21], a nonlinear sliding mode controller has been used to control and synchronize the chaos of the Josephson junctions considering the uncertainty of the model. Also, the Lyapunov stability theory has been used to analyze the stability of the system. In [22,23], an iterative learning control has been used for the linearized model of the error dynamics between two Josephson junctions. A real-time feed -forward procedure that uses iterative learning, to modify the trajectory error between systems for tracking two non-identical systems, has been used. In [24], a nonlinear controller based on sliding mode and neural fuzzy has been used for control and synchronization of the error dynamics. The neural fuzzy controller is used to provide a feedback linearization and sliding mode is used to deal with uncertainty in the model. In [25] a backstepping controller is used to achieve a hybrid combination synchronization of three Josephson junctions. One chaotic Josephson junction as the master and two Josephson junctions as the slaves.

Model Predictive Control (MPC) is an interesting subject in control engineering. The benefit of MPC methods is their capability to handle dynamics with nonlinear elements and constraints [26]. MPC approaches have been employed in several practical examples, such as DC-DC Boost Converter [27], a six pulse rectifier [28], a Boost Converter [29], a quadrotor helicopter [30], and large-scale systems [31]. MPCs are classified into nonlinear and linear ones. Nonlinear Model Predictive Control (NMPC) typically involves non-convex optimization problems. An MPC problem can be expressed as an estimation problem. Likewise, an estimation problem can be expressed as a dynamic optimization problem. The combination of MPC and particle-based algorithms provides a tool for the calculation of the control signal in control [32]. In references [32–36], particle-based heuristic methods are used to compute the control signal. Also, the above-mentioned references have not used particle-based heuristic methods to synchronize two Josephson junction models with slightly different parameters.

The contribution of the current study is summarized as follows: a nonlinear model predictive control approach based on a generic particle filter is proposed to synchronize two Josephson junction models with different parameters. For this purpose, an appropriate objective function is defined to assess the particles within the state space. This objective function minimizes simultaneously the tracking error, control effort, and control smoothness. This nonlinear model predictive control problem, which is the dynamic optimization problem is solved using a generic particle filter. To the author's knowledge, the use of a generic particle filter to synchronize two Josephson junction models with different parameters has not been proposed yet. The performance of the suggested approach is achieved in simulations using the Resistive Capacitive Inductive Shunted Josephson model. Numerical simulations are made to confirm the validity of the suggested controller. Moreover, to verify the implementation capability of the proposed algorithm, a processor in the loop experiment is performed.

In this paper, the nonlinear Josephson junction equations are described in section 2. Section 3 explains the controller design. In Section 4, the results of nonlinear simulation and controller performance are presented. Finally, the conclusion is presented.

## II. STATEMENT OF THE PROBLEM

The Josephson junction can be described with various electrical models such as Resistive Shunted Josephson (RCJ), Resistive Capacitive Shunted Josephson (RCSJ), and Resistive Capacitive Inductive Shunted Josephson (RCLSJ) [1,2]. Fig. 1 shows the RCSJ model; here, $\theta$ is the phase difference between the two superconductors in the junction, $R$ is the junction resistance, and $C$ is the junction capacitor.

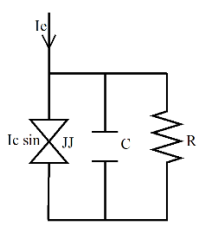


**Fig. 1** RCSJ Model

When the external current $I_e$ containing a direct current and alternating current is applied to the junction, the voltage of the two ends of the junction decreases. According to the I-V curve of the junction shown in Fig. 2, the hysteresis behavior is observable in the current-voltage characteristic of the junction.

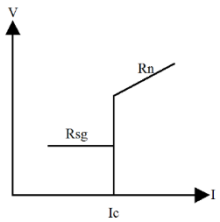


**Fig. 2** Current-voltage diagram of Josephson junction

Where $R_n$ is the normal junction resistance, $R_{sg}$ is the sub-gap junction resistance, and $I_C$ is the critical current of the junction. The differential equations governing the model presented in Fig. 1 are as follows [17,20]:

$$c\frac{dv}{dt}+\frac{v}{R}+I_c\sin\theta=I_e=i_o+i_1\sin(\omega t) \quad (1)$$

$$(\frac{h}{2\pi e})\frac{d\theta}{dt}=v \quad (2)$$

Where $v$ is the voltage of the two ends of the junction, $h$ is the Planck constant, $e$ is the electric charge. Dynamic equations show that applying external direct current, ( $I_e=i_0$ ), results in chaotic behavior. The following equation has been achieved by inserting equation 2 in equation 1 and normalizing it [17]:

$$\frac{d^2\theta}{dt^2}+\beta\frac{d\theta}{dt}+\Omega_0^2\sin\theta=A_0+A_1\sin(\omega t) \quad (3)$$

Where $\beta=1/RC$ , $\Omega_0=(2\pi eI_c/hC)^{0.5}$ , $A_0=(2\pi ei_0/hC)$ , and $A_1=(2\pi ei_1/hC)$ . When the external alternating current is applied to the Josephson junction, the chaotic behavior is visible at a critical value of the current which is due to the hysteresis behavior of the junction curve [37]. Another model is presented regarding hysteresis behavior, in which the linear resistance in the RCSJ model is replaced with the nonlinear model, $R(V)$ , and is defined as follows:

$$R(V)=\begin{cases}R_n & \text{if } |V|>V_g\\ R_{sg} & \text{if } |V|\le V_g\end{cases} \quad (4)$$

Where $V_g$ is the junction gap voltage, $R(V)$ is the step function of the two resistors $R_n$ and $R_{sg}$ which is synchronized well with the practical behavior of the junction. Such parallel resistors are required in high-frequency applications such as Josephson resonators. These parallel resistors and associated wiring result in series resistor inductor effects. Numerical studies conducted on this inductive effect confirm the practical characterization results of the junction at different temperature conditions. Then, the revised RCLSJ model including parallel self-induction is proposed. The RCLSJ model of the Josephson junction is shown in Fig. 3.

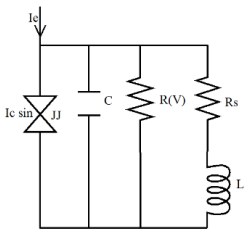


**Fig. 3** RCLSJ model

Here, $R_s$ and $L$ are respectively the parallel resistance and parallel self- induction. Also, $I_s$ is the current passing the parallel self- induction. The dynamic equations of this junction are as follows [17,20]:

$$c\frac{dv}{dt}+\frac{v}{R}+I_c\sin\theta+I_s=I_e=i_o+i_1\sin(\omega t) \quad (5)$$

$$(\frac{h}{2\pi e})\frac{d\theta}{dt}=v \quad (6)$$

$$L\frac{dI_s}{dt}+R_sI_s=v \quad (7)$$

The normalized mathematical model of the equations is as follows [17]:

$$\beta_C\ddot{\theta}+g(V)\dot{\theta}+\sin\theta+I_s=i_o+i_1\sin((\omega/\omega_0)\tau) \quad (8)$$

$$\dot{\theta}=V \quad (9)$$

$$\beta_L\dot{I}_s+I_s=V \quad (10)$$

Where $\tau=\omega_0 t$ and $V=(v/I_sR_s)$ . Here, the Josephson junction shows chaotic behavior by choosing values of $\beta_C=0.707$ , $\beta_L=2.6$ , $i_0=1.20$ , and initial values of $(0.8,0.58,0.4)$ for states of the system [18]. The purpose of this paper is to synchronize Josephson junction involving chaotic behavior with Josephson junction that does not show chaotic behavior by appropriate initial values and fixed parameters. Assuming $\theta=x_1$ , $V=x_2$ , and $I_s=x_3$ , the state space equations are rewritten as follows:

$$\dot{x}_1=x_2+u_1 \quad (11)$$

$$\dot{x}_2=\frac{1}{\beta_C}(i_0+i_1\sin(\frac{\omega}{\omega_0}\tau)-g(x_2)x_2 \quad (12)$$
$$-\sin(x_1)-x_3)+u_2$$

$$\dot{x}_3=\frac{1}{\beta_L}(x_2-x_3)+u_3 \quad (13)$$

$$g(V)=\begin{cases}0.366 & \text{if } |V|>2.9\\ 0.061 & \text{if } |V|\le 2.9\end{cases} \quad (14)$$

Now, the nonlinear model predictive control based on Particle Filter (PF) will be expressed for chaotic system synchronization. For this purpose, the slave system will be considered with the following equations:

$$\dot{\mathbf{x}}_s = \mathbf{F}_s(\mathbf{x}_s) + \mathbf{u} \quad (15)$$

In equation (15), $\mathbf{x}_s$ is the state variable, $\mathbf{u}$ is the input, and $\mathbf{F}_s$ is the function with appropriate dimensions. Also, the master system equations are considered as follows:

$$\dot{\mathbf{x}}_m = \mathbf{F}_m(\mathbf{x}_m) \quad (16)$$

Here, the purpose is to design the control law in a way that the slave state variables follow the master system state variables. To do this, the synchronization error is defined as: $\mathbf{e(t)} = \mathbf{x}_s - \mathbf{x}_m$. The system error equations can be written as follows using equations (15) and (16):

$$\dot{\mathbf{e}} = \mathbf{F}_s(\mathbf{x}_s) - \mathbf{F}_m(\mathbf{x}_m) + \mathbf{u} \quad (17)$$

**Algorithm. 1** Pseudo-Code of the proposed control algorithm

Set the number of particles, prediction horizon, and weighting factors.
Initialize randomly the vector of future control sequence, $\mathbf{u}_j(0)$, for $j \in [1, N]$.
**While** (until the end of simulation) **do**
Generate the control signals by Eq. (18)
**for** $j = 1$ to N **do**
Predict the future states by Eq.(19).
Calculate the cost function and weights by Equations (20)-(21).
Normalize the weights by Eq. (22).
Resample the particles
Calculate the control signals by Eq.(24).
**end for**
**end while**

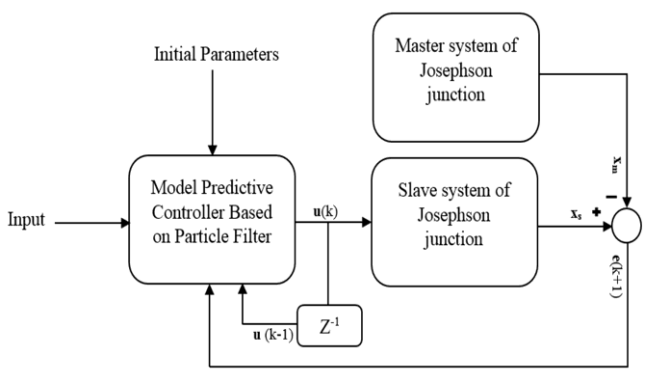


**Fig. 4**. Block diagram of nonlinear model predictive controller

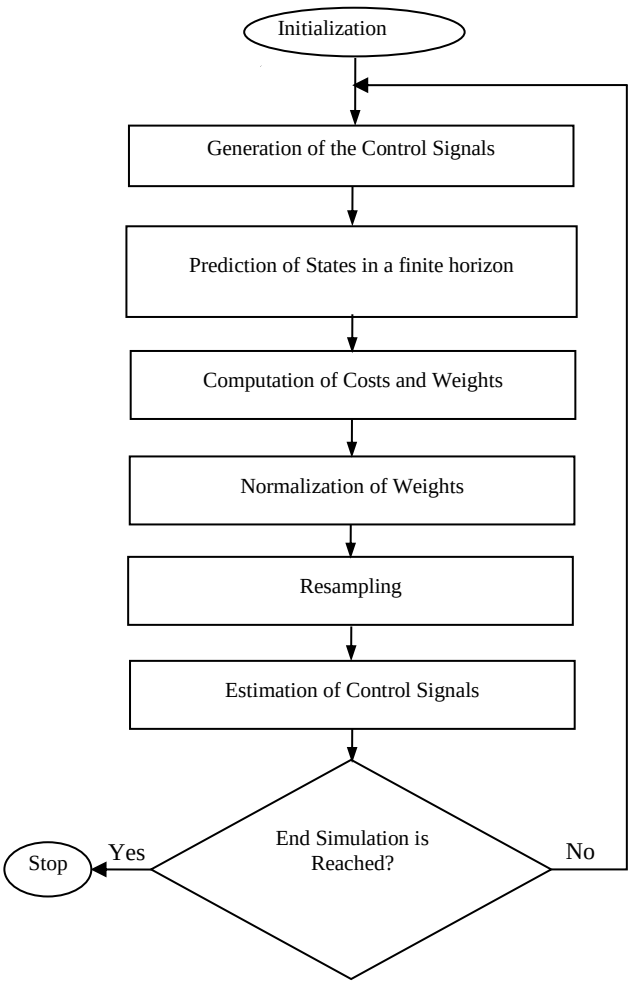


**Fig. 5** Flowchart of nonlinear model predictive controller

## III. Nonlinear Model Predictive Control Based on Particle Filter

The current study utilizes a single generic particle filter to estimate the finite horizon optimal controls in order to synchronize the chaos in the Josephson junction. The block diagram and flowchart of the proposed control algorithm are illustrated in Fig. 4 and Fig. 5, respectively. The proposed control algorithm has a main loop; it iterates until the end time of the simulation. At first, the initial control signals are generated, randomly. Then, the future control signals are calculated in a finite horizon, using $u(k) = u(k-1) + v(k-1)$, as proposed in [34]. Next, the future states are predicted using the control signals and, the defined cost function is calculated for each particle. A weight is assigned to each particle based on its cost. Weights are normalized. Resampling is performed. Finally, the control signals are estimated based on the current distribution of resampled particles. In addition, the pseudo-code of the PSO-DGG is shown in the algorithm. 1. In the next subsections, these steps are explained in detail.

*A. Initialization*

The proposed control algorithm has some parameters, set at the beginning. Moreover, for the $j$-th particle $(j=1,...,\mathrm{N})$, the initial value of future control sequence ($\mathbf{u}_j$) is sampled. A uniform random generator is used to generate $\mathbf{u}_j$ within an adequate range of control.

*B. Generation of the Future Control Signals*

The future control signals are generated for particle *j* as

$$\mathbf{u}_j(k+i-1)=\mathbf{u}_j(k+i-2)+\boldsymbol{\upsilon}_j(k+i-2), \quad (i=1,\ldots,\mathrm{T_p}) \tag{18}$$

Where, $\boldsymbol{\upsilon}$ is a Gaussian random variable; also, $k$ and $\mathrm{T_p}$ are the time step and the prediction horizon, respectively. It should be noted that $\mathbf{u}_j(k-1)=\hat{\mathbf{u}}(k-1)$.

*C. Prediction of the Future States*

Using the model presented in equation (17), the future of particles are predicted as:

$$\mathbf{e}_j(k+i)=\mathbf{F}_s(\mathbf{x}_{s_j}(k+i-1))-\mathbf{F}_m(\mathbf{x}_{m_j}(k+i-1))+\mathbf{u}_j(k+i-1) \quad (i=1,\ldots,\mathrm{T_p}) \tag{19}$$

*D. Computation and Normalization of Weights*

A weight is assigned to each particle based on its cost. The cost of the particle $j$ at time step $k$, denoted by $J_j(k)$, is computed as

$$J_j(k)=\mathrm{w_{TE}}\sum_{i=k}^{k+\mathrm{T_p}}\left(\mathbf{e}_\mathrm{d}(i)-\mathbf{e}_j(i)\right)^\mathrm{T}\left(\mathbf{e}_\mathrm{d}(i)-\mathbf{e}_j(i)\right)+\mathrm{w_{CE}}\sum_{i=k}^{k+\mathrm{T_p}-1}\mathbf{u}_j(i)^\mathrm{T}\mathbf{u}_j(i)+\mathrm{w_{CS}}\sum_{i=k}^{k+\mathrm{T_p}-1}\Delta\mathbf{u}_j(i)^\mathrm{T}\Delta\mathbf{u}_j(i) \tag{20}$$

where $\mathrm{w_{CS}}$, $\mathrm{w_{CE}}$, and $\mathrm{w_{TE}}$ are weighting factors that control the importance of Control Smoothness (CS), Control Effort (CE), and Tracking Error (TE), respectively. After calculation of the cost, the weight of particle $j$ at time step $k$, denoted by $w_j(k)$, is evaluated using the following normal function, proposed in [38]:

$$w_j(k)\equiv\exp\left(-0.5J_j(k)\right) \tag{21}$$

Finally, the weights are normalized as follows:

$$\overline{w}_j(k)=\frac{w_j(k)}{\sum_{j=1}^{\mathrm{N}}w_j(k)} \tag{22}$$

Where $\overline{w}_j(k)$ is the normalized weight of particle $j$ at time step $k$. Therefore, the summation of normalized particles' weight is one.

*E. Resampling*

After a few iterations, most particles will have negligible weights. Therefore, a large computational effort is spent to update particles whose contribution to the estimation of states is negligible. In other words, the number of effective particles is decreased. This phenomenon is called degeneracy. This phenomenon is an unwanted effect in particle filters. A suitable measure of degeneracy is the effective sample size, defined as [39]:

$$\hat{N}_{\mathrm{eff}}=\frac{1}{\sum_{j=1}^{\mathrm{N}}(\overline{w}_j(k))^2} \tag{23}$$

Considering extreme cases of the problem, it can easily be shown that $1\le\hat{N}_{\mathrm{eff}}\le\mathrm{N}$. Small effective sample size indicates significant degeneracy, i.e., when $\hat{N}_{\mathrm{eff}}$ falls below some threshold $N_\mathrm{T}$ [39]. Whenever a significant degeneracy is observed, resampling can be used to reduce the effect of degeneracy [39]. Resampling is performed in different ways. In this paper, systematic resampling [40] is utilized and performed in every iteration. In this method, $\tilde{\mu}\sim U[0,1)$ and $\mu_j=(\tilde{\mu}+(j-1))/\mathrm{N}$ are defined. Then, $\mu_j$ is used to select the new *j*-th particle as described in [40]. Resampling is performed based on the normalized particles' weight. The particles' weight depends on their control smoothness, tracking error, and control effort.

In systematic resampling, a particle may be selected more than one time (replication) and a particle may never be selected. In other words, high-performance particles have more chance to be selected or replicated and low performance particles have less chance to be survived. A selected particle has an estimation of the future control sequence, $u(k+i-1)$, $(i=1,...,\mathrm{T_p})$. The estimation of control is performed using the estimated control of resampled particles.

*F. Estimation of Control Signal*

After resampling, the control signal vector of particle $j$ at time step $k$ is estimated as:

$$\hat{\mathbf{u}}(k)\approx\sum_{j=1}^{N}\overline{w}_j(k)\mathbf{u}_j(k) \tag{24}$$

Where the normalized weights $\overline{w}_j(k)$ are calculated using equation (22). The estimated vector consists of the estimated control sequences. Therefore, the estimated control signals for time step $k$ (elements $1, \mathrm{T_p}, 2\mathrm{T_p}$ of $\hat{\mathbf{u}}$) are calculated using the estimated control signals of N resampled particles (element $1, \mathrm{T_p}, 2\mathrm{T_p}$ of $\hat{\mathbf{u}}_j, j=1,...,\mathrm{N}$).

## IV. Simulation Results

In this section, the results of the simulations, in Matlab software, are presented. The purpose of the simulation is to synchronize the slave with the master system. So that, the error between master and slave variables converges to zero. The constant parameter values of the dynamic equations of the Josephson junction are given in TABLE I. To solve the differential equations, the Matlab Ordinary Differential Equation function solver (ODE45) is used. Also, the values of the control parameters are as follows: $w_{TE} = 20$, $w_{CE} = 1$, $w_{CS} = 0.5$, $T_P = 10$, $N = 300$, and $\sigma_v = 0.1$. The relative importance of the corresponding performance indices determines the value of weighting factors. The value of the prediction horizon affects the overshoot of the system [41]. Also, The lower and upper bounds of the control signal determine the maximum value of $\sigma_v$ [34]. The performance and the computational outlay of the proposed algorithm depend on the number of particles.

**TABLE I**
Parameters of RCLSJ Problem

| Parameter | Master Model | Slave Model |
|---|---|---|
| $\beta_C$ | -0.05 | 0.707 |
| $\beta_L$ | 2.6 | 2.6 |
| $i_0$ | 0.9 | 1.20 |

The slave system phase portrait has been shown in Fig. 6 (a) for the initial conditions (0.8,0.5,0.4). As can be seen, the slave system has chaotic behavior for these parameters and initial conditions. Fig. 6 (b)-(d) show the phase difference between the two superconductors at the junction, voltage, and current, respectively. The results of these initial conditions show that the value of phase difference has an unstable and incremental behavior over time, while the values of voltage and current show an oscillatory behavior. This oscillatory behavior in the Josephson junction characteristic curve will be unfavorable in the form of a high-frequency system, and controlling this chaotic behavior is required in order to use this segment in the middle class of a system.

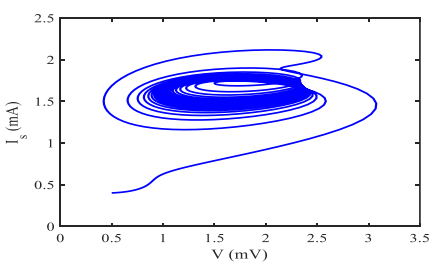

(a) the phase portrait

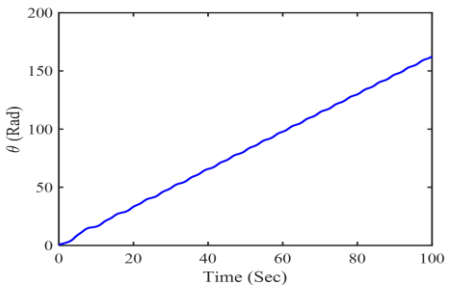

(b) the phase difference

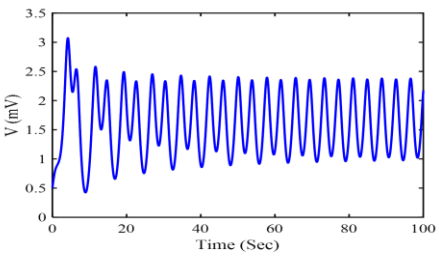

(c) the voltage

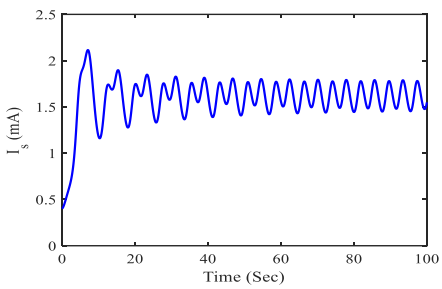

(d) the current versus time

**Fig. 6** The slave system: (a) the phase portrait; (b) the phase difference; (c) the voltage; (d) the current versus time.

Moreover, the master system phase portrait has been shown in Fig. 7 (a) for the initial conditions (0,0,0). The master system has stable behavior for these parameters and initial conditions. Fig. 6 (b)-(d) show the phase difference, voltage, and current, respectively. It is clear that the two systems are definitely unsynchronized for different initial conditions. As can be seen in Fig. 7, if the current through the junction is varying with time then the phase difference across it must also be changing with time, and it can be shown, Eq. (9), that a voltage V is developed across it, related to the rate of the phase difference.

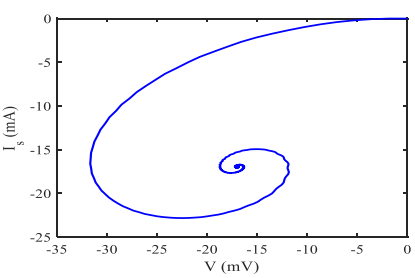

(a) the phase portrait

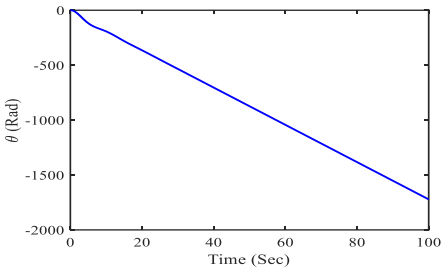


(b) the phase difference

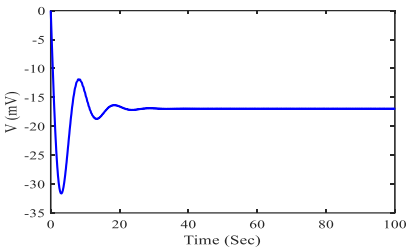


(c) the voltage

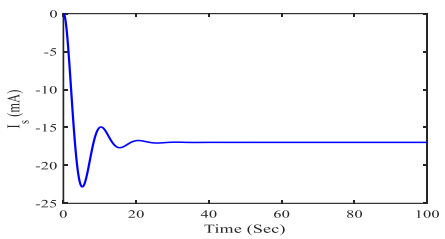


(d) the current versus time

**Fig. 7**. The master system: (a) the phase portrait; (b) the phase difference; (c) the voltage; (d) the current versus time

Fig. 8 shows the state variables of the master and slave systems. As shown in Fig. 8 (a)-(c), the objective is to synchronize the slave system with the master system. In this simulation scenario, the desired value of the phase difference is a ramp with slope -17 Rad, the desired values of the voltage is -17 V, and the desired values of the current is -17 mA. By comparing the simulation results, it is clear that the system has improved from its chaotic behavior and shows a stable manner. The results show that the phase difference, the voltage, and the current of the slave system will reach the desired value after about 3, 3, and 4 seconds, respectively.

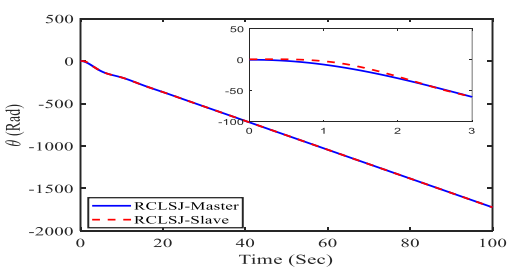


(a) phase difference

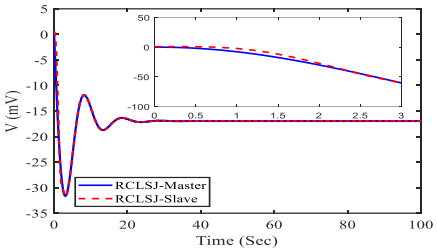


(b) voltage

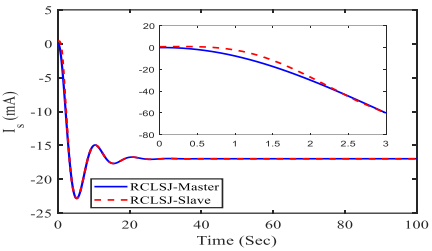


(c) current versus time.

**Fig. 8**. The state variable of the slave and master systems when the controller is applied: (a) phase difference; (b) voltage; (c) current versus time.

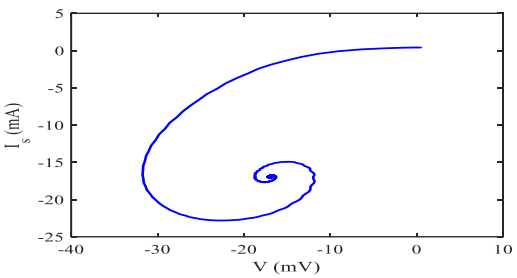


**Fig. 9.** Slave system phase plane when the controller is applied

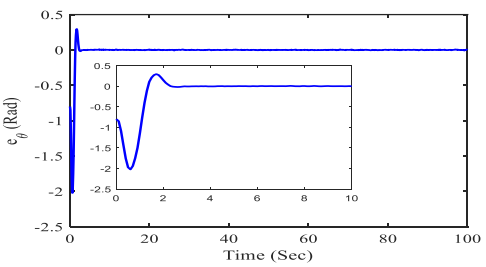


(a) Phase difference tracking error

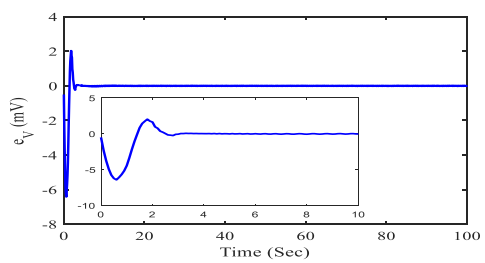


(b) voltage tracking error

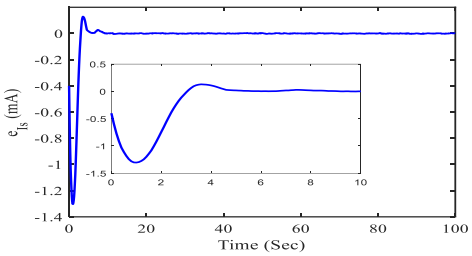


(c) current tracking error when the controller is applied.

**Fig. 10.** The tracking error of state variables: (a) Phase difference tracking error; (b) voltage tracking error; (c) current tracking error when the controller is applied.

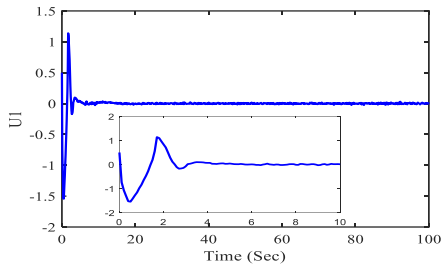


(a) $u_1$ versus time

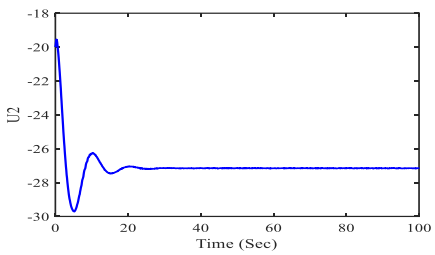


(b) $u_2$ versus time

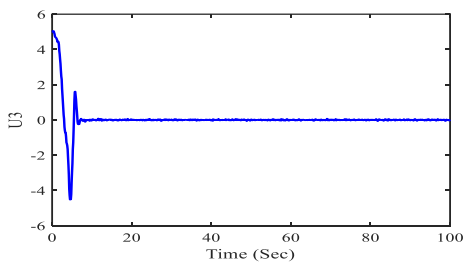


(c) $u_3$ versus time

**Fig. 11**. Control signals versus time: (a) $u_1$ versus time; (b) $u_2$ versus time; (c) $u_3$ versus time

Fig. 9 shows the slave system phase plane when the controller is applied. It is clear that the slave systems are now well synchronized and have a stable response. Fig. 10 (a)-(c) illustrates the tracking error of the state variables. As can be seen in Fig. 10, the error dynamics of state variables have been reached zero. Furthermore, the simulation results show how these control signals are able to make the two systems synchronized. For additional investigation, Fig. 11 shows the time history of the control signals. As can be seen, the control signals become stable after a while. Also, the performance of the suggested controller is compared with the Proportional Integral Derivative (PID) controller and sliding mode controller [21]. For assessment, certain criteria, including Integral of Time multiplied Absolute Error (ITAE), Integral of Absolute Error (IAE), Integral of Time multiplied Square Error (ITSE), and Integral of Square Error (ISE) are calculated for the three system state variables. Control effort is also calculated to show energy consumption and their values are shown in TABLE II. For this purpose, the mean square integral of the control signals is calculated. Parameters of the PID controller are as: $P = 6.7$ , $I = 0.6$ , and $D = 2.1$ . These parameters are achieved using the Ant Colony optimization algorithm to minimize the IAE. As shown in Table 2, results demonstrate the benefit of the suggested method in comparison with the PID and [21]. Fig. 12 compares the performance of the proposed algorithm with [21]. As presented in Fig. 12, the overshoot and the settling time of the proposed controller are less than those of [21]. Also, a Monte Carlo [42] simulation is achieved to compute the statistical performance and convergence of the suggested control algorithm. For this purpose, the ISE is calculated for the tracking error of the voltage. The average of the ISE versus the number of runs is shown in Fig. 13 for 50, 100, 200, and 500 runs. According to Fig. 13, performing 100 runs seems to be enough for convergence of the statistical properties.

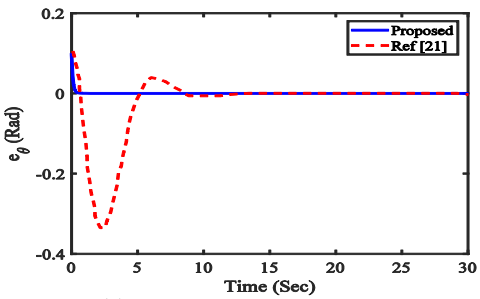


(a) Phase difference tracking error

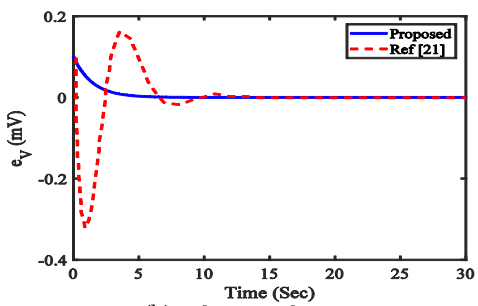


(b) voltage tracking error

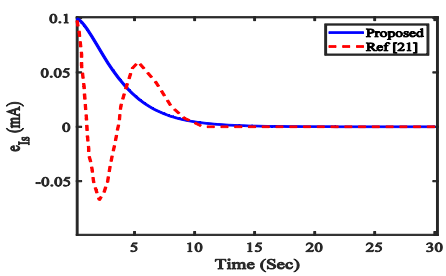


(c) current tracking error

**Fig. 12**. Comparison with reference [21]: (a) Phase difference tracking error; (b) voltage tracking error; (c) current tracking error

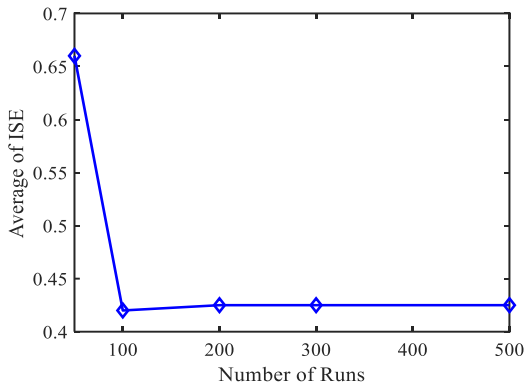


**Fig. 13** Average of the ISE versus the number of run

**TABLE II**
Comparison of the Proposed Controller with PID and Ref [21]

| Controller | Control effort | State variable | Time | ISE | IAE | ITSE | ITAE |
|---|---|---|---|---|---|---|---|
| Proposed control algorithm | $2.45\times10^5$ | $\theta$ | 20 | 2.54 | 4.75 | 0.46 | 4.79 |
| | | $V$ | | 0.66 | 6.56 | 1.25 | 40.75 |
| | | $I_s$ | | 10.46 | 13.94 | 7.36 | 14.51 |
| PID | $2.84\times10^5$ | $\theta$ | 20 | 2.83 | 4.98 | 0.52 | 5.01 |
| | | $V$ | | 0.74 | 6.85 | 1.51 | 42.34 |
| | | $I_s$ | | 11.01 | 14.21 | 7.79 | 14.86 |
| Proposed control algorithm | $3.34\times10^5$ | $\theta$ | 30 | 0.09 | 1.33 | 0.02 | 0.83 |
| | | $V$ | | 0.12 | 1.59 | 0.02 | 0.76 |
| | | $I_s$ | | 0.06 | 1.19 | 0.11 | 2.58 |
| Ref [21] | $3.79\times10^5$ | $\theta$ | 30 | 1.29 | 5.82 | 2.97 | 14.18 |
| | | $V$ | | 1.02 | 5.12 | 1.23 | 8.33 |
| | | $I_s$ | | 0.19 | 2.44 | 0.15 | 4.66 |

To achieve the effect of some parameters in the proposed control algorithm based on PF, a sensitivity evaluation is done on the error signal. The effect of the number of particles has been illustrated in Fig.14 (a). As can be seen, reducing the value of particles increases the error. Fig.14 (b) illustrate the effect of the prediction horizon. Increasing the value of the prediction horizon reduces overshoot. Moreover, reducing the weight of the tracking error to 10 causes the divergence of the error. The authors have implemented proposed controller in MATLAB, and a computer with a Core 5 Duo 2.9 GHz CPU and 4 GByte RAM is used for simulation. The computing time for one step of the problem, is approximately 0.0089 sec, while the sampling time of this problem is 0.01 sec.

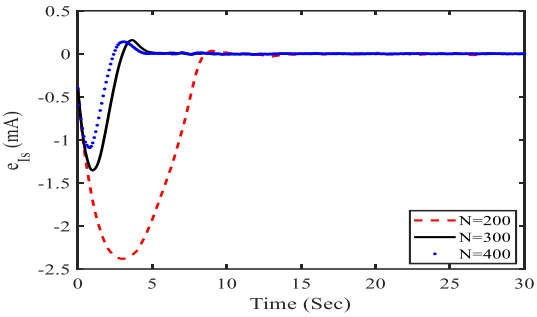


(a) effect of particle numbers

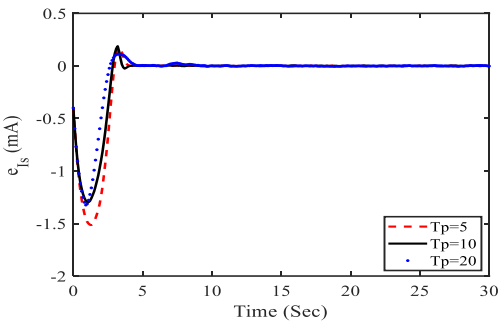


(b) prediction horizon

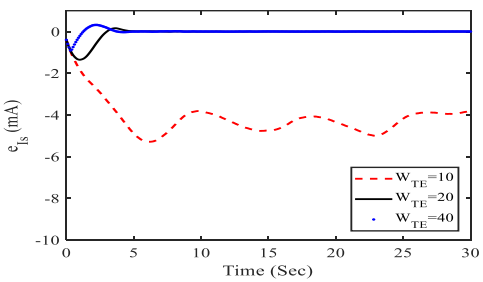


(c) the weight of tracking error

**Fig. 14** Sensitivity evaluation of the offered control algorithm: (a) effect of particle numbers; (b) prediction horizon; (c) the weight of tracking error

### *A. Processor in the Loop Experiment*

In this section, the proposed control algorithm is evaluated through a PIL experiment. PIL is used to show the implementation capability of the algorithm [43]. Schematic of the experiment is illustrated in Fig. 15. To perform the PIL experiment, "Simulink Real-Time" is utilized. Simulink Real-Time [44] enables real-time execution of the pursuer-target simulation model. Moreover, the "run on hardware" tool compiles C code generating from the proposed algorithm and programs the hardware device (Arduino Due) using the Simulink Coder. A serial link is used to send the outputs of the pursuer-target simulation to the hardware. The hardware device calculates the pursuer acceleration command and sends it back to the computer to simulate the pursuer-target engagement in the next time step. Results of the PIL experiment are shown in Fig. 16. Comparison of the implementation results and the numerical simulation are provided in Fig. 16 (a) and (b) for the Phase difference tracking

error and the control signal, respectively. These results demonstrate that the proposed algorithm has been successfully implemented on the processor. Ideally, the PIL test and simulation results should be the same. There are small differences between the experimental results obtained using the PIL test and the simulation results. These differences are usually caused by practical problems such as the delay of received packets and the stochastic nature of the noise from one experiment to another. By using the User Datagram Protocol (UDP) protocol, instead of serial connection, send and receive data is done without any connection delay and reliable packets.

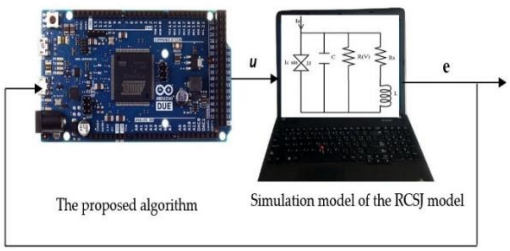


**Fig. 15.** Schematic of the PIL experiment used to verify the proposed algorithm

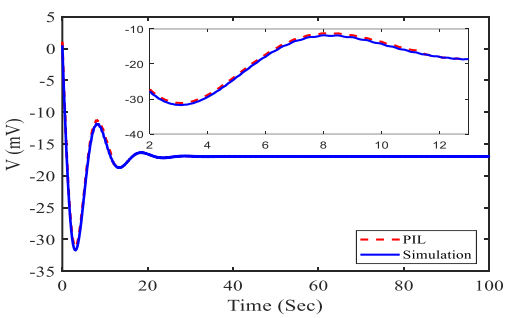


(a) the voltage versus time

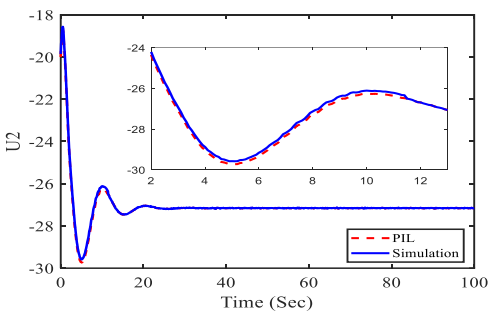


(b) the control signal versus time.

**Fig. 16**. Comparison of the PIL experiment with numerical simulation: (a) the voltage versus time; (b) the control signal versus time.

## V. Conclusion

In this paper, a control approach based on the generic particle filter was proposed to synchronize two Josephson junction models with different parameters. For this purpose, an appropriate cost function was defined to calculate the particles within the state space. The synchronization was obtained using the slave–master technique. Here, Josephson junction is described with Resistive Capacitive Inductive Shunted Josephson model. Moreover, the implementation of the proposed algorithm on a target platform was conducted successfully through the PIL experiment. A Monte Carlo simulation was done to calculate the statistical performance of the offered algorithm. The performance of the suggested method was compared with the PID and sliding mode controller. Also, a sensitivity evaluation was done on the error signal to achieve the effect of the controller parameters. The results show that the offered approach can effectively synchronize two Josephson junction models with different parameters. Clearly, there are some weaknesses. First, calculating the analytical stability of the proposed algorithm is hard. Secondly, in some cases, one cannot say anything about the number of particles needed for calculating the control signals. For future work, it is recommended to work on these two weaknesses. That is, to prove the stability analytically and to present a systematic method for the optimal determination of the number of particles.

## References

[1] KK. Likharev, *Dynamics of Josephson Junctions and Circuits*, 1th ed, Gordon and Breach science publishers, 1986.

[2] SK. Dana, DC. Sengupta, KD.Edoh, “Chaotic Dynamics in Josephson Junction”. *IEEE Trans Circuits Syst I Fundam Theory*, Vol. 48, No. 8, pp. 990-996, Apr 2001.

[3] F. Salam, S.Sastry, “Dynamics of the Forced Josephson Junction Circuit: the Regions of Chaos”. *IEEE Trans Circuits Syst*, Vol. 32, No. 8, pp. 784-796, Aug 1985.

[4] H. Mehrara, F. Raissi, A. Erfanian, “Vortex-Antivortex Pair Interaction With Microwave Standing Waves: A Chaos Analysis of Josephson Fluxonic Diode for Microwave Applications”, *IEEE Trans Appl Supercond*, Vol. 29, No. 7, pp. 150-158, Oct 2019.

[5] B. Rezaie, M.R.J. Motlagh, M. Analoui, S. Khorsandi, “Stabilizing fixed points of time-delay systems close to the Hopf bifurcation using a dynamic delayed feedback control method”, *J. Phys. A Math. Theor*, Vol. 42, No. 39, pp. 1-24, Sep 2009.

[6] S.H. Shahalami, F. Rajab Nejad, “Design of Adaptive Back-Stepping Controller for Chaos Control in Boost Converter and Controller Coefficients Optimization Using CHPSO Algorithm”, *Int. J. Ind. Electron. Control Optim*, Vol. 3, No. 3, pp. 249–257, Sum 2020.

[7] K. Akbari, B. Rezaie, S. Khari, “Designing full-order sliding mode controller based on ANFIS approximator for uncertain nonlinear chaotic systems”, *Int. J. Ind. Electron. Control Optim*, Vol. 2, No. 1, pp. 39–46, Win 2019.

[8] C. Eichler, A. Wallraff, “Controlling the Dynamic Range of a Josephson Parametric Amplifier”, *EPJ Quantum Technol*, Vol. 1, No. 2, pp. 1–19, Dec 2014.

[9] S.P. Benz, C.A. Hamilton, “Application of the Josephson effect to voltage metrology”. *Proc. IEEE, pp.* 1617–1629, 2004.

[10] DS. Goldobin, LS. Klimenko, “Resonances and Multistability in a Josephson Junction Connected to a Resonator”, *Phys Rev E*, Vol. 97, No. 2, pp. 022203, Feb 2018.

[11] J. Diggins, JF. Ralph, TP. Spiller, TD. Clark, H. Prance, RJ. Prance, et al, “Chaos Generated Noise in Radio Frequency

SQUID Magnetometers". *AIP Conf. Proc.*, Vol. 371, Apr 1996

[12] F. Raissi, A. Khooshemehri, A.Erfanian, "Three-Terminal Superconducting Digital Transistor". *IEEE Trans Appl Supercond*, Vol. 29, No. 4, pp. 1-6, Dec 2018.

[13] CA. Donnelly, JA. Brevik, NE. Flowers-Jacobs, AE. Fox, PD. Dresselhaus, PF. Hopkins, et al, "Quantized Pulse Propagation in Josephson Junction Arrays", *IEEE Trans Appl Supercond*, Vol. 30, No. 3, pp. 1-8, Jul 2019.

[14] Y. Zhang, P. Zhou, J. Tang, J. Ma, "Mode selection in a neuron driven by Josephson junction current in presence of magnetic field", *Chinese J. Phys*, Vol. 71, No. 1, pp. 72–84, Jun 2021.

[15] Y. Zhang, Y. Xu, Z. Yao, J. Ma, "A feasible neuron for estimating the magnetic field effect", *Nonlinear Dyn*. Vol. 102, No. 3, pp. 1849–1867, Nov 2020.

[16] A. Uçar, KE. Lonngren, E-W, Bai, "Chaos Synchronization in RCL-Shunted Josephson Junction Via Active Control". *Chaos, Solitons & Fractals*, Vol. 31, No. 1, pp. 105–111, Jan 2007.

[17] AM. Harb, BA. Harb, "Controlling Chaos in Josephson-Junction Using Nonlinear Backstepping Controller". *IEEE Trans Appl Supercond*, Vol. 16, No. 4, pp. 1988-1998, Dec 2006.

[18] UE. Vincent, A. Ucar, JA. Laoye, SO. Kareem, "Control and Synchronization of Chaos in RCL-Shunted Josephson Junction Using Backstepping Design". *Phys C Supercond*, Vol. 485, No. 5, pp. 374-382, Mar 2008.

[19] A.N. Njah, K.S. Ojo, G.A. Adebayo, A.O. Obawole, "Generalized control and synchronization of chaos in RCL-shunted Josephson junction using backstepping design", *Phys. C Supercond*, Vol. 470, No. 13, pp. 558–564, Jul 2010.

[20] AM. Harb, BA. Harb, "Chaos Synchronization in Josephson Junctions". *J Supercond Nov Magn*, Vol. 25, No. 6, pp. 1647-1653, Aug 2012.

[21] D-Y. Chen, W-L. Zhao, X-Y. Ma, R-F. Zhang, "Control and Synchronization of Chaos in RCL-Shunted Josephson Junction with Noise Disturbance Using Only One Controller Term". *Abstr. Appl. Anal.*, Vol 2012, No. 1, pp. 1-15, Jul 2012.

[22] C.-K. Cheng, P.C.-P. Chao, "Trajectory tracking between Josephson junction and classical chaotic system via iterative learning control", *Appl. Sci*. Vol. 8, No. 8, pp. 1285, Aug 2018.

[23] C-K .Cheng, PC-P. Chao, "Chaos Synchronization Between Josephson Junction and Classical Chaotic System via Iterative Learning Control". IEEE Int. Conf. Appl. Syst. Invent, pp. 1232–5, Jun 2018.

[24] TBT. Nguyen, "Adaptive MIMO Controller Design for Chaos Synchronization in Coupled Josephson Junctions via Fuzzy Neural Networks". *J Adv Eng Comput*, Vol. 1, No. 1, pp. 80-86, Dec 2017.

[25] K.S. Ojo, A.N. Njah, O.I. Olusola, M.O. Omeike, "Generalized reduced-order hybrid combination synchronization of three Josephson junctions via backstepping technique", *Nonlinear Dyn*, Vol. 77, No. 3, pp. 583–595, Aug 2014.

[26] E. Camacho, Alba C. *Model Predictive Control*, Springer science & business media, 2013.

[27] M. Ehsani, M. Saeidi, H. Radmanesh, A. Abrishamifar, "Comparisons between Generalized Predictive Control and Linear Controllers in Multi-Input DC-DC Boost Converter", *Int. J. Ind. Electron. Control Optim*. Vol. 3, No. 1, pp. 27–34 , Win 2020.

[28] H. Radmanesh, M. Saeidi, "Linear Modelling of Six Pulse Rectifier and Designee of Model Predictive Controller with Stability Analysis". *Int. J. Ind. Electron. Control Optim*, Vol. 3, No. 4, pp. 491–501, Sum 2020.

[29] M. Heidari, "Maximum Wind Energy Extraction by Using Neural Network Estimation and Predictive Control of Boost Converter", *Int. J. Ind. Electron. Control Optim*. Vol. 1, No. 2 pp. 115–120, Sum 2018.

[30] S. Jalili, B. Rezaie, Z. Rahmani, "A novel hybrid model predictive control design with application to a quadrotor helicopter". *Optim. Control Appl. Methods*, Vol. 39, No. 4, pp. 1301–1322, Jul 2018.

[31] A. Mirzaei, A. Ramezani, "Cooperative distributed constrained model predictive control for uncertain nonlinear large scale systems". *Int. J. Ind. Electron. Control Optim*. Vol. 4, No. 1, pp. 87-98, Jan 2020.

[32] H. Nobahari, S. Nasrollahi, "A Non-Linear Estimation and Model Predictive Control Algorithm Based on Ant Colony Optimization". *Trans Inst Meas Control*, Vol. 41, No. 4, pp. 1123-1138, Feb 2019.

[33] S. Botchu, S. Ungarala, "Nonlinear Model Predictive Control Based on Sequential Monte Carlo State Estimation". *IFAC Proc*, Vol. 40, Jan 2007.

[34] D. Stahl, J. Hauth , "PF-MPC: Particle Filter-Model Predictive Control". *Syst & Control Lett*, Vol. 60, No. 8, pp. 632-643, Aug 2011.

[35] M. Sarailoo, Z. Rahmani, B. Rezaie, "A Novel Model Predictive Control Scheme Based on Bees Algorithm in a Class of Nonlinear Systems: Application to a Three Tank System". *Neurocomputing*, Vol. 152, No. 1, pp. 294-304, Mar 2015.

[36] F. Rajabi, B. Rezaie, Z. Rahmani, "A Novel Nonlinear Model Predictive Control Design Based on a Hybrid Particle Swarm Optimization-Sequential Quadratic Programming Algorithm: Application to an Evaporator System". *Trans Inst Meas Control*, Vol. 38, No. 1, pp. 23-32, Dec 2016.

[37] T. Van Duzer, CW. Turner, *Principles of Superconductive Devices and Circuits*, Edward Arnold, USA, 1981.

[38] D. Simon, *Optimal state estimation: Kalman, H infinity, and nonlinear approaches*; John Wiley & Sons, 2006.

[39] M.S. Arulampalam, S. Maskell, N. Gordon, T. A Clapp, "Tutorial on particle filters for online nonlinear/non-Gaussian Bayesian tracking " *Signal Process IEEE Trans*, Vol. 50, No. 2, pp. 174–188, Aug 2002.

[40] B. Ristic, S. Arulampalam, N. Gordon, *Beyond the Kalman filter: Particle filters for tracking applications*, Artech house Boston Press, 2004.

[41] J.A. Rossiter, *Model-based predictive control: a practical approach*, CRC press, 2003.

[42] R.Y. Rubinstein, D.P. Kroese, *Simulation and the Monte Carlo method*, John Wiley & Sons press, 2016.

[43] H. Nobahari, Hadi, S. Nasrollahi, "A nonlinear robust model predictive differential game guidance algorithm based on the particle swarm optimization", *J Franklin Inst*, Vol. 357, No. 15, pp. 11042-11071, Aug 2020.

[44] A. Kurniawan, *Getting Started with Matlab Simulink and Arduino*, PE Press, 2013.

**Aylar Khooshehmehri** received the B.S degree in Electrical Engineering from K. N. Toosi University of Technology, Tehran, Iran, in 2007. Also, she received the M.S. and PhD degree in Electrical Engineering from Malek-Ashtar University of Technology in 2011 and 2018,

respectively. Her research interests include superconducting amplifying and detector devices, MEMS, HRG and semiconductor field effect devices.

**Saeed Nasrollahi** received the B.S. and M.S. degrees in Electrical Engineering from Malek-Ashtar University of Technology, Tehran, Iran, in 2007 and 2010, respectively. Also he received Ph.D. degree in aerospace engineering from Sharif University of Technology in 2019. He is currently working as an assistant professor at the electrical engineering department at the Malek-Ashtar University of Technology. His research interests are nonlinear control, model predictive control, nonlinear estimation, and their application in guidance and navigation.

**Morteza Aliyari** was born in Zanjan province, Iran in 1996. He received his bachelor in Electrical Engineering, Control Systems field in 2015. He has hands-on experience in robotic, artificial intelligence and path planning. He was a member of the robotic group which attended at FIRA cup competition and accomplished the third rank of competition. In 2017, he received his master degree in the same field and work as a research assistant in the same university concurrently. His current research interests include robotics, UAVs, Path planning, Navigation, FOG and RLG sensors.

International Journal of Industrial Electronics, Control and Optimization. © 2021 IECO
Vol. 4, No. 3, pp. 367-376, July (2021)

# Determining the Necessity and Timing of Controlled Islanding in Power System: a wide-area intelligent-based method

Hojatollah Makvandi[1], Mahmood Joorabian[2, †], Hassan Barati[3]

[1,3] Department of Electrical Engineering, Dezful Branch, Islamic Azad University, Dezful, Iran
[2]Department of Electrical Engineering, Faculty of Engineering, Shahid Chamran University of Ahvaz, Ahvaz, Iran

**ABSTRACT**

*The present study introduces a new extensive-area ANFIS (Adaptive Neuro-Fuzzy Interface System)-based method to detect wide area instability and control the time of controlled islanding execution within power systems. The ANFIS parameters are optimized by the PSO method to increase the method's accuracy at various disturbances and loading circumstances. In addition, to take various stability margins within the areas into account, a novel parallel ANFIS network (P-ANFIS) is implemented in which a distinct ANFIS is allocated for every nearby area. Extended off-line studies are performed to train ANFIS to respond in real-time accurately based on the selected wide area input signals. These parameters are monitored continuously through a wide area measurement system (WAMS) and the proposed P-ANFIS starts to assess the stability between related areas in real-time in the case of potentially unstable oscillations. Once an unstable oscillation is detected, the islanding command is transmitted to perform the controlled islanding scheme. The suggested technique is used in an IEEE 39 bus power system and its performance is demonstrated at different disturbances in terms of both speed and accuracy. It is found that the suggested ANFIS-based technique can determine islanding requirement and its time of execution properly at different disturbances.*

**Article Info**

***Keywords:***
ANFIS, Islanding detection, PSO, WAMS

***Article History:***
**Received** 2020-09-15
**Accepted** 2021-04-02

## NOMENCLATURE

| | |
|---|---|
| $\delta_i$ | Rotor angle of generator *i* |
| $\delta_j$ | Rotor angle of generator *j* |
| $x_i$ | *i*th particle |
| *pbesti* | the best former position of $x_i$ |
| *gbest* | is the best particle between the whole population |
| $t^{initials}$ | the time of simulation starting in transient stability studies |
| $t^{final}$ | the time of simulation ending in transient stability studies |
| $\mu$ | Threshold value for coherency determination between generators |
| $\mu_{A_j^i}(x)$ | Membership function for the ith input variable |
| $\Delta\bar{\delta}_{\mathrm{COI}_{m,n}}$ | difference of the center-of-inertia (COI) of rotor angles of two preliminary areas |
| $N_t$ | number of units in area *m* |
| $N_k$ | number of units in area *n* |
| $M_t$ | total inertia of *t*th group based on $N_j$ generators |
| $\Delta\bar{\theta}_{m,n}$ | Difference of the average voltage angles between two areas *m* and *n* |
| $\theta_i$ | Buses' voltage angles in group *m* |
| $\theta_j$ | Buses' voltage angles in group *n* |
| $\Delta\bar{\omega}_{m,n}$ | Average frequency difference between two areas *m* and *n* |

**†Corresponding Author**: mjoorabian@scu.ac.ir
Tel: +98-9161183017, Department of Electrical Engineering, Faculty of Engineering, Shahid Chamran University of Ahvaz, Ahvaz, Iran

## I. INTRODUCTION

Wide-area asynchronous oscillations and local distance operations relay in response to these oscillations is the main reason for some recent blackouts [1-2]. These oscillations are propagated in the power system from the initial happening location and could result in the initiation of a cascade outage and considerable power outages [3-4]. The controlled islanding application is the last resort protective scheme in power systems to stop disturbance propagation and avoid wide-area blackouts [5]. One of the main parts of controlled islanding is its necessity and execution time [6]. The controlled islanding should be performed correctly to avoid unnecessary disconnection of lines between areas. In addition, the islanding command should be sent fast once unstable oscillations between areas are detected [7]. The conventional way to this action is the installation of local R-Rdot relays in predetermined interconnected lines to act once unstable oscillations are detected. But, the performance of these local relays at different scenarios and network structures is not satisfactory because of the offline setting and anticipated oscillations in power systems.

A decision tree (DT) is introduced in [8] to detect wide-area instability and send arming signals to the installed local relays. By this method, the unwanted operation of these local relays is avoided and islanding execution can be performed at proper locations. The coherent areas of the network are determined offline and different DTs are assigned to each of them for stability assessment. In this method, the confidence level of different DTs is investigated and a final decision is made based on the outputs of different DTs.

In [9], a neural network technique is used to detect islanding requirements. The recurrent neural network is trained offline to detect and send the islanding command in the case of unstable oscillations. The Lyapunov Maximal Exponent (LME) method is another wide area-based method for real-time stability assessment and the determination of asynchronous oscillations based on WAMS data [10]. The positive LME value represents the loss of generators' synchronism within the network. However, as mentioned in [11], the performance of this method is highly dependent on the selected input data time interval and the algorithm applied for LME computation. It should be indicated that the islanding detection technique could distinguish between inter-area and local oscillations and respond only to the latter [12-13].

In [14], controlled islanding time is determined by using new indices. In this method, by applying the concept of inertia for coherent generators and modeling two oscillating areas with a Generalized Single Machine Infinite Bus System (GSMIB) model, an equivalent power-angle curve is derived from which equivalent Unstable Equilibrium Point (UEP) point associated with the inter-area oscillation is evaluated. The curve is, then, used to derive new instability indices associated with inter-area oscillation. In [15], a splitting strategy is developed as an MILP problem considering coherency and frequency stability constraints. A switching constraint and a frequency stability

constraint are proposed to limit the number of line switchings and assure the stability of the resulted islands, respectively. The switching constraint proposed in this paper reduces the searching space of splitting strategies and the Benders Decomposition (BD)-based algorithm shortens the calculation time.

In [16], a straightforward multi-solution approach is proposed in which a hierarchical spectral clustering algorithm is used. Its power system islanding algorithm is based on the minimum active power flow disruption approach. The most convenient islanding scenario can be selected by a desired secondary objective function to satisfy the operational requirements. The proposed algorithm is based on an improved hierarchical clustering theory to have the ability to accompany the generator coherency constraint in the clustering process. In [17], by analyzing the voltage frequency characteristics of an electrical center and a non-electrical center at different voltage amplitude ratios for the out-of-step condition of the power grid, an out-of-step splitting criterion based on bus voltage frequency is presented.

In this study, a novel extensive-area intelligent scheme is constructed based on the ANFIS algorithm for detecting controlled islanding necessity and its execution time fast and accurately. The power system is split into different initial coherent areas based on offline stability works at various loading conditions and disturbances. Any of these initial areas could be separated and form inherent stable islands based on the location of disturbances or could be aggregated together and form larger stable islands. The network oscillations are monitored continuously after disturbance occurrence and final coherency is determined in real-time on the basis of WAMS data. The distinct ANFIS is allocated to each nearby initial area for stability investigation optimized by the PSO method. As an unstable inter-area oscillation is found by the proposed technique and the islanding command is sent, the related areas are separated as soon as possible. A comparison is also made for the proposed intelligent method's performance and the ANN method [9] in an IEEE 39-bus power system at two various cases.

## I. CONTROLLED ISLANDING TIMING

The islanding execution time is a key element to obtain a reliable and effective controlled islanding structure within large interconnected power systems [7]. As a result of asynchronous inter-area oscillations, the network needs to be divided into stable islands prior to the uncontrolled separation

of the network. Figure 1 presents the proposed algorithm's flowchart for determining the real islanding execution time. In this algorithm, WAMS measurement plays a critical role in providing wide-area information to the algorithm. Like [9], to have an adaptive and fast scheme in real-time, many actions should be performed in offline and online steps. These actions are explained in the following sections.

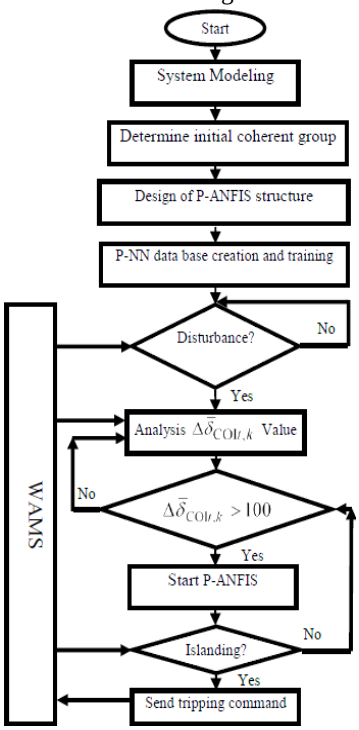


**Fig. 1.** The flowchart of the proposed scheme

## II. Offline Actions

The main procedures in the offline part tend to increase the speed and accuracy of islanding detection. As shown in the following sections, these steps include system modeling, the determination of initial areas, and ANFIS training.

### *A. System modeling*

System modeling consists of two steps, i.e., static and dynamic modeling. In addition to static data such as the nominal voltages of buses, the length of lines, the capacity of transformers, impedances, and load values, the dynamic data of the studied power system such as the parameters of generators, AVRs, and governors are modeled.

### *B. Determination of initial areas*

The coherency of generators is altered based on the disturbance location and network structure. In this step, the initial areas consisting of coherent generators at different conditions are determined based on offline studies. The coherency of the generators in these initial areas is kept at different loading conditions and disturbances in interconnected lines. The final coherent areas following different disturbances are determined in real time based on the COI of rotor angle between adjacent initial areas.

To determine the initial coherency, the criteria are used as shown in (1). The parameters $\delta_i$ and $\delta_k$ indicate the rotor angle of generators $i$ and $k$, respectively. The value of 120 degrees is applied for μ and the total time of simulation is selected to be 10 seconds.

$$\left|\delta_i(t) - \delta_k(t)\right| \le \mu \qquad t^{initial} \le t \le t^{final} \tag{1}$$

This study is performed at three different loading conditions including the outage of network elements following different disturbance locations.

The output of this step is potential islands whose generators are stable and could be merged with stable adjacent areas to form larger islands with respect to disturbances and network configuration.

## III. The Proposed P-ANFIS Structure

As mentioned in [12] and is derived by offline stability, the stability margins between adjacent areas are different based on the loading circumstances and their connections before and after disturbances. The stability margins are higher for highly meshed areas than for weaker interconnected areas. These differences could not be accounted for by the single ANFIS structure with inputs from all of the areas. Therefore, the new parallel ANFIS (P-ANFIS) is constructed (Fig. 2). At this scheme, a distinct ANFIS is allocated for each of the two nearby primary groups that are responsible for investigating the stability between them in real-time. Each ANFIS of P-ANFIS is trained separately with proper related wide-area inputs.

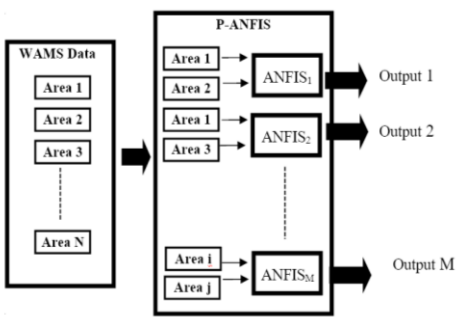


**Fig. 2.** The planned P-ANFIS structure

### *A. Individual ANFIS structure*

The ANFIS structure used here is a 3-structure type with five different layers as shown in Fig. 3 [18]. Considering a first-order Sugeno fuzzy model possessing one output and two inputs, the rules are organized as follows:

*First rule*: If $x$ is $A_1$ and y is $B_1$, then $f_1 = p_1x + q_1y + r_1$

*Second rule*: If $x$ is $A_2$ and y is $B_2$, then $f_2 = p_2x + q_2y + r_2$

The Gaussian membership functions are utilized for input

and output variables. Therefore, the *j*th membership function for the *i*th input variable is [19]:

$$\mu_{A_j^i}(x) = exp(-(\frac{x_i - c_i^j}{a_i^j})^2) \quad (2)$$

where ai and ci denote the width and center of the associated membership function, respectively.

Layer 1: Here, every node i represents a square node with a node function of:

$$O_i^1 = \mu_{A_i}(x) \quad (3)$$

in which *x* denotes the input to node *i* and *A* represents the linguistic label (small and large) connected to this node function.

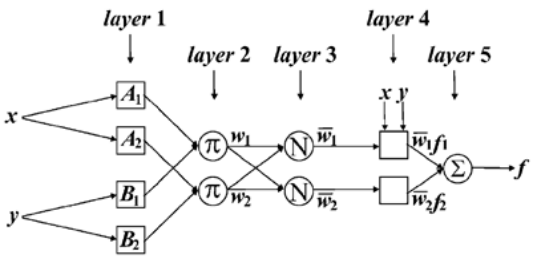


**Fig. 3.** The ANFIS 3-structure type

Second layer: The output is the product of all arriving signals. Here, every output node provides a rule's firing strength.

$$O_i^2 = \omega_i = \mu_{A_i}(x).\mu_{B_i}(y) \quad ,i = 1,2 \quad (4)$$

Layer 3: Here, the outputs, termed the normalized firing strengths, are determined as follows:

$$O_i^3 = \bar{\omega}_i = \frac{\omega_i}{\omega_1 + \omega_2} \quad ,i = 1,2 \quad (5)$$

Layer 4: This layer's node function is:

$$O_i^4 = \bar{\omega}_i\ f_i = \bar{\omega}_i\,(p_i x + q_i y + r_i) \quad (6)$$

The elements of the parameter set are determined as the consequent parameters, $\{p_i, q_i, r_i\}$.

*Fifth layer*: The general output is determined as the sum of all incoming signals through the following equation.

$$O_i^5 = \sum_i \bar{\omega}_i\ f_i = \frac{\sum_i \omega_i\ f_i}{\sum \omega_i} \quad (7)$$

As mentioned in [19], these two parameters are much effective in ANFIS performance and there is no straightforward procedure for their determination. Therefore, the PSO is used in this paper to optimally determine these two parameters.

### B. Particle swarm optimization

Particle Swarm Optimization (PSO) is a population-based search algorithm that was first presented by Eberhart and Kennedy and is extensively used to solve numerous optimization problems [20]. As shown in [21], the optimization procedure can be classified into 6 steps from the initialization step to the output result, which gives the best solution within the optimization procedure. The updating rules for the PSO algorithm are as follows:

$$v_i^{k+1} = w.v_i^k + c_1 \cdot rand_1(x_{pbesti} - x_i^k) + c_2 \cdot rand_2(x_{gbest} - x_i^k) \quad (7)$$

$$x_i^{k+1} = x_i^k + v_i^k \quad (8)$$

in which $c_1$ and $c_2$ denote the positive constants (as acceleration coefficients), *w* represents inertia weight factor, $rand_1$ and $rand_2$ denote random functions ranging in [0,1], $x_i$ denotes the *i*th particle, $pbest_i$ is the best former position of $x_i$, and *gbest* represents the best particle between the whole population. The parameter $v_i$ is the velocity of particle $x_i$.

### C. Hybrid learning by PSO and GD

The conventional way for ANFIS training including the backward and forward passes is the combination of both the backpropagation gradient descent algorithm and least-squares estimator. However, in this paper, the PSO and gradient descent are applied in ANFIS parameters updating in ANFIS training. The antecedent part with Gaussian membership function parameters including $\{a_i, c_i\}$ is updated through PSO while the gradient descent is used for updating conclusion parameters such as $\{p_i, q_i, r_i\}$ [22].

### D. P-ANFIS inputs -outputs

The following three parameters are selected as the P-ANFIS inputs that are measured by WAMS. The first parameter is shown in (8).

$$\Delta\bar{\delta}_{\mathrm{COI}_{m,n}} = (\frac{1}{M_t}\sum_{i=1}^{N_t} M_i\delta_i - \frac{1}{M_k}\sum_{i=1}^{N_k} M_i\delta_i) \quad (9)$$

$$, M_t = \sum_{i=1}^{N_j} M_i$$

in which $\Delta\bar{\delta}_{\mathrm{COI}_{m,n}}$ represents the differences in the COI (center-of-inertia) of the rotor angles between two adjacent determined initial areas, $N_t$ and $N_k$ denote the number of generators in two areas *m* and *n*, and $M_t$ represents the total inertia of the *t*th group. In addition to the signal presented in (8), another input signal is:

$$\Delta\bar{\theta}_{m,n} = (\frac{1}{N}\sum_{i=1}^{N}\theta_i - \frac{1}{M}\sum_{j=1}^{M}\theta_j) \quad (10)$$

In (8), the voltage angles between two areas *m* and *n* are averaged and their difference is used as the input. $\theta_i$ and $\theta_j$ denote the buses' voltage angles at two areas *m* and *n* with *N* and *M* PMUs. The average frequency difference ( $\Delta\bar{\omega}_{t,k}$ ) is:

$$\Delta\overline{\omega}_{m,n} = \frac{d\Delta\overline{\theta}_{m,n}}{dt} \quad (11)$$

The ANN inputs are the chosen signals in (8) to (10) and their five delayed values. The ANN's output is supposed as 0 for stable cases and 1 for unstable cases.

### *E. P-ANFIS Database*

A systematic approach is designed to create a proper database for ANFIS training based on comprehensive offline stability studies. To do this, the following operating conditions are investigated:

1-Three different loading conditions of the network

2-Considering the outage of elements in three different loading conditions

After constructing the above-mentioned operating conditions, the following systematic method is used at various network structures and loading circumstances:

Step 1: Three-phase and single-phase fault is used at various positions of the network with normal fault clearing time corresponding to the main protection relays.

Step 2: The fault clearing is increased to the corresponding time of back-up relays to consider the failure of the main protection systems.

Step 3: The second disturbance at different locations is applied following the first disturbance prior to the operations of the present corrective actions.

The generated data set containing input-output pairs is used to train every ANFIS in the proposed P-ANFIS.

## IV. On-line Actions

Two main actions are performed online including (i) disturbance detection and (ii) continuous monitoring of $\Delta\overline{\delta}_{\mathrm{COI}_{t,k}}$ after disturbance detection. The method proposed in [23-25] is used for disturbance occurrence in a power system based on monitoring both voltage magnitude and its rate of changes of generator buses with time. As the disturbance is detected, the signal introduced in (8) based on the COI-referred angle of each area is computed and fed continuously to the algorithm. By investigation of $\Delta\overline{\delta}_{\mathrm{COI}_{t,k}}$, the possible angle separation between areas is predicted. If the $\Delta\overline{\delta}_{\mathrm{COI}_{t,k}}$ value between any of the areas becomes larger than 100 degrees, the alarm signal is sent to the P-ANFIS to assess the network stability in real-time based on the input data from WAMS.

## V. Real-time Actions

The P-ANFIS assessed the stability between every nearby area that has a distinct ANFIS trained offline with proper inter-area-based signals that are measured through WAMS. As unstable inter-area oscillations are detected, (Output=O=1), the tripping signal is sent through WAMS to the P-ANFIS. To detect the asynchronous oscillations (output=*Y*=1) by every individual NNs, the tripping signal is sent via WAMPAC to separate the associated areas from each other. While the $\Delta\overline{\delta}_{\mathrm{COI}_{t,k}}$ values between areas become less than 100 degrees and remain for 5 seconds less than 100, the P-ANFIS analysis is stopped and wait for the next possible alarm to start stability assessment.

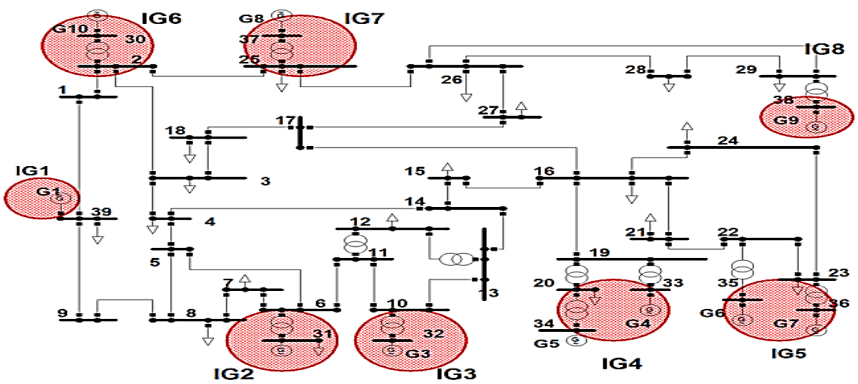


**Fig. 4.** The New England 39-bus and defined primary groups

## VI. Simulation Results

The behavior of the suggested P-ANFIS algorithm is assessed on a New England 39-bus power system.

### *A. The New England 39-bus system*

Figure 4 presents the single line chart of the New England 39-bus power system [26]. The initial areas determined offline are shown in Fig. 4 and agree with the FC-Mdd method applied in [9]. Here, two various cases are taken into account to represent the efficiency of the designed P-ANFIS structure. The performance of the proposed method is investigated with the proposed ANN technique [9].

### *B. Case study 1*

The faults applied in this case are as follows:

A three-phase fault is applied in lines 9-39 at 0.1s and is cleared 0.3s later by the outage of the line. Moreover, another fault occurs in 0.5s in lines 4-5 and is removed 0.2s later by line breakers. The rotor angle oscillation of generators is shown in Fig. 5. As can be seen, the network stability is lost following these disturbances. Three different coherent groups are identified and it is necessary to apply network islanding to avoid the wide-area blackout. The voltage magnitude of generator buses as a disturbance indicator is shown in Fig. 6. After the detection of disturbance occurrence, monitoring of $\Delta\bar{\delta}_{\mathrm{COI}_{t,k}}$ between initially determined areas is started by the proposed algorithm. As the $\Delta\bar{\delta}_{\mathrm{COI}_{t,k}}$ value between each of the areas exceeds the threshold value (100 degrees), the P-ANFIS starts stability assessment based on wide-area input signals.

Fig. 7 represents the $\Delta\bar{\delta}_{\mathrm{COI}_{t,k}}$ values between some of the initial areas. The $\Delta\bar{\delta}_{\mathrm{COI}_{t,k}}$ values between IG1 and two of its adjacent areas (IG2 and IG6) in Fig. 4 are increased continuously after the first disturbance. Therefore, IG1 swings separately and should be split from the network. By investigating Fig. 7, the network should be split into three following islands that are in agreement with Fig. 5:

Area 1 (island1), Area2-Area3 (island2) and Area4-Area8 (island3)

The outputs of the proposed P-ANFIS method optimized with PSO should be analyzed to investigate the performance of the suggested technique in correct islanding detection. The outputs of some ANFISs are shown in Fig. 8.

According to this figure, the output of ANFIS 1, which is responsible for stability assessment between areas 1 and 6, becomes unity earlier than other output indicating that area 1 should be separated from area 6, which is a correct decision

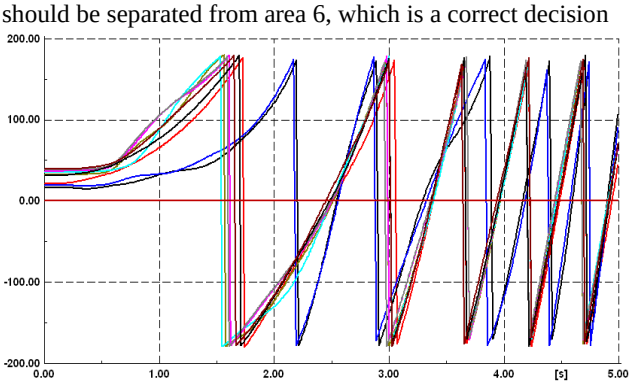


**Fig. 5.** rotor angle oscillation of generators in case

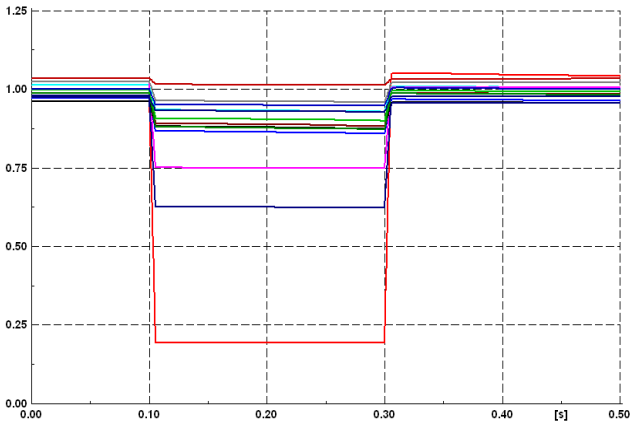


**Fig. 6.** The voltage magnitude of the generator

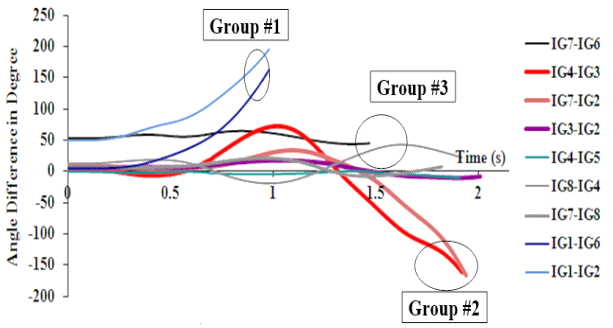


**Fig .7.** $\Delta\bar{\delta}_{\mathrm{COI}_{t,k}}$ between some initial areas in the 39-bus network at case1

In addition, the output of ANFIS 5 becomes near to unity (0.999) in 1.4 s, indicating that area 3 should be separated from area 4 that is a correct decision according to Fig. 7. As shown in Fig. 8, the outputs of assigned ANFISs between stable areas are too low and therefore the islanding command is not sent between these areas. The outputs of ANFIS 11 (area 8-area4) and ANFIS 7 (area 2-area3) are low as shown in this figure, indicating that these areas are coherent groups.

As shown in Table I, the islanding command is sent earlier by the proposed optimized P-ANFIS method than actual angle separation with enough margins to apply proper corrective actions. The time of islanding command to separate area 1 from area 6 is sent in 0.66 s, which is actually 0.38s before actual instability.

The outputs of some proposed ANFISs are provided in Tables II and III and are demonstrated with the ANN [9] and proposed ANFIS method in [12] where, there is no PSO application. According to these results, the stability/instability between areas is predicted with high accuracy before their actual uncontrolled separation that gives the proper time to perform a controlled islanding scheme. In addition, in comparison with both of the ANN and ANFIS method, the islanding necessity is predicted earlier between areas by proposed optimized ANFIS with PSO as shown in Tables II and III. This early detection gives more time to avoid

instability in coherent areas.

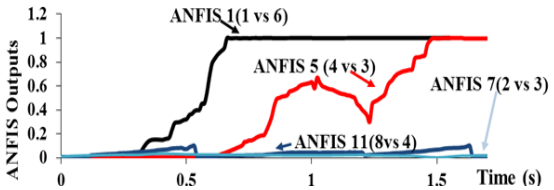


**Fig.8.** outputs of some optimized ANFISs with PSO in the P-ANFIS structure

*C. Case study 2*

The following faults are applied in this case:

A three-phase fault is applied in 0.1s in line 1-39 and is cleared in 0.3s by line breakers. The second fault is occurred in 0.5s and is cleared in 0.7s by opening the faulted line. $\Delta\bar{\delta}_{\mathrm{COI}_{t,k}}$ between areas in this case are presented in Fig. 9. A look at Fig. 9 indicates that the network should be split into three following coherent islands in that the areas belonged to each island are different from those in case 1:

Area 1 (island1), Area2-Area3 and Area6-Area8 (island2), Area4-Area5 (island 3)

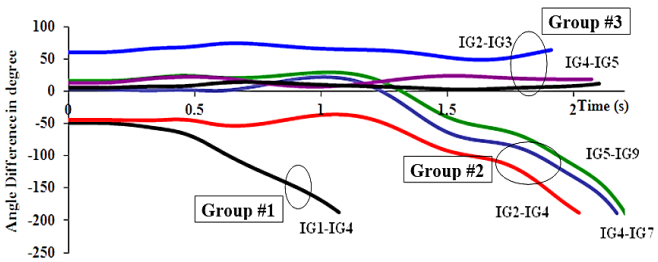


**Fig. 9.** $\Delta\bar{\delta}_{\mathrm{COI}_{t,k}}$ between some areas in case 2 at the 39-bus network

The outputs of some ANFISs are shown in Fig. 10. The early and correct detection of islanding necessity by P-ANFIS outputs are evident with the comparison of Figs. 9 and 10. According to Fig. 10, the islanding command is sent to separate area 2 from area 4 as a correct decision. The islanding command is sent in 1.42s, and the actual angle separation between these two IGs happens in 1.83s. The outputs of the proposed P-ANFISs are given in Tables IV and V and are demonstrated with other two methods including ANN and ANFIS without PSO application.

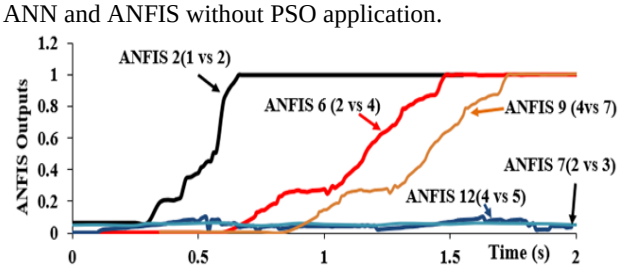


**Fig. 10.** The outputs of some optimized ANFISs with PSO in the P-ANFIS structure

By comparing the proposed method with the ANN results (Table IV), the P-ANFIS shows a more accurate and faster response than the ANN method. Like previous case, as shown in Table V, the performance of the proposed optimized ANFIS parameters with PSO is faster than applied ANFIS method in [12].

Therefore, there is enough time to conduct islanding and split the network into coherent stable islands.

## VII. CONCLUSION

In this study, a novel extensive-area intelligent technique is introduced to accurately and fast detect islanding necessity in power systems. The PSO algorithm is used in ANFIS training to determine the optimum membership function parameters and improve the speed and accuracy of islanding detection necessity. The proper inter-area-based extensive area signals are chosen and extensive stability studies are performed to create a proper training database.

After disturbance detection by the proposed method, the wide-area input signals are monitored by an algorithm and in the case of possible asynchronous oscillations, investigating the stability between areas in real-time is initiated by the P-ANFIS algorithm. As the oscillations are detected to be unstable, the islanding command is sent to split related areas from each other to construct stable islands.

The proposed technique is employed for New England 39-bus and demonstrated with the ANN method indicating that the islanding necessity and the time of islanding execution are determined with high accuracy and speed in all disturbances.

## APPENDIX

**TABLE I**

The time of islanding detection by P-ANFIS method and actual angle separation

| Areas | Time of detection by P-ANFIS (s) | Time of angle separation (s) |
|---|---|---|
| 1 vs 2 | 1.43 | 1.81 |
| 1 vs 6 | 0.66 | 1.04 |
| 2 vs 7 | 1.43 | 1.84 |
| 3vs 4 | 1.43 | 1.81 |

**TABLE II**

The outputs of some ANFISs optimized with PSO in New England 39-bus network at case1

| P-ANFIS-PSO method | | | | ANN method [9] | | | |
|---|---|---|---|---|---|---|---|
| ANFIS No. | Allocated Areas | Output | Time of detection (s) | ANN No. | Assigned Areas | Output | Time of detection (s) |

| | | | | | | | |
|---|---|---|---|---|---|---|---|
| 1 | 1 vs 6 | 0.999 | 0.75 | 1 | 1 vs 6 | 0.998 | 0.79 |
| 2 | 1 vs 2 | 0.989 | 0.72 | 2 | 1 vs 2 | 0.986 | 0.77 |
| 3 | 7 vs 8 | 0.015 | stable | 3 | 7 vs 8 | 0.032 | stable |
| 4 | 2 vs 8 | 0.999 | 1.48 | 4 | 2 vs 8 | 0.998 | 1.495 |
| 5 | 3vs 4 | 0.998 | 1.42 | 5 | 3vs 4 | 0.999 | 1.435 |
| 7 | 2 vs 3 | 0.012 | stable | 7 | 2 vs 3 | 0.0048 | stable |
| 8 | 2 vs 6 | 0.999 | 1.43 | 8 | 2 vs 6 | 0.997 | 1.444 |
| 10 | 3 vs 5 | 0.996 | 1.46 | 10 | 3 vs 5 | 0.997 | 1.471 |
| 11 | 8 vs 4 | 0.021 | stable | 11 | 8 vs 4 | 0.032 | stable |
| 12 | 4 vs 5 | 0.032 | stable | 12 | 4 vs 5 | 0.037 | stable |

**TABLE III**

The outputs of some ANFISs optimized with PSO in New England 39-bus network at case1

| **P-ANFIS-PSO method** | | | | **P-ANFIS method [12]** | | | |
|---|---|---|---|---|---|---|---|
| ANFIS No. | Allocated Areas | Output | Time of detection (s) | ANFIS No. | Assigned Areas | Output | Time of detection (s) |
| 1 | 1 vs 6 | 0.999 | 0.75 | 1 | 1 vs 6 | 0.997 | 0.77 |
| 2 | 1 vs 2 | 0.989 | 0.72 | 2 | 1 vs 2 | 0.984 | 0.75 |
| 3 | 7 vs 8 | 0.015 | stable | 3 | 7 vs 8 | 0.024 | stable |
| 4 | 2 vs 8 | 0.999 | 1.48 | 4 | 2 vs 8 | 0.967 | 1.612 |
| 5 | 3vs 4 | 0.998 | 1.42 | 5 | 3vs 4 | 0.989 | 1.402 |
| 7 | 2 vs 3 | 0.012 | stable | 7 | 2 vs 3 | 0.012 | stable |
| 8 | 2 vs 6 | 0.999 | 1.43 | 8 | 2 vs 6 | 0.965 | 1.487 |
| 10 | 3 vs 5 | 0.996 | 1.46 | 10 | 3 vs 5 | 0.999 | 1.468 |
| 11 | 8 vs 4 | 0.021 | stable | 11 | 8 vs 4 | 0.036 | stable |
| 12 | 4 vs 5 | 0.032 | stable | 12 | 4 vs 5 | 0.042 | stable |

**TABLE IV**

The outputs of some ANFISs optimized with PSO in New England 39-bus network at case2

| **P-ANFIS method** | | | | **ANN method [9]** | | | |
|---|---|---|---|---|---|---|---|
| ANFIS No. | Allocated Areas | Output | Time of detection (s) | ANFIS No. | Assigned Areas | Output | Time of detection (s) |
| 1 | 1 vs 6 | 0.998 | 0.546 | 1 | 1 vs 6 | 0.998 | 0.576 |
| 2 | 1 vs 2 | 0.999 | 0.54 | 2 | 1 vs 2 | 0.999 | 0.565 |
| 3 | 7 vs 8 | 0.998 | stable | 3 | 7 vs 8 | 0.998 | stable |
| 5 | 3vs 4 | 0.997 | 1.42 | 5 | 3vs 4 | 0.997 | 1.47 |
| 7 | 2 vs 3 | 0.017 | stable | 7 | 2 vs 3 | 0.017 | stable |
| 8 | 2 vs 6 | 0.988 | stable | 8 | 2 vs 6 | 0.988 | stable |
| 9 | 4 vs 6 | 0.996 | 1.52 | 9 | 4 vs 6 | 0.996 | 1.59 |
| 10 | 3 vs 5 | 0.998 | 1.44 | 10 | 3 vs 5 | 0.998 | 1.52 |
| 11 | 8 vs 4 | 0.997 | 1.47 | 11 | 8 vs 4 | 0.997 | 1.54 |
| 12 | 4 vs 5 | 0.043 | stable | 12 | 4 vs 5 | 0.043 | stable |

**TABLE V**

The outputs of some ANFISs optimized with PSO in New England 39-bus network at case2

| **P-ANFIS-PSO method** | | | | **P-ANFIS method [12]** | | | |
|---|---|---|---|---|---|---|---|
| ANFIS No. | Allocated Areas | Output | Time of detection (s) | ANFIS No. | Assigned Areas | Output | Time of detection (s) |
| 1 | 1 vs 6 | 0.998 | 0.546 | 1 | 1 vs 6 | 0.998 | 0.582 |
| 2 | 1 vs 2 | 0.999 | 0.54 | 2 | 1 vs 2 | 0.999 | 0.556 |
| 3 | 7 vs 8 | 0.998 | stable | 3 | 7 vs 8 | 0.998 | stable |
| 5 | 3vs 4 | 0.997 | 1.42 | 5 | 3vs 4 | 0.997 | 1.52 |
| 7 | 2 vs 3 | 0.017 | stable | 7 | 2 vs 3 | 0.017 | stable |
| 8 | 2 vs 6 | 0.988 | stable | 8 | 2 vs 6 | 0.988 | stable |
| 9 | 4 vs 6 | 0.996 | 1.52 | 9 | 4 vs 6 | 0.996 | 1.55 |
| 10 | 3 vs 5 | 0.998 | 1.44 | 10 | 3 vs 5 | 0.998 | 1.57 |
| 11 | 8 vs 4 | 0.997 | 1.47 | 11 | 8 vs 4 | 0.997 | 1.62 |
| 12 | 4 vs 5 | 0.043 | stable | 12 | 4 vs 5 | 0.043 | stable |

## REFERENCES

[1] L.L. Lai, H.T. Zhang, C.S. Lai, F.Y. Xu, S. Mishra,"Investigation on July 2012 Indian blackout.", *International Conference on Machine Learning and Cybernetics*, pp. 92-97, Jul. 2013

[2] Y. Makarov, Y, Reshetov, Y. Strojev, N. Voropai, "Blackout prevention in the United States, Europe, and Russia", *Proceedings of the IEEE*, Vol. 93, No. 11, pp, 1942 - 1955, Nov. 2005,

[3] K. Yamashita, S.K. Joo, J. Li, P. Zhang, C.C. Liu. "Analysis, control, and economic impact assessment of major blackout events", *European Transactions on electrical Power*, Vol. 18, No. 8, pp. 854-871, Nov. 2008

[4] M. Abasi, M. Joorabian, A. Saffarian, S.G. Seifossadat, "A novel complete dynamic and static model of 48-pulse VSC-based GUPFC for parallel transmission lines", *International Journal of Industrial Electronics, Control and Optimization*, Vol. 3, No. 4, pp. 447-457, Mar. 2020

[5] M.M. Adibi, R.J Kafka, S. Maram, L.M. Mili, "On power system controlled separation". *IEEE Transaction on Power Systems*, Vol. 21, No. 4, pp. 1894 – 1902, Nov. 2006

[6] L. Ding, F, Gonzalez, P. Wall, V. Terzija, "Two-step spectral clustering-controlled islanding algorithm", *IEEE Transaction on Power Systems*, Vol. 28, No. 1, pp. 75 - 84 Feb. 2013

[7] N. Senroy, G.T. Heydt, "Timing of a controlled islanding strategy." *2005/2006 IEEE/PES Transmission and Distribution Conference and Exhibition*, pp, 483-491, May. 2016.

[8] N. Senroy, G.T. Heydt, V. Vittal, "Decision tree assisted controlled islanding.", *IEEE Transaction on Power Systems*, Vol. 21, No. 4, pp. 1790-1797, Nov. 2006.

[9] Gh. Isazadeh, A. Khodabakhshian, E. Gholipour, "A new intelligent wide area controlled islanding detection method in interconnected power systems", *International Transaction on electrical energy systems*, Vol. 27, No 7, Jul. 2017

[10] J. Yan, C.C. Liu, U. Vaidya, "PMU-based monitoring of rotor angle dynamics", *IEEE Transaction on Power Systems*, Vol 26, No. 4, pp. 2125 - 2133, Nov. 2011

[11] D.P. Wadduwage, C.Q. Wu, U.D. Annakkage."Power system transient stability analysis via the concept of Lyapunov exponents". *Electric Power System Research*, Vol. 104, pp. 183-192, Nov. 2013.

[12] Gh. Isazadeh, A. Khodabakhshian, E. Gholipour. "A New Intelligent Controlled Islanding Scheme in Large Interconnected Power Systems", *IET generation transmission Distribution*, Vol. 9, No. 16, pp. 2686 – 2696, Dec. 2015.

[13] K. Sun, K. Hur, P. Zhang. "A new unified scheme for controlled power system separation using synchronized phasor measurements", *IEEE Transaction on Power Systems*, Vol. 26, No. 3, pp. 1544 – 1554, Aug. 2011

[14] M.R. Salimian, M.R Aghamohammadi, "A new index based on proximity of inter-area oscillation to UEP point for predicting proper time of controlled islanding", *International Journal of Electrical Power & Energy Systems*, Vol. 104, pp. 383-400, Jan. 2019,

[15] T. Amraee, H. Saberi, "Controlled islanding using transmission switching and load shedding for enhancing power grid resilience", *International Journal of Electrical Power & Energy Systems*, Vol. 91, pp. 135-143, Oct. 2017.

[16] M. Amini, H. Samet, A.R. Seifi, M. Al-Dhaifallah, Z.M. Ali, "An Effective Multi-Solution Approach for Power System Islanding". *IEEE Access*, pp. 93200 – 93210, May. 2020.

[17] F. TANG, J. YANG, Q. LIAO, et al. "Out-of-step oscillation splitting criterion based on bus voltage frequency.", *Journal of Modern Power Systems and Clean Energy*, Vol. 3, No. 3, pp. 341 - 352, Sep. 2015.

[18] S. Mohagheghi, G.K. Venayagamoorthy, R.G. Harley," Optimal neuro-fuzzy external controller for a STATCOM in the 12-Bus benchmark power system", *IEEE Trans. Power Delivery*, Vol. 22, No. 4, pp. 2548-2558, Oct. 2007.

[19] R. Jang, T. Sun, and E. Mizutani, "Neuro-Fuzzy and Soft Computing a Computational Approach to Learning and Machine Intelligence." *IEEE Transactions on Automatic Control*, (1997). Vol. 42, No. 10 , pp. 1482 – 1484, Oct. 1997

[20] J.-S. R. Jang, "ANFIS: Adaptive Network-Based Fuzzy Inference Systems", *IEEE Transactions on Systems., Man, Cybern*, Vol. 23, No. 3, pp. 665 – 685, May. /Jun. 1993

[21] Y.del Valle, G.K Venayagamoorthy, S. Mohagheghi, J.-C. Hernandez, R.G. Harley, "Particle Swarm Optimization: Basic Concepts, Variants and Applications in Power Systems", *IEEE Transaction on Evolutionary Computation*, Vol. 12, No. 2, Apr. 2008

[22] H. Yoshida, K. Kawata, Y. Fukuyama, S. Takayama, Y. Nakanishi, A Particle Swarm Optimization for Reactive Power and Voltage Control Considering Voltage Security Assessment", *IEEE Transaction on Power Sytems*, Vol. 15, No. 4, pp. 1232 – 1239, Nov. 2000

[23] R. Gurusinghe, A. D. Rajapakse, "Post-Disturbance Transient Stability Status Prediction Using Synchrophasor Measurements", *IEEE Trans. on Power Systems*, Vol. 31, No. 5, pp. 3656-3664, Sep. 2016.

[24] M. Abasi, M. Razaz, G. Seifossadat, S. Moosapour "Presenting a New Formulation to Analyze and Determine Unbalance Voltage Produced at the Place of Load Resulting from Network and Loads Unbalance and Asymmetry of Transmission Lines in Radial Power Systems'', *Majlesi Journal of Energy Management*, Vol. 4, No. 3, pp.1-7, Sep. 2015.

[25] M. Abasi, S.G. Seifossadat, M. Razaz, S.S. Moosapour "Determining the contribution of different effective factors to individual voltage unbalance emission in n-bus radial power systems, Journal International Journal of

Electrical Power & Energy Systems", *International Journal of Electrical Power & Energy Systems*, Vol. 94, No.12, pp.393-404, Jan. 2018.

[26] Power Systems Test Case Archive, https://www.ee.washington.edu/research/pstca/39 bus, 05/06/2020

**Hojatollah Makvandi** is a PhD student in power engineering at Department of Electrical Engineering, Dezful Branch, Islamic Azad University, Dezful, Iran. He is a utility &power plant manager in the Abadan oil refining company. His research interests include Gas & steam turbine, Micro-grid and islanding, FACTS devices.

**Mahmood Joorabian** was born in Shooshtar, Iran, in 1961. He received his B.E.E degree from University of New Haven, CT, USA, M.Sc. degree in Electrical Power Engineering from Rensselaer Polytechnic Institute, NY, USA and Ph.D. degree in Electrical Engineering from University of Bath, Bath, UK in 1983, 1985 and 1996, respectively. He has been with the Department of Electrical Engineering at Shahid Chamran University as Senior Lecturer (1985), Assistant Professor (1996), Associate Professor (2004) and Professor (2009). His main research interests are fault location, facts devices, power system protection, power quality, and applications of intelligence technique in power systems.

**Hassan Barati** was born in Dezful, Iran, in 1969. He received the B.Sc. degree in electronic engineering from the Isfahan University of Technology, Isfahan, Iran, in 1993, the M.Sc. degree in electrical engineering from the Tabriz University, Tabriz, Iran, in 1996 and the Ph.D. degree in Electrical Engineering from the Islamic Azad University, Science and Research Branch, Tehran, Iran, in 2007. Currently, he is an Associate Professor in the Electrical Engineering Department, Dezful Branch, Islamic Azad University, Dezful, Iran. His research interests are power systems operation & Reliability, restructured power systems, Micro-grids and Smart Grids, FACTS devices.